Real-Time Fault Diagnosis of Permanent Magnet Synchronous Motor and Drive System

Saeed Hasan Ebrahimi

UiA University of Agder

Doctoral Dissertations at the University of Agder 414

Saeed Hasan Ebrahimi

Real-Time Fault Diagnosis of Permanent Magnet Synchronous Motor and Drive System

Doctoral Dissertation for the Degree *Philosophiae Doctor (PhD)* at
the Faculty of Engineering and Science, Specialisation in Mechatronics

University of Agder
Faculty of Engineering and Science
2023

Doctoral Dissertations at the University of Agder 414
ISSN: 1504-9272
ISBN: 978-82-8427-129-3

Printed by Make!Graphics
Kristiansand

Preface

The research presented in this thesis was conducted in the Faculty of Engineering and Science of the University of Agder (UiA), under the supervision of associate professor Martin Choux and co-supervision of professor Van Khang Huynh.

I started my university education in electrical engineering when I was admitted to the Iran University of Science and Technology, one of the most competitive engineering Universities in the country, with a full scholarship in 2009. After passing five semesters in general electrical engineering and learning more about different types of research fields, I became extremely interested in electrical machines and power electronics and this led me to choose electrical power engineering and continued the next three semesters in this specialization. After graduating with a bachelor's degree, I did not hesitate a moment and continued my studies for a master's degree at the same university with a full scholarship. During my master's studies, I focused on both doing research and experimental analysis. I was a research assistant in Special Electrical Machines & Drives Lab, mainly focused on the analysis and design of electrical machines using FEM. I assisted two Ph.D. students with several projects in the design and optimization of electrical machines and drive systems. Becoming skillful in working with microprocessors, programming, and hands-on experiments, I also designed and fabricated several power electronic devices including DC and AC motor drives, charge controllers for Lithium-ion batteries, DC-DC converters, and an electronic centrifugal switch for single-phase induction motors.

Considering both personal interests and career aspirations, I decided to pursue a Ph.D. degree at the University of Agder, with a specialization in Mechatronics. Therefore, I started working as Ph.D. research fellow in February 2018. I learned a lot of new useful skills during my doctoral project like signal processing, machine learning, and structural analysis which are very practical for fault diagnosis purposes. Combining my prior and existent knowledge and experience, I have been able to deploy fascinating experiments including assembly, control, and fault diagnosis of electric motors while taking benefit of the hardware-in-the-loop.

During my bachelor's and master's studies, I was immersed in the design, analysis, control, and optimization of electrical machines and power electronic converters. As for the Ph.D. project topic, I felt it is essential to be related to electrical machines and drive systems. Therefore, I found UiA's graduate program as the ideal platform to achieve these goals and constantly develop myself under the university's research-oriented culture.

During my study and research at UiA, I experienced a lot of great moments as I learned new skills and did fascinating experiments. However, I also faced some serious challenges that slowed down the progress or delayed the results. One of the big challenges was the

amount of time that was dedicated to each phase of the research. The research presented here consists of several different phases in the span of three years. Therefore, facing a limited amount of time to spend on each of the phases, compromises have been made to achieve certain goals and move on to the next stage. Moreover, the timing of the research was another major limiting factor. Extra effort was made to get acceptable results before specific conference deadlines, especially international conferences. Further, the COVID-19 pandemic not only had a huge mental and psychological impact but also occurred in one of the most crucial phases of this research. During the lockdown, the UiA's machine lab was closed and thus, experimental analysis and results were delayed. Nevertheless, I managed to assemble a great experimental setup in the lab, get some interesting results, and publish several papers as a result of this study.

Acknowledgments

I would like to express my gratitude to my primary supervisor, Martin Choux, whose encouragement, support, and assistance guided me throughout this project. I would also like to thank my co-supervisor, Van Khang Huynh, who supported me and offered deep insight into this study.

I would like to thank Michael Rygaard Hansen, Dean of faculty of engineering and science, Geir Grasmo, Head of the department of engineering sciences, Emma Elisabeth Horneman, senior advisor, and Kristine Evensen Reinfjord, Ph.D. advisor for their support. I wish to extend my special thanks to the engineers in the Machine Lab of the University of Agder including Roy Werner Folgerø, Steve Schading, Carl Thomas Duus, Karl Berge Rød, Harald Sauvik, and Jan Christian Bjerke Strandene who facilitated the assembly of the project test-setups by providing technical support and guidance. I would also like to show my deep appreciation to my colleagues and friends especially Rafael Tavares, Jagath Senanyaka, Shaun Falconer, Jannik Jakobsen, Sveinung Attestog, and Arild Bergesen Husebø for all the mental/technical support but more importantly, for the great scientific discussions.

Last but not the least, I want to express my deepest gratitude to my family who has supported me in every matter during my whole life. Words cannot adequately express my gratitude to my dear mother, father, sister, and brothers.

Saeed Hasan Ebrahimi
Grimstad, Norway
December 2022

Abstract

Permanent Magnet Synchronous Motors (PMSMs) have gained massive popularity in industrial applications such as electric vehicles, robotic systems, and offshore industries due to their merits of efficiency, power density, and controllability. PMSMs working in such applications are constantly exposed to electrical, thermal, and mechanical stresses, resulting in different faults such as electrical, mechanical, and magnetic faults. These faults may lead to efficiency reduction, excessive heat, and even catastrophic system breakdown if not diagnosed in time. Therefore, developing methods for real-time condition monitoring and detection of faults at early stages can substantially lower maintenance costs, downtime of the system, and productivity loss.

In this dissertation, condition monitoring and detection of the three most common faults in PMSMs and drive systems, namely inter-turn short circuit, demagnetization, and sensor faults are studied. First, modeling and detection of inter-turn short circuit fault is investigated by proposing one FEM-based model, and one analytical model. In these two models, efforts are made to extract either fault indicators or adjustments for being used in combination with more complex detection methods. Subsequently, a systematic fault diagnosis of PMSM and drive system containing multiple faults based on structural analysis is presented. After implementing structural analysis and obtaining the redundant part of the PMSM and drive system, several sequential residuals are designed and implemented based on the fault terms that appear in each of the redundant sets to detect and isolate the studied faults which are applied at different time intervals. Finally, real-time detection of faults in PMSMs and drive systems by using a powerful statistical signal-processing detector such as generalized likelihood ratio test is investigated. By using generalized likelihood ratio test, a threshold was obtained based on choosing the probability of a false alarm and the probability of detection for each detector based on which decision was made to indicate the presence of the studied faults. To improve the detection and recovery delay time, a recursive cumulative GLRT with an adaptive threshold algorithm is implemented. As a result, a more processed fault indicator is achieved by this recursive algorithm that is compared to an arbitrary threshold, and a decision is made in real-time performance. The experimental results show that the statistical detector is able to efficiently detect all the unexpected faults in the presence of unknown noise and without experiencing any false alarm, proving the effectiveness of this diagnostic approach.

Sammendrag

Permanent magnet synkronmotorer har fått enorm popularitet i industrielle applikasjoner som elektriske kjøretøy, robotsystemer og offshore-industrier på grunn av deres fordeler med effektivitet, krafttetthet og kontrollerbarhet. PMSM-er som jobber i slike applikasjoner er konstant utsatt for elektriske, termiske og mekaniske påkjenninger, noe som resulterer i forskjellige feil som elektriske, mekaniske og magnetiske feil. Disse feilene kan føre til effektivitetsreduksjon, overdreven varme og til og med katastrofalt systembrudd hvis de ikke blir diagnostisert tidlig. Derfor kan utvikling av metoder for sanntids tilstandsovervåking og oppdagelse av feil på tidlige stadier redusere vedlikeholdskostnadene, nedetid av systemet og produktivitetstap betydelig.

I denne avhandlingen studeres tilstandsovervåking og deteksjon av de tre vanligste feilene i PMSM-er og drivsystemer, nemlig inter-turn kortslutning, demagnetisering og sensorfeil. Først undersøkes modellering og deteksjon av inter-turn kortslutningsfeil ved å foreslå en FEM-basert modell og en analytisk modell. I disse to modellene arbeides det med å trekke ut enten feilindikatorer eller justeringer for bruk i kombinasjon med mer komplekse deteksjonsmetoder. Deretter presenteres en systematisk feildiagnose av PMSM og drivsystem som inneholder flere feil basert på strukturell analyse. Etter å ha implementert strukturanalyse og oppnådd den redundante delen av PMSM og drivsystemet, blir flere sekvensielle rester designet og implementert basert på feilbegrepene som vises i hvert av de redundante settene for å oppdage og isolere de studerte feilene som brukes ved forskjellige tidsintervaller . Til slutt undersøkes sanntidsdeteksjon av feil i PMSM-er og drivsystemer ved å bruke en kraftig statistisk signalbehandlingsdetektor som generalisert sannsynlighetsforholdstest. Ved å bruke generalisert sannsynlighetsratiotest ble det oppnådd en terskel basert på å velge sannsynligheten for en falsk alarm og sannsynligheten for deteksjon for hver detektor basert på hvilken beslutning som ble tatt for å indikere tilstedeværelsen av de studerte feilene. For å forbedre deteksjons- og gjenopprettingsforsinkelsestiden, implementeres en rekursiv kumulativ GLRT med en adaptiv terskelalgoritme. Som et resultat oppnås en mer behandlet feilindikator av denne rekursive algoritmen som sammenlignes med en vilkårlig terskel, og en avgjørelse tas i sanntidsytelse. De eksperimentelle resultatene viser at den statistiske detektoren er i stand til effektivt å oppdage alle uventede feil i nærvær av ukjent støy og uten å oppleve noen falsk alarm, noe som beviser effektiviteten til denne diagnostiske tilnærmingen.

Publications

The following publications are based on research activities conducted by the author and have been published or submitted for publication in peer-reviewed journals or conference proceedings.

Paper A S. H. Ebrahimi, M. Choux, and V. K. Huynh. Modelling Incipient Inter-Turn Short Circuit Fault in Permanent Magnet Synchronous Motors. In *Proceedings of the 22nd International Conference on the Computation of Electromagnetic Fields (COMPUMAG 2019)*, 2019.

Paper B S. H. Ebrahimi, M. Choux, and V. K. Huynh. Modeling Stator Winding Inter-Turn Short Circuit Faults in PMSMs including Cross Effects. In *Proceedings of 2020 International Conference on Electrical Machines (ICEM)*, 2020. ISBN: 978-1-7281-9946-7.

Paper C S. H. Ebrahimi, M. Choux, and V. K. Huynh. Detection and Discrimination of Inter-Turn Short Circuit and Demagnetization Faults in PMSMs Based on Structural Analysis. In *Proceedings of 2021 22nd IEEE International Conference on Industrial Technology (ICIT)*, 2021. ISBN: 978-1-7281-5731-3.

Paper D S. H. Ebrahimi, M. Choux, and V. K. Huynh. Diagnosis of Sensor Faults in PMSM and Drive System Based on Structural Analysis. In *Proceedings of 2021 IEEE International Conference on Mechatronics (ICM)*, 2021. ISBN: 978-1-7281-4443-6.

Paper E S. H. Ebrahimi, M. Choux, and V. K. Huynh. Real-Time Detection of Incipient Inter-Turn Short Circuit and Sensor Faults in Permanent Magnet Synchronous Motor Drives Based on Generalized Likelihood Ratio Test and Structural Analysis. In *MDPI - Sensors*, 2022. EISSN 1424-8220.

Paper F S. H. Ebrahimi, M. Choux, and V. K. Huynh. Statistical Detection of Demagnetization and Inter-Turn Short Circuit Faults in PMSM Using Recursive GLRT with Adaptive Threshold. Under review in *IEEE Transactions on Industrial Electronics*, 2022. ISSN 0278-0046.

The following publication is within the framework and published during the time of this project, but is not included in this dissertation.

Paper G V. Szabo, S. H. Ebrahimi, M. Choux, M. Goodwin. ITSC Fault Diagnosis in Permanent Magnet Synchronous Motor Drives Using Shallow CNNs. In *Proceedings of 23rd International Conference on Engineering Applications of Neural Networks*, 2022. ISSN: 1865-0937.

Contents

List of Figures

List of Tables

Chapter 1

Introduction

1.1 Background

Permanent magnet synchronous motors (PMSMs) have been used in a wide range of industrial applications due to their high efficiency, high power density, and high reliability [1–3]. These features and advantages make PMSMs more interesting candidates especially for transportation, robotic systems, medical systems, renewable energy, and military applications compared to other electric motors. On the other hand, this widespread utilization of PMSMs has raised certain reliability concerns due to the possibility of unexpected component failures [4].

PMSMs are often hired to be used in harsh industrial environments, and therefore, are constantly exposed to high voltage, electrical loading, thermal stress, mechanical stress, winding vibration, power surge, aging, environmental contamination, and foreign objects [5,6]. These phenomena can gradually or instantly create the basis for various types of faults in PMSM structure such as stator short circuit and demagnetization faults, as well as faults in PMSM's peripheral devices such as inverter faults, rotor feedback faults, and sensor faults. These faults will eventually result in system breakdown, costly downtimes, expensive repairing costs, efficiency reduction, and even human casualties. Therefore, to overcome these issues and to improve the system's reliability, accurate condition monitoring of PMSMs is necessary [7].

In this dissertation, detection and isolation of common faults in PSMS and drive system including inter-turn short circuit (ITSC), demagnetization, rotor feedback device, and sensor faults in the drive system are discussed. Primarily, a model-based fault detection technique called structural analysis is designed and implemented to inform us about the presence of each fault and then followed by a statistical signal processing detector to trip the alarm. To evaluate the overall effectiveness of the developed diagnosis methodology, a laboratory test setup is built in UiA's machine lab as shown in Figure 1.1. The test setup consists of a permanent magnet synchronous motor/generator drive-train set, torque transducer, incremental encoder feedback device, 3-phase inverter with embedded voltage and current sensors, dc supplies, and protection relays. Furthermore, a dSpace MicroLabBox is used to implement motor control strategy, diagnostic system, and to collect data.

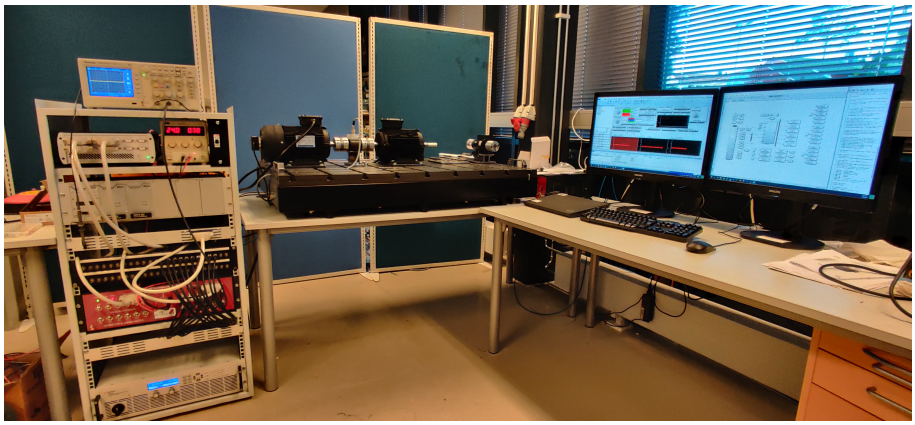

Figure 1.1: PMSM and drive system.

1.2 Motivation and challenges

Condition monitoring and fault diagnosis of electrical machines have gained significant attention in both industry and academia and various approaches have been proposed to detect faults in electric motors. Each diagnostic method has its own advantages and disadvantages. Therefore, a preferable diagnostic system must have reasonable justification based on the following criteria:

1.2.1 Accuracy, robustness, and reliability

Complex diagnostic systems play a key role in preventing catastrophic failures. Such systems have often been developed through inevitable uncertainties linked to assumptions and limited information on model parameters, signal estimations, manufacturing imprecision, environmental or sensor noise, and description of loads. The propagation of these uncertainties adversely affects the performance of the diagnostic system and, consequently, leads to increased false alarms, poor detection, unexpected failures, and even system shutdown [8]. Hence, employing a diagnosis methodology that performs well in presence of the issues mentioned above is of great importance and can guarantee the accuracy, robustness, and reliability of the whole system [9].

1.2.2 Computational processing power, hardware complexity, and time demand

Depending on the type of method used for fault detection, different levels of processing power, hardware, and time are required. Some methods monitor one or more motor signals and further process the data using time-frequency tools such as Fourier transform [10], wavelet transform [11], and Kalman filter [12] to extract fault features. Furthermore, drive systems and other fault types may produce similar patterns in the signal spectra and this has convinced some researchers to employ an external resistor network or use the neutral point connection of the stator windings [13]. Some other methods such as the finite-element method (FEM) are very accurate and robust, however, they are computationally heavy and challenging to use in real-time diagnosis. Thus, a diagnostic procedure is

recommended that is cost-effective and has a reasonable trade-off between performance and hardware requirements.

1.2.3 Prior knowledge and required data for training

In addition to accuracy and hardware complexity, the amount of required knowledge and observed data is an important factor in designing the diagnostic system. For example, FEM-based diagnosis techniques require deep knowledge of the system, e.g. detailed dimensions, and material characteristics [1]. On the other hand, data-driven methods such as neural network, require a lot of data for training to be considered robust and reliable [14–16]. Therefore, not only must the diagnostic methodology be accurate and easy to implement, but also its performance should not be greatly dependent on the amount of prior knowledge and data.

1.2.4 Problem statement

This research aims to address theoretical and practical research problems related to the diagnosis of faults in PMSM and drive system. These problems are summarized as:

- How do different faults affect the performance of the PMSM and drive system?
- How could machine dynamic equations be used in forming residuals and fault observers?
- How could a systematic diagnostic structure be formed to include various faults in real-time observers?
- How could faults be effectively detected with corresponding alarms in the decision-making system?

1.3 Contributions of the dissertation

The scientific contributions of this dissertation are withdrawn from six research papers, either published or submitted for publication in international journals and conference proceedings.

Paper A: Modeling Incipient Inter-Turn Short Circuit Fault in Permanent Magnet Synchronous Motors

Summary: This paper presents a FEM-based model of the stator winding inter-turn short circuit faults in PMSM. Inter-turn short circuit fault occurs when a few turns in the stator winding are shorted over time due to insulation degradation. Many previous studies have modeled this as a symmetrical phenomenon while short circuit fault causes unbalance in flux distribution more around the faulty coil and therefore, it should be modeled using an unsymmetrical FEM-based model. In addition, motor signals are obtained from the time-stepping FEA, including torque, currents, instantaneous power of phase-a, and

input power. Finally, a signal-processing tool, Fast Fourier Transform (FFT), is used to transform the time-domain results into the frequency domain and a comparison is made between different fault indicators.

Contributions: Conventional lumped-parameter models in the literature have limitations in precisely addressing the ITSC faults. This is because $dq0$ models assume that the shape of MMF wave-form is sinusoidal in ac machines while this assumption is not considered valid due to loss of winding symmetries under abnormal conditions. As a result, localized ITSC faults in the coils of each phase winding and their effect on other coils and phase windings are not modeled realistically. Here, A FEM model of the faulty PMSM is proposed that allows the investigation of local ITSC faults. An asymmetric ITSC fault in one of the coils of the phase winding is implemented that replicates the realistic faulty phenomenon. Due to the asymmetric nature of the fault, the magnetic flux in the stator and rotor cores are unbalanced. Based on the results obtained from FEM simulation, different fault indicators for the detection of ITSC fault are obtained. The performance of these fault indicators are compared by using a time-frequency FFT analysis. The FFT analysis of currents, phase-a instantaneous power and torque signals shows that certain harmonics can be observed in spectra under an ITSC fault case. Since some of these components under the faulty condition can be affected either by load change and noise or are inconsistent at higher frequencies, using input power as the ITSC fault indicator is recommended instead.

This paper has been published as: S. H. Ebrahimi, M. Choux, and V. K. Huynh. Modelling Incipient Inter-Turn Short Circuit Fault in Permanent Magnet Synchronous Motors. In *Proceedings of the 22nd International Conference on the Computation of Electromagnetic Fields (COMPUMAG 2019)*, 2019.

Paper B: Modeling Stator Winding Inter-Turn Short Circuit Faults in PMSMs including Cross Effects

Summary: This paper presents a detailed analytical model of the stator winding inter-turn short circuit faults in PMSM. It is assumed that the phase-windings consist of multiple coils in series and the short circuit appears only in a few turns of one of the coils. The short circuit is modeled based on deformed fluxes or inductance variations caused by flux linkages, depending on the distribution of the coils in the same phase winding or other phase windings. Therefore, this model can be used for investigating multiple short circuits in different phase windings as well. In addition, the insulation degradation is modeled as resistance and different fault ratios are investigated to evaluate different fault severity and scenarios. Finally, the proposed model is verified by a 2-D finite element analysis (FEA), and the results show a good agreement between the analytical model and FEA.

Contributions: Modeling the interaction of one fault on other phases is important to understand the behavior of magnetic flux and output characteristics of an unbalance PMSM

under faults. This type of modeling is specifically useful when developing a fault indicator in both steady and transient states. This study presents a novel analytical modeling of a faulty PMSM that models asymmetric ITSC faults in different coils of phase windings. The model is established based on how to deal with local ITSC faults in single coils of each phase winding. Therefore, not only are the cross effects between healthy and faulty coils in each phase winding taken into account but also the cross effects between healthy and faulty coils of different phase windings are considered. As a result, the model is able to simulate not only single faults but also simultaneous ITSC faults in any of the phases. The comparison of results achieved from the model to FEM results verifies that this analytical model is a good choice to be coupled with model-based diagnosis methods such as structural analysis due to its simplicity and decent accuracy. Unlike FEM-based models, the presented dynamic model can properly model the behavior of PMSM under different fault scenarios, without demanding high processing power, time, detailed dimensions, and material information.

This paper has been published as: S. H. Ebrahimi, M. Choux, and V. K. Huynh. Modeling Stator Winding Inter-Turn Short Circuit Faults in PMSMs including Cross Effects. In *Proceedings of 2020 International Conference on Electrical Machines (ICEM)*, 2020. ISBN: 978-1-7281-9946-7.

Paper C: Detection and Discrimination of Inter-Turn Short Circuit and Demagnetization Faults in PMSMs Based on Structural Analysis

Summary: This paper presents a fault diagnosis methodology based on structural analysis for the investigation of ITSC and demagnetization faults in a PMSM. A healthy dynamic mathematical model of PMSM in the *abc* frame is used including specific added terms relevant to the presence of ITSC and demagnetization faults in the corresponding equations. The added terms account for deviations in the resistance and inductance of the stator winding caused by the ITSC fault, and the deviations in the PM linkage flux caused by a demagnetization fault which appears in the three-phase flux and voltage equations. Moreover, the analytical redundancy of the model is determined based on the PMSM's structural model and based on that, four sequential residuals are designed to inspect the presence of each fault. Finally, the proposed model is implemented in Matlab/Simulink to verify its effectiveness in different fault scenarios with embedded white Gaussian noise in the measured signals.

Contributions: Detection and isolation of internal faults in PMSMs is not present in the studies that have developed models based on structural analysis. Here, a model-based fault detection and isolation methodology is developed based on structural analysis to investigate ITSC and demagnetization faults in PMSM. Four residuals are obtained from the redundant part of the structural model and coupled with the analytical model proposed in paper B. ITSC faults in each phase and demagnetization fault are applied on the motor and simulation results are obtained. In addition, white Gaussian noise is added

to the measured signals to make the results more realistic. The parameters of the white Gaussian noise are derived from experimental measurements in the lab. The results show that residuals are able to efficiently detect and isolate even small faults in the presence of noise, proving the effectiveness of this diagnostic approach.

This paper has been published as: S. H. Ebrahimi, M. Choux, and V. K. Huynh. Detection and Discrimination of Inter-Turn Short Circuit and Demagnetization Faults in PMSMs Based on Structural Analysis. In *Proceedings of 2021 22nd IEEE International Conference on Industrial Technology (ICIT)*, 2021. ISBN: 978-1-7281-5731-3.

Paper D: Diagnosis of Sensor Faults in PMSM and Drive System Based on Structural Analysis

Summary: Paper D presents a model-based fault detection and isolation methodology based on structural analysis for investigating eleven measurement faults in PMSMs. These faults include three-phase voltage and current sensors, DC bus voltage and current sensors, the motor's angular velocity, position, and load torque. A structure model is built using a combination of healthy dynamic mathematical models of PMSM both in *abc* and *dq* frames including all the aforementioned measurements, and specific terms related to each fault are added to the corresponding equations. Furthermore, the analytical redundancy of the model is determined based on the system's structural model and the redundant model is then subdivided into smaller over-determined testable subsystems, in which the faults are detectable and isolable. Nine sequential residuals are designed and implemented from which a certain combination of these residuals can be employed to observe and isolate each fault. Finally, the effectiveness of the proposed model is validated on an experimental setup of inverter-fed PM synchronous motors.

Contributions: A model-based fault detection and isolation methodology is developed based on structural analysis to investigate sensor faults in PMSM and drive system. This model is more generalized compared to previous studies and includes dc link voltage and current as well as load torque measurements. The faults in sensors are introduced as dc offsets, gain change, and amplitude unbalance. The designed residuals are implemented on a real-time PMSM drive system and responses obtained show great sensitivity to the presence of the introduced faults.

This paper has been published as: S. H. Ebrahimi, M. Choux, and V. K. Huynh. Diagnosis of Sensor Faults in PMSM and Drive System Based on Structural Analysis. In *Proceedings of 2021 IEEE International Conference on Mechatronics (ICM)*, 2021. ISBN: 978-1-7281-4443-6.

Paper E: Real-Time Detection of Incipient Inter-Turn Short Circuit and Sensor Faults in Permanent Magnet Synchronous Motor Drives Based on Generalized Likelihood Ratio Test and Structural Analysis

Summary: Paper E presents a systematic fault diagnosis methodology based on structural analysis for detecting ITSC faults and measurement faults in the rotor feedback device. A healthy dynamic mathematical model of PMSM is defined in *abc* frame using dynamic equations, measurements, and derivatives including specific additive faults terms which represent the deviations in the stator winding voltage, flux, and currents caused by ITSC fault as well as angular speed and angle measured signals to account for the faults in the rotor feedback device. Subsequently, the analytical redundant part of the structural model is extracted and divided into minimally over-determined subsystems, based on which five sequential residuals are obtained based on the error in the current signal of each phase. Finally, a GLRT-based statistical detector is developed to detect the faults in the resultant residual under unknown amplitude and unknown variance assumptions for the noise signal.

Contributions: Structural analysis has not previously been implemented in the real-time diagnosis of an industrial PMSM for the detection of ITSC faults. This study presents a model-based fault detection methodology based on structural analysis to investigate ITSC and encoder faults in the PMSM drive system. In addition, the lowest level of ITSC fault, with one shorted turn in stator phase winding is detected. Two other physical ITSC faults, with 3 and 5 shorted turns out of 102 turns, are also implemented in other stator phase windings. In addition, the degradation path is modeled with external resistors. This allows a lower fault current in the degradation path as compared to shorted turns to achieve the early detection of an ITSC fault. Specific residuals are designed to detect ITSC faults and encoder faults. Moreover, a GLRT-based statistical detector is designed based on null and alternative hypotheses and coupled to the residuals. The noise in drive system measurement signals is modeled with unknown amplitude and variance to consider a realistic diagnostic approach. Finally, a threshold is calculated based on the probability of false alarm while maintaining the probability of detection high. The experimental results show that the designed GLRT-based detector can effectively detect the small ITSC and encoder faults in the presence of noise.

This paper has been published as: S. H. Ebrahimi, M. Choux, and V. K. Huynh. Real-Time Detection of Incipient Inter-Turn Short Circuit and Sensor Faults in Permanent Magnet Synchronous Motor Drives Based on Generalized Likelihood Ratio Test and Structural Analysis. In *MDPI - Sensors*, 2022. EISSN 1424-8220.

Paper F: Statistical Detection of Demagnetization and Inter-Turn Short Circuit Faults in PMSM Using Recursive GLRT with Adaptive Threshold

Summary: Paper F presents a real-time model-based technique for detecting demagnetization and ITSC faults in PMSMs. A structural analysis is implemented on the dynamic mathematical model of the PMSM in *abc* and *dq* reference frames and specific additive fault terms are added to the model to account for the distortion caused by demagnetization and inter-turn short circuit faults. Subsequently, the analytical redundant part of the structural model is extracted and divided into minimally over-determined subsystems, based on which five sequential residuals are obtained based on the error in the current signal of each phase. Finally, a statistical decision-making diagnostic system is designed based on generalized likelihood ratio test considering unknown noise parameters, fault level, and arrival time. A recursive cumulative algorithm is set on the GLRT to obtain an adaptive threshold, which results in the detection of all the studied faults with low detection and recovery time delay, and without facing any false alarm.

Contributions: Real-time early diagnosis of most likely internal faults in industrial PMSMs such as demagnetization and ITSC faults is not present in the studies that have developed models based on structural analysis. This study presents a model-based fault detection methodology based on structural analysis to investigate ITSC and demagnetization faults. While physical ITSC faults are implemented on the stator winding of the PMSM, the drive strategy is modified in a way to implement reversible demagnetization faults by controlling the *dq* flux components. Three levels of ITSC faults, namely 1%, 3%, and 5% as well as three levels of reversible demagnetization faults, namely 2%, 5%, and 9% are applied to the motor in different time intervals and real-time residuals are obtained. A GLRT-based statistical detector is designed based on null and alternative hypotheses. In addition to unknown noise parameters such as mean and variance, unknown arrival time is taken into consideration when designing the test statistic. In addition, a recursive algorithm is implemented to obtain a more processed fault indicator that decreases the detection and recovery delay time. The experimental results show that the statistical detector with an adaptive threshold is able to efficiently detect all the unexpected faults in the presence of unknown noise, has a low detection time and recovery time delay, yields a high probability of detection, and experiences no false alarm. an adaptive threshold that yields a high probability of detection while facing no false alarms.

This paper has been submitted as: S. H. Ebrahimi, M. Choux, and V. K. Huynh. Statistical Detection of Demagnetization and Inter-Turn Short Circuit Faults in PMSM Using Recursive GLRT with Adaptive Threshold. Under review in *IEEE Transactions on Industrial Electronics*, 2022. ISSN 0278-0046.

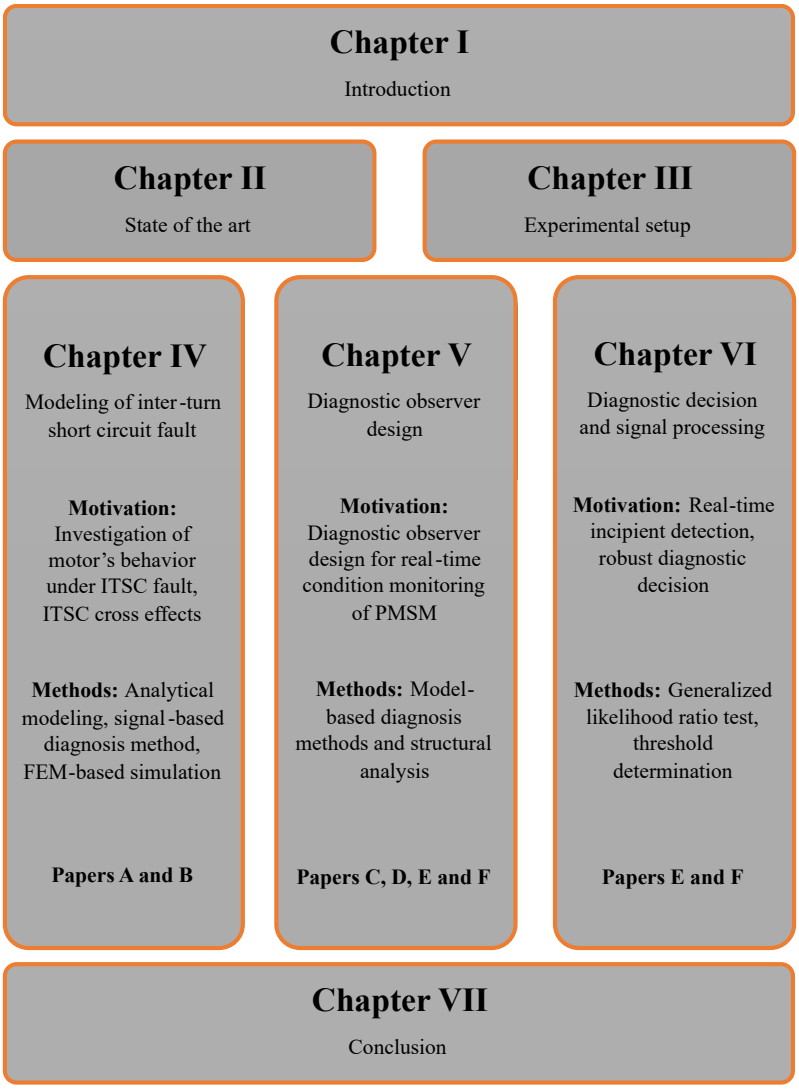

Figure 1.2: Summary of chapter contents.

1.4 Outline of the dissertation

This dissertation consists of seven chapters, followed by appended research papers. The first chapter is the introduction chapter which gives an overview of the dissertation and a summary of the research conducted. In Chapter 2, the state of the art for fault diagnosis of PMSM, faults in PMSM, detection techniques, diagnostic observer design, and diagnostic test decisions are presented and the research methodology is explained. The experiments, equipment, and governing motor control strategy used for developing the data acquisition methods are summarized in Chapter 3. Chapter 4 discusses the modeling and analysis of inter-turn short circuit faults in PMSMs. Subsequently, chapter 5 summarizes the proposed diagnostics method for designing model-based observers sensitive to the presence of various faults based on structural analysis. In Chapter 6, signal processing of residual responses is presented and the process for obtaining a diagnostic decision based on generalized likelihood ratio test is given. Finally, the conclusions of the dissertation are presented in Chapter 7. Figure 1.2 shows the summary of chapter contents.

Chapter 2

State of the art

In this chapter, the state-of-the-art real-tine fault diagnosis of PM synchronous motors is explained. First, the common types of faults and their origin is discussed. Then, different methods for detecting these faults in PMSMs and drive systems are stated. Finally, a summary is given where the studied faults and experimented diagnostic methods in the framework of this dissertation are pointed out.

2.1 Faults in PM synchronous motors

Faults in permanent magnet motors are classified as electrical, magnetic, and mechanical faults [17]. Electrical faults (which are also considered stator faults) represent one of the most common sources of faults in electric motors and include inter-turn short circuit (ITSC), phase-to-phase short circuit, and open-circuit faults [18]. Furthermore, magnetic faults usually occur due to thermal stresses, environmental factors, or even electrical faults and include demagnetization and magnet damage [1]. In addition, mechanical faults as a common phenomenon in rotary electromechanical systems are categorized as bearing faults and eccentricity [19]. There are also faults in electric drive systems which can occur either in power converter or in controller [20]. Open-circuit faults and short circuit faults of the power switches are the most common faults in the inverter [21]. Additionally, the controllers are supported by feedback signals such as rotor speed and stator phase currents, etc. Therefore, failures of these sensors might also degrade the system performance, or even cause the system breakdown [22]. Thus, the control and diagnostic systems' performance can be ensued if sensor faults are detected and dealt with.

2.1.1 Stator faults

The stator of PMSMs contains distributed three-phase windings that produce a rotary Magnetomotive Force (MMF) together. Through distributed three-phase windings of the stator, bundles of wires each of which is associated with one phase, are often wrapped together to form coils that produce the necessary rotary MMF [3]. The insulator of the wires used in the stator winding is subject to continuous degradation due to high voltage, electrical loading, thermal stress, mechanical stress, winding vibration, power

surge, environmental contamination, and foreign objects [4–6]. According to the surveys mentioned in [3, 23, 24], electrical failures related to stator winding account for 21% − 37% of the total machine failures. Stator winding insulator degradation may lead to different types of faults including inter-turn short circuit (ITSC), phase-to-phase short circuit (PPSC), and phase-to-ground short circuit (PGSC) [25].

2.1.1.1 Inter-turn short circuit fault

Among all the faults in the stator winding, the inter-turn short circuit fault is considered the most critical fault case [24]. Following the occurrence of the fault, the faulty turns create a loop coupled to the whole phase winding. In this condition, the induced back-EMF and mutual inductances act as voltage sources, while the impedance of faulty turns and the fault resistance act as current limiters [4]. Since ITSC involves only a few turns, the faulty turns' impedance is very low which sometimes results in a higher circulating current than the rated current. The I^2R losses due to this elevated current level further increases the thermal stress on the faulty winding resulting in further degradation of the insulation between windings and lamination [3]. As a result, the number of faulty turns further increases which might cause the corresponding phase winding to be partially or fully bypassed. As the fault propagates, ITSC may also lead to other forms of faults including phase-to-phase short-circuit, or phase to ground short-circuit, irreversible demagnetization, or eventually complete failure [26]. According to a study cited in [27], 80% of motor stator faults begin as ITSC faults which clearly proves the necessity of monitoring and early detection of ITSC faults.

2.1.1.2 Phase-to-phase short circuit fault

The nature of phase-to-phase short-circuit (PPSC) fault is different from the ITSC fault as the short circuit occurs between the windings of different phases [28]. PPSC fault can create a huge unbalance magnetic pull (UMP) and asymmetry in the flux, which will eventually result in complete machine failure. Thus, preventing this fault can save costs and downtimes.

2.1.1.3 Phase-to-ground short circuit fault

Phase-to-ground short circuit (PGSC) fault occurs when there is a short circuit between a phase winding and the ground. Although PPSC and PGSC are the worst faults among stator faults [29], extensive research has been devoted to the detection and diagnosis of the ITSC faults. This is due to the fact that basically, PPSC and PGSC faults are the consequence of ITSC faults and therefore, early detection of ITSC can lead to the prevention of more dangerous fault cases such as PPSC and PGSC [30].

2.1.2 Magnetic faults

Permanent Magnets (PMs) are among the most critical and expensive materials used in PMSMs, which may get damaged or demagnetized due to various causes [31, 32]. PMs are very sensitive and may lose their performance partially or fully, in harsh working

conditions [33]. Due to thermal stress, external demagnetizing MMF, electrical faults (e.g. terminal short circuits), environmental factors (e.g. oxidation), unbalanced load, and rotor faults (e.g. eccentricities, damaged rotor magnets), magnetic faults are becoming inevitable in real operations, and thus, monitoring and detection of magnetic faults in early stages of growth will result in prevention of important downtimes and maintenance cost [34, 35].

2.1.2.1 Demagnetization fault

When permanent magnets are exposed to excessive temperature rises caused by either high load currents or short-circuit currents in the stator, their magnetization may be lost partially or completely, and hence, an irreversible demagnetization fault occurs [36, 37]. Low and average-power electric motors are normally designed to withstand demagnetization conditions under expected fault cases such as terminal short circuit faults. However, due to their rapidly expanded applications in the emerging fields (e.g. shale or oil mining applications) with new environmental uncertainties (e.g. extremely low or high-temperature scenarios), demagnetization has been continuously reported until today [1]. Demagnetization can have a negative impact on the performance, efficiency, and reliability of a machine system and may lead to a reduced or unbalanced rotor flux along with overload, increased vibrations, and rotor faults which are ultimately manifested through thermal and magnetic phenomena [38, 39].

To avoid or minimize the chance of occurrence of demagnetization fault, one solution is to use permanent magnets of a higher temperature class. However, these magnets are more expensive and have a lower remanence. As a result, setting up a condition monitoring system to detect the demagnetization fault in time is considered a better solution [40]. Comprehensive reviews of demagnetization diagnosis techniques are found in [41] and [42].

2.1.2.2 Magnet-damage fault

Unbalanced load, manufacturing imperfection, poor quality material, and rotor faults such as eccentricities may result in damaged rotor magnets. Although not as common as demagnetization fault, damaged magnet fault might lead to catastrophic system failures due to the huge magnetic and mechanical imbalance.

2.1.3 Mechanical faults

Mechanical faults in electric motors represent $60\% - 70\%$ of total failures [43]. Therefore, monitoring and diagnosis of these faults can lead to a huge reduction in downtimes and repair costs [44]. Mechanical faults include bearing faults and eccentricity and the research on these faults has been going on as follows.

2.1.3.1 Bearing fault

Bearing is a key component in electric motors because it supports the motor shaft and the load that rotates at high speeds [45]. However, bearings are most susceptible to failure due to the harsh working environment, humidity, high temperature, mechanical stress, and

variable load. Around $40\% - 50\%$ of total motor faults are caused by bearing failure [7] which raises the necessity of condition monitoring and fault diagnosis of bearing fault to increase the reliability of the system.

2.1.3.2 Eccentricity fault

Eccentricity fault is another mechanical fault that is classified into static eccentricity (SE), dynamic eccentricity (DE), and mixed eccentricity (ME). Eccentricity is mainly caused due to manufacturing imperfection but may also appear due to mechanical and thermal stress. Eccentricity fault may grow as time goes on and results in unbalanced magnetic pull (UMP) [46], vibration [47], noise, and energy loss. Accurate eccentricity fault detection is difficult since online access to the rotor is not easily possible [17].

2.1.4 Electric drive faults

2.1.4.1 Sensor faults

PMSM drive systems rely on different sensors to achieve the full functionality and controllability of the overall system [48, 49]. On the controller side, sensor failure is one of the most common faults in industrial drive applications [50]. In recent years, growing concerns about sensor faults have led some researchers to focus their efforts on developing diagnostic systems of sensor faults in an electric drive system [51, 52]

Generally, a voltage-source-inverter (VSI) is the most popular variable-speed drive for PMSMs which utilizes two or three phase-current sensors, a position or speed transducer, and a dc-link voltage sensor. Various sensor faults in different combinations of sensors involved in a drive system are investigated in the literature. For instance, observer-based speed and load torque sensor faults have been investigated in [52]. In [53], a fault-tolerant control strategy is proposed by the authors to study current and speed sensor faults for an induction machine. In [50], an adaptive observer has been employed to detect speed, dc bus voltage, and current faults by estimating sensor signals values [50]. In [54], authors have proposed a structural method to deal with eight sensor faults in a PMSM drive system which includes gain change, amplitude change, and unbalance in the output of voltage, current, position, and speed measurements. Detection of sensor faults and fault-tolerant drive strategies continue to be an interesting subject since they will help to reduce downtime costs and avoid expensive repairs.

2.1.4.2 Switch faults

Power semiconductor switches such as Insulated Gate Bipolar Transistor (IGBT) and Metal Oxide Semiconductor Field Effect Transistor (MOSFET) are the most popular switches used in motor drive systems. In recent years, emerging power switches including SiC and GaN have been widely studied and applied in motor drive applications [1]. These switches are subject to electrical, thermal, and mechanical stresses during the operation of the drive system and are prone to unexpected failure. According to a survey, switch faults account for 34% of all faults in PM drive systems [55].

The switch faults can further be classified as open switch faults and shorted switch faults. Shorted switch results in catastrophic damage to the drive system due to the excessive heat generated. However, modern drive systems have a direct hardware trip strategy included in their design to bypass the effect of such faults without computational delay in a short time. On the other hand, open switch fault mainly occurs due to wire-bond lift-off in the semiconductor switch package. Although motor drive systems are usually designed to allow the operation for a specific period of time when an open switch fault occurs, this fault may result in other secondary faults [56]. Therefore, detection of switch faults has gained paramount importance in fault diagnosis of motor drive systems and will lead to the prevention of costly repair costs, downtimes, and catastrophic damages.

2.2 Fault detection techniques

Different approaches have been proposed for real-time detection of faults in electric motors. Generally speaking, there are three major methodologies for fault diagnosis: Signal-based, model-based, and data-driven techniques.

2.2.1 Signal-based methods

Compared to other diagnostic techniques, signal-based methods are probably the most adopted approaches [57]. Signal-based methods monitor one or multiple motor signals namely, a current signal, voltage, vibration, temperature, etc, and the data is further processed using time-frequency signal processing tools. Most of fault detection techniques are based on current signal analysis (CSA) since it is fast and efficient [58–64]. Faults usually generate a specific component (2nd harmonic for ITSC fault) in the synchronous dq axis reference frame [65]. Consequently, the same harmonics of currents, voltages, active power, and reactive power in synchronous reference frame can be investigated as fault indicators [66–70]. The drawback of this method is that drive systems and other faults produce similar patterns in the current spectra [32]. Trying to eliminate the disturbances caused by the motor drive, zero-sequence voltage component (ZSVC) harmonic monitoring has been proposed and investigated [13, 71–73]. However, the implementation of an external resistor network and requiring the neutral point connection of the stator windings have made this method a bit difficult. Other types of voltage signal analysis (VSA) for ITSC fault detection include negative sequence voltage [74] or the phase of the zero sequence voltage [75]. Using space vectors of the stator current and voltage, fault detection based on the pendulous oscillation phenomenon has been investigated [76–79]. Other signal-based approaches include torque spectral analysis [80–82], acoustic behavior monitoring [82–84], vibration analysis [85–88], magnetic-flux analysis [26, 89, 90], and thermal analysis [64].

The commonly used signal processing tools in these signal-based analysis methods are fast Fourier transform [10, 68], short-time Fourier transform [91], wavelet transform [92–94], Wigner-Ville analysis [95], and Vold–Kalman filter [12, 96]. The problem with these methods is that not only are they dependent on the operating condition of the motor for identifying the fault severity, but also they can barely detect turn faults at different

locations of the same phase [23]. Consequently, several researchers have proposed using the flux of stator teeth as the indicator of turn fault [97–99].

2.2.2 Model-based methods

After signal-based methods, model-based approaches are the second most popular technique in real-time condition monitoring and fault diagnosis of electric motors. These models, which use mathematical models to imitate motor behavior, include lumped-parameters, dynamic model, finite element method (FEM) model, field reconstruction method (FRM), magnetic equivalent circuit (MEC), and winding function approach (WFA). In most model-based methods, a state observer is designed to detect and identify stator windings faults using a residual signal [100, 101]. Finite element analysis (FEA) is widely employed and recommended to be used for accurate modeling since it takes into consideration the loss of winding symmetries under abnormal conditions and the inherent discrete nature of the stator MMF waveforms, especially in the calculations of inductances [36, 37, 102–105]. However, due to high computational complexity of FEA, many researchers have considered more efficient models like dynamic models [40, 106] for real-time fault diagnosis.

Lumped-parameter models (both in $dq0$ and abc reference frames) have been intensively used for fault diagnosis, using the dynamic equations of the system. Although their accuracy is lower due to the many simplifying assumptions in the derivation of their equations, they are proven to be very simple, fast, and efficient [99, 107–110]. On the other hand, some researchers have mentioned the fact that $dq0$ models cannot be used for modeling internal faults due to the loss of symmetry. This impinges directly on the fact that the $dq0$ model of ac machines is based on the assumption that the shape of the magneto motive force (MMF) waveforms is sinusoidal, where this assumption is rendered not valid due to loss of winding symmetries under abnormal conditions [1]. In order to overcome this, FEA-assisted $dq0$ models [73] and FRM [111, 112] have been proposed and implemented. Again, due to the assumption that the flux linkage of the windings is sinusoidal, only uniform faults can be modeled by FEA-assisted $dq0$ models [113]. Although some faults can be accurately dealt with FRM, it is difficult to integrate it with a drive control scheme and different severity of faults requires separate FEA results [40]. MEC models [97, 114–116] are accurate enough and computationally efficient and do not have the aforementioned limitations. However, the implementation process of MEC is very time demanding due to the complicated mathematics. System identification methods such as language theoretic [117] can also lead to very accurate results. Their limitations are requiring long time series of input voltages, currents, and system output to be trained well, and being sensitive to noise. Generally speaking, the main disadvantages of model-based techniques are complex calculations, model uncertainties, back-EMF estimation, parameter variations, or manufacturing imprecision of the motor and these might degrade the robustness and reliability of the model-based diagnosis methods [118].

2.2.3 Data-driven methods

Data-driven techniques have also been extensively used for detecting faults in electric motors. These techniques take advantage of a large number of historic datasets acquired from the investigated system under healthy and faulty conditions. The data is then further processed using Machine Learning or advanced statistical algorithms to obtain an estimated model of the system [57,119]. These algorithms learn from data in order to discover hidden patterns represented in the information redundancy among the system variables and are especially experimented on systems that are too complex to have an explicit analytic model or signal symptoms of faulty behavior. In other terms, these algorithms extract inherent characteristics of data to classify faults from healthy conditions. Neural networks and Fuzzy and neuro-Fuzzy systems based artificial techniques are the most adopted data-driven methods for fault diagnosis of electric motors [14–16, 93, 120–123].

Artificial neural network (ANN) is a data-driven approach that is based on small processing elements called neurons which are interconnected in a similar manner to the human brain. The amount of influence that one neuron exerts on another is determined by the weight factor. This weight factor corresponds to the interconnection between the neurons and is a tunable parameter of the network. This method has been applied to classify faults in permanent magnet motors into one healthy scenario and six fault cases [15]. Adaline Neural Network, which is a modified approach, has been used to estimate rotor flux linkages of PMSMs by intentionally adding position offset in machine parameter estimation for the diagnosis of permanent magnet fault and winding fault in an electric machine [124]. Another method of classification is Fuzzy inference system which can be implemented using a set of conditional rules. In addition, adaptive neuro-fuzzy inference systems (ANFIS) are adaptive versions of the classical Fuzzy inference systems, where the fuzzy parameters are tuned in a similar way. ANFIS has been applied to locate short-circuit faults occurring in phase-modulation brushless dc motors from DFT of the voltage waveforms as input [125]. Moreover, a fuzzy min-max (FMM) neural network is proposed in [126] which utilizes classification and regression tree (CART) for online detection of faults in a PM machine. Although many recent studies have adopted data-driven methods to detect faults in electric motors, the main drawback of the data-driven method is the availability of the data itself. Therefore, these methods require a lot of data for training to be considered robust and reliable and this can be challenging for many industrial applications [14, 15, 120].

2.3 Summary

The content of this thesis covers several stages of the research, conducted in the modeling and detection of ITSC fault in PMSM motors. In the first stage, an attempt was made to compare different indicators for the detection of ITSC fault based on finite-element analysis in paper A. Next, the analytical modeling of ITSC became an interesting subject. Thus, an ITSC modeling with physical considerations such as the location of the ITSC fault in coils as well as coil-coil and phase-phase cross effects was proposed in paper B. In the next stage, the whole focus was on real-time detection of ITSC fault based on analytic

redundant relations and structural analysis. Subsequently, a model-based detection of ITSC and demagnetization was presented in paper C and the results were verified by Matlab-Simulink simulation. Basically, several residuals were designed that could react to the presence of an introduced ITSC fault, using the same ITSC model presented in paper B, by obtaining a nonzero value. To make the diagnosis model more realistic, the motor signal data collected from other research were analyzed based and the parameters of the present noise signal were extracted. This led to residuals containing a realistic WGN under the healthy case and WGN+signal under the faulty case. Afterward, the diagnosis of sensor faults in a generic drive system with eleven sensors is studied in paper D. The structural analysis algorithm is implemented on a mathematical model of this drive, and analytical redundancy of the structural model is determined. Subsequently, several residuals are designed and implemented on a real-time experimental setup based on which, all the studied sensor faults are detected. However, the effect of noise as a nuisance factor on the decision-making system is not investigated. Therefore, an effort is made in paper E to design a GLRT-based detector on top of residuals to detect sensor faults along with an internal PMSM fault, i.e. ITSC fault. In paper E, experimental analysis of physical ITSC fault was studied where a statistical decision-making system, namely GLRT, was added to the diagnosis system to deal with the model uncertainties such as unknown noise variance and arrival of signal in the diagnosis framework. Implementation of the GLRT led to setting a realistic threshold based on an accepted probability of false alarm that could confidently segregate a healthy case from a faulty case while maintaining a high probability of detection. However, it was noticed that using moving average and variance in forming the test statistic and a fixed threshold could cause detection and recovery delays and potentially false alarms in real-time diagnosis. As a result, a recursive cumulative GLRT with an adaptive threshold and upper bounded was implemented in paper F to create a fault indicator based on the test statistic which can be used as the reference for the decision-making system. This method helped reduce the time to detect common motor faults such as ITSC and demagnetization, reduce the false alarm rate, revert to the non-faulty case when a fault disappears, and increase the detection probability in real-time diagnosis. Figure 2.1 shows the summary of PMSM and drive system faults in which studied faults are highlighted. Figure 2.2 shows the methods that are employed for modeling, observer design, and detection of faults in this study.

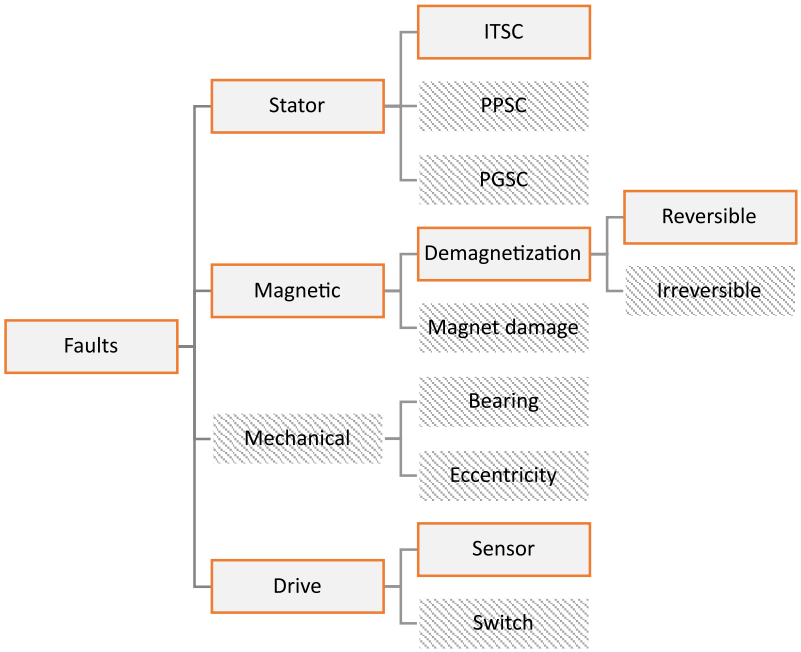

Figure 2.1: Summary of the studied faults in PMSM and drive system.

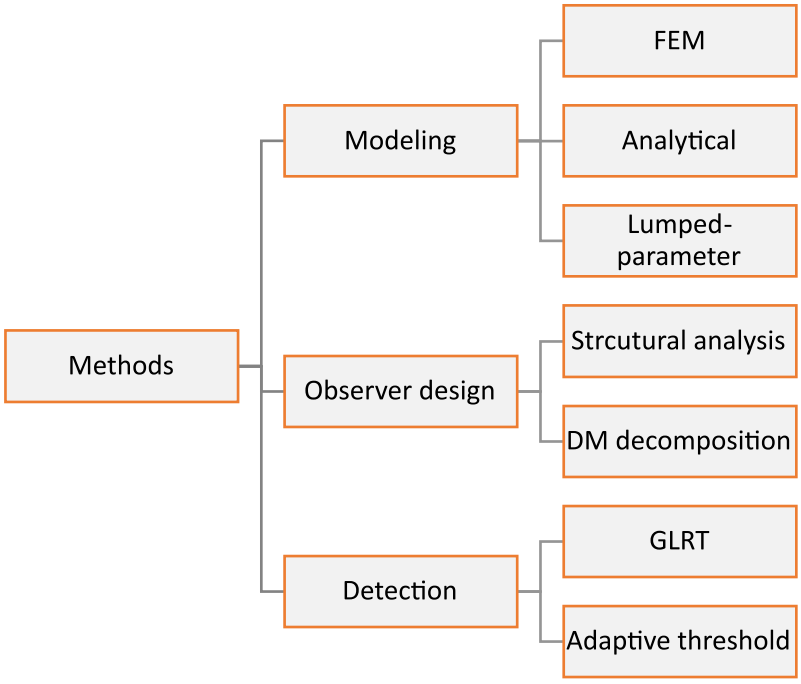

Figure 2.2: Summary of the studied faults in PMSM and drive system.

Chapter 3

Experimental test assembly and data acquisition

Detection of faults in a system, e.g. an electric motor, requires a special test setup that can monitor the status of the investigated system under realistic operating conditions. In addition, it is necessary to have various informational data available, i.e. when the system is healthy or experiencing a certain type of fault. Given the fact that real industrial machine failure data is not very available due to confidentiality and accessibility, the alternative is to obtain this data by using a data acquisition device embedded in the test setup. This chapter gives a detailed description of a test setup developed at the University of Agder's Machine Lab for the diagnosis of various faults in PMSM and electric drive systems.

3.1 Electric drive system and PM synchronous motors

The electrical schematic of the test setup is shown in Figure 3.1. The variable-frequency drive system consists of Keysight N8949A dc supply which converts $400V$ three-phase grid line voltage into a $0-750V$ dc voltage. This dc link voltage is connected to the first input of a Watt&Well DEMT dual voltage source inverter and the three-phase output of the inverter is connected to motor terminals. The main PM synchronous motor is coupled mechanically by the shaft to a secondary machine of the same type which acts as the load to the main motor. Figure 3.2 shows drive system assembly for PM synchronous motor. Further, the secondary machine has mechanical input from the main motor and therefore, operates in generative mode. The electrical output of the generator is connected to the second module in Watt&Well DEMT dual voltage source inverter which includes a three-phase rectifier and dc-dc buck converter. The output which is a dc link load voltage is then connected to a resistive load and can be set to different loading values by adjusting the duty cycle in the dc-dc buck converter. Figure 3.2b shows the electrical resistive load used for PM synchronous generator.

In addition to the drive system assembly, several PM synchronous motors are used in this project. These motors include ABB BSM100N-1250AA, Yunsheng 90YSK30FWJ302,

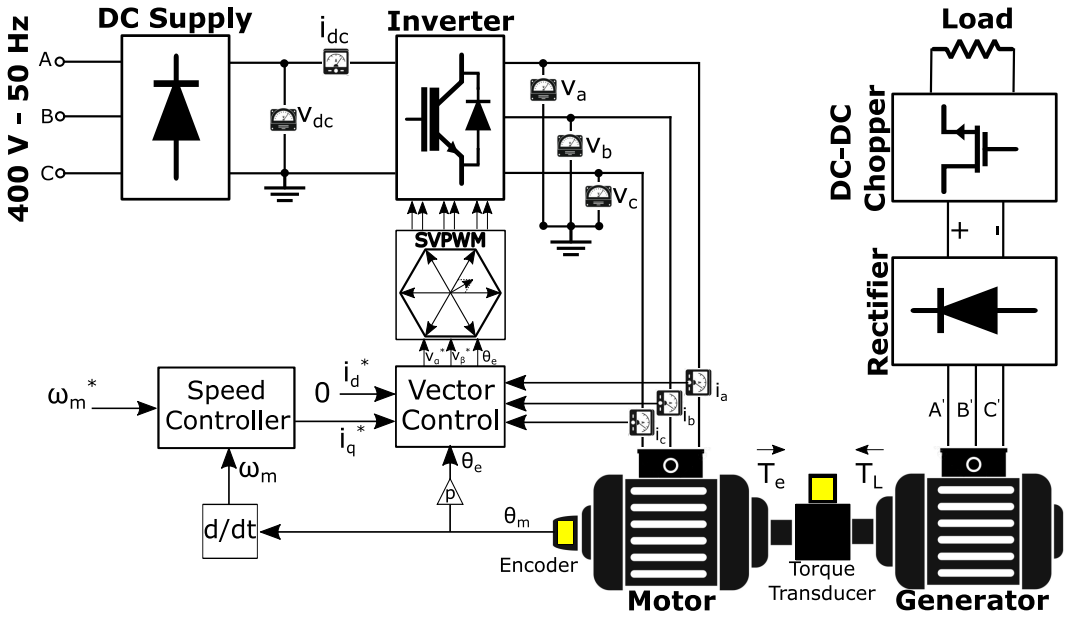

Figure 3.1: Electric drive system schematic for PMSM.

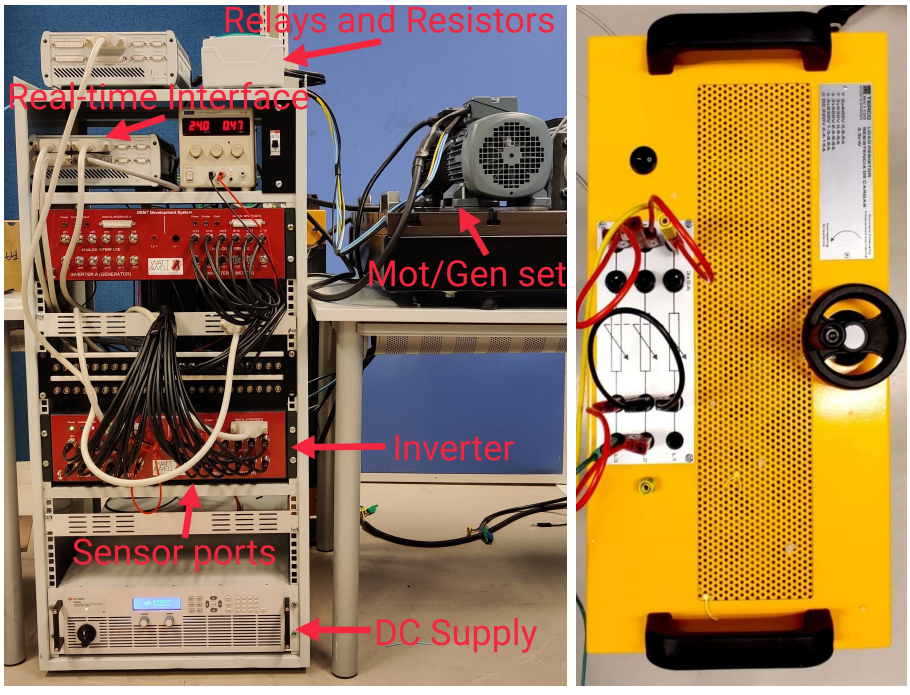

(a) (b)

Figure 3.2: Drive system assembly of PM synchronous motor (a) electrical drive (b) electrical resistive load.

and VEM IE5-PS2R-100L4H-TPM140 and are shown in Figure 3.3.

Table 3.1: Parameters of PM Synchronous Motor

Parameter (Unit)	Value		
	BSM100N-1250AA	90YSK30FWJ302	IE5-PS2R-100L4H-TPM140
Rated dc bus voltage, V_{dc} (V)	320	220	280
Rated rms phase current, I_s (A)	5.9	14	5
Rated Output Torque, T_{out}(N.m)	14	19.1	7
Rated speed, n_s (rpm)	1200	1500	1500
Phase resistance, R_s (Ω)	1.125	1.34	0.8
D-axis inductance, L_d (mH)	8.75	11.5	8.5
Q-axis inductance, L_q (mH)	8.75	27.5	8.5
Rotor inertia, J $(kg.m^2)$	0.0013	0.002695	0.0026
Rotor damping factor, b $(N.m.s/rad)$	0.002	0.0043	0.00382
Flux linkage of PMs, λ_m $(Web - turns)$	0.3107	0.3963	0.3509
Pole-pairs, p	4	2	2

3.2 Sensors and measurement units

As shown in Figure 3.1, a field-oriented control (FOC) technique is used to drive the PMSM to the desired operating point. When the speed reference is changed by the user or load influence, the supervisory speed controller requires the actual speed of the motor. This feedback speed is compared to the reference speed in the PI speed controller and an error is generated. The speed error is converted to a torque reference (T_e^*), which is then converted into a q-axis current reference (i_q^*). To deliver the requested torque, the FOC system also needs to measure the output three-phase current of the motor. These measured currents (i_a, i_b, i_c) in abc frame are converted to i_d and i_q currents using Park transformation, and delivered to i_d and i_q PI current controllers. In FOC technique, d-axis voltage component v_d controls the flux in motor and q-axis voltage component i_q controls the electromagnetic torque. Since the flux is provided by permanent magnets in PMSM and to achieve maximum torque-to-current ratio, the d-axis reference current component is set to be zero and a resultant d-axis voltage reference (v_d^*) is generated. On the other hand, the q-axis PI current controller compares the measured i_q from the Park transformation block with the reference i_q^* from speed controller output to generate a subsequent v_q^* for producing the required torque in the PMSM. The dq reference voltages are then converted to $\alpha\beta$ voltages using Clark transformation and handed over to the space vector modulation (SVM) unit, which creates the reference signals for the IGBT switches of the inverter. The three-phase inverter uses these gate signal commands $(S1 - S6)$ to generate the abc voltages, with desired amplitude and frequency, for the motor by converting the dc voltage of the dc link.

Each module of the Watt&Well DEMT dual inverter unit, has 12 analog channels

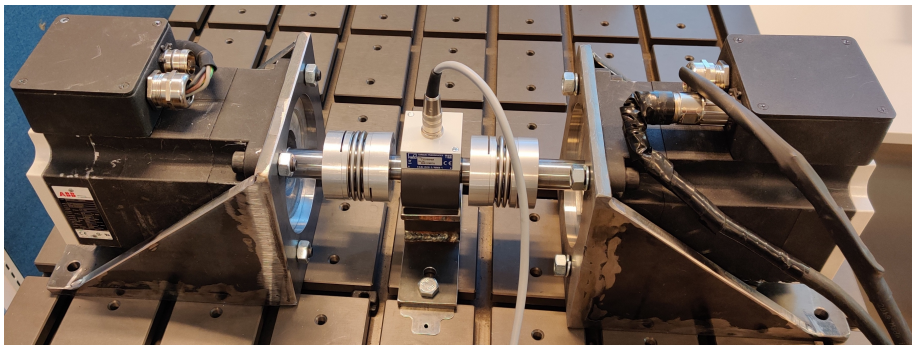

(a)

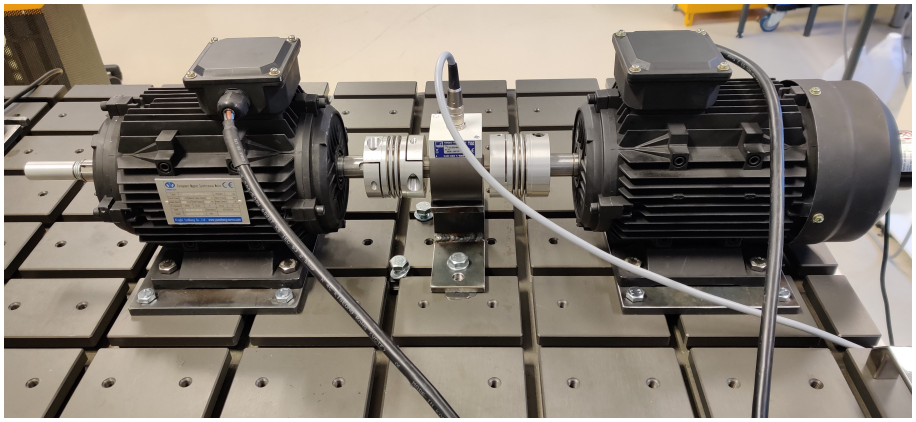

(b)

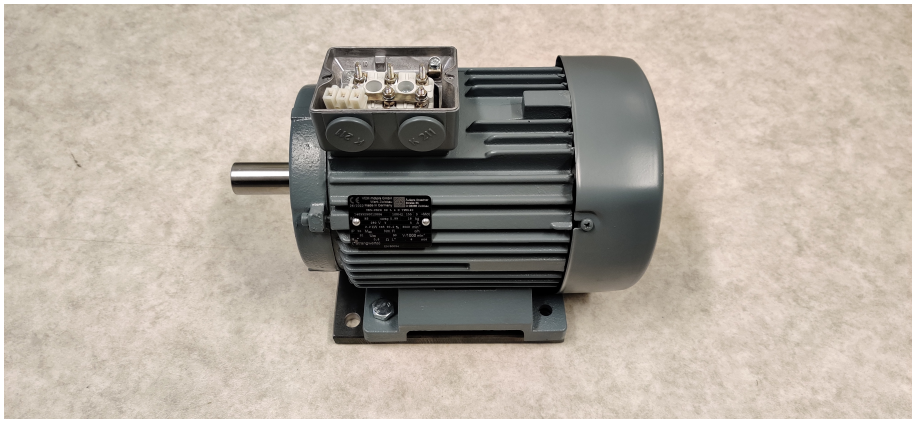

(c)

Figure 3.3: PM synchronous motors (a) BSM100N-1250AA (b) 90YSK30FWJ302 (c) IE5-PS2R-100L4H-TPM140.

Figure 3.4: Dual inverter's sensor panel.

(a) (b)

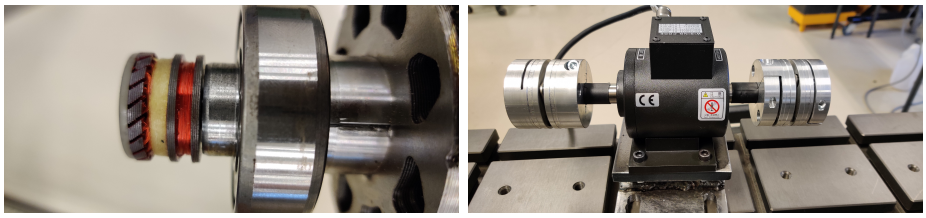

(c) (d)

Figure 3.5: (a) Motor with encoder (b) incremental encoder (c) rotary resolver (d) torque transducer.

which provide access to 9 embedded sensors including three-phase currents (i_a, i_b, i_c), three-phase voltages (v_a, v_b, v_c), dc link current and voltage (i_{dc}, v_{dc}), and phase-b switch joint temperature (T_{j_b}). In addition, the other 3 channels can be used for 2 external temperature sensors and 1 torque sensor. Figure 3.4 shows the sensor panel of the Watt&Well DEMT dual inverter.

To measure the rotor feedback signals, i.e. the rotor's angle (θ) and angular speed (ω), two different rotary encoders have been used. With Yunsheng 90YSK30FWJ302 motors (Figure 3.5a), an optical incremental encoder E60H20-5000-3-N-24 from Autonics has been integrated which is shown in Figure 3.5b. For ABB BSM100N-1250AA motors, a rotary resolver has been assembled on the shaft by the manufacturer, which is shown in Figure 3.5c. Furthermore, a T22 torque transducer from HBM has been coupled mechanically to the shafts of the motor/generator set to measure the load torque based on a differential concept (Figure 3.5d).

Figure 3.6: dSpace MicroLabBox for data acquisition.

Figure 3.7: Real-time interface of dSpace Control Desk and Matlab/Simulink.

3.3 Data acquisition system

Figure 3.6 shows a picture of dSpace MicroLabBox which is used as the data acquisition system for collecting and recording data from sensors for later analysis. In addition, it is used as the real-time interface device for implementing the control strategy of Figure 3.1, from Matlab/Simulink with a sampling time of $50\mu s$.

The dSpace MicroLabBox has two DB50 digital ports each of which is used to communicate with one of Watt&Well DEMT modules for tasks such as, enable/disable, fault status, braking chopper, cooling fan, quadrature encoder, inverter switches gate signals, etc. Further, it has 48 analog channels, either 48 BNC connectors or two DB50 ports, which are used with the analog interface of Watt&Well DEMT for current, voltage, torque, and temperature measurements. The resolver port is separate and other pots include CAN, sensor supply, PC communication, etc. Figure 3.7 shows a picture of the real-time interface of dSpace with Matlab/Simulink control model and dSpace Control Desk software for online monitoring of the device.

3.4 Applied faults and experiments

In this study, several faults in the PMSM and drive system are considered. These faults include drive system measurement faults, inter-turn short circuit faults in PMSM, and

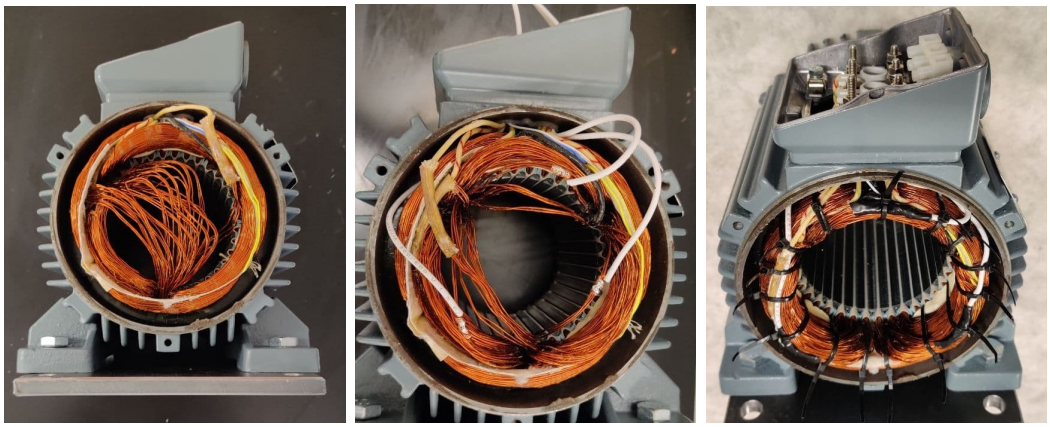

(a) (b) (c)

Figure 3.8: Sequence of applying ITSC fault on PMSM stator winding.

demagnetization faults. The measurement faults have been applied using BSM100N-1250AA and include phase voltage measurement faults $f_{v_a}, f_{v_b}, f_{v_c}$, phase current measurement faults $f_{i_a}, f_{i_b}, f_{i_c}$, dc link voltage and current $f_{v_{dc}}, f_{i_{dc}}$, resolver's angle f_ω and angular speed f_θ, and torque transducer measurement fault f_T. To cover all the possible scenarios, different measurement errors have been applied including dc offset values for current sensors, speed sensor, and torque sensor, gain change for voltage sensors, and imbalance in rotor angular position measurement.

In addition to measurement faults, inter-turn short circuit fault in PMSM stator winding is also investigated. This fault is applied on VEM IE5-PS2R-100L4H-TPM140 motors and the sequence of applying the fault is shown in Figure 3.8. Each phase phase-winding of the motor has two coils in series each of which has 51 turns with 3 parallel branches. For phase a, one of the turns is short-circuited, giving 0.98% fault level. For phases b and c, 3 and 5 turns are short-circuited, resulting in 2.94% and 4.9% fault severity, respectively. The connection wires to these extra taps in the phase-windings are taken out of the motor and connected to $100m\Omega$ resistors both to limit the short circuit current and to simulate the winding insulator degradation, as shown in Figure 3.9. Furthermore, controllable relays are placed in between winding taps and fault resistors to activate or deactivate the fault.

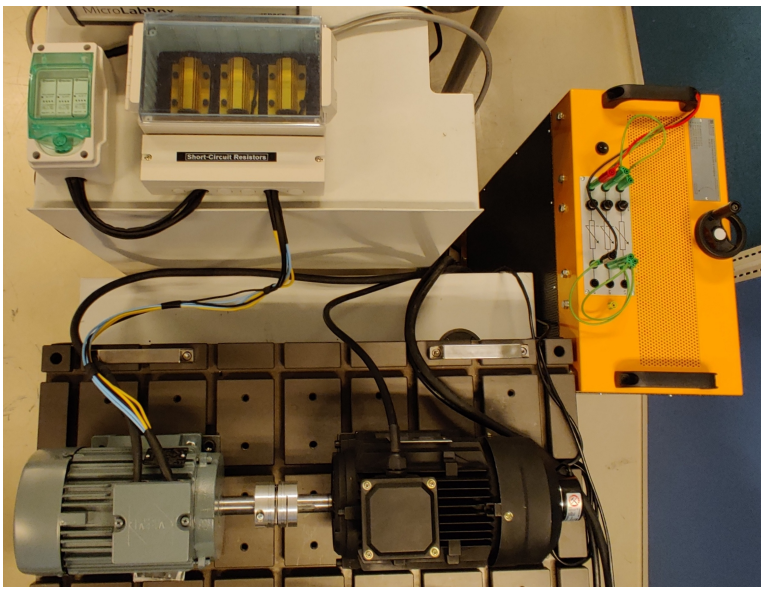

Figure 3.9: Top view of the test setup, resistor box, and relays.

Chapter 4

Modeling and analysis of inter-turn short circuit fault

The wire insulator of the stator windings is subjected to various electrical, mechanical, and thermal stresses. These stresses degrade the wire insulator over time and cause a few turns to be shorted which is known as ITSC fault. ITSC is considered the most dangerous fault due to its growing nature and may lead to other electrical faults and eventually, total failure of the machine [24]. The degraded insulator between the shorted turns is modeled as a non-zero resistance and provides the path for a circulating fault current. As a result, not only appears copper losses in the shorted turns but also excessive heat is generated due to the low impedance of the few shorted turns. As the heat traps in, the degradation escalates and even propagates to adjacent turns, causing the fault to grow bigger and involve the phase winding partially or fully. Therefore, monitoring and detecting the ITSC fault at early stages leads to less repair costs, downtimes, and critical failures.

The content of this chapter covers the research conducted in modeling and analysis of ITSC fault in PMSM motors. First, an attempt was made to compare different indicators for the detection of ITSC fault based on finite-element analysis in paper A. Second, the analytical modeling of ITSC became interesting of a subject. Thus, an ITSC modeling with physical considerations such as the location of the ITSC fault in coils as well as coil-coil and phase-phase cross effects was proposed in paper B. As a result, two different methods for modeling ITSC fault in PMSMs are studied. Section 4.1 presents the proposed FEM model of ITSC fault based on a 2D structure of a 1.7 kW PMSM. Section 4.2 presents the proposed mathematical model of ITSC fault in PMSMs which includes the cross-effects of faulty coils and healthy coils.

4.1 The FEM-based model of inter-turn short circuit fault

The proposed FEM-based model of ITSC fault in PMSM is implemented on a 2D structure of an 8-pole, 1.7 kW IPMSM. Figure 4.1 shows the motor's structure, which is designed and implemented in Ansys Maxwell. The motor winding has 2 slots per pole per phase; therefore, each phase consists of 8 coils connected in series. It is assumed that half of one

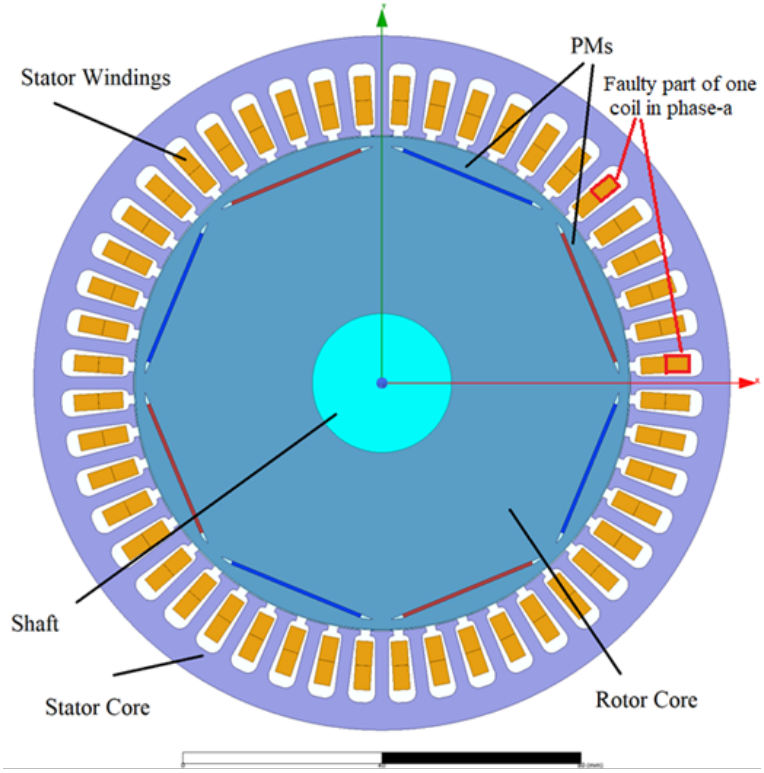

Figure 4.1: 2-D FEM model of an interior permanent magnet synchronous motor.

coil in phase-a, marked in Figure 4.1, is short-circuited. Since 8 coils are in series in each phase, 6.25% or 1/16 of phase-a is considered to be short-circuited.

As mentioned before, ITSC fault usually starts in a few turns and as the heat traps in due to the high current circulating in these few turns, the insulator degrades more and more and the fault propagates to adjacent turns and grows further. Therefore, to model early ITSC fault, a few shorted turns in one coil and not the whole winding should be considered. The FEM model shown in Figure 4.1 is implemented in a way to be as close as possible to a realistic early ITSC fault by involving a few shorted turns. Furthermore, the FEM-based ITSC fault is placed in 1/8 of the whole winding, which creates the same asymmetry that a real ITSC fault does. Paper A provides more detail about the structure of the motor and the FEM model.

4.2 The analytical model of inter-turn short circuit fault

Lumped-parameter ITSC fault models generally ignore the flux coupling factor between healthy and faulty coils in the same phase winding which makes them inaccurate when applied to multi-pole PMSMs. Modeling the interaction of one ITSC fault with other phases is important to understand the behavior of magnetic flux and output characteristics of an unbalance PMSM under faults, and is useful to develop a fault indicator in both steady and transient states. Here, an analytical model of a faulty PMSM considering simultaneous ITSC faults in each of the three-phase windings is presented, in which the

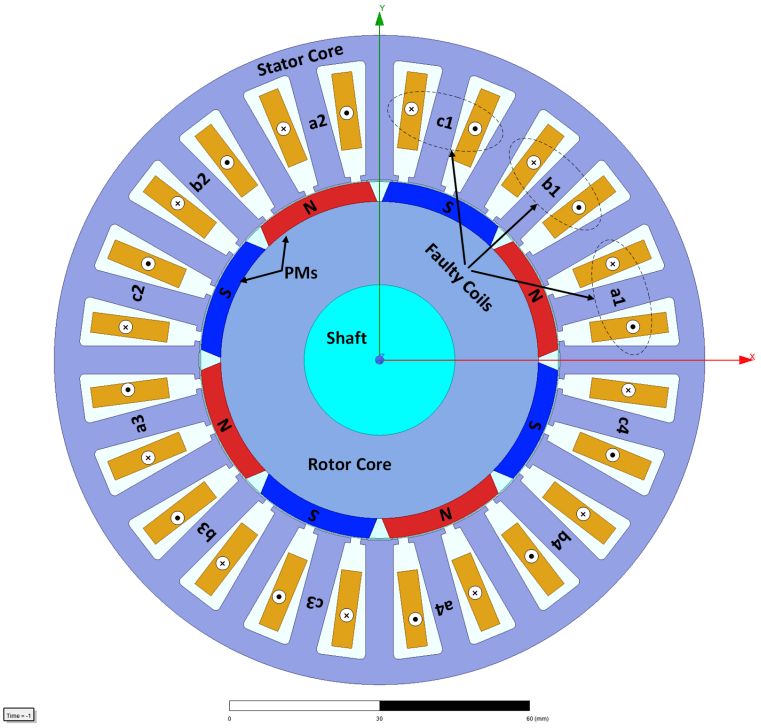

Figure 4.2: 2D Structure of PM Synchronous Motor.

insulation degradation and the flux coupling between healthy and faulty coils in each phase are modeled as a resistance (R_f) and a factor (γ), respectively. Further, the cross-effect of fault currents in different phases is analyzed by modified mutual inductances and coupling factors, allowing the modeling to be more comprehensive to understand the machine behaviors in a wide range of operations in different fault scenarios. The fault model is developed in a way to obtain deformed fluxes based on inductance variations caused by cross flux linkages, depending on the distribution of the coils in the same phase winding and cross-effects of fault currents in different phases.

The proposed ITSC fault model has been implemented on an 8-pole surface-mounted PMSM with concentrated winding with different severity in each phase. Figure 4.2 shows a 2D view of the case-study PMSM where the location of faults is specified in the first of the four series coils in each phase. The ITSC fault splits each faulty coil into one faulty part and one healthy part. The fault severity $\mu_{a,b,c}$ is defined as the ratio of the number of the shorted turns to the total number of turns per coil. In addition, the phase fault resistances and circulating fault currents in the degraded path are denoted by $R_{af,bf,cf}$ and $i_{af,bf,cf}$, respectively.

Figure 4.3 shows the schematic of winding configuration of series connection under three simultaneous faults in the three phases. The flux linkages between different coils are modeled which includes the interaction between the faulty part and healthy part of the same coil with other healthy coils in the same winding. This interaction is considered in the modeling with a coupling factor γ and is especially important in PMSMs with multiple pole pairs ($p > 1$), where the flux linkages between coils in the same phase winding are affected by many possible flux paths. However, the suggested method is only valid for ITSC in one phase. To extend and generalize the concept for other phases, the

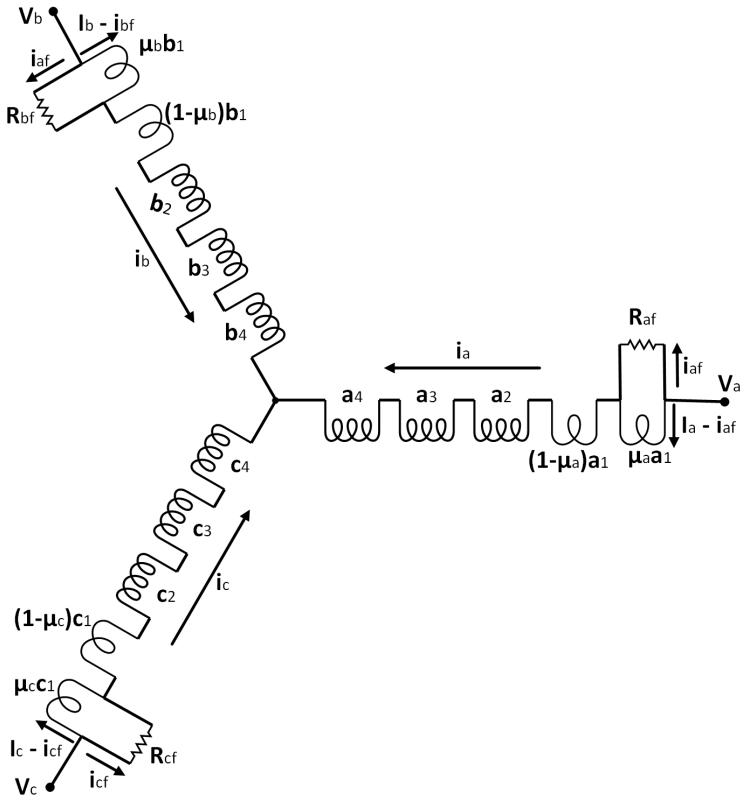

Figure 4.3: Winding configuration with series connected coils under a 3-phase ITSC fault.

cross effect of ITSC faults in different phases is modeled in this work.

By following the ITSC fault modeling in Paper B, the three-phase voltage-current equations of the PMSM under ITSC fault are derived as follows:

$$\begin{aligned}
\begin{bmatrix} v_a \\ v_b \\ v_c \end{bmatrix} &= R_s \begin{bmatrix} i_a \\ i_b \\ i_c \end{bmatrix} + \begin{bmatrix} L_m + L_l & -\frac{L_m}{2} & -\frac{L_m}{2} \\ -\frac{L_m}{2} & L_m + L_l & -\frac{L_m}{2} \\ -\frac{L_m}{2} & -\frac{L_m}{2} & L_m + L_l \end{bmatrix} \begin{bmatrix} \frac{di_a}{dt} \\ \frac{di_b}{dt} \\ \frac{di_c}{dt} \end{bmatrix} \\
&+ \omega_e \lambda_m \begin{bmatrix} \cos\theta \\ \cos(\theta - \frac{2\pi}{3}) \\ \cos(\theta + \frac{2\pi}{3}) \end{bmatrix} - \frac{R_s}{p} \begin{bmatrix} \mu_a & 0 & 0 \\ 0 & \mu_b & 0 \\ 0 & 0 & \mu_c \end{bmatrix} \begin{bmatrix} i_a \\ i_b \\ i_c \end{bmatrix} \\
&- \frac{1}{p} \begin{bmatrix} L_m + L_l & -\frac{L_m}{2} & -\frac{L_m}{2} \\ -\frac{L_m}{2} & L_m + L_l & -\frac{L_m}{2} \\ -\frac{L_m}{2} & -\frac{L_m}{2} & L_m + L_l \end{bmatrix} \begin{bmatrix} \mu_a & 0 & 0 \\ 0 & \mu_b & 0 \\ 0 & 0 & \mu_c \end{bmatrix} \begin{bmatrix} \frac{di_a}{dt} \\ \frac{di_b}{dt} \\ \frac{di_c}{dt} \end{bmatrix}
\end{aligned} \tag{4.1}$$

where the effect of faults appears as additive terms to phase-voltages. The fault currents can be obtained from phase voltages as follows:

$$\begin{aligned}
v_a &= [\frac{pR_{af}}{\mu_a} + R_s(1 - \frac{\mu_a}{p})]i_{af} + \frac{\mu_a}{p}[L_m(\frac{p - 1 + \gamma}{1 - \gamma}) + L_l(p - 1)]\frac{di_a}{dt} \\
v_b &= [\frac{pR_{bf}}{\mu_b} + R_s(1 - \frac{\mu_b}{p})]i_{bf} + \frac{\mu_b}{p}[L_m(\frac{p - 1 + \gamma}{1 - \gamma}) + L_l(p - 1)]\frac{di_b}{dt} \\
v_c &= [\frac{pR_{cf}}{\mu_c} + R_s(1 - \frac{\mu_c}{p})]i_{ac} + \frac{\mu_c}{p}[L_m(\frac{p - 1 + \gamma}{1 - \gamma}) + L_l(p - 1)]\frac{di_c}{dt}
\end{aligned} \tag{4.2}$$

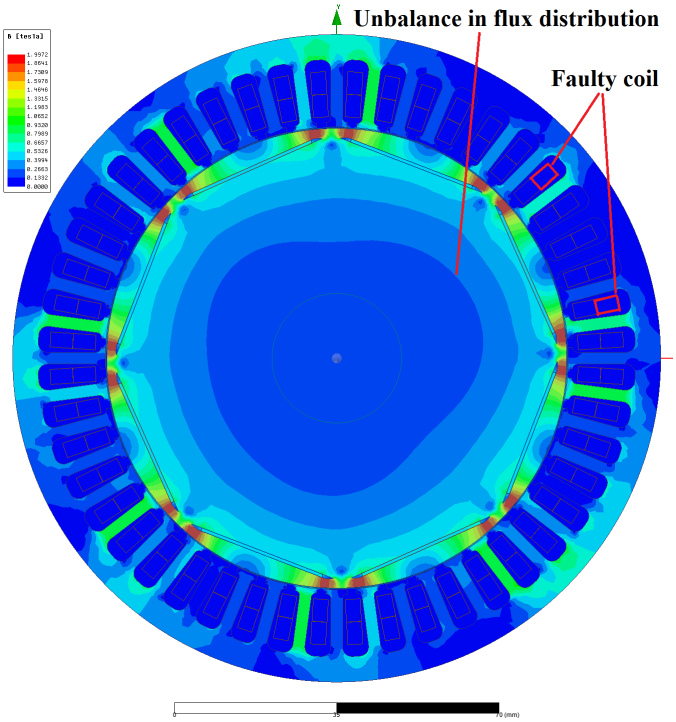

Figure 4.4: Flux distribution in PMSM under ITSC fault.

4.3 FEM results and discussion

A 2-D time-stepping FEA has been conducted on the IPMSM in 4.1 to analyze the motor's behavior under a 6.25% ITSC fault in phase a. Figure 4.4 shows the flux distribution in the stator and rotor cores where the unbalance in flux distribution under the faulty coil created by the applied ITSC fault is visible.

Figure 4.5 shows the frequency analysis of the phase a current, where the single-sided amplitude spectrum of $I_a(t)$ under healthy and faulty conditions are compared. The comparison shows that 3^{rd} harmonic of the motor current can be used as a strong indicator of the presence of a small ITSC fault under these assumptions.

The frequency analysis of the motor's input power is obtained and shown in Figure 4.6,

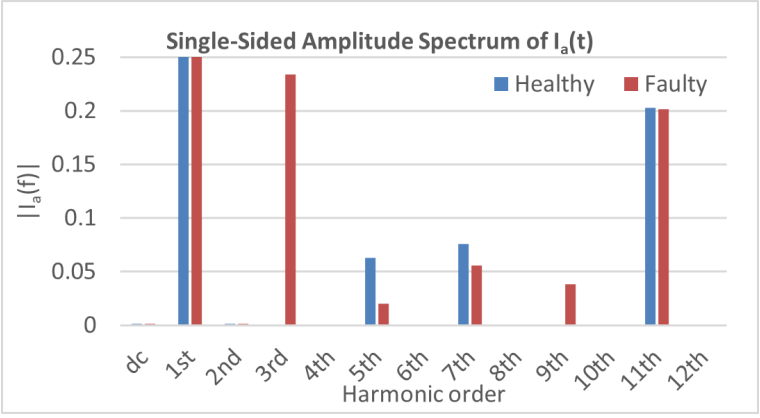

Figure 4.5: Comparison of spectrum of I_a in PMSM under healthy and faulty conditions.

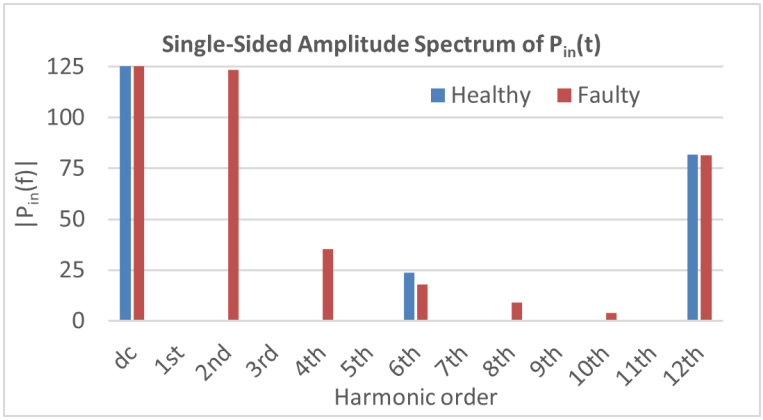

Figure 4.6: Comparison of spectrum of P_{in} in PMSM under healthy and faulty condition.

where the single-sided amplitude spectrum of $P_{in}(t)$ under healthy and faulty conditions are compared. The comparison shows that 2^{nd}, 4^{th}, 8^{th}, and 10^{th} harmonics of the motor current indicators of the presence of the applied ITSC fault. The comparison also shows that as the order of harmonic increases the amplitude decrease. While the 2^{nd} and 4^{th} harmonics created by the fault maintain an acceptable value for being used as a strong indicator, the 8^{nd} and 10^{th} harmonics are not recommended. This is due to the fact that even a small unbalance caused by noise, load change, etc can cause such indicators to react and lead to a false alarm.

To test the analytical model proposed in 4.2, a 2D FEA of the PMSM is conducted in Ansys-Maxwell. Four different cases including healthy condition, a single ITSC fault in phase a, two simultaneous ITSC faults in phases b and c, and three simultaneous ITSC faults in abc phases are implemented to check the accuracy of the proposed model. Output torque, angular speed, three-phase currents, and fault currents characteristics are obtained. In addition, the fault resistances are considered to be $R_{af,bf,cf} = 0.1\Omega$ to consider the incipient fault condition in which the ITSC starts with a high degraded path resistance.

Figure 4.7 shows the comparison of the motor's three-phase currents obtained from the proposed model and FEA. Since there is not any faults in the motor, the proposed model three-phase currents match those obtained from FEA. Figure 4.8 shows the comparison of motor's three-phase currents obtained from the proposed model and FEA when the PMSM is experiencing one single ITSC fault in phase-a with 31 shorted turns (out of 71 total turns) and therefore, $\mu_a = 0.4366$, $\mu_b = 0$, and $\mu_c = 0$.. The ITSC fault in phase-a has caused the phase-a current to be higher than two other phase currents. Figure 4.9 shows the comparison of motor's three-phase currents obtained from the proposed model and FEA when the PMSM is operating under two simultaneous ITSC faults in phase-b with 40 shorted turns and phase-c with 20 shorted turns (out of 71 total turns) and therefore, $\mu_a = 0$, $\mu_b = 0.5634$, and $\mu_c = 0.2617$. The ITSC faults in phase-b and phase-c have caused the currents to be higher than phase a current. Figure 4.10 shows the comparison of motor's three-phase currents obtained from the proposed model and FEA when the motor is experiencing three simultaneous ITSC faults in phase-a with 31 shorted turns, phase-b with 40 shorted turns, and phase-c with 20 shorted turns (out of 71 total

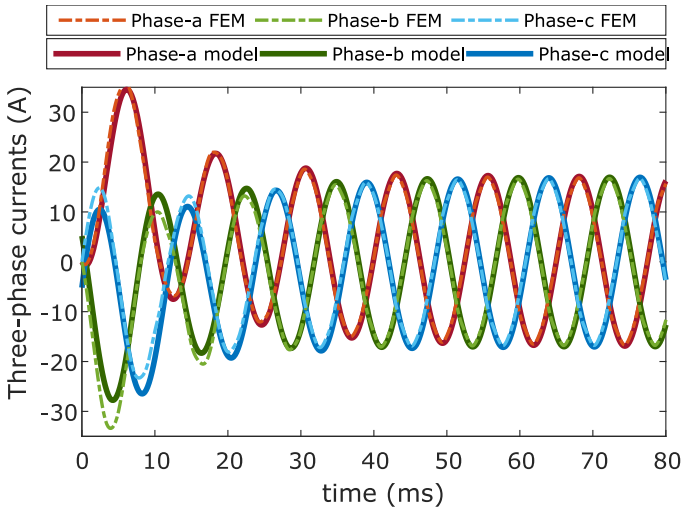

Figure 4.7: Three-phase currents under healthy conditions.

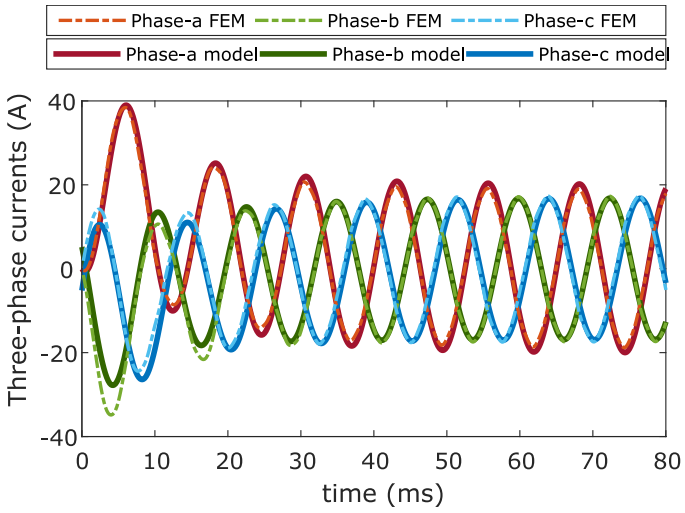

Figure 4.8: Three-phase currents under $\mu_a = 0.4366$.

turns) or $\mu_a = 0.4366$, $\mu_b = 0.5634$, and $\mu_c = 0.2617$. The ITSC faults in each phase have caused the currents to be higher compared to the healthy condition.

This ITSC fault model was developed based on deformed fluxes and inductance variations, which are caused by cross flux linkages depending on the distribution of the coils in the same phase winding. As seen, modeling the cross-effect of fault currents in different phases enabled the model to consider not only single faults but also simultaneous ITSC faults in any of the phases. This ITSC fault model requires only three-phase currents, three-phase voltages, and parameters of the motor as input. Unlike FEA, the presented dynamic model can well and quickly model the behavior of PMSM under different fault scenarios, without using detailed dimensions or material information. This allows such a model to be used in combination with other fault detection techniques such as structural analysis which is covered in the following section.

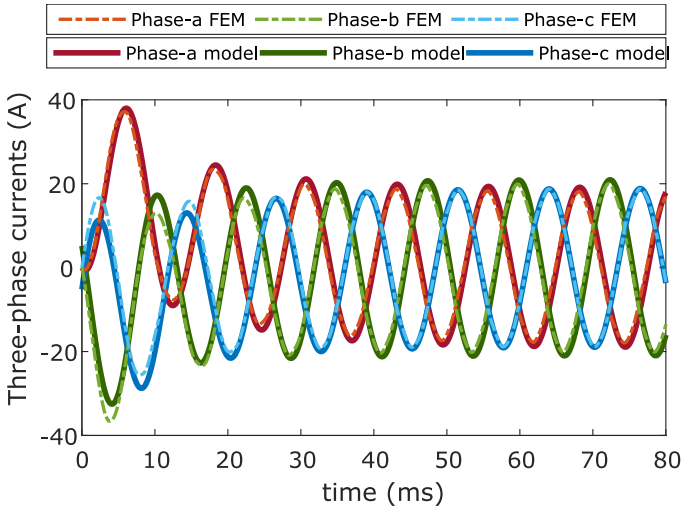

Figure 4.9: Three-phase currents under $\mu_b = 0.5634$, and $\mu_c = 0.2617$.

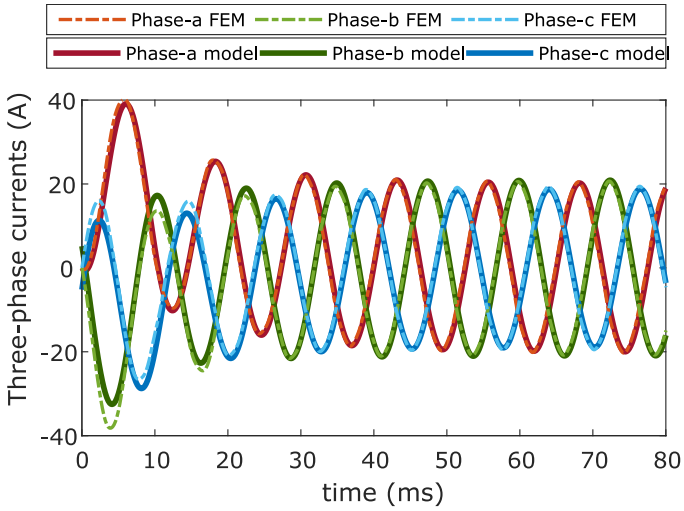

Figure 4.10: Three-phase currents under $\mu_a = 0.4366$, $\mu_b = 0.5634$, and $\mu_c = 0.2617$.

4.4 Summary

This chapter focuses on modeling and analysis of ITSC faults in PMSMs, presenting two types of modeling. In 4.1, a 2D FEM model of a 1.7 kW PMSM structure with 8 coils in series is presented where a small ITSC fault (6.25%) is applied in one of the phase-coils and different fault indicators are obtained during motor's operation under faulty condition. Results show that certain harmonics in the single-sided amplitude spectrum of $I_a(t)$ and $P_{in}(t)$ can be used as reliable ITSC fault indicators, using a signal-based detection method. Section 4.2 proposes an extensive analytical model of ITSC fault in PMSMs that includes the cross-effects of faulty coils and healthy coils. This mathematical model is verified by a 2D FEM-based simulation in Ansys-Maxwell and four different cases including healthy condition, a single ITSC fault in phase a, two simultaneous ITSC faults in phases b and c, and three simultaneous ITSC faults in abc phases are studied.

Chapter 5

Diagnostic observer design based on structural analysis

Structural analysis is a model-based fault diagnosis methodology that uses the structural model of a system to identify the analytic redundant relations (ARRs). The ARRs of a system are obtained based on the mathematical equations describing systems' dynamics and could be used for diagnosing various faults in the system [127, 128]. What makes the structural analysis interesting is that the algorithm can efficiently analyze the detectability and isolability properties of various faults that could occur in complex dynamic systems, where deep prior knowledge of the system dynamics or exact mathematical equations are not available. This is achieved by forming the system's structure in graphical or matrix form, where the analytic redundant part of the system can be mathematically derived and be used for the design of diagnostic tests. Therefore, it is applicable in the early stages of the design process to any diagnosis system, when the final design of the diagnosis system is not completed. Another advantage of the structural analysis methodology is that it decomposes a complex system into smaller subsystems which allows for the effective design of diagnostic algorithms that are more easily implementable. In particular, this approach is efficient in the diagnosis of large complex systems that have many describing equations. Considering the challenges for implementation in a real-time processor, computational complexity, and training data in other diagnosis methods, structural analysis is proposed as an alternative solution for detecting real-time faults in electrical motors [54]. During the past two decades, the structural analysis algorithm has been well studied and theoretically developed in the literature [129–135]. The structural analysis approach has been applied to different engineering systems for fault diagnosis including automotive engine [136–138], hybrid vehicle [139, 140], battery system [141], electric vehicles [54, 142], and electric motors [143, 144].

In this chapter, model-based fault diagnosis based on structural analysis and the design of real-time diagnostic observers for various faults in PMSMs are covered. Four different diagnostic designs in papers C, D, E, and F are presented. These diagnostic systems focus on the detection of ITSC, demagnetization, and sensor faults in PMSM drive system and operate based on observers that are sensitive to the presence of these faults. The procedure of designing such observers is explained in the following sections.

5.1 Theoretical background

Structural analysis algorithm relies on redundancy in a system (a redundant part of the complex system) and yields residuals for fault detection and isolation (FDI) based on ARRs. Assuming that a model M has outputs z and inputs u, a residuals is extracted by eliminating all the unknown variables, i.e substituting an unknown variable with its equivalent obtained value through a redundant path. Therefore, it leads to a relation that contains only the known variables $r(u, z) = 0$ which is known as an ARR if the observation z is consistent with the system model [128]. As a result, this residual's response will maintain a zero value under the null hypothesis (nonfaulty case) $\mathcal{H}_0$, and a nonzero value under an alternative hypothesis (faulty case) $\mathcal{H}_1$ as follows:

$$\begin{aligned} \mathcal{H}_0 &: r(u, z) = 0 \\ \mathcal{H}_1 &: r(u, z) \neq 0 \end{aligned} \tag{5.1}$$

To be able to detect specific faults in a redundant system, faults must first be introduced to the model, and then, a proper diagnostic test that contains the considered fault is selected. A diagnostic test is a set of equations (or consistency relations) extracted from the system model, in which at least one equation is violated in case of the presence of a considered fault. A system model is called a redundant model if the system model consists of more equations than unknown variables. Let unknown variables $var_X(M)$ be the subset of all variables X in model M ($var_X(M) \subseteq X$). The degree of redundancy of the model M is defined as:

$$\varphi(M) = |M| - |var_X| \tag{5.2}$$

where $|M|$ denotes the number of equations and $|var_X|$ is the number of unknown variables contained in the model M.

Depending on the degree of redundancy, the structural algorithm yields several diagnostic tests and each diagnostic test may contain several faults. Thus, to isolate any specific fault, a combination of diagnostic tests is required such that the signatures of other faults are left out and the targeted fault is isolated. In addition, each diagnostic test contains several equations which are a subset of the whole structural model equations. Each diagnostic test can be used to form a residual such as $r_i = g(u, z_i)$, where z_i is the observation set corresponding to each diagnostic test. The residual r_i is nonzero if any of the equations in the test is violated, which means that a fault is present.

The structural analysis algorithm can be used as a systematic design tool for the detection and discrimination of multiple faults in a complex system. First, the structural analysis evaluates a system by forming its structural model. The structural model is usually represented by an incidence matrix, where each row of the matrix represents an equation and is connected to the specific unknown, known, and fault variables [127, 128]. The known variables are obtained through measurements by means of different sensors and form the known inputs. On the other hand, the rest of the variables including the dynamics states and all the intermediate algebraic variables, are considered unknown variables and will be obtained through achieved redundant paths if used in a diagnostic test. By rearranging the rows and columns of the original sparse matrix by applying a

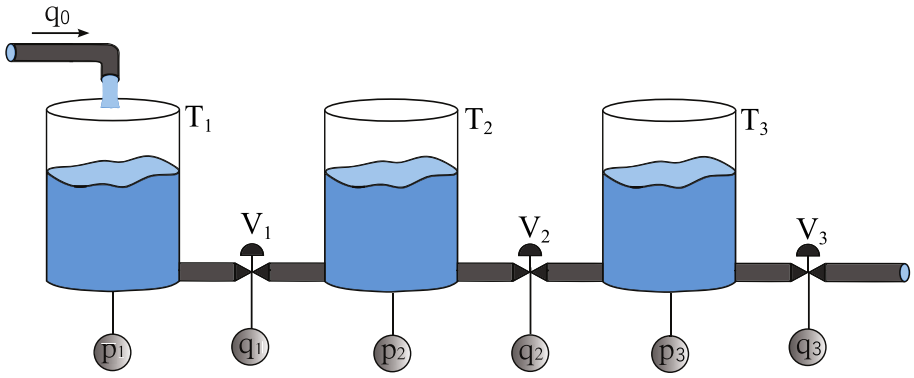

Figure 5.1: Modeling diagram of three-tank system.

Dulmage–Mendelsohn (DM) decomposition tool on the incidence matrix, a bipartite graph is obtained which extracts and portrays the system's analytic redundancy in graphical form [145]. Using the analytic redundant part of the system, a set of diagnostic tests can be extracted for the detection and discrimination of multiple faults.

5.2 Structural model

The structure of a model is formed based on the mathematical dynamic equations of the model and represented by a bipartite graph with equations $(e_1, ..., e_n)$ and variables $(x_1, ..., x_m)$ as node sets [131]. If variable x_i is included in equation e_j, there is an edge in the bipartite graph that represents this connection. The structural model can also be shown by an incidence matrix in which rows represent the equations while columns represent the variables. For a better demonstration of the structural model, a simple example model from [146] is used. Figure 5.1 shows the modeling diagram of the three-tank system and the model equations are defined in Equation 5.3.

$$
\begin{aligned}
e_1 : q_1 &= \frac{1}{R_{V_1}}(p_1 - p_2) \quad + f_{V_1} & e_7 : y_1 &= p_1 \\
e_2 : q_2 &= \frac{1}{R_{V_2}}(p_2 - p_3) \quad + f_{V_2} & e_8 : y_2 &= q_2 \\
e_3 : q_3 &= \frac{1}{R_{V_3}}(p_3) \quad + f_{V_3} & e_9 : y_3 &= q_0 \\
e_4 : \dot{p}_1 &= \frac{1}{C_{T_1}}(q_0 - q_1) \quad + f_{T_1} & e_{10} : \dot{p}_1 &= \frac{dp_1}{dt} \\
e_5 : \dot{p}_2 &= \frac{1}{C_{T_2}}(q_1 - q_2) \quad + f_{T_2} & e_{11} : \dot{p}_2 &= \frac{dp_2}{dt} \\
e_6 : \dot{p}_3 &= \frac{1}{C_{T_3}}(q_2 - q_3) \quad + f_{T_3} & e_{12} : \dot{p}_3 &= \frac{dp_3}{dt}
\end{aligned}
\tag{5.3}
$$

where the pressure in tank i is denoted by p_i, the flow through valve i by q_i, the flow resistance of valve i by R_{V_i}, and C_{T_i} is the capacitance of tank i. In addition, three measured values y_1, y_2, and y_3 are obtained from sensors and measure p_1, q_2, and q_0, respectively. In this example, six parametric additive faults are considered in the model

which are colored red in Equation 5.3. The faults f_{T_1}, f_{T_2}, and f_{T_3} represent the change in the capacity of the tanks, i.e C_{T_1}, C_{T_2}, and C_{T_3} while the faults f_{V_1}, f_{V_1}, and f_{V_3} represent partial blocks in the valves R_{V_1}, R_{V_2}, and R_{V_3}. The reason that faults are considered as additive terms is that any change in capacity of one tank leads to an increase/decrease in the pressure derivative of that tank while a partial block in one valve leads to an additive change in the flow of water in that valve.

Now that the model is defined, variables and parameters can be organized by using symbolic expressions before applying the structural algorithm as follows:

$$\begin{aligned} x &= \{p_1, p_2, p_3, q_0, q_1, q_2, q_3, dp_1, dp_2, dp_3\} \\ f &= \{f_{V_1}, f_{V_2}, f_{V_3}, f_{T_1}, f_{T_2}, f_{T_3}\} \\ z &= \{y_1, y_2, y_3\} \\ p &= \{R_{V_1}, R_{V_2}, R_{V_3}, C_{T_1}, C_{T_2}, C_{T_3}\} \end{aligned} \tag{5.4}$$

where x contains the unknown variables, f contains the faults, z contains the known variables, and p contains the parameters. Using the structural fault diagnosis toolbox in [147], the structural model of the three-tank system can be obtained as a bipartite graph, shown in Figure 5.2. In the structural graph of the three-tank system, variables, faults, and equations are shown as nodes and if any of the variables or faults are contained in each equation, there is an edge that connects these nodes together. A better and more informative way of presenting the structural model is by using an incidence matrix instead of a graph. Figure 5.3 shows the structural incidence matrix of the three-tank system in which rows represent the equations, and columns represent all the variables that can be sub-categorized as unknown, known, and fault variables. If any of the unknown variable x_j, known variable z_j, or fault variable f_j are present in equation e_i, the (i, j) component of the incidence matrix contains a blue, black, or red filled circle to show this connection, respectively. Moreover, if the nature of relation between unknown variable x_j and equation e_i is of derivative or integrative form, the (i, j) component of the incidence matrix contains a $''D''$ or $''I''$ character, respectively.

5.3 Analytical redundancy analysis

Dulmage and Mendelsohn [145] have proposed that the analytic redundancy of a structural model can be found if rows and columns of the incidence matrix are rearranged in a way that it acquires an upper triangular form. This is achieved using a DM decomposition tool which reorganizes the structural model M to be structured into three main sub-models (shown in Figure 5.4):

- M^-: structurally under-determined part of the model M, where lies fewer equations than unknown variables and the degree of redundancy is negative $\varphi(M) < 0$.
- M^0: structurally just-determined part of the model M, where lies equal equations and unknown variables and the degree of redundancy is zero $\varphi(M) = 0$.
- M^+: structurally over-determined part of the model M, where lies more equations than unknown variables and the degree of redundancy is positive $\varphi(M) > 0$.

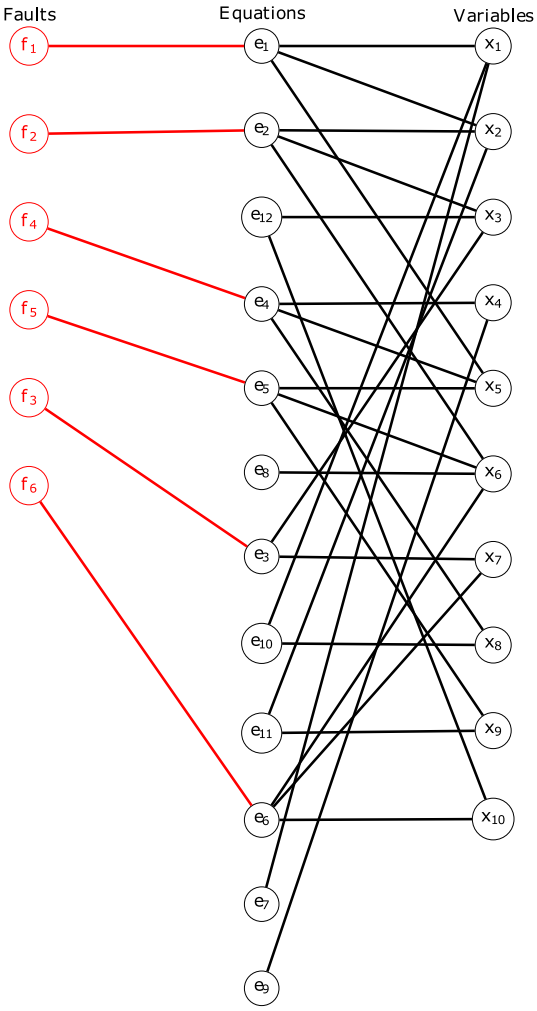

Figure 5.2: Structural model demonstration of three-tank system by a bipartite graph.

5.3.1 Detectablility analysis

According to Krysander and Frisk [132], a fault is detectable if it lies in the over-determined part (M^+) of the model. This claim is based on the fact that redundant paths must be available to successfully detect and isolate a fault. The DM decomposition tool has been applied to the structural model of the three-tank system and the result is shown in Figure 5.5. The blue box denotes the canonical decomposition of the overdetermined part (M^+) of the three-tank system structural model with the indication of faults. The parametric faults $\{f_{V_1}, f_{V_2}, f_{V_3}, f_{T_1}, f_{T_2}, f_{T_3}\}$, shown by red dashed lines, affect equations $e_1 - e_6$. All the six faults lie in the M^+ sub-model and as a result, all the modeled parametric faults are detectable. The gray boxes are minimal structurally overdetermined sets which will be explained in the following section.

5.3.2 Isolability analysis

Now that detectability analysis has been performed and all the faults are proven to be detectable, isolability analysis can be performed to check if individual faults can be isolated from each other. According to the definition given by Krysander and Frisk [132], a fault

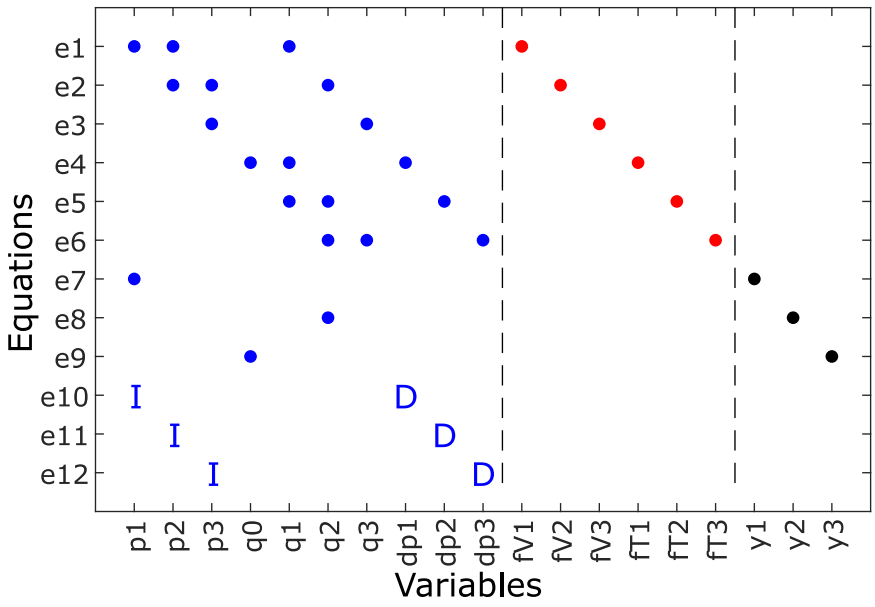

Figure 5.3: Structural model demonstration of three-tank system by incidence matrix.

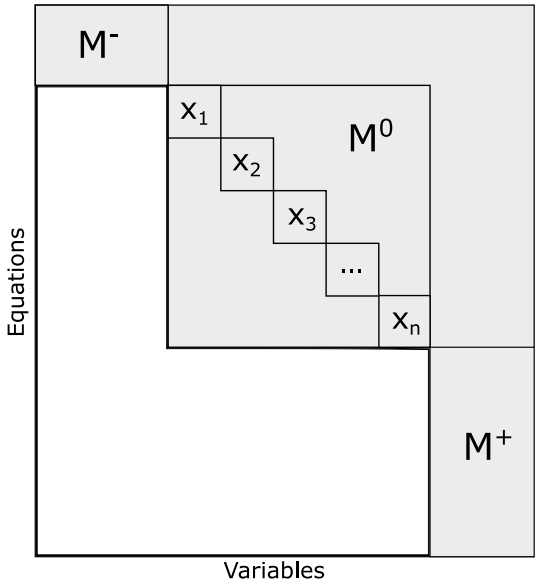

Figure 5.4: Rearranged triangular form of the structural model.

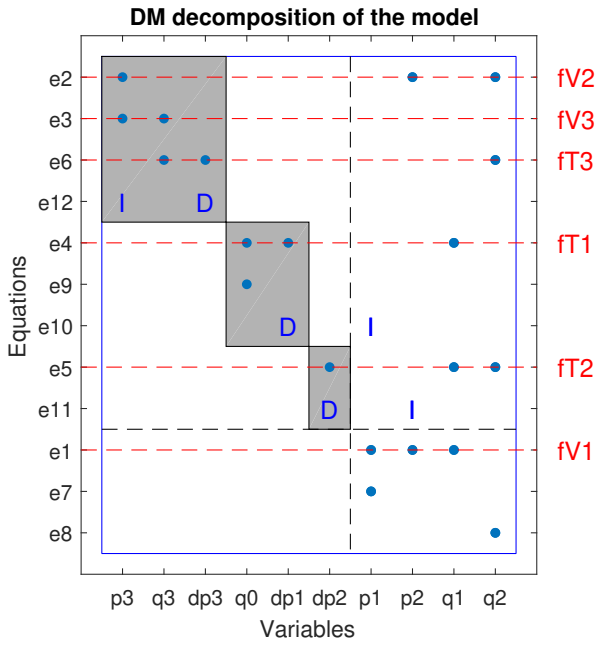

Figure 5.5: DM decomposition of the three-tank system structural model.

f_i can be structurally isolated from another fault f_j if the equation that contains f_i lies in the structurally overdetermined part of the model, excluding the equation that contains f_j as follows [54]:

$$e_{f_i} \in (M/e_{f_j})^+ \tag{5.5}$$

Based on Equation 5.5, an isolability analysis has been performed for the parametric faults considered in the model. Using the algorithm in [146], it is also possible to see what isolability type is possible and advantageous by using derivative, integral, or mixed causality residual generators. Figure 5.6 shows the isolability analysis of the three-tank system structural model based on derivative, integral, and mixed causality. Figure 5.6c shows the full structural isolability properties of the model, i.e., performance in mixed causality which benefits the performance of both derivative and integral causality. As can be seen, it is possible to uniquely isolate the individual faults in $\{f_{V_1}, f_{T_1}, f_{T_2}\}$. However, the group of faults $\{f_{V_2}, f_{V_3}, f_{T_3}\}$ can be detected and isolated from the other faults, while can not be separated from each other.

5.4 Diagnostic test design

In this section, the design procedure of diagnostic tests for real-time fault detection is explained. First, Minimum Structurally Over-determined (MSO) Sets are obtained using the algorithm given in [131]. In addition, a special subset of MSO sets called Minimal test equation support (MTES) sets are introduced which are beneficial when investigating large and complex systems by using the algorithm proposed in [134]. After that, a diagnosability index is stated which was proposed by [135] and can be used for proper selection of either

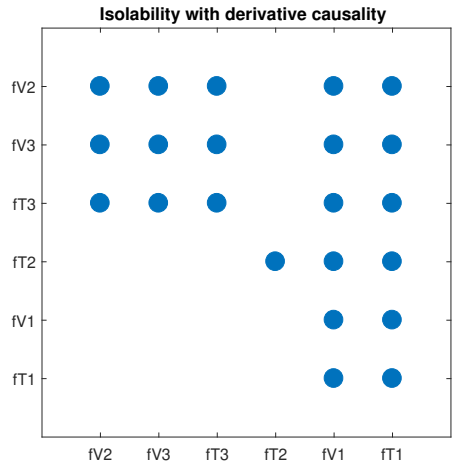

(a)

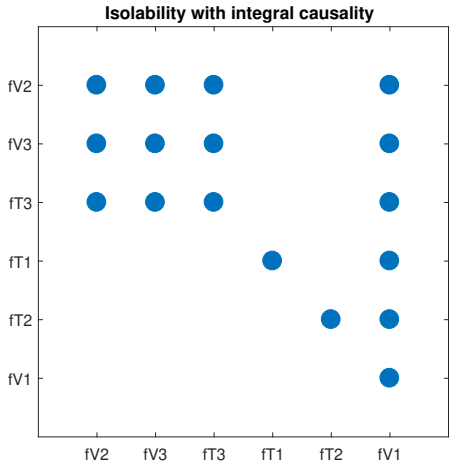

(b)

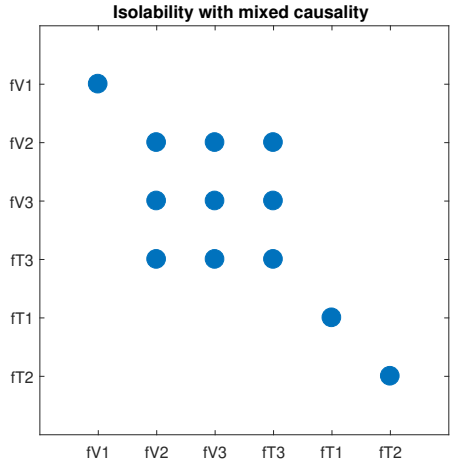

(c)

Figure 5.6: Isolability analysis of the three-tank system structural model based on (a) derivative (b) integral (c) mixed causality.

MSO sets or MTES sets to be used in residual generators. Finally, the derivation of sequential residual generators are explained and several residuals are obtained for the detection of parametric faults in the three-tank system.

5.4.1 Minimal structurally overdetermined sets

According to [131], a structurally overdetermined set of equations is an MSO set if no proper subset is a structurally overdetermined set. In other words, the set of equations M is an MSO set if and only if M is a proper structurally overdetermined set and $\varphi(M) = 1$. This means that an MSO set has the degree of redundancy of one, having exactly one more equation than unknown variables. The idea of using MSO sets is to decompose a complex system into smaller and simpler sub-models, from which it is more efficient to design residuals and apply specific diagnostic algorithms because MSO sets are designed to

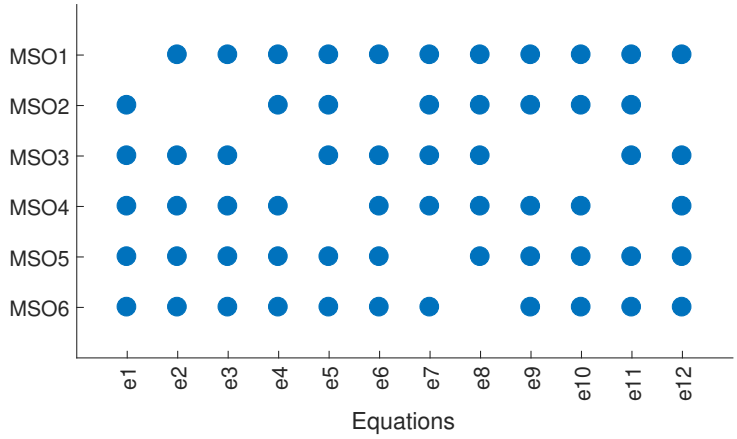

Figure 5.7: MSO sets of the three-tank system structural model.

use as fewest equations as possible while maintaining redundancy to detect specific faults [129, 130]. One of the equations included in each MSO can be chosen as the consistency relation that is used to form a residual by summarizing all the other MSO equations. This is done by eliminating all the unknown variables sequentially from the associated equations in the MSO set, except for the one that is selected to generate a residual. This method of obtaining residuals is called sequential residual generator and has been used in [128, 129, 140]. Krysander [131] has proposed an efficient algorithm for finding all the MSO sets which is a major advantage in the selection of proper diagnostic tests to detect and isolate the investigated faults.

Depending on the requirements of the diagnostic problem and the specifics of the system, either one MSO or multiple MSO sets might be selected to be used for FDI. An MSO set may contain multiple sensors (known variables) and faults in any of these sensors can lead to a nonzero residual, causing difficulty in making a proper diagnostic decision. To overcome this issue, a combination of various MSO sets can be utilized to effectively identify and isolate the faults since different faults affect these MSO sets via different equations [54]. In the process of selecting the MSO sets, special attention must be paid to the computational complexity and robustness of each MSO set [148]. When the MSO sets contain a lot of equations or a large number of faults, the robustness of the diagnostic system is decreased significantly. Thus, selecting an MSO set with fewer equations for the detection of certain faults is preferable. One other consideration that should be taken into account in the process of selecting MSO sets is potential nonlinearity in the calculation of unknown variables. It is recommended to avoid nonlinearities as much as possible in computing each variable so that unique solutions are found more easily.

The algorithm for finding MSO sets in [131] has been applied to the three-tank system and the result is shown in Figure 5.7. It can be seen that these 6 are the minimal sets of equations which has redundancy and therefore, can be used to design residual generators. Figure 5.8 shows the fault signature matrix of the obtained MSO sets for the three-tank system and indicates which faults are included in each MSO set.

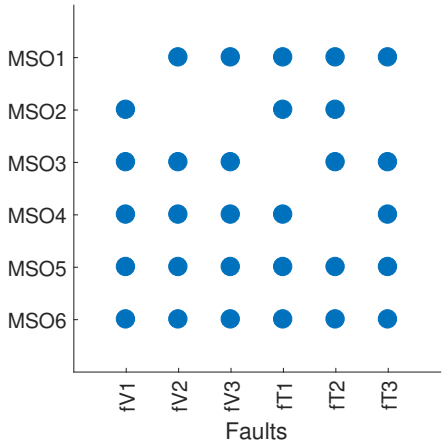

Figure 5.8: Fault signature of the MSO sets.

5.4.2 Minimal test equation support sets

A common problem with using MSO sets in the body of diagnostic tests is that the number of MSO sets grows exponentially as the degree of redundancy of the model increases. As a result, for a system with many sensors (known variables), the number of obtained MSO sets will be large and therefore, computational complexity will increase dramatically. It becomes almost possible to either compute all MSO sets or to design residuals for each of them [134]. To overcome this issue, Krysander [134] has proposed to search for a smaller set of testable models instead of searching for all MSO sets. The idea is that from a diagnosis point of view, it might not be necessary to conduct a search algorithm to find and use all possible tests since there might exist a significantly smaller number of tests with the sufficient capability of distinguishing between different faults. These smaller sub-models are called Test Equation Support (TES) sets, where in addition to redundancy, the effect of faults is taken into account. As a result, the obtained number of testable models as well as the computational complexity of finding them are reduced without reducing the possible diagnosis by simply including fault information in the searching algorithm. According to the definition given by [134], an equation set M is a TES set if:

1. $F(M) \neq \varnothing$.
2. M is a proper structurally over-determined set.
3. For any $M^{'} \supsetneq M$ where $M^{'}$ is proper structurally over-determined set, it holds that $F(M^{'}) \supsetneq F(M)$.

where $F(M)$ is the set of faults that influence any of the equations in M. A TES M is a Minimal Test Equation Support (MTES) if there exists no subset of M that is a TES, holding the degree of redundancy of one. The algorithm for finding MTES sets in [134] has been applied to the three-tank system and the result is shown in Figure 5.9. It can be seen that 4 obtained MTES sets $MTES_1 - MTES_4$ are similar to $MSO_1 - MSO_4$ in Figure 5.7. MSO_5 and MSO_6 are not considered as MTES sets because they violate the third condition given by the definition of TES sets. This can be especially useful in complex systems with a high degree of redundancy, where MSO sets that either do not

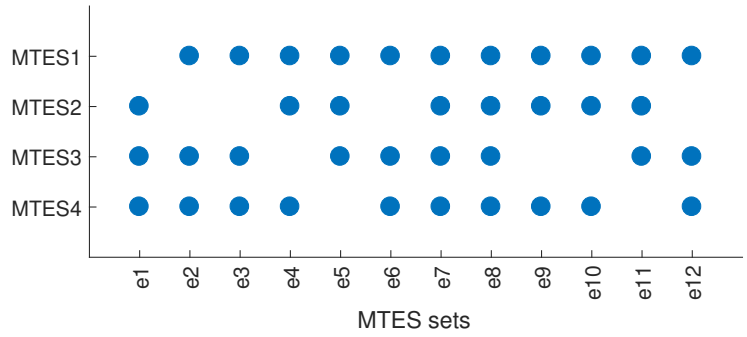

Figure 5.9: MTES sets of the three-tank system structural model.

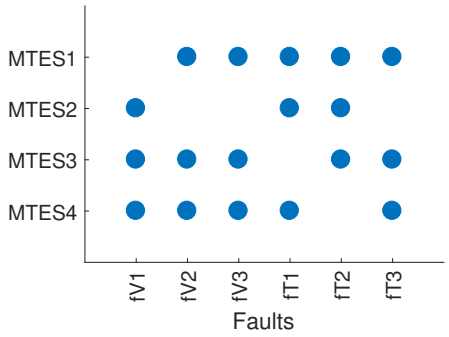

Figure 5.10: Fault signature of the MTES sets.

take influence from any of the faults or have the effect of all the faults are not considered since they will not contribute to the performance of the diagnostic system. Moreover, Figure 5.10 shows the fault signature matrix of the obtained MTES sets for the three-tank system and indicates which faults are included in each MTES set.

5.4.3 Diagnosability index

An important criterion for selecting MSO/MTES sets is to satisfy diagnosability requirements. This includes the detectability of any single fault, as well as isolability between any two faults. Here, an index for proper selection of MSO/MTES which are suitable to be used in sequential residual generators is introduced. Zhang [135] has proposed a diagnosability index that is aimed at achieving the maximum degree of diagnosability for each residual, by comparing the distance between the fault signature matrices of MTES/MSO sets.

Before introducing the diagnosability index, it is necessary to define the distance between two fault signatures. The distance between two fault signatures is defined as the Hamming distance [149] between the two fault signature strings, i.e, the absolute difference between fault vectors i and j in the fault signature matrix. Let S be the number of obtained MSO/MTES sets, V_{f_i} and V_{f_j} be the fault vectors of faults f_i and f_j across MSO/MTES sets (row i and row j in the fault signature matrix), the distance

between these two fault signatures becomes:

$$D(V_{f_i}, V_{f_j}) = \sum_{n=1}^{S} |V_{f_i} - V_{f_j}| \tag{5.6}$$

In other words, the distance between two fault signature vectors can be interpreted as the number of fault signature matrix rows that the elements of the corresponding fault signatures are different. As an example, the distances between the fault signatures f_{V_2}, f_{V_3}, and f_{T_1} in the fault signature matrix of MTES sets (Figure 5.10) can be computed as:

$$\begin{aligned} D(V_{f_{V_2}}, V_{f_{V_3}}) &= 0 \\ D(V_{f_{V_2}}, V_{f_{T_1}}) &= 2 \\ D(V_{f_{V_3}}, V_{f_{T_1}}) &= 2 \end{aligned} \tag{5.7}$$

Using the distance between two fault signatures, a measure for the degree of diagnosability is proposed by [135] as follows: Let n be the number of faults considered in a diagnostic system, a diagnosability index for measuring the degree of diagnosability is computed as:

$$m_D = \frac{1}{\binom{n+1}{2}} \sum_{i=0}^{n-1} \sum_{j=i+1}^{n} D(V_{f_i}, V_{f_j}) \tag{5.8}$$

where$D(V_{f_0}, V_{f_j})$ stands for the distance between fault signature of f_j and the healthy case and measures the detectability of fault f_j. $\binom{n+1}{2}$ denotes the combinations of $n+1$ elements taken 2 at a time. The diagnosability index (degree of diagnosability) reflects the average distance between any two fault signature vectors and a larger value of m_D means a higher degree of diagnosability for a diagnostic system.

Another important criterion before forming residuals is the number of selected MSO/MTES sets that ensure full detectability and isolability of all defined faults. To achieve higher robustness and avoid unnecessary computational complexity, it is desirable to use the least number of diagnostic tests possible that satisfy this requirement [135]. In other words, the least number of MSO/MTES sets that maximize the diagnosability degree should be selected so that each fault has a distinct non-zero fault signature in the fault signature matrix. For any considered system with a total number of n_f faults considered, a least k diagnostic tests are required so that $2k - 1 \geq n_f$, to achieve full isolability. Choosing k diagnostic tests out of N candidate MSO/MTES sets yields $\binom{N+1}{k}$ possible combinations. This can be a very large number for big complex systems where N is large. However, by selecting a lower number of MSO/MTES sets that achieve an acceptable diagnosability index, the number of candidate equation sets and thus computational complexity is reduced significantly.

Here, for the three-tank system with the total number of 6 faults, at least 3 diagnostic tests are needed to isolate all of the faults. Just for comparison, the diagnosability index

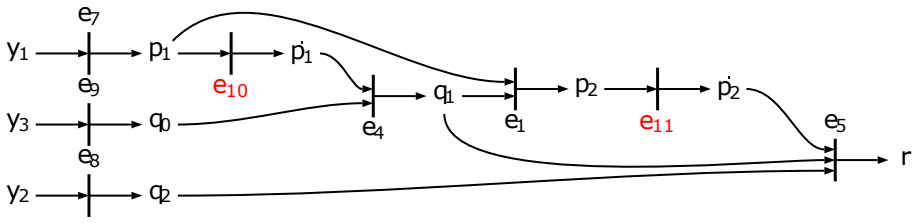

Figure 5.11: Derivation of sequential residual R_1.

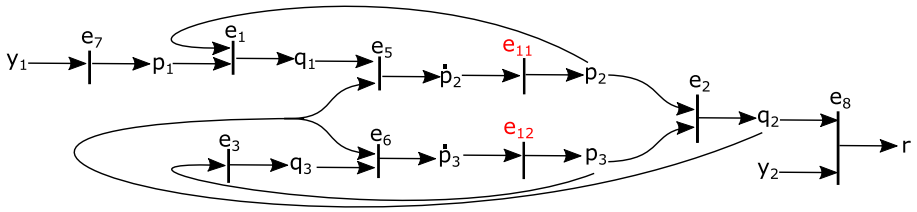

Figure 5.12: Derivation of sequential residual R_2.

for MSO sets with 6 diagnostic tests, and MTES sets with 4 diagnostic tests are calculated using Equation 5.8 as follows:

$$\begin{aligned} m_{D_{MSO}} &= 2.5714 \\ m_{D_{MTES}} &= 2.0 \end{aligned} \tag{5.9}$$

As can be seen, the higher the number of considered diagnostic tests, the better the diagnosability index gets. However, as was explained, there should be a trade-off between the number of selected diagnostic tests and the achieved diagnosability index since a higher number of MSO/MTES sets brings unnecessary computational complexity.

5.4.4 Design procedure of sequential residual generators

At this stage, the acquired MSO/MTES sets of equations are used to generate real-time sequential residuals. For demonstration purposes, 4 different sequential residual generators are derived. The first one is in derivative causality (R_1), the second one is in integral causality (R_2), and the next two are in mixed causality (R_3 and R_4). The first residual generator is based on the MSO_2 set and uses equation e_5 as a residual equation (the equation that is used as consistency relation) and the remaining equations (exactly determined part of MSO_2) are utilized to compute the unknown variables. Figure 5.11 shows the corresponding computational graph, by connecting the known variables through equations to obtain unknown variables. As can be seen, the residual generator is in derivative causality, because all differential constraints (e_{10} and e_{11}) compute the differentiated variable ($\dot{x}$) from the source variable (x).

The second residual generator is based on the MSO_3 set and uses equation e_8 as a residual equation. Figure 5.12 shows the corresponding computational graph and it is clear that the residual generator is in integral causality, because all integral constraints (e_{11} and e_{12}) computes the source variable (x) from the differentiated variable ($\dot{x}$).

The third residual generator is based on the MSO_1 set and uses equation e_2 as a residual equation. Figure 5.13 shows the corresponding computational graph and it is

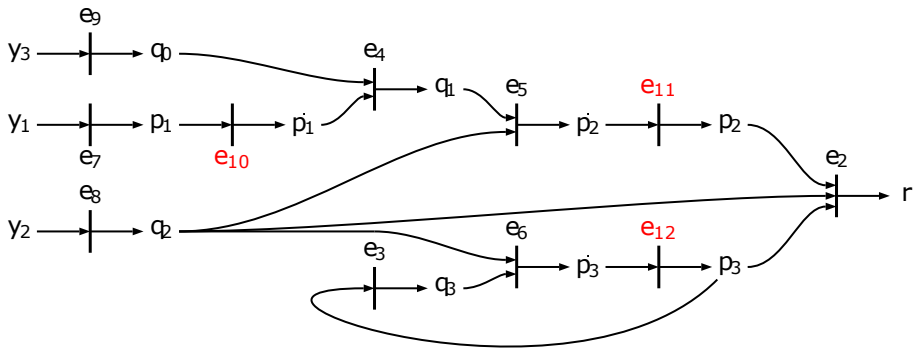

Figure 5.13: Derivation of sequential residual R_3.

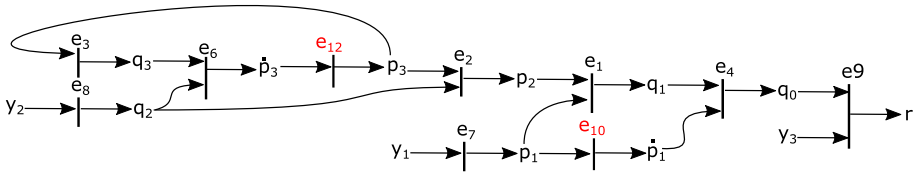

Figure 5.14: Fault signature matrix.

clear that the residual generator is in mixed causality, because both derivative (e_{10}) and integral constraints (e_{11} and e_{12}) are used to connect the source variable (x) to or from the differentiated variable ($\dot{x}$). Finally, the fourth residual generator is based on the MSO_4 set and uses equation e_9 as a residual equation. Figure 5.14 shows the corresponding computational graph and it is obvious that the residual generator is in mixed causality because both derivative (e_{10}) and integral constraints (e_{12}) are used to connect the source variable (x) to or from the differentiated variable ($\dot{x}$).

Moreover, the isolability analysis for these four particular residual generators is performed and the results are shown in Figure 5.15. Each of these residuals is sensitive to specific faults, which are shown in Figure 5.15a. As was discussed before, all the faults in Figure 5.15b are isolable from each other except the group of faults $\{f_{V_2}, f_{V_3}, f_{T_3}\}$ which cannot be isolated from each other. However, it is possible to separate the whole group from other faults and this is the best that could be achieved in this case.

5.5 Results and discussion

5.5.1 Observer design for modeled ITSC and demagnetization faults

5.5.1.1 The proposed diagnostic observer

A structural analysis is proposed in paper C for specific investigation of ITSC and demagnetization faults in a PMSM. A healthy dynamic mathematical model of PMSM in the *abc* frame is employed, and specific terms relevant to the presence of ITSC and demagnetization faults are added to the corresponding equations. These added terms include the deviations in the resistance and inductance of the stator winding caused by the ITSC fault, and the deviations in the PM linkage flux caused by a demagnetization fault, ap-

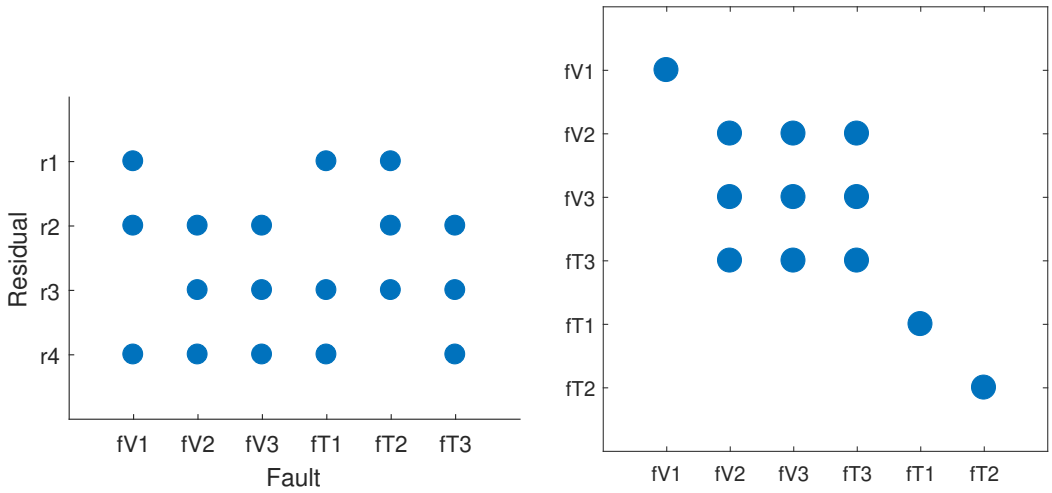

Figure 5.15: (a) Fault signature matrix (FSM) and (b) isolability properties for the four residuals $R_1 - R_4$.

pearing in the three-phase flux and voltage equations. Further, the analytical redundancy of the model is determined based on the PMSM's structural model. The system is subdivided into smaller over-determined subsystems, in which the faults are detected and discriminated and four sequential residuals are designed to show the presence of each fault. Eventually, the proposed model is implemented in Matlab/Simulink to verify its effectiveness in different faulty cases with the presence of white Gaussian noise in the measured signals. The modeling diagram for this purpose is proposed in Figure 5.16 and is based on the analytical model (Figure 4.3) proposed in paper B.

When an ITSC fault appears in one of the phases of motor winding, both resistance and inductance values of that phase are influenced. Here, f_{R_a} and f_{L_a} are added to the corresponding equations of the healthy PMSM to account for ITSC fault in phase a. Similarly, f_{R_b}, f_{L_b}, f_{R_c}, and f_{L_c} terms are added to account for ITSC faults in phases b and c, respectively. On the other hand, when a demagnetization fault appears in one of the PMs of the rotor, the flux established by PMs is influenced. Here, $f_{\lambda_{ma}}$, $f_{\lambda_{mb}}$, $f_{\lambda_{mc}}$, and $f_{\lambda_{mt}}$ terms are added to the corresponding equations of the healthy PMSM to account for demagnetization fault in the PMs.

The structural model of the PMSM drive system in Figure 5.16 is obtained and shown as an incidence matrix in Figure 5.17. The incidence matrix contains 24 rows, representing the 12 dynamic equations, 7 measured known variables including the three-phase voltages,three-phase currents, and angular speed, as well as the 5 differential constraints of the unknown variables. The columns of the matrix is subdivided into three groups of unknown variables, known variables, and faults, and each equation is connected to its relevant constraint in any of the three groups through each row.

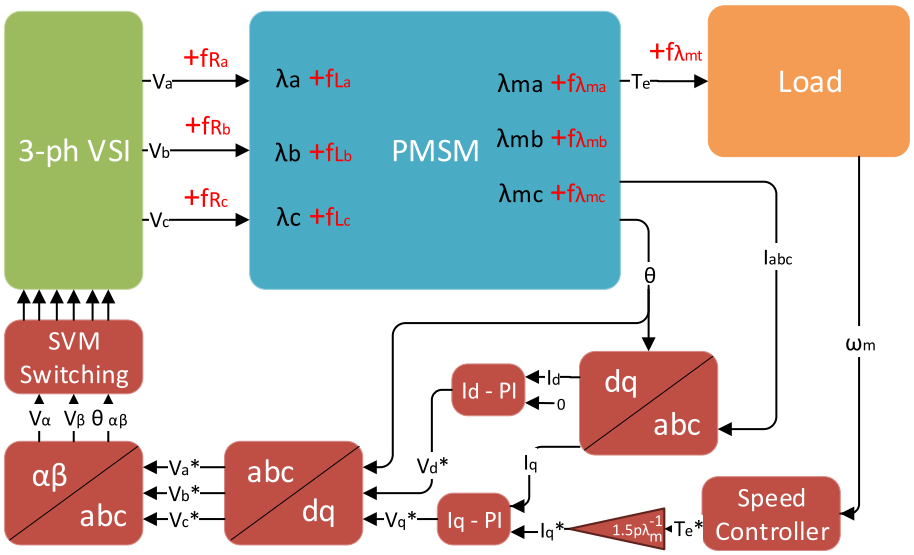

Figure 5.16: Modeling diagram of PMSM and drive system in paper C.

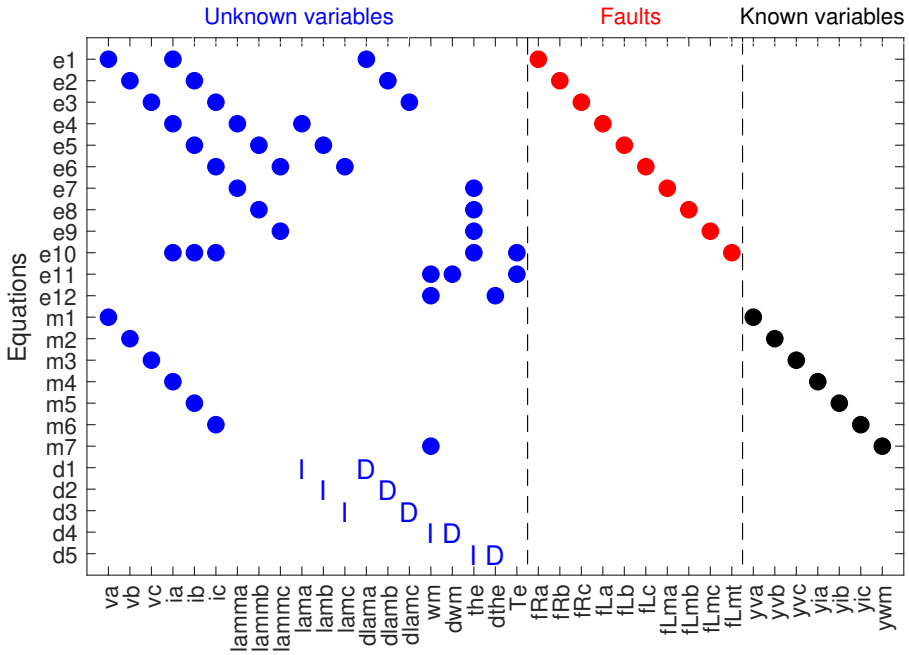

Figure 5.17: PMSM drive system structural model in paper C.

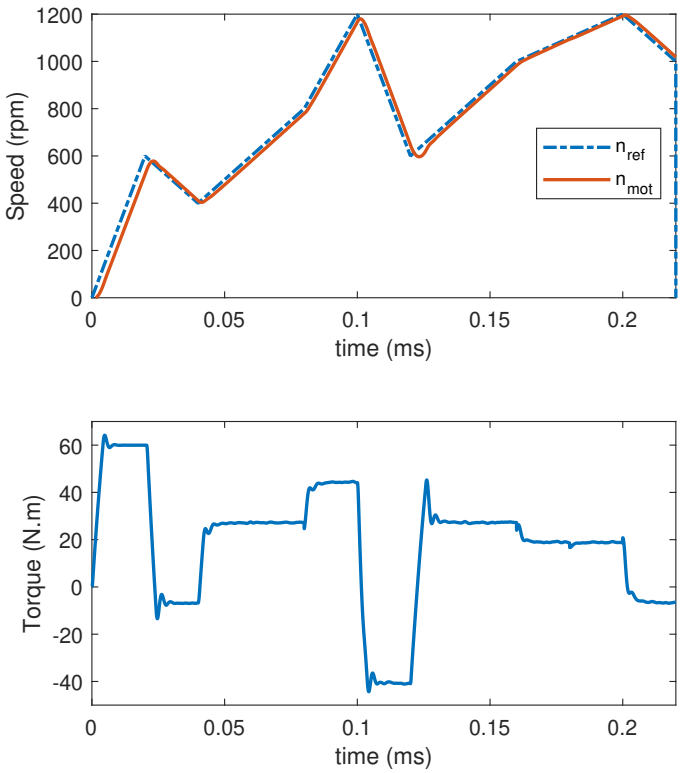

Figure 5.18: Output speed and torque characteristics of the PMSM.

5.5.1.2 Simulation results and discussion

To verify the proposed modeling diagram in Figure 5.17, a Matlab/Simulink model of a PMSM is implemented based on the ITSC fault modeling proposed in 4.2. Using this model, three ITSC faults in each of the *abc* phases are applied and motor signals are obtained. Further, the reference for the motor drive's speed controller is set to be variable to investigate the residuals' dynamic response under variable operating conditions. Figure 5.18a shows the speed reference and the motor's speed and Figure 5.18b shows the output torque of the motor during the time of the simulation. As can be seen in Figure 5.18a, it takes time for the actual speed of the motor to catch the reference speed (which comes from the controller), since the motor is considered to be stationary in the beginning.

During the simulation, the ITSC and demagnetization faults are applied at different time intervals. At $t = 0.06 - 0.08s$, there appears an ITSC fault in phase a with 5% fault severity (number of shorted turns to total turns in one phase); at $t = 0.1 - 0.12s$, there is an ITSC fault in phase b with 5% fault severity; and at $t = 0.14 - 0.16s$, the motor has an ITSC fault in phase c with 5% fault severity; at $t = 0.18 - 0.2s$, appears a demagnetization fault with 20% fault severity (the flux linkage of PMs is decreased by 20%).

To test the effectiveness of the residual responses realistically, band-limited Gaussian noise signals are added to the measured values. Without considering the noise in the measurements, the residuals can be triggered by any small abnormality in the system. Therefore, the diagnostic system will be able to theoretically detect faults with very low

severity (e.g. 0.1%) which is not plausible in reality. The noise signal $w(t)$ is generated by a dynamic filter as follows [127]:

$$H(s) = \frac{\sqrt{2\beta}}{s+\beta}\sigma_\omega \tag{5.10}$$

The dynamic filter has the random signal $v(t)$ as input and $w(t)$ as output. The signal $v(t)$ has an amplitude equal to 1, which indicates the noise has a total power equal to 1. Based on the data from the previous experimental studies and measurements in UiA Machine Lab, parameters of different noise signals are extracted and used in this study.

The residual responses for the mentioned faults are obtained and shown in Figure 5.19. Before the faults are applied, the motor is operating in healthy mode ($t = 0-0.06s$) and all the residuals remain zero (neglecting the noise) since there is not any difference between the measured signals and the calculated ones used in each residual. When the ITSC fault in phase a is applied, only R_1 is affected and obtains a non-zero value. Since ITSC fault in phase a (faults in f_{R_a}, f_{L_a}) is only observable in R_1, other residuals remain zero when the motor is experiencing this fault. The same logic can be used for R_2 and R_3 as they obtain non-zero values and only these two residuals are affected when ITSC faults in phase-b and phase-c are applied to the motor. However, when the demagnetization fault is applied on the motor between $t = 0 - 0.06s$, all the residuals obtain a non-zero value.

Isolation of the faults based on the response of the residuals is done by using logical blocks. For instance, to detect and isolate ITSC fault in phase a, R_1 should be non-zero while other residuals remain zero. For ITSC fault in phase b, R_2 should be non-zero while other residuals remain zero. For detection and isolation of ITSC in phase c, R_3 should be non-zero while other residuals remain zero. When all four residuals have a non-zero value, it means that the motor is experiencing a demagnetization fault. A a result, all the studied faults are detected and isolated from the others in Figure 5.20, by using a logical decision-making system based on the moving average of the residual responses.

5.5.2 Observer design for sensor faults

5.5.2.1 The proposed diagnostic observer

The structural analysis approach is applied to a more generalized electric drive system where eleven different sensors are used for condition monitoring of the system. The considered measurements include three-phase voltages and currents sensors, DC bus voltage and current sensors, the motor's angular velocity and position, and load torque transducer. In the structural model, a combination of healthy dynamic mathematical models of PMSM both in *abc* and *dq* frames including all the investigated sensors are included, and specific terms related to each fault are added to the corresponding measurement equations. These added terms include the deviations in the measured signals of each sensor caused by dc offsets, gain change, amplitude imbalance, and generally any sort of anomaly appearing in the corresponding equations.

Figure 5.21 shows the diagnostic drive configuration that was introduced in paper C. The modeling diagram illustrates a closed-loop vector-control of PMSM based on SVPWM switching. The PMSM is mechanically coupled to an identical machine via shaft that

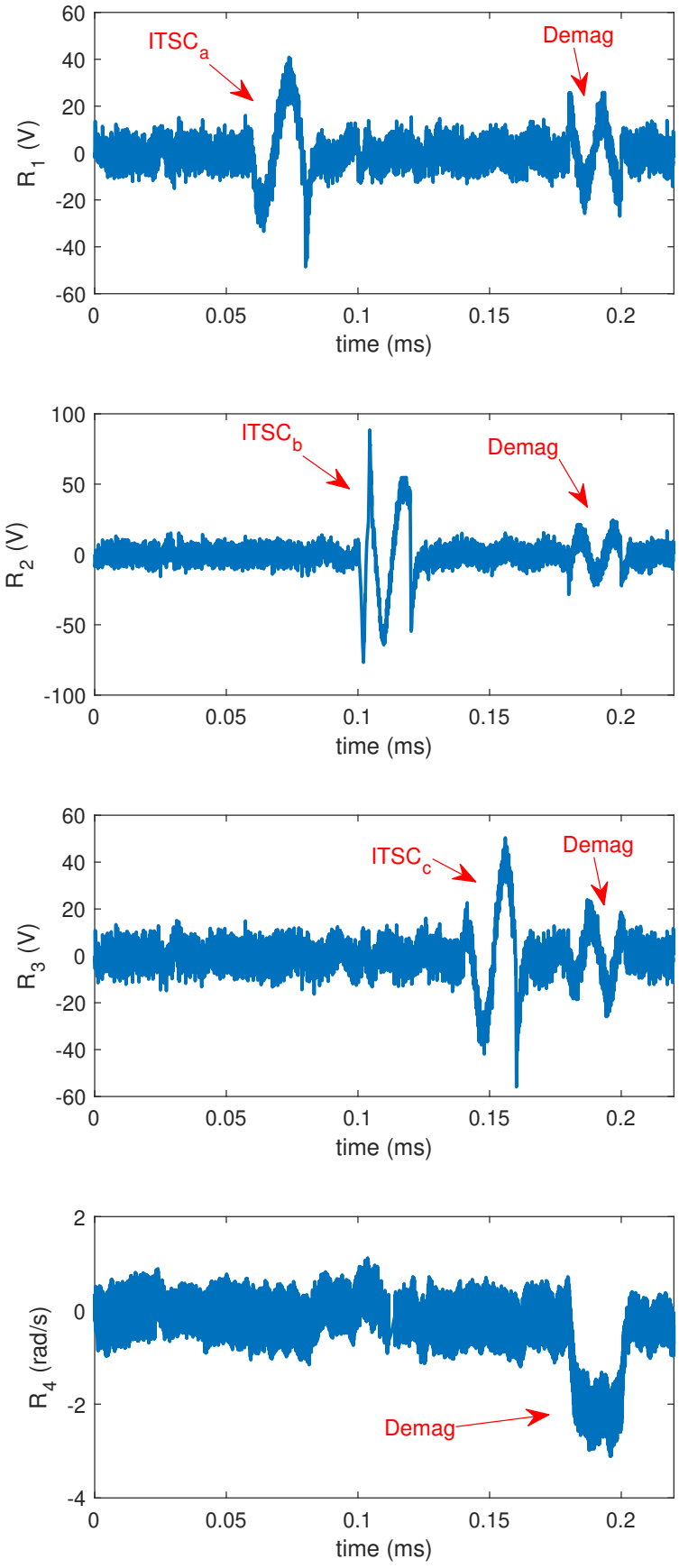

Figure 5.19: Response of residuals in paper C.

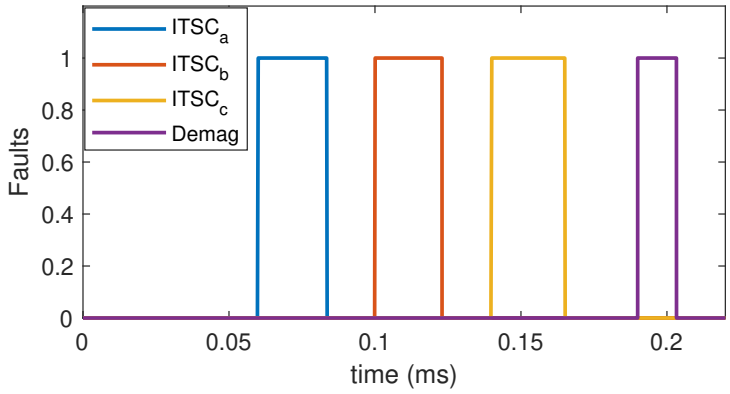

Figure 5.20: Discrimination of ITSC and demagnetization faults.

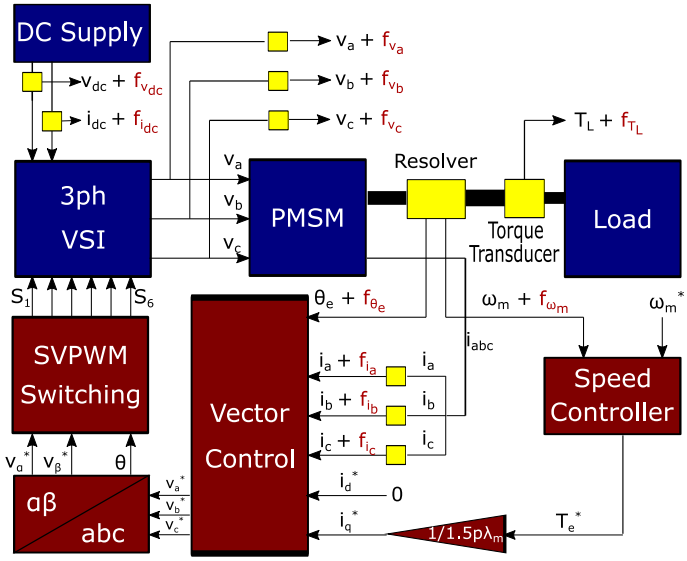

Figure 5.21: Modeling diagram of PMSM and drive system in paper D.

represents mechanical load. After applying the structural analysis, the structural model of the PMSM drive system is obtained and shown as an incidence matrix in Figure 5.22. The incidence matrix contains 24 rows, representing the 11 dynamic equations, 11 measured known variables including the three-phase voltages, three-phase currents, dc bus voltage and current, load torque, and angular position and speed, as well as the 4 differential constraints of the unknown variables. The columns of the matrix are subdivided into three groups of unknown variables, known variables, and faults, and each equation is connected to its relevant constraint in any of the three groups through each row.

The analytical redundant relations of the structural model are obtained using a DM decomposition tool, and the algorithm yields 168 MTES sets. A combination of MTES sets is selected which leads to an acceptable value for diagnosability index $m_D = 4.45$. Subsequently, 9 sequential residuals ($R_1 - R_9$) are derived based on the selected MTES sets. These residuals aim to detect all the considered faults and a combination of them can be used to isolate each fault. The process of designing each sequential residual is given in detail in paper D.

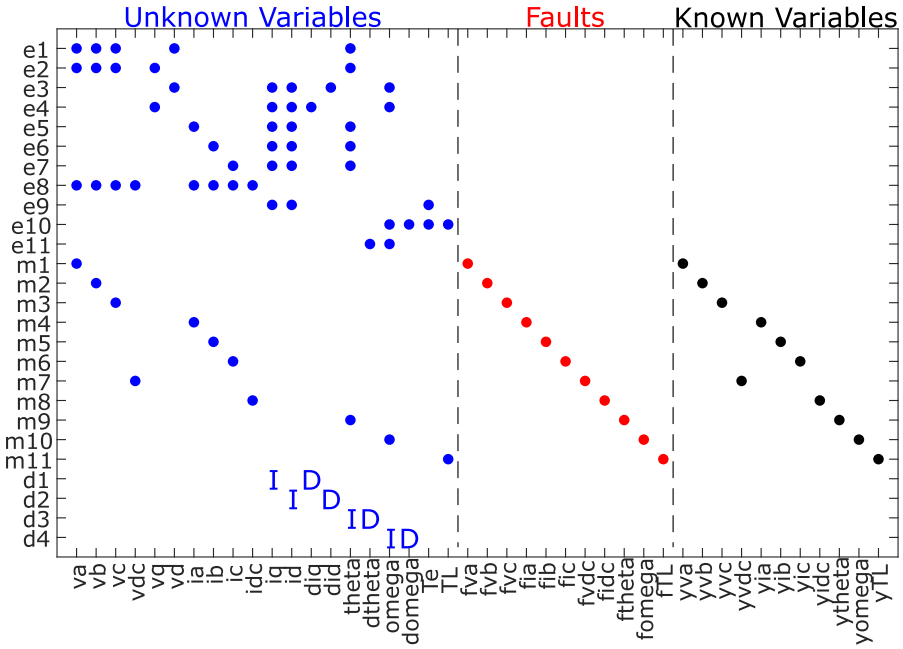

Figure 5.22: PMSM drive structural model.

5.5.2.2 Experimental results and discussion

The structural analysis is implemented on the structural model in Figure 5.22 and the proposed diagnostic method is validated through experimental results using the setup in Figure 3.2. The PMSM is driven up to the nominal operating point (1200 rpm of speed and 14 N.m of load torque) and after reaching steady-state mode, the measurement faults are applied at different time intervals.

To cover all the possible measurement errors, different measurement errors have been applied including dc offset values for current sensors, speed and torque sensors, gain change for voltage sensors, and imbalance in angle measurement. At $t = 1 - 2s$, there appears a $+0.2rad/s$ offset in ω_m measurement; at $t = 3 - 4s$, there is a $+1N.m$ offset in T_L measurement; at $t = 5 - 6s$, the inverter has a $+2\%$ gain increase in v_{dc} measurement; at $t = 7 - 8s$, the inverter has a $+0.04A$ offset in i_{dc} measurement; at $t = 10 - 11s$, there appears a $+4\%$ gain change in v_a measurement;at $t = 12 - 13s$, there is a $+4\%$ gain change in v_b measurement;at $t = 14 - 15s$, appears a $+4\%$ gain change in v_c measurement;at $t = 17 - 18s$, there is a $+2A$ offset in i_a measurement;at $t = 19 - 20s$, there is a $+2A$ offset in i_b measurement;at $t = 21 - 22s$, there is a $+2A$ offset in i_b measurement; and finally at $t = 23 - 24s$, there is a $+0.01$ amplitude imbalance in θ_e measurement. Furthermore, nine sequential residuals are designed and implemented to observe the presence of these measurement faults. The residual responses for the sensor faults are obtained and filtered using a low-pass filter for better demonstration and are shown in Figure 5.23.

As shown in Fig. 5.23, all the faults can be detected based on their presence in one or several residual responses $R_1 - R_9$. The faults $f_{v_{dc}}$ and $f_{i_{dc}}$ can be detected but not isolated because they appear in the same residual only. The faults f_{ω_m} and f_{T_L} can be easily detected and isolated because they trigger only one of the residuals during their presence in the system. The rest trigger multiple but unique combinations of residuals

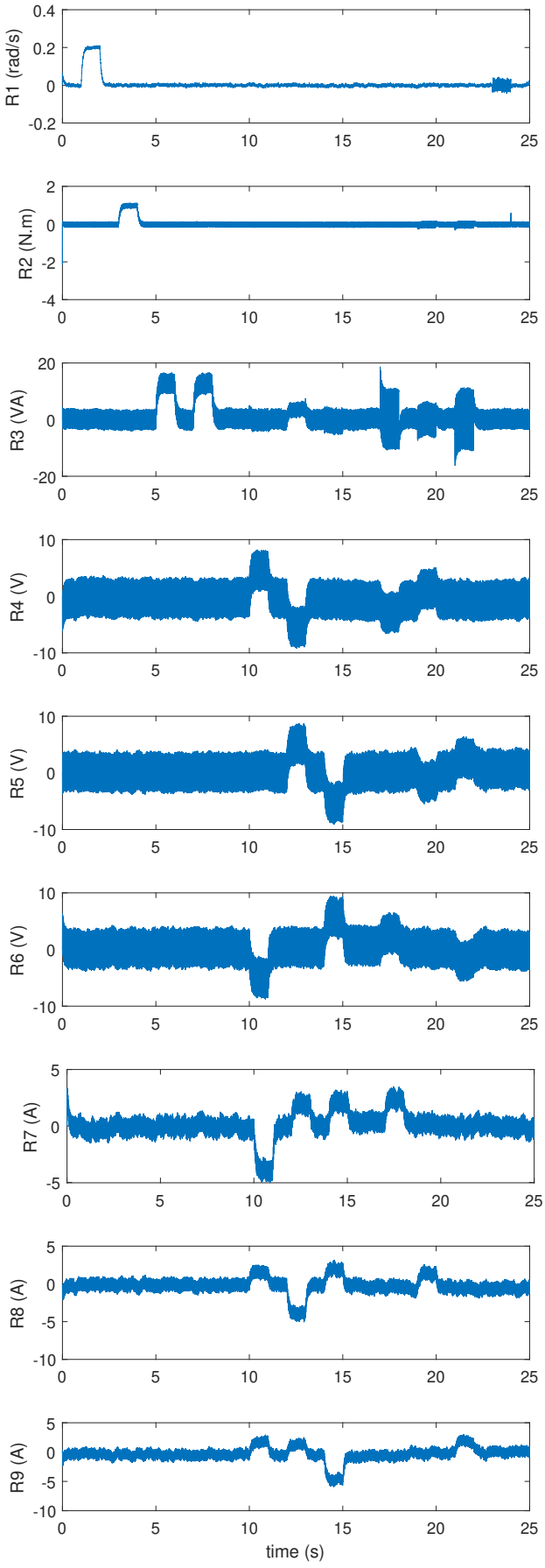

Figure 5.23: Response of residuals R_1–R_9 in paper D.

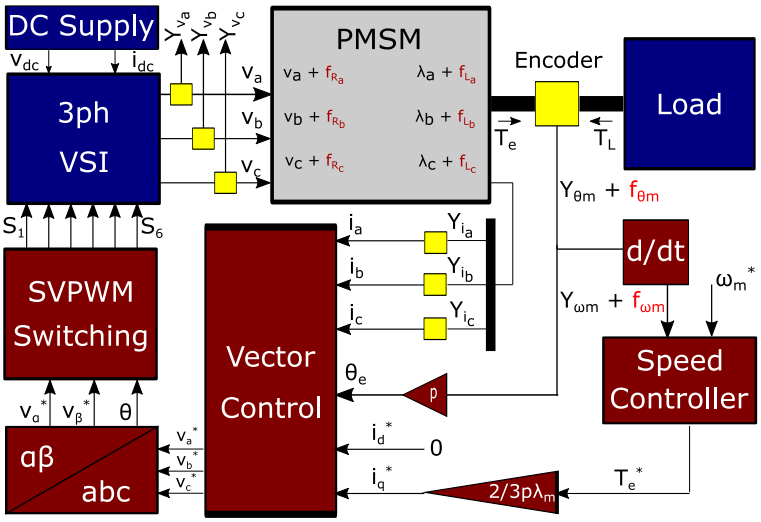

Figure 5.24: Modeling diagram of PMSM and drive system in paper E.

and therefore, specific combinations of residuals can be used as the ground for detection and isolation of these faults in the PMSM and drive system.

5.5.3 Observer design for ITSC and encoder faults

5.5.3.1 The proposed diagnostic observer

In paper E, attempts were made to implement the structural analysis on the test setup in 3.2 and obtain experimental results. As a result, the modeling diagram in Figure 5.24 was proposed in paper E to detect ITSC and encoder faults.

As discussed in 4.2, an ITSC fault splits the phase winding into a faulty part with resistance and inductance of μR_s and μL_s and a healthy part with resistance and inductance of $(1-\mu)R_s$ and $(1-\mu)L_s$. The changed resistance and inductance of the winding have a direct correlation with voltage equations and flux equations. Under a healthy condition, the model of PMSM, especially voltage and flux equations, have no fault terms. Therefore, any changes in the inductance will affect both voltage and flux equations directly, and any changes in the resistance will affect only voltage equations directly. Here, f_{v_a} and f_{i_a} are added to the corresponding equations of the healthy PMSM to account for the ITSC fault in phase a. Similarly, f_{v_b}, f_{v_c}, f_{i_b}, and f_{i_c} terms are added to account for ITSC faults in phases b and c, respectively.

The structural model of the PMSM drive system in Figure 5.24 is obtained and shown as an incidence matrix in Figure 5.25. The incidence matrix contains 22 rows, representing the 9 dynamic equations, 8 known variables, and the 5 differential constraints of unknown variables. The columns of the matrix are subdivided into three groups of unknown variables, known variables, and faults. The known variables are obtained directly from the measurements, while the unknown variables can be calculated based on the known variables. The faults considered in the structural model are variations in phase voltage and flux to represent ITSC faults in each phase.

The analytical redundant sub-model of the structural model in Figure 5.25 is obtained using a DM decomposition tool and as a result, 10 MTES sets are found. A combination

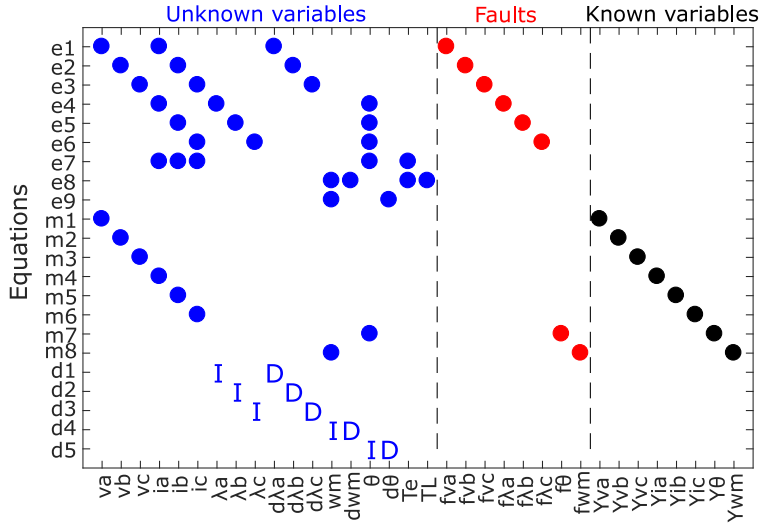

Figure 5.25: PMSM drive system structural model in paper E.

of MTES sets is selected that both achieves an acceptable value for diagnosability index $m_D = 1.88$, and detects all the considered faults. Next, 4 sequential residuals ($R_1 - R_4$) are derived based on the selected MTES sets. The process of obtaining analytical redundancy, selection of MTES sets, and designing the sequential residual are fully given in paper E.

5.5.3.2 Experimental results and discussion

The proposed diagnostic model in Figure 5.25 is implemented and validated through the in-house experimental setup in Figure 3.2. The ITSC faults are applied to the phase windings of a four-pole PMSM, as shown in Figure 3.8. Each phase winding of the motor has two coils in series, each of which has 51 turns with three parallel branches. For phase a, one of the turns was short-circuited, or about a 1% fault level. For the phases b and c, three and five turns were short-circuited, resulting in almost 3% and 5% fault severity, respectively. The connection wires to these extra taps in the phase windings were taken out of the motor and connected to 100 mΩ resistors to limit the short circuit current and to simulate the winding insulation degradation, as shown in Figure 3.9. Furthermore, controllable relays were placed between winding taps and fault resistors to activate or deactivate the fault. To test the residual responses and effectiveness of the diagnostic system, the motor was driven from stationary to nominal speed, i.e., 1500 rpm, and kept in a steady-state condition. During the operation of the motor, the encoder and ITSC faults were applied at different time intervals using controllable relays. At t = 1–3 s, the encoder measurement fault was applied with a 1 rad/s error. At t = 4.471–7.238 s, the ITSC fault in phase a was applied which had 1% fault severity (one shorted turn in phase a winding); at t = 9.613–12.76 s, the ITSC fault in phase b appeared with 3% fault severity (three shorted turn in phase b winding); at t = 15.6–18.41 s, the ITSC fault in phase c with 5% fault severity (five shorted turn in phase c winding) was applied on the motor.

The residual responses for the mentioned faults were obtained and are shown in Figure 5.26. First, the encoder fault is applied at t = 1–3 s, with a 1 rad/s amplitude error.

Before the encoder fault is applied, the motor is operating in a healthy mode (t = 0–1 s), and R_4 remains averagely zero (neglecting the noise). This is because there was no error between the measured angular speed signal and the redundant calculated one.

When the encoder fault appears, R_4 obtained a nonzero dc value, and it went back to average zero as soon as the fault disappears. Before the ITSC faults were applied (t = 0–4.471 s), all the residuals remained averagely zero (neglecting the noise). This is because there was no error between the measured signals and the calculated ones used in each residual. First, the ITSC fault in phase a was applied (t = 4.471–7.238 s), R_1 was directly affected, and obtained a higher oscillating value. Due to mutual induction of the fault current, this fault was also observable in R_2 and R_3 (t = 9.613–12.76 s and t = 15.6–18.41 s). In addition, the controller response had a role in the increase of other phase currents. Since a part of the winding was gone, more I_q was required to keep the motor speed constant at 1500 rpm. The same logic can be used for ITSC faults in phases b and c as the residuals obtain higher oscillating values. Therefore, the encoder fault can be detected and isolated from all the other faults while ITSC faults can be detected and isolated only from the encoder fault and not each other. The behavior and response of the residuals during each ITSC fault can be used as the ground for the detection and isolation of the two groups of faults in the PMSM.

5.5.4 Observer design for ITSC and demagnetization faults

5.5.4.1 The proposed diagnostic observer

Subsequently, the modeling diagram of the PMSM drive system was adjusted in a way to include the effects of not only the ITSC fault but also the demagnetization fault. Moreover, the control loop needed to be redefined to diminish the effect of speed controller noise injected into motor signals. As a result, the modeling diagram shown in Figure 5.27 was proposed in paper F to detect ITSC and demagnetization faults. Here, the dynamic equations of a PMSM and drive system are represented by equations in both *abc* and *dq* frames. ITSC and demagnetization faults may have different signatures, but both influence the flux and currents of the PMSM. Therefore, to account for the deviations caused by these two faults, specific fault terms are added to relevant equations. Here, f_{v_d} and f_{v_q} terms are added to the v_d and v_q equations to include the effect of flux deviation caused by either of the faults. Similarly, f_{i_a}, f_{i_b}, and f_{i_c} terms are added to the equations i_{abc} to account for the changes caused by faults in phases b and c currents, respectively.

The structural model of the PMSM drive system in Figure 5.27 is obtained and portrayed in form of an incidence matrix in Figure 5.28. The incidence matrix contains 21 rows, representing the 10 dynamic equations, 7 measured known variables, and the 4 differential constraints of unknown variables. The columns of the incidence matrix represent model variables and are categorized as unknown variables (blue dots), known variables (red dots), and fault variables (black dots). Each row of the incidence matrix represents an equation in the model and is connected to the corresponding variables if they are present in that specific equation.

The analytical redundant sub-model of the structural model in Figure 5.28 is obtained using a DM decomposition tool and as a result, 10 MTES sets are found. A combination

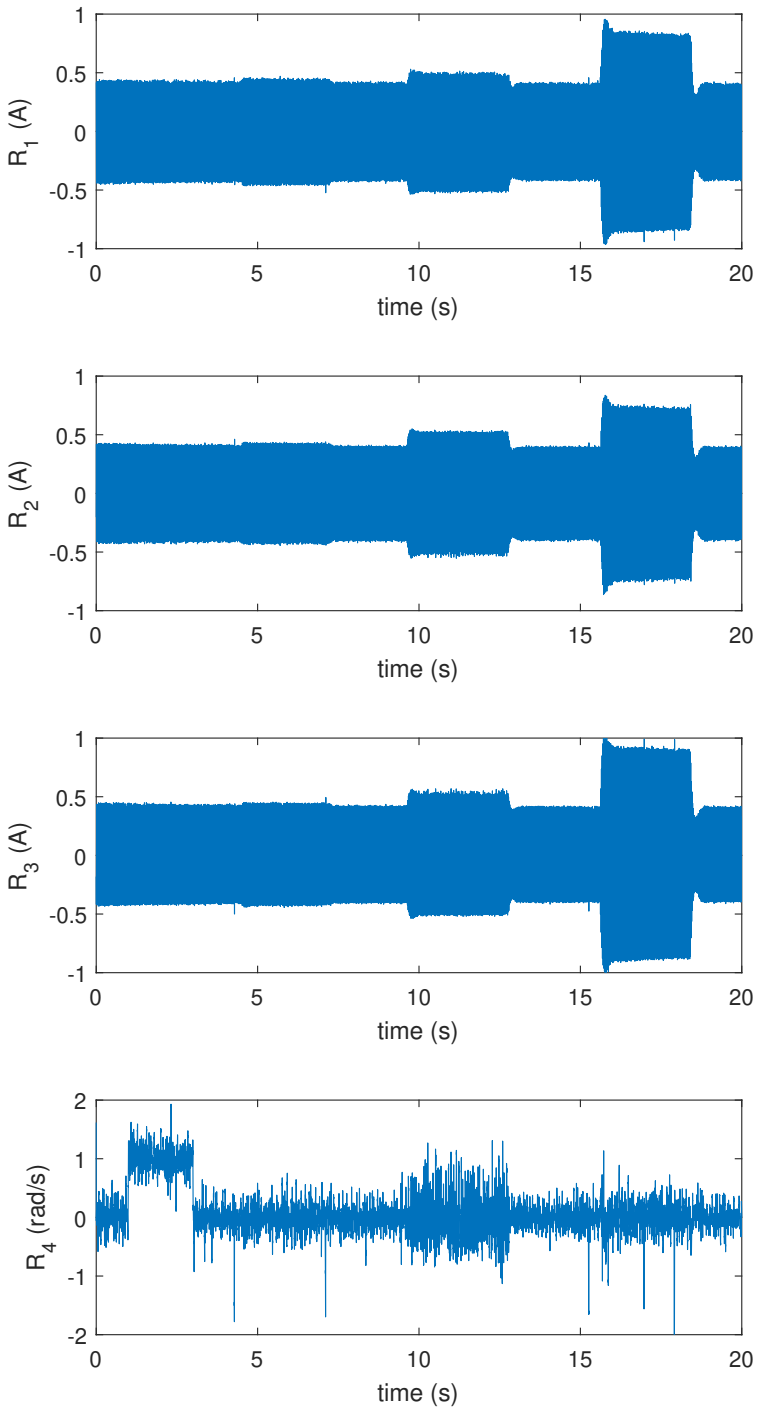

Figure 5.26: Response of residuals in paper E.

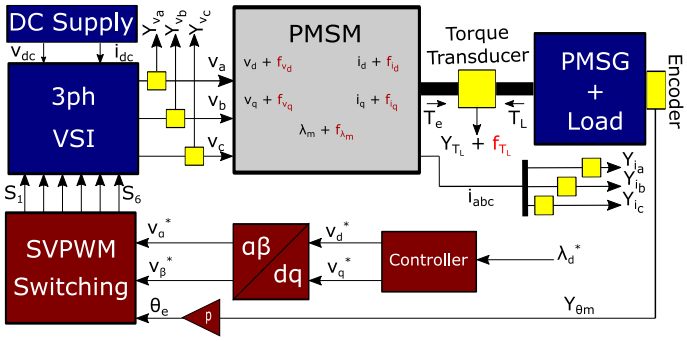

Figure 5.27: Modeling diagram of PMSM and drive system in paper F.

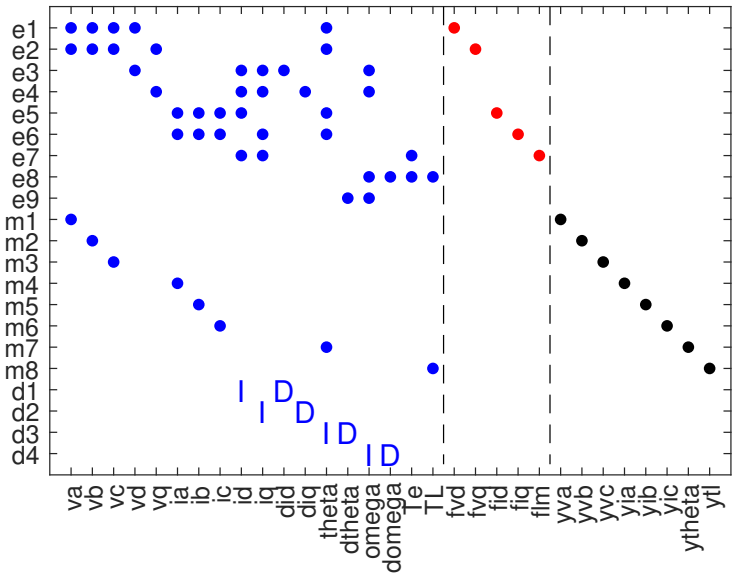

Figure 5.28: PMSM drive system structural model in paper F.

of MTES sets is selected that both achieves an acceptable value for diagnosability index, and detects all the considered faults. Next, 5 sequential residuals are derived based on the selected MTES sets. Out of the acquired 5 residuals, R_2 is chosen as the ideal candidate to detect both ITSC and demagnetization faults and hence, further processed.

5.5.4.2 Experimental results and discussion

The proposed diagnostic model in Figure 5.28 is implemented and validated through the in-house experimental setup in Figure 3.2. The same motor with ITSC faults was investigated in this case study as well, which is shown in Figure 3.8. Using the drive strategy in Figure 5.27, the PMSM is started by setting a flux reference. After reaching the steady-state mode, the ITSC faults are applied at different time intervals using controllable relays and flux reference. After the last ITSC fault is removed, the reversible demagnetization faults are applied by creating a reverse field in the stator winding as opposed to the field of PMs on the rotor. This moves the operating point of the PM to another point just above the knee on PM's BH curve and hence, when the reverse field is removed, the original residual flux density of B_r is restored. This is done by controlling v_d and v_q reference voltages and using a field-weakening technique while keeping the terminal voltage constant. The severity of a demagnetization fault is defined as:

$$f_{DM} = 1 - \frac{\lambda_{linkage_F}}{\lambda_{linkage_H}} \tag{5.11}$$

where $\lambda_{linkage_H}$ is the linkage flux under a healthy condition and $\lambda_{linkage_F}$ is the weakened linkage flux after the demagnetization fault has appeared. At $t = 2.022 - 6.174s$, the ITSC fault in phase a is applied which has 1% fault severity (1 shorted turn in phase a winding); at $t = 9.918 - 13.73s$, the ITSC fault in phase b appears with 3% fault severity (3 shorted turn in phase a winding); and at $t = 17.7 - 22.82s$, the ITSC fault in phase c with 5% fault severity (5 shorted turn in phase a winding) is applied; at $t = 25.83 - 30.48s$, the first reversible demagnetization with 2% severity is applied; at $t = 33.92 - 38.01s$, the second reversible demagnetization with 5% severity is applied; and at $t = 40.91 - 45.2s$, the third reversible demagnetization with 9% severity is applied on the PMSM. Figure 5.29 and Figure 5.30 show the real-time dc bus current and linkage flux signals during the operation of the PMSM.

During the operation of the PMSM in $50s$, the real-time residual responses for ITSC and demagnetization faults are obtained and shown in Figure 5.31. Before each fault is applied, the motor is operating under a healthy condition and the residual remains averagely zero, only containing noise. The residual shows a decent reaction to the presence of all the faults by creating a distinctive dc level change and keeping an average zero value under a healthy condition.

Based on the response of the residual, Each group of faults, i.e. demagnetization faults and ITSC faults can be detected and isolated from the other group of faults while faults in the same group cannot be isolated from each other. The behavior and response of the residuals during each ITSC fault can be used as the ground for the detection and isolation of the two groups of faults in the PMSM.

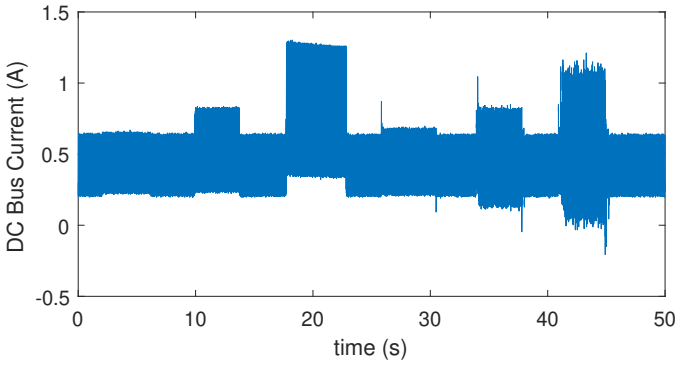

Figure 5.29: DC bus current of PMSM drive.

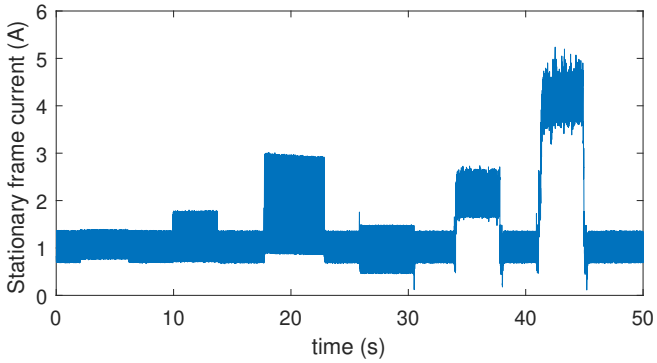

Figure 5.30: Linkage flux in the PMSM.

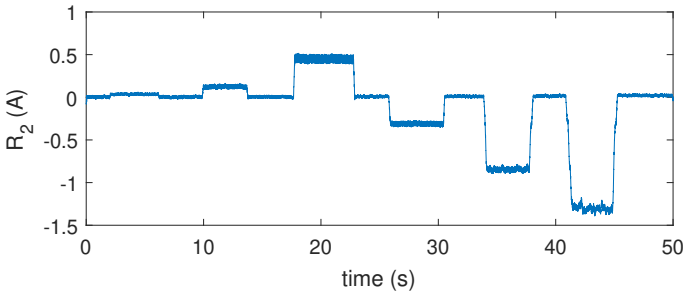

Figure 5.31: Residual 2 in paper F.

5.6 Summary

This chapter focuses on model-based detection of ITSC, demagnetization, and sensor faults in the PMSM drive system based on structural analysis. First, the theoretical background of structural analysis and implementation of the structural model for fault diagnosis of a system are given in sections 5.1 and 5.2. Analytical redundancy analysis of a structural model including detectability analysis and isolability analysis is given in section 5.3. Subsequently, the process of designing diagnostic tests by obtaining MSO sets or MTES sets as well as diagnosability index are given in section 5.4. Section 5.5.1.1 presents a structural analysis of the PMSM drive system for specific investigation of ITSC and demagnetization faults, based on the model described in paper B, and simulation results of residual responses are presented in 5.5.1.2. In section 5.5.2.1, a more generalized electric drive system is studied in which eleven different sensors are used for condition-monitoring of the system. After implementing structural analysis and deriving the structural model, nine sequential residuals are designed and implemented on the experimental drive system setup in 5.5.2.2. Eleven faults including three-phase voltages and currents sensors, DC bus voltage and current sensors, motor's angular velocity and position, and load torque transducer are applied to the system and the residual responses are obtained. In section 5.5.3.1, a structural analysis of the PMSM drive system for detection of ITSC and encoder faults is presented and experimental results of residual responses are shown in 5.5.3.2. Finally, a structural analysis of the PMSM drive system for detection of ITSC and demagnetization faults is presented in section 5.5.4.1 and experimental results of residual responses are shown in 5.5.4.2.

Chapter 6

Diagnostic decision and signal processing

By implementing a structural analysis, the goal was to form residuals that have a zero value in a healthy scenario and a nonzero value in a faulty scenario. However, derivatives, integrals, and even uncertainties in the dynamic model affect the calculation of unknown variables and cause some distortion in the variable output signal. In addition, phenomena such as environmental noise and switching noise affect the signals. These lead to a residual output signal that fluctuates around zero instead of having a perfect signal that holds the absolute zero value in a healthy scenario. Even in a faulty scenario, the residual signal fluctuates around a nonzero value. Therefore, extra signal processing is required to deal with model uncertainties and environmental noise, to be able to distinguish and isolate the indicator signal from noise.

After obtaining residual responses that maintain a zero value under a nonfaulty condition (null hypothesis), and a nonzero value under a faulty condition (alternative hypothesis), a decision should be made to inform the operator of the status of the diagnostic system. This decision is normally made based on a processed signal, called test statistic, a threshold that acts as the boundary between the two hypotheses. In this chapter, designing the real-time diagnostic test statistics using Generalized Likelihood Ratio Test (GLRT) approach is introduced. In addition, the process of obtaining thresholds for fault detection based on the probability of false-alarm (P_{FA}) is explained, and other detection characteristics such as the probability of detection (P_D) and receiver operating characteristics (ROC) are analyzed. Finally, a recursive cumulative GLRT with an adaptive threshold algorithm is implemented to obtain a more processed fault indicator that decreases the detection and recovery delay time.

6.1 Generalized likelihood ratio test approach

To detect a signal in a realistic way, it is commonly assumed that we do not have complete knowledge of the probability density functions (PDFs) of the signal under the null hypothesis ($\mathcal{H}_0$) and alternative hypothesis ($\mathcal{H}_1$). For example, the amplitude of a dc signal or the frequency of an ac signal may not be known upon arrival. Thus, in each hypothesis,

the signal portion of the PDF may not be known due to unknown parameters. On the other hand, signals are affected by noise due to environmental conditions and similarly, the noise characteristics may not be known a priori. In this case, the noise can be reasonably modeled as White Gaussian Noise (WGN). Designing an effective detector that addresses the unknown parameters in the PDF is therefore of great practical importance.

Generalized Likelihood Ratio Test (GLRT) is a composite hypothesis testing approach that addresses the unknown parameters, i.e. (μ) and variance (σ^2) values in PDF of a signal, for use in likelihood test [150]. The way that GLRT deals with these unknown parameters is by replacing them by their Maximum Likelihood Estimates (MLEs). The general problem is to make a decision between $\mathcal{H}_0$ and $\mathcal{H}_1$, where the PDFs depend on unknown parameter sets. It is assumed that the vector parameters θ_0 and θ_1 are unknown under $\mathcal{H}_0$ and $\mathcal{H}_1$, respectively. If data x has the PDF $p(x;\hat{\theta_0},\mathcal{H}_0)$ under null hypothesis $\mathcal{H}_0$ and $p(x;\hat{\theta_1},\mathcal{H}_1)$ under alternative hypothesis $\mathcal{H}_1$, the GLRT decides $\mathcal{H}_1$ if:

$$L_G(x) = \frac{p(x;\hat{\theta_1},\mathcal{H}_1)}{p(x;\hat{\theta_0},\mathcal{H}_0)} > \gamma \tag{6.1}$$

where $\hat{\theta_1}$ is the MLE of θ_1 assuming $\mathcal{H}_1$ is true, $\hat{\theta_0}$ is the MLE of θ_0 assuming $\mathcal{H}_0$ is true, and γ is the threshold. GLRT approach works quite well in practice though there is no optimality associated with it. In addition, the GLRT approach is more commonly used compared to its competitor approach, the Bayesian approach, due to its ease of implementation and less restrictive assumptions [150].

6.1.1 Design of test statistic based on GLRT

For better understanding of the approach, a GLRT-based detector is designed here to detect a dc level in WGN with unknown amplitude and variance using the example in [150]. In this example, the data is considered as only noise (modeled as WGN) under non-faulty hypothesis $\mathcal{H}_0$, and an added dc level value to the noise under faulty hypothesis $\mathcal{H}_1$. Thus, the detection problem becomes as follows:

$$\begin{aligned} &\mathcal{H}_0 : x[n] = w[n] \qquad n = 0, 1, ..., N-1 \\ &\mathcal{H}_1 : x[n] = A + w[n] \quad n = 0, 1, ..., N-1 \end{aligned} \tag{6.2}$$

where A is unknown amplitude with $-\infty < A < \infty$ and $w[n]$ is WGN with unknown positive variance $0 < \sigma^2 < \infty$. Here, a Uniformly Most powerful (UMP) test does not exist because the equivalent test parameter A is two-sided and can take both positive and negative values. Furthermore, the hypothesis test contains a nuisance parameter σ^2 which enters into the problem by affecting the PDFs under $\mathcal{H}_0$ and $\mathcal{H}_1$. The GLRT decides $\mathcal{H}_1$ if:

$$L_G(x) = \frac{p(x;\hat{A},\hat{\sigma_1}^2,\mathcal{H}_1)}{p(x;\hat{\sigma_0}^2,\mathcal{H}_0)} > \gamma \tag{6.3}$$

where $\hat{\theta_1} = [\hat{A}\,\hat{\sigma_1}^2]^T$ is the MLE of vector parameter $\theta_1 = [A\,\sigma_1^2]^T$ under $\mathcal{H}_1$ and $\hat{\sigma_0}^2$ is the MLE of the parameter $\theta_0 = \sigma_0^2$ under $\mathcal{H}_0$. As can be seen, the variance must be estimated

under both hypotheses. The PDF of $x[n]$ under $\mathcal{H}_1$ is as follows:

$$p(x; A, \sigma^2, \mathcal{H}_1) = \frac{1}{(2\pi\sigma^2)^{\frac{N}{2}}} \exp[-\frac{1}{2\sigma^2} \sum_{N=0}^{N-1} (x[n] - A)^2] \tag{6.4}$$

By maximizing $p(x; A, \sigma^2, \mathcal{H}_1)$ over A and σ_1^2, parameters $\hat{A}$ and $\hat{\sigma_1}^2$ are obtained as follows [151]:

$$\begin{aligned} \frac{\partial p(x; A, \sigma^2, \mathcal{H}_1)}{\partial A} = 0 \Rightarrow \hat{A} = \bar{x} \\ \frac{\partial p(x; A, \sigma^2, \mathcal{H}_1)}{\partial \sigma_1^2} = 0 \Rightarrow \hat{\sigma_1}^2 = \frac{1}{N} \sum_{N=0}^{N-1} (x[n] - A)^2 \end{aligned} \tag{6.5}$$

which results in:

$$p(x; \hat{A}, \hat{\sigma_1}^2, \mathcal{H}_1) = \frac{1}{(2\pi\hat{\sigma_1}^2)^{\frac{N}{2}}} \exp(-\frac{N}{2}) \tag{6.6}$$

Further, the PDF of $x[n]$ under $\mathcal{H}_0$ is as follows:

$$p(x; \sigma^2, \mathcal{H}_0) = \frac{1}{(2\pi\sigma^2)^{\frac{N}{2}})} \exp(-\frac{1}{2\sigma^2} \sum_{N=0}^{N-1} x^2[n]) \tag{6.7}$$

In a similar way, by maximizing $p(x; \hat{\sigma_0}^2, \mathcal{H}_0)$ over σ_0^2, $\hat{\sigma_0}^2$ is obtained as follows:

$$\frac{\partial p(x; \sigma^2, \mathcal{H}_0)}{\partial \sigma_0^2} = 0 \Rightarrow \hat{\sigma_0}^2 = \frac{1}{N} \sum_{N=0}^{N-1} x^2[n] \tag{6.8}$$

which results in:

$$p(x; \hat{\sigma_0}^2, \mathcal{H}_0) = \frac{1}{(2\pi\hat{\sigma_0}^2)^{\frac{N}{2}}} \exp(-\frac{N}{2}) \tag{6.9}$$

Therefore, Equation 6.3 becomes:

$$L_G(x) = (\frac{\hat{\sigma_0}^2}{\hat{\sigma_1}^2})^{\frac{N}{2}} \tag{6.10}$$

which is equivalent to:

$$2lnL_G(x) = Nln\frac{\hat{\sigma_0}^2}{\hat{\sigma_1}^2} \tag{6.11}$$

As a result, the GLRT detector decides $\mathcal{H}_1$ if the fit to the data of the signal $\hat{A} = \bar{x}$ generates a much smaller error as measured by $\hat{\sigma_1}^2 = (1/N) \sum_{n=0}^{N-1} (x[n] - \hat{A})^2$ than a fit of no dc level signal as measured by $\hat{\sigma_0}^2 = (1/N) \sum_{n=0}^{N-1} x[n]^2$. Intuitively, $\hat{\sigma_1}^2$ can be obtained from Equation 6.5 and Equation 6.8 as follows:

$$\begin{aligned} \hat{\sigma_1}^2 &= \frac{1}{N} \sum_{N=0}^{N-1} (x[n] - A)^2 = \frac{1}{N} \sum_{N=0}^{N-1} (x[n] - \bar{x})^2 \\ &= \frac{1}{N} \sum_{N=0}^{N-1} (x[n]^2 - 2x[n]\bar{x} + \bar{x}^2) = \frac{1}{N} \sum_{N=0}^{N-1} x[n]^2 - \bar{x}^2 \\ &= \hat{\sigma_0}^2 - \bar{x}^2 \end{aligned} \tag{6.12}$$

which yields:

$$2lnL_G(x) = Nln(1 + \frac{\bar{x}^2}{\hat{\sigma_1}^2}) \tag{6.13}$$

Since $ln(1 + \frac{\bar{x}^2}{\hat{\sigma_1}^2})$ is monotonically increasing with respect to $\frac{\bar{x}^2}{\hat{\sigma_1}^2}$, an equivalent and normalized test statistic can be obtained as follows:

$$T(x) = \frac{\bar{x}^2}{\hat{\sigma_1}^2} > \gamma' \tag{6.14}$$

As can been seen, the GLRT has normalized the statistic by $\hat{\sigma_1}^2$ which allows the threshold to be determined. Since the PDF of $T(x)$ under null hypothesis $\mathcal{H}_0$ does not depend on σ^2, the threshold is independent of the value σ^2. To establish this, let $w[n] = \sigma u[n]$, where $u[n]$ is WGN with variance one. Using Equation 6.14 with $x[n] = w[n]$ under $\mathcal{H}_0$ [150], $T(x)$ becomes:

$$T(x) = \frac{(\frac{1}{N}\sum_{n=0}^{N-1} w[n])^2}{\frac{1}{N}\sum_{n=0}^{N-1}(w[n] - \bar{w})^2} = \frac{(\frac{1}{N}\sum_{n=0}^{N-1} \sigma u[n])^2}{\frac{1}{N}\sum_{n=0}^{N-1}(\sigma u[n] - \sigma\bar{u})^2} = \frac{(\frac{1}{N}\sum_{n=0}^{N-1} u[n])^2}{\frac{1}{N}\sum_{n=0}^{N-1}(u[n] - \bar{u})^2} \tag{6.15}$$

whose PDF is independent from σ^2. Therefore, the $2\ln L_G(x)$ in Equation 6.13 has a PDF that does not depend on σ^2 under $\mathcal{H}_0$, either. It is not surprising to see that the detection performance of the GLRT detector in Equation 6.13 will end up slightly poorer compared to the case when σ^2 is known. However, the degradation will be quite small if large data records are explored ($N \longrightarrow \infty$).

6.1.2 Performance of GLRT for large data records

As $N \longrightarrow \infty$, the asymptotic PDFs of $\bar{x}$ will converge to normal distributions under both hypotheses as follows:

$$\bar{x} \sim \begin{cases} \mathcal{N}(0, \sigma^2) & \text{under } \mathcal{H}_0 \\ \mathcal{N}(A, \sigma^2) & \text{under } \mathcal{H}_1 \end{cases} \tag{6.16}$$

and therefore:

$$\frac{\bar{x}}{\sigma} \sim \begin{cases} \mathcal{N}(0, 1) & \text{under } \mathcal{H}_0 \\ \mathcal{N}(\frac{A}{\sigma}, 1) & \text{under } \mathcal{H}_1 \end{cases} \tag{6.17}$$

Squaring the normalized statistic in Equation 6.17 will lead to the modified test statistic $T(x)$ in Equation 6.14 which produces a central chi-squared distribution under $\mathcal{H}_0$ and a non-central chi-squared distribution under $\mathcal{H}_0$, with one degree of freedom:

$$T(x) = \frac{\bar{x}^2}{\sigma^2} \sim \begin{cases} \mathcal{X}_1^2 & \text{under } \mathcal{H}_0 \\ \mathcal{X'}_1^2(\lambda) & \text{under } \mathcal{H}_1 \end{cases} \tag{6.18}$$

where λ is the non-centrality parameter and is calculated as [150]:

$$\lambda = \frac{A^2}{\sigma^2} = \frac{\bar{x}^2}{\sigma^2} \tag{6.19}$$

It was shown in Equation 6.18 that $T(x)$ has a non-central chi-squared distribution with one degree of freedom, and it is equal to the square of random variable x in Equation 6.17, therefore $x \sim \mathcal{N}(\sqrt{\lambda}, 1)$. Thus, the probability of false-alarm (P_{FA}) can be obtained as:

$$\begin{aligned} P_{FA} &= Pr\{T(x) > \gamma'; \mathcal{H}_0\} \\ &= Pr\{x > \sqrt{\gamma'}; \mathcal{H}_0\} + Pr\{x < -\sqrt{\gamma'}; \mathcal{H}_0\} \\ &= 2Q(\sqrt{\gamma'}) \end{aligned} \tag{6.20}$$

where $Q(x)$ is the right-tail probability of random variable x. Thus, the threshold can be obtained as follows:

$$\gamma' = [Q^{-1}(\frac{P_{FA}}{2})]^2 \tag{6.21}$$

Similarly, the probability of detection P_D can be obtained as follows:

$$\begin{aligned} P_D &= Pr\{T(x) > \gamma'; \mathcal{H}_1\} \\ &= Pr\{x > \sqrt{\gamma'}; \mathcal{H}_1\} + Pr\{x < -\sqrt{\gamma'}; \mathcal{H}_1\} \\ &= Q(\sqrt{\gamma'} - \sqrt{\lambda}) + Q(\sqrt{\gamma'} + \sqrt{\lambda}) \\ &= Q(Q^{-1}(\frac{P_{FA}}{2}) - \sqrt{\lambda}) + Q(Q^{-1}(\frac{P_{FA}}{2}) + \sqrt{\lambda}) \end{aligned} \tag{6.22}$$

As a result, by choosing a value for P_{FA}, a theoretical threshold can be found to be used in the diagnostic system. Figure 6.1 shows the obtained threshold versus probability of false alarm based on Equation 6.21. Moreover, the receiver operating characteristic can be

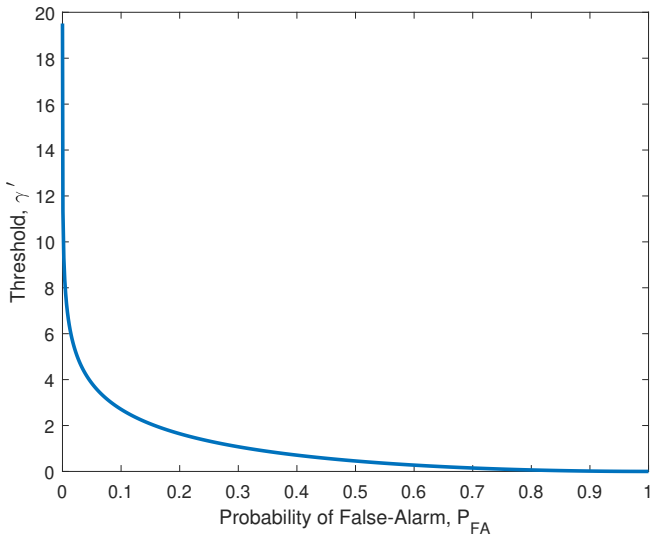

Figure 6.1: Threshold versus probability of false-alarm.

found using Equation 6.22 to see how choosing a specific probability of false alarm affects the probability of detection. For demonstration purposes, the non-centrality parameter has been chosen as $\lambda = 5$ and the result is shown in Figure 6.2.

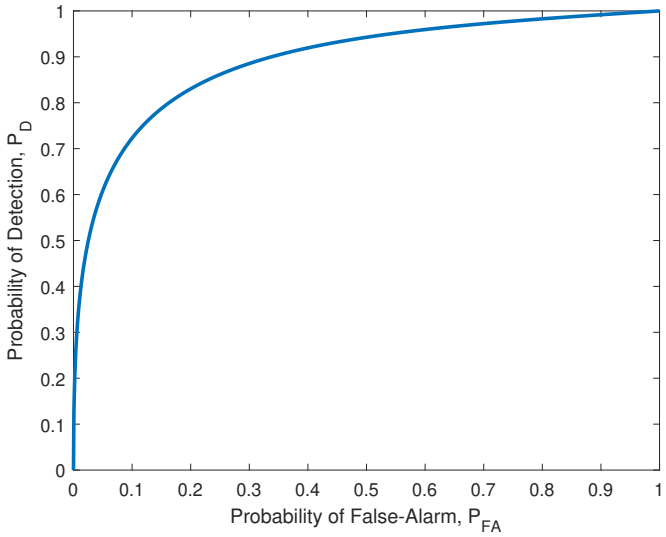

Figure 6.2: Receiver operating characteristic.

6.1.3 Nonexclusive GLRT for unknown noise parameters and DC levels

A more nonexclusive form of GLRT is considered to deal with unknown arrival times and avoid using moving average and moving variance functions in real-time fault detection. First, it is assumed that the arrival time of the fault is known (M) while the PDF of the signal is not completely known, meaning the parameters mean μ and variance σ^2 are to be estimated using MLE. Furthermore, the noise in the residual signal under the healthy condition is modeled as WGN. In a generalized form, the residual (R_1) has different dc levels (A_1 and A_2) before and after the jump time M. Therefore, it is assumed that $A_1 = A_2$ under non-faulty hypothesis $\mathcal{H}_0$, and $A_1 \neq A_2$ under faulty hypothesis $\mathcal{H}_1$. Thus, the detection problem becomes as follows:

$$\begin{aligned} &\mathcal{H}_0 : x[n] = A + w[n] \qquad n = 0, 1, ..., N-1 \\ &\mathcal{H}_1 : \begin{cases} x[n] = A_1 + w[n] & n = 0, 1, ..., M-1 \\ x[n] = A_2 + w[n] & n = M, ..., N-1 \end{cases} \end{aligned} \tag{6.23}$$

where the jump time occurs after M observations $0 < M < N-1$. The GLRT decides $\mathcal{H}_1$ if:

$$L_G(x) = \frac{p(x; \hat{A}_1, \hat{A}_2, \hat{\sigma_1}^2, \hat{\sigma_2}^2, \mathcal{H}_1)}{p(x; \hat{A}, \hat{\sigma_0}^2, \mathcal{H}_0)} > \gamma \tag{6.24}$$

where $\hat{A}$ and $\hat{\sigma_0}^2$ are the MLE of parameters A and σ_0^2 under $\mathcal{H}_0$ and $\hat{A}_1$, $\hat{A}_2$, $\hat{\sigma_1}^2$, and $\hat{\sigma_2}^2$ are the MLEs of the parameters A_1, A_2, σ_1^2, and σ_2^2 under $\mathcal{H}_1$. The MLEs are determined by maximizing $p(x; \hat{A}_1, \hat{A}_2, \hat{\sigma_1}^2, \hat{\sigma_2}^2, \mathcal{H}_1)$ and $p(x; \hat{A}, \hat{\sigma_0}^2, \mathcal{H}_0)$ over containing

unknown parameters and are obtained as follows [1]:

$$\hat{A} = \frac{1}{N}\sum_{N=0}^{N-1} x[n], \qquad \hat{A}_1 = \frac{1}{M}\sum_{N=0}^{M-1} x[n] \tag{6.25}$$

$$\hat{A}_2 = \frac{1}{N-M}\sum_{N=M}^{N-1} x[n], \quad \hat{\sigma_0}^2 = \frac{1}{N}\sum_{N=0}^{N-1}(x[n]-A)^2$$

$$\hat{\sigma_1}^2 = \frac{1}{M}\sum_{N=0}^{M-1}(x[n]-\hat{A}_1)^2, \quad \hat{\sigma_2}^2 = \frac{1}{N-M}\sum_{N=M}^{N-1}(x[n]-\hat{A}_2)^2$$

By using MLEs in the PDFs under $\mathcal{H}_0$ and $\mathcal{H}_1$, the Equation6.24 becomes:

$$2lnL_G(x) = Nln(\frac{\hat{\sigma_0}^2}{(\hat{\sigma_1}^2)^{\frac{M}{N}}(\hat{\sigma_2}^2)^{\frac{N-M}{N}}}) > \gamma' \tag{6.26}$$

where $\gamma' = 2ln\gamma$.

6.1.4 GLRT for unknown noise parameters, DC levels, and arrival time

To account for the unknown jump time, it is assumed that it occurs far from the boundaries of the observation interval, i.e. $M_{min} < M < M_{max}$ where $M_{min} >> 0$ and $M_{max} << N-1$. Therefore, the GLRT decides $\mathcal{H}_1$ if:

$$L_G(x) = \frac{p(x;\hat{M},\hat{A}_1,\hat{A}_2,\hat{\sigma_1}^2,\hat{\sigma_2}^2,\mathcal{H}_1)}{p(x;\hat{A},\hat{\sigma_0}^2,\mathcal{H}_0)} > \gamma \tag{6.27}$$

where $\hat{M}$ is the MLE of arrival time M under $\mathcal{H}_1$. Equivalently:

$$L_G(x) = \frac{\max_M p(x;\hat{M},\mathcal{H}_1)}{p(x;\mathcal{H}_0)} \tag{6.28}$$

Since the PDF under $\mathcal{H}_0$ does not depend on M and is non-negative, the test becomes:

$$L_G(x) = \max_M(2ln\frac{p(x;\hat{M},\mathcal{H}_1)}{p(x;\mathcal{H}_0)}) > 2ln\gamma \tag{6.29}$$

And the GLRT decides $\mathcal{H}_1$ if:

$$L_G(x) = \max_M(Nln(\frac{\hat{\sigma_0}^2}{(\hat{\sigma_1}^2)^{\frac{M}{N}}(\hat{\sigma_2}^2)^{\frac{N-M}{N}}})) > \gamma' \tag{6.30}$$

where $\gamma' = 2ln\gamma$.

6.1.5 Recursive cumulative GLRT with adaptive threshold

A recursive cumulative GLRT with adaptive threshold and upper bounded is implemented to create a fault indicator based on the test statistic obtained in 6.30 which can be used as the reference for the decision-making system. This method helps reduce the time to detect motor faults, reduce the false alarm rate, revert to the non-faulty case when a fault disappears, and increase the detection probability. The algorithm is described as follows [2]:

- Initialization:

$$\begin{aligned} h &= 90 \qquad \text{Upper bound} \\ \gamma_0 &= 40 \qquad \text{Initial threshold} \end{aligned}$$

- Loop

$$\begin{aligned} g_k &= L_G(x_k) - \gamma_{k-1} \\ \gamma_k &= L_G(x_k) - sign(L_G(x_k)) \min(|g_k|, |g_k - h|) \\ g_k &= max(0, g_{k-1} + g_k) \\ g_k &= min(h, g_k) \end{aligned} \tag{6.31}$$

- Result:

$$g_k \text{ for increasing time } t_k$$

6.2 The proposed detection method with fixed probability of false alarm

The R_1–R_3 residuals obtained in Figure 5.26, are designed based on *abc* frame voltage equations, and an ITSC fault in any phase creates unbalance in the residual output. Before feeding these ITSC fault residual responses to the statistical detector and to form a better index that obtains a nonzero dc value in case of an ITSC fault, the residuals in the *abc* frame are taken into an $\alpha\beta$ frame using the power invariant Clarke transformation as follows:

$$\begin{bmatrix} R_\alpha \\ R_\beta \end{bmatrix} = \sqrt{\frac{2}{3}} \begin{bmatrix} 1 & -\frac{1}{2} & -\frac{1}{2} \\ 0 & \frac{\sqrt{3}}{2} & -\frac{\sqrt{3}}{2} \end{bmatrix} \begin{bmatrix} R_1 \\ R_2 \\ R_3 \end{bmatrix} \tag{6.32}$$

The absolute value of the resultant is calculated:

$$R_r = |R_\alpha + jR_\beta| \tag{6.33}$$

Figure 6.3 shows the absolute value of the resultant residual in an $\alpha\beta$ frame where ITSC faults in all phases are more obvious compared to *abc* residuals R_1–R_3.

The statistical detector is designed in a way that detects even the smallest ITSC fault ($< 1\%$) and therefore, the non-centrality parameter λ is calculated based on the implementation of 6.19 on the resultant residual. At $t = 4.471s - 7.238s$ when the motor is experiencing the lowest ITSC fault level in phase a winding, $\lambda = 6.78$ is obtained. Using this value, the ROC of the detector is obtained based on 6.20 - 6.22 and shown in

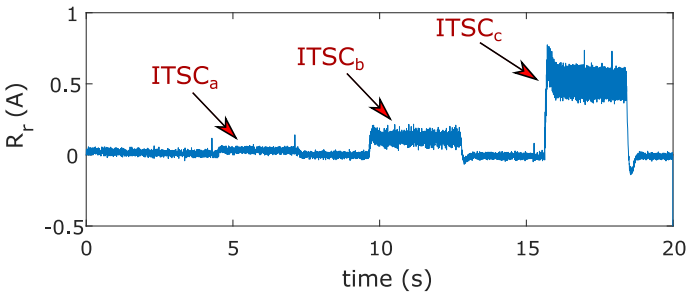

Figure 6.3: Resultant residual in paper E.

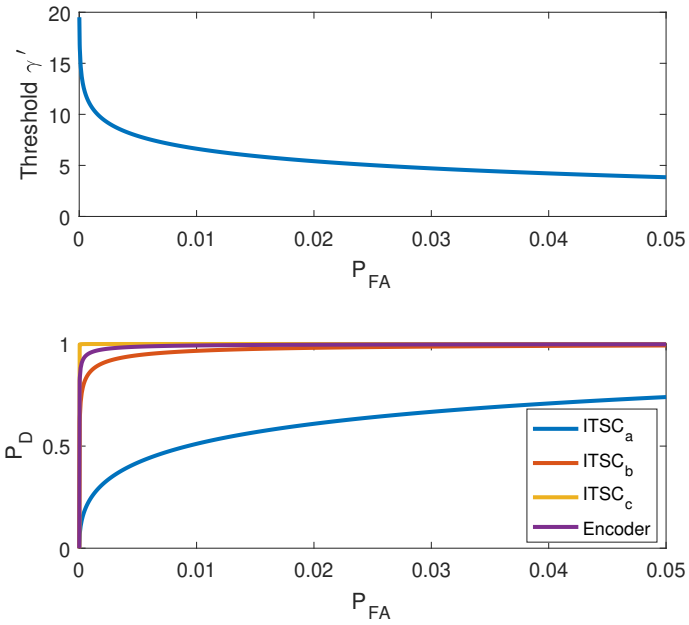

Figure 6.4: Threshold and ROC for low values of P_{FA}.

Figure 6.4b. The P_{FA} values here are for the lowest ITSC fault level in phase a, which means other ITSC faults in Phases b and c have lower P_{FA} values. Using $P_{FA} = 2\%$ in Figure 6.4a, the threshold is obtained as $\gamma' = 5.41$ and this results in $P_D = 60.93\%$ for ITSC in phase a. Furthermore, the probability of detection for ITSC faults in phases b and c, and encoder fault are calculated $P_D = 98.13\%$, $P_D = 100\%$, and $P_D = 99.65\%$, respectively.

The test statistics were implemented on the resultant residual and the result is fed into a real-time decision-making system that notifies the user of the presence of an ITSC fault, as shown in Figure 6.5. Figure 6.5aa shows the output of test statistic on resultant residual along with the threshold of $\gamma' = 5.41$. The test statistic's output value is compared with the threshold value over time, and if it exceeds the threshold, the fault alarm is tripped accordingly. Figure 6.5c shows the detector's logical output value which attains a low value in a healthy condition and a high value during a faulty case. This proves that the detector has successfully detected all the faults that are fairly close to expected values of P_D while experiencing no false alarm. In addition, the detection and recovery time of the faults indicates the agility of a decision-making system. The detection time is the delay

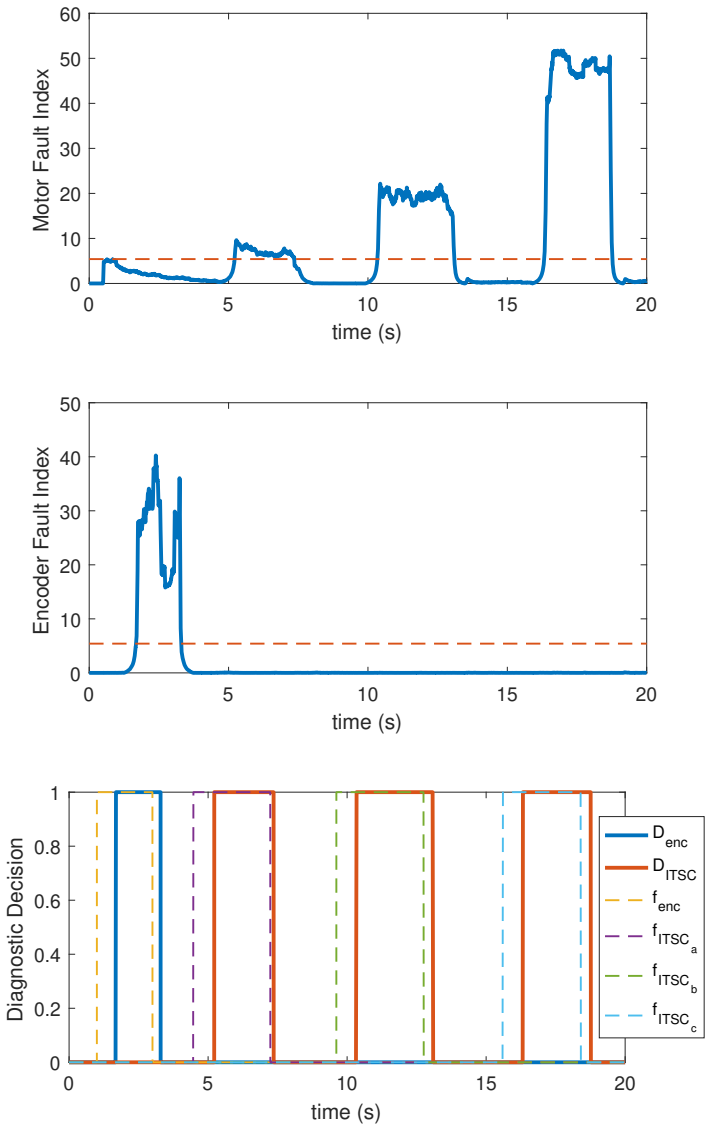

Figure 6.5: Test statistic and decision for presence of ITSC fault in paper E.

between the rise of the actual fault and the rise of the detector's logical output value to one, while the recovery time is the delay between the fall of the actual fault and the fall of the detector's logical output value to zero (Figure 6.6). The detection and recovery time of the faults in paper E are listed in Table 6.1.

6.3 The proposed detection method with adaptive threshold

As noticed in paper E results, using moving average and variance in forming the test statistic and a fixed threshold can cause detection and recovery delays and potentially false alarms in real-time mode. The GLRT test statistics of the faults $f_1 - f_6$ are obtained using Equation 6.30 and shown in Figure 6.7. Using the recursive cumulative GLRT with adaptive threshold algorithm in paper F, the fault indicators are determined. The

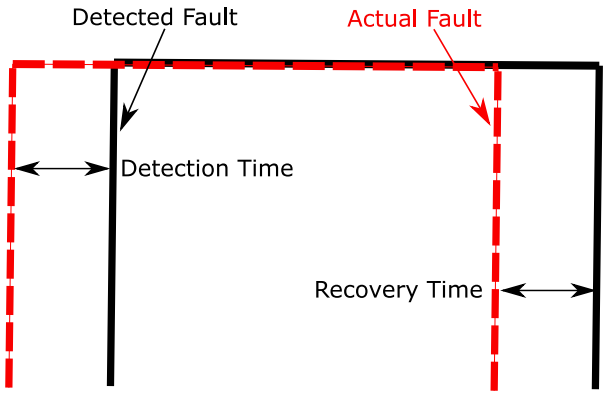

Figure 6.6: Detection and recovery time of a fault.

Table 6.1: Detection and recovery time of the faults in paper E

Time	Faults			
	f_{enc}	f_{ITSC_a}	f_{ITSC_b}	f_{ITSC_c}
Detection (ms)	687	751	727	720
Recovery (ms)	293	121	340	360

recursive algorithm described in paper F saturates the output signal between min and max values (0 and 90) and therefore, the false-alarm condition is not a nuisance factor anymore. Thus, an arbitrary threshold of 10 is chosen for the decision-making system. The fault indicator's output value is compared with the threshold value over time, and if it exceeds the threshold the fault alarm is tripped accordingly. The decision for the presence of ITSC and demagnetization faults $f_1 - f_6$ as well as the actual faults are shown in Figure 6.7. The detector's logical output value attains a low value under healthy conditions and a high value during a faulty case. As a result, the detector has successfully detected all the faults, while experiencing no false alarm.

Further, the detection and recovery time of the faults in paper F are listed in Table 6.2. As can be seen, these values have significantly improved compared to the results from paper E. For instance, the detection and recovery time for f_{ITSC_a} in paper E were 751 ms and 121 ms, while these values were 45 ms and 55 ms for the same fault in paper F.

Table 6.2: Detection and recovery time of the faults in paper F

Time	Faults					
	f_1	f_2	f_3	f_4	f_5	f_6
Detection (ms)	45	5	20	70	70	50
Recovery (ms)	55	10	10	30	50	50

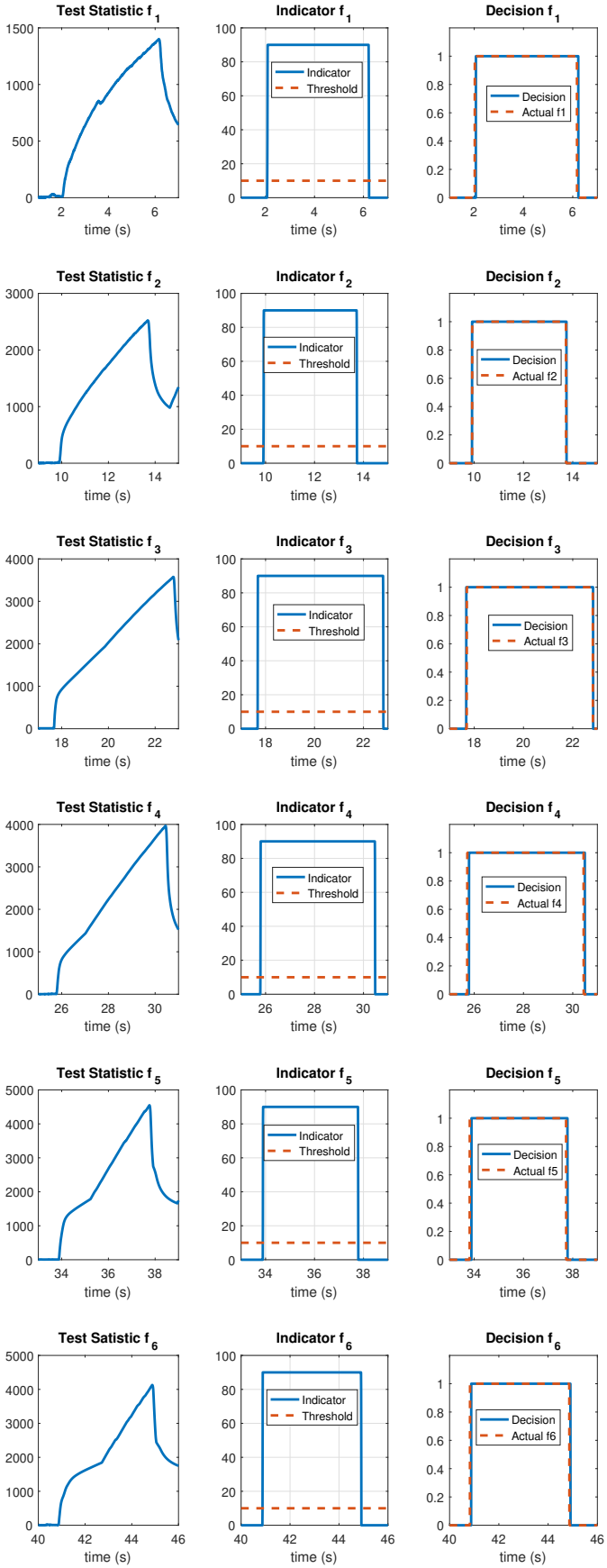

Figure 6.7: Teat statistic, fault indicator, and decision of faults.

6.4 Summary

This chapter focuses on real-time statistical detection of ITSC and demagnetization faults in PMSMs as well as sensor faults in drive systems based on generalized likelihood ratio test. Section 6.1 presents the design of a GLRT-based detector to deal with uncertainties created by noise in the residuals. First, a GLRT detector based on a fixed threshold is introduced where the fixed threshold is obtained based on a fixed value for the probability of false alarm. The probability of detection and receiver operating characteristics of the detector are also obtained based on the probability of false alarm and are used to use a threshold with the maximum probability of detection. Second, a nonexclusive GLRT detector is introduced which considers unknown arrival time in addition to unknown noise parameters and dc levels before and after the jump time. Third, a recursive cumulative GLRT with an adaptive threshold algorithm is implemented to obtain a more processed fault indicator that decreases the detection and recovery delay time. The fault indicator achieved by this recursive algorithm is compared to an arbitrary threshold and a decision is made in real-time performance.

Section 6.2 presents a detection model that is based on GLRT with a fixed threshold and probability of false alarm. This GLRT detector is coupled with the residual response obtained in paper E and leads to the detection of three ITSC faults with 1%, 3%, and 5% severity as well as an encoder fault. The experimental results obtained from this detection model show that the diagnostic system is able to detect all the applied faults and maintains the probability of detection high. Finally, a detection model that is based on GLRT with unknown arrival times is presented in section 6.3. Further, a recursive cumulative GLRT with an adaptive threshold algorithm is implemented to obtain a more processed fault indicator that decreases the detection and recovery delay time. The fault indicator achieved by this recursive algorithm is compared to an arbitrary threshold and a decision is made in real-time performance. The experimental results show that the statistical detector is able to efficiently detect all the unexpected faults including three levels of ITSC faults with 1%, 3%, and 5% severity as well as three levels of reversible demagnetization faults with 2%, 5%, and 9% severity. The faults are detected in the presence of unknown noise and without experiencing any false alarm, proving the effectiveness of this diagnostic approach.

Chapter 7

Concluding Remarks

7.1 Conclusions

This research focuses on the real-time diagnosis of faults in permanent magnet synchronous motors and drive systems. Most existing research and industrial products aim at single fault detection using signal-based techniques, namely Fourier transform and wavelet frequency analysis tools. Systematic fault detection of faults in complex PMSM drive systems is limited in the literature and thus, an effort is made to fill this research gap. Several research topics and problems were identified within the diagnosis of faults in permanent magnet synchronous motors and drive systems and state-of-the-art diagnosis schemes are proposed based on a model-based approach to address the problems.

The first research phase focuses on the realistic modeling of inter-turn short circuit faults in PMSMs. Thus, two different models of PMSM under ITSC faults are proposed including the FEM-based model and the analytical model in papers A and B. In paper A, A 2-D time stepping finite element analysis has been performed on an 8-pole IPMSM both in healthy condition and under an ITSC fault in the stator winding. Initial analysis of transform currents, phase-a instantaneous powers, and torque, signals using FFT shows that certain harmonics due to an ITSC fault can be observed in spectra. Subsequently, detailed modeling of ITSC faults in PMSMs is presented in paper B where a fault model was developed to obtain deformed fluxes based on inductance variations. These variations are caused by cross flux linkages and depend on the distribution of the coils in the same phase winding. In addition, the cross-effect of fault currents in different phases was modeled, enabling the model to model not only single faults but also simultaneous ITSC faults in any of the phases. The fault model requires only three-phase currents, three-phase voltages, and parameters of the motor as input. A FEM-based model similar to the one proposed in paper A was implemented to validate the results obtained from the analytical faulty PMSM model. Unlike FEA, the proposed dynamic model can well and quickly model the behavior of PMSM under different fault scenarios, without using detailed dimensions or material information which could be used for developing fault indicators or in combination with other detection methods such as structural analysis.

The next research phase focuses on combining the proposed analytical model proposed in paper B with structural analysis to detect internal physical faults in PMSMs such as ITSC and demagnetization faults in a systematic methodology. Therefore, structural

analysis is implemented on a healthy mathematical model of the PMSM in paper C, and specific fault terms are added to PMSM equations to detect and isolate the mentioned faults in the system. After obtaining the redundant part of the structural model by employing a DM decomposition tool, several sequential residuals are derived based on the fault terms that are sensitive to the presence of four faults in the system including ITSC in phase a, ITSC in phase b, ITSC in phase c, and demagnetization. The proposed model is implemented in Matlab-Simulink and the mentioned faults are applied to the analytical PMSM model at different time intervals. The results show that residuals are able to efficiently detect and isolate even small faults in the presence of noise, proving the effectiveness of this diagnostic approach.

In the third research phase, all the focus is redirected to the systematic diagnosis of multiple faults in a real-time experimental setup of PMSM and drive system. First, paper D presented a systematic fault detection methodology based on structural analysis which was conducted on a PMSM drive system containing eleven sensor faults. This comprehensive diagnostic model includes measurement errors in the signal of the phase voltages and currents, angular position and velocity, inverter dc bus voltage and current, and load torque sensors. After implementing structural analysis and obtaining the redundant part of the PMSM drive system using DM decomposition, nine sequential residuals are designed and implemented based on the fault terms that appear in each of the redundant sets to detect and isolate the studied sensor faults which are applied at different time intervals. Second, a structural analysis of the PMSM and drive system was presented in paper E for the detection of incipient ITSC and encoder faults. After forming the structural model and extracting the redundant part, several residuals were designed to detect ITSC and encoder faults. The proposed diagnostic model was implemented on an industrial PMSM with faults being applied to the system at different time intervals, and residual responses were obtained. Third, a structural analysis of the PMSM and drive system was presented in paper F for the detection of incipient demagnetization and ITSC faults. After forming the structural model and extracting the redundant part, several residuals were designed to detect demagnetization and ITSC faults. Learning from the experience in paper E, the drive strategy was changed to be able to apply demagnetization fault and also to eliminate the effect of PI controllers on the quality of the acquired signals. The proposed diagnostic model was implemented on an industrial PMSM with faults being applied to the system at different time intervals, and residual responses were obtained.

In the fourth research phase, the focus is on the real-time detection of faults in PMSMs and drive systems by using a powerful statistical signal-processing detector such as generalized likelihood ratio test. To achieve this, a GLRT-based detector was designed and implemented based on the behavior of the residuals during healthy (only noise) and faulty (noise + signal) conditions in paper E. To make the GLRT-based detector effective to deal with such a realistic problem, the parameters such as mean and variance values in the probability density function of the noise signal were considered to be unknown. By replacing these unknown parameters with their maximum likelihood estimates, a test statistic was achieved for the GLRT-based ITSC and encoder fault detector. Following this step, a threshold was obtained based on choosing the probability of a false alarm and the probability of detection for each detector based on which decision was made to indicate the

presence of the fault. The experimental results showed that the designed GLRT-based detector is able to efficiently detect even small ITSC and encoder faults in the presence of noise, proving the effectiveness of this diagnostic approach. Finally, a nonexclusive GLRT detector is introduced in paper F that considers unknown arrival time in addition to unknown noise parameters and dc levels before and after the jump time. Further, a recursive cumulative GLRT with an adaptive threshold algorithm is implemented to obtain a more processed fault indicator that decreases the detection and recovery delay time. The fault indicator achieved by this recursive algorithm is compared to an arbitrary threshold and a decision is made in real-time performance. The experimental results show that the statistical detector is able to efficiently detect all the unexpected faults in the presence of unknown noise and without experiencing any false alarm, proving the effectiveness of this diagnostic approach. Moreover, the detection and recovery time of the faults were significantly improved by using after implementing the recursive cumulative GLRT with adaptive threshold. For instance, the initial detection time of 751 ms for the ITSC fault in phase a was decreased to 45 ms, and the initial recovery time of 121 ms was decreased to 55 ms. This improvement in the agility and performance of the recursive cumulative GLRT with adaptive threshold is a great accomplishment, especially for a real-time diagnostic system.

7.2 Research limitations and future work

In this dissertation, an effort is made to identify, study, model, and detect the most common faults that affect the performance of PMSMs and drive systems. During each stage of this study, there may have been some possible limitations that have impacted the quality of the research and the presented results. The limitations of this study mainly include methods and data collection process which could be addressed in future research.

As with the majority of model-based fault diagnosis studies, the analytical method for modeling ITSC fault, presented in Chapter. 4, has limitations in precisely addressing the faults. This is due to the fact that the $dq0$ models assume that the shape of MMF wave-form is sinusoidal in ac machines while this assumption is rendered not valid due to loss of winding symmetries under abnormal conditions. Although a great effort was made to close the gap between modeling and empirical results, it is well clear that this is not completely possible. Nonetheless, extra considerations were taken into account to address the issues that were not assumed in the modeling. For instance, the ITSC model presented in paper B was used in the diagnostic strategy of paper C, and simulation results led to the successful detection and isolation of the ITSC faults in any of the winding phases. However, experimental results from the test setup could not bring about the same isolation we observed in simulation results. The ITSC fault applied in one of the phases was also observable in other phases due to the mutual induction of the fault current. The speed controller also played a key role in the increase of other phase currents by setting a higher reference I_q to compensate for the lost part of the winding as a result of the ITSC fault. Therefore, a power invariant Clarke transformation was implemented on the residuals that were designed based on stator-phase currents. Though a very powerful method to properly

detect the smallest ITSC fault (1 shorted coil turn), this led to sacrificing detectability over isolability of the investigated faults. However, a reasonable justification was that when an electric motor is diagnosed with an ITSC fault in any of the phases, the whole stator winding (including other healthy coils) is replaced in practice. Knowing that this also applies to demagnetization fault, the focus was redirected to the detection of the group of ITSC faults and the group of demagnetization faults in paper F, without trying to isolate the faults of the same group.

Furthermore, some challenges were faced in the process of diagnostic observer design based on structural analysis (Chapter. 5). As more faults are considered in a structural model, the model redundancy grows and it becomes more difficult and time-demanding to select proper MSO and MTES sets as candidates for forming residuals. The limitations related to experimental analysis and data collection process were also substantial. These include all the time spent on ordering, assembling, and debugging the test setup for making it operational. In addition, applying physical faults such as ITSC was a huge challenge since it required precision and motors with accessible winding.

Future works can be established by learning from the limitations, experiments, and results of this study. First, the structural models that were presented here, could be expanded to include other faults in PMSM and drive systems. In addition, a lot of effort has been made to build the experimental test setup in a generic style and this could be used for developing, implementing, and investigating other methods and various faults in the future. Finally, the obtained results could be used for further processing in data-driven and hybrid fault diagnosis techniques which may lead to better detection performance. As a collaboration, the data collected from experimental analysis of ITSC fault in paper E was used in [152] where ITSC faults were detected by using a 2D convolutional neural network. The main advantage of this data-driven method was the ability to deliver high-accuracy detection without high calculation costs and the necessity for feature pre-processing.

Bibliography

[1] Seungdeog Choi, Moinul Shahidul Haque, Md Tawhid Bin Tarek, Vamsi Mulpuri, Yao Duan, Sanjoy Das, Vijay Garg, Dan M Ionel, M Abul Masrur, Behrooz Mirafzal, et al. Fault diagnosis techniques for permanent magnet ac machine and drives—a review of current state of the art. *IEEE Transactions on Transportation Electrification*, 4(2):444–463, 2018.

[2] Seokbae Moon, Hyeyun Jeong, Hojin Lee, and Sang Woo Kim. Interturn short fault diagnosis in a pmsm by voltage and current residual analysis with the faulty winding model. *IEEE Transactions on Energy Conversion*, 33(1):190–198, 2017.

[3] Richard T Meyer, Raymond A DeCarlo, Scott C Johnson, and Steve Pekarek. Short-circuit fault detection observer design in a pmsm. *IEEE Transactions on Aerospace and Electronic Systems*, 54(6):3004–3017, 2018.

[4] Yuan Qi, Emine Bostanci, Vigneshwaran Gurusamy, and Bilal Akin. A comprehensive analysis of short-circuit current behavior in pmsm interturn short-circuit faults. *IEEE Transactions on Power Electronics*, 33(12):10784–10793, 2018.

[5] Austin H Bonnett and George C Soukup. Cause and analysis of stator and rotor failures in three-phase squirrel-cage induction motors. *IEEE Transactions on Industry applications*, 28(4):921–937, 1992.

[6] Bon-Gwan Gu, Jun-Hyuk Choi, and In-Soung Jung. Development and analysis of interturn short fault model of pmsms with series and parallel winding connections. *IEEE Transactions on Power Electronics*, 29(4):2016–2026, 2013.

[7] Subhasis Nandi, Hamid A Toliyat, and Xiaodong Li. Condition monitoring and fault diagnosis of electrical motors—a review. *IEEE transactions on energy conversion*, 20(4):719–729, 2005.

[8] Manolis N Chatzis, Eleni N Chatzi, and Costas Papadimitriou. Robust monitoring, diagnostic methods and tools for engineered systems. *Frontiers in Built Environment*, 6:125, 2020.

[9] Jagath Sri Lal Senanayaka. *Online Condition Monitoring of Electric Powertrains using Machine Learning and Data Fusion*. PhD thesis, University of Agder, 2020.

[10] Bashir Mahdi Ebrahimi and Jawad Faiz. Feature extraction for short-circuit fault detection in permanent-magnet synchronous motors using stator-current monitoring. *IEEE Transactions on Power Electronics*, 25(10):2673–2682, 2010.

[11] Jeevanand Seshadrinath, Bhim Singh, and Bijaya Ketan Panigrahi. Investigation of vibration signatures for multiple fault diagnosis in variable frequency drives using complex wavelets. *IEEE Transactions on Power Electronics*, 29(2):936–945, 2013.

[12] Brice Aubert, Jeremi Regnier, Stephane Caux, and Dominique Alejo. Kalman-filter-based indicator for online interturn short circuits detection in permanent-magnet synchronous generators. *IEEE Transactions on Industrial Electronics*, 62(3):1921–1930, 2014.

[13] Jun Hang, Jianzhong Zhang, Ming Cheng, and Jin Huang. Online interturn fault diagnosis of permanent magnet synchronous machine using zero-sequence components. *IEEE Transactions on Power Electronics*, 30(12):6731–6741, 2015.

[14] Mohamed A Awadallah, Medhat M Morcos, Suresh Gopalakrishnan, and Thomas W Nehl. A neuro-fuzzy approach to automatic diagnosis and location of stator inter-turn faults in csi-fed pm brushless dc motors. *IEEE Transactions on Energy Conversion*, 20(2):253–259, 2005.

[15] Xiang-Qun Liu, Hong-Yue Zhang, Jun Liu, and Jing Yang. Fault detection and diagnosis of permanent-magnet dc motor based on parameter estimation and neural network. *IEEE transactions on industrial electronics*, 47(5):1021–1030, 2000.

[16] Yaw Nyanteh, Chris Edrington, Sanjeev Srivastava, and David Cartes. Application of artificial intelligence to real-time fault detection in permanent-magnet synchronous machines. *IEEE transactions on industry applications*, 49(3):1205–1214, 2013.

[17] Bashir Mahdi Ebrahimi, Mehrsan Javan Roshtkhari, Jawad Faiz, and Seyed Vahid Khatami. Advanced eccentricity fault recognition in permanent magnet synchronous motors using stator current signature analysis. *IEEE Transactions on Industrial Electronics*, 61(4):2041–2052, 2013.

[18] Reemon Z Haddad, Cristian A Lopez, Shanelle N Foster, and Elias G Strangas. A voltage-based approach for fault detection and separation in permanent magnet synchronous machines. *IEEE Transactions on Industry Applications*, 53(6):5305–5314, 2017.

[19] Miguel Delgado Prieto, Giansalvo Cirrincione, Antonio Garcia Espinosa, Juan Antonio Ortega, and Humberto Henao. Bearing fault detection by a novel condition-monitoring scheme based on statistical-time features and neural networks. *IEEE Transactions on Industrial Electronics*, 60(8):3398–3407, 2012.

[20] Farzad R Salmasi. A self-healing induction motor drive with model free sensor tampering and sensor fault detection, isolation, and compensation. *IEEE Transactions on Industrial Electronics*, 64(8):6105–6115, 2017.

[21] Hao Yan, Yongxiang Xu, Feiyang Cai, He Zhang, Weiduo Zhao, and Chris Gerada. Pwm-vsi fault diagnosis for a pmsm drive based on the fuzzy logic approach. *IEEE Transactions on Power Electronics*, 34(1):759–768, 2018.

[22] Yong Yu, Yongzheng Zhao, Bo Wang, Xiaolei Huang, and Dianguo Xu. Current sensor fault diagnosis and tolerant control for vsi-based induction motor drives. *IEEE Transactions on Power Electronics*, 33(5):4238–4248, 2017.

[23] Chong Zeng, Song Huang, Yongming Yang, and Dun Wu. Inter-turn fault diagnosis of permanent magnet synchronous machine based on tooth magnetic flux analysis. *IET Electric Power Applications*, 12(6):837–844, 2018.

[24] Bo Wang, Jiabin Wang, Antonio Griffo, and Bhaskar Sen. Stator turn fault detection by second harmonic in instantaneous power for a triple-redundant fault-tolerant pm drive. *IEEE Transactions on Industrial Electronics*, 65(9):7279–7289, 2018.

[25] Arun Gandhi, Timothy Corrigan, and Leila Parsa. Recent advances in modeling and online detection of stator interturn faults in electrical motors. *IEEE Transactions on Industrial Electronics*, 58(5):1564–1575, 2010.

[26] Jewon Lee, Yong-Ju Jeon, Doo-chul Choi, SeungHun Kim, and Sang Woo Kim. Demagnetization fault diagnosis method for pmsm of electric vehicle. In *IECON 2013-39th Annual Conference of the IEEE Industrial Electronics Society*, pages 2709–2713. IEEE, 2013.

[27] Chunyan Lai, Aiswarya Balamurali, Vicki Bousaba, K Lakshmi Varaha Iyer, and Narayan C Kar. Analysis of stator winding inter-turn short-circuit fault in interior and surface mounted permanent magnet traction machines. In *2014 IEEE Transportation Electrification Conference and Expo (ITEC)*, pages 1–6. IEEE, 2014.

[28] Jun Hang, Jianzhong Zhang, Shichuan Ding, and Ming Cheng. Modelling and analysis of ppf in pmsm. *IET Electric Power Applications*, 11(3):434–440, 2017.

[29] Alberto Bellini, Fiorenzo Filippetti, Carla Tassoni, and Gérard-André Capolino. Advances in diagnostic techniques for induction machines. *IEEE Transactions on industrial electronics*, 55(12):4109–4126, 2008.

[30] Monia Ben Khader Bouzid and Gérard Champenois. New expressions of symmetrical components of the induction motor under stator faults. *IEEE Transactions on Industrial Electronics*, 60(9):4093–4102, 2012.

[31] Ehsan Mazaheri-Tehrani, Jawad Faiz, Mohsen Zafarani, and Bilal Akin. A fast phase variable *abc* model of brushless pm motors under demagnetization faults. *IEEE Transactions on Industrial Electronics*, 66(7):5070–5080, 2018.

[32] Yao Duan and Hamid Toliyat. A review of condition monitoring and fault diagnosis for permanent magnet machines. In *2012 IEEE Power and Energy Society General Meeting*, pages 1–4. IEEE, 2012.

[33] Martin Riera Guasp, Jose A Antonino Daviu, and Gérard-André Capolino. Advances in electrical machine, power electronic, and drive condition monitoring and fault detection: state of the art. *IEEE Transactions on Industrial Electronics*, 62(3):1746–1759, 2014.

[34] Hongwen He, Nana Zhou, Jinquan Guo, Zheng Zhang, Bing Lu, and Chao Sun. Tolerance analysis of electrified vehicles on the motor demagnetization fault: From an energy perspective. *Applied Energy*, 227:239–248, 2018.

[35] Gilbert Hock Beng Foo, Xinan Zhang, and D Mahinda Vilathgamuwa. A sensor fault detection and isolation method in interior permanent-magnet synchronous motor drives based on an extended kalman filter. *IEEE Transactions on Industrial Electronics*, 60(8):3485–3495, 2013.

[36] Radu Fratila, Abdelkader Benabou, Abdelmounaim Tounzi, and Jean Claude Mipo. Nonlinear modeling of magnetization loss in permanent magnets. *IEEE Transactions on Magnetics*, 48(11):2957–2960, 2012.

[37] Ki-Doek Lee, Won-Ho Kim, Chang-Sung Jin, and Ju Lee. Local demagnetisation analysis of a permanent magnet motor. *IET Electric Power Applications*, 9(3):280–286, 2015.

[38] Tomy Sebastian. Temperature effects on torque production and efficiency of pm motors using ndfeb magnets. *IEEE Transactions on Industry Applications*, 31(2):353–357, 1995.

[39] HD Glass, BC Brown, GW Foster, WB Fowler, R Gustafson, GP Jackson, J-F Ostiguy, and JT Volk. Stability tests of permanent magnets built with strontium ferrite. In *Proceedings of the 1997 Particle Accelerator Conference (Cat. No. 97CH36167)*, volume 3, pages 3260–3262. IEEE, 1997.

[40] Jan De Bisschop, Ahmed Abou-Elyazied Abdallh, Peter Sergeant, and Luc Dupré. Analysis and selection of harmonics sensitive to demagnetisation faults intended for condition monitoring of double rotor axial flux permanent magnet synchronous machines. *IET Electric Power Applications*, 12(4):486–493, 2018.

[41] Jawad Faiz and Ehsan Mazaheri-Tehrani. Demagnetization modeling and fault diagnosing techniques in permanent magnet machines under stationary and nonstationary conditions: An overview. *IEEE Transactions on Industry Applications*, 53(3):2772–2785, 2016.

[42] Gérard-André Capolino, Jose A Antonino-Daviu, and Martin Riera-Guasp. Modern diagnostics techniques for electrical machines, power electronics, and drives. *IEEE Transactions on Industrial Electronics*, 62(3):1738–1745, 2015.

[43] Austin H Bonnett and Chuck Yung. Increased efficiency versus increased reliability. *IEEE Industry Applications Magazine*, 14(1):29–36, 2008.

[44] Mohamed Lamine Masmoudi, Erik Etien, Sandrine Moreau, and Anas Sakout. Amplification of single mechanical fault signatures using full adaptive pmsm observer. *IEEE Transactions on industrial electronics*, 64(1):615–623, 2016.

[45] Siliang Lu, Qingbo He, and Jiwen Zhao. Bearing fault diagnosis of a permanent magnet synchronous motor via a fast and online order analysis method in an embedded system. *Mechanical Systems and Signal Processing*, 113:36–49, 2018.

[46] S-M Jang, Sung-Ho Lee, Han-Wook Cho, and Sung-Kook Cho. Analysis of unbalanced force for high-speed slotless permanent magnet machine with halbach array. *IEEE Transactions on Magnetics*, 39(5):3265–3267, 2003.

[47] Taeyong Yoon. Magnetically induced vibration in a permanent-magnet brushless dc motor with symmetric pole-slot configuration. *IEEE Transactions on Magnetics*, 41(6):2173–2179, 2005.

[48] Faa-Jeng Lin and Yueh-Shan Lin. A robust pm synchronous motor drive with adaptive uncertainty observer. *IEEE Transactions on Energy Conversion*, 14(4):989–995, 1999.

[49] Se-Kyo Chung, Hyun-Soo Kim, Chang-Gyun Kim, and Myung-Joong Youn. A new instantaneous torque control of pm synchronous motor for high-performance direct-drive applications. *IEEE Transactions on Power Electronics*, 13(3):388–400, 1998.

[50] Tooraj Abbasian Najafabadi, Farzad R Salmasi, and Parviz Jabehdar-Maralani. Detection and isolation of speed-, dc-link voltage-, and current-sensor faults based on an adaptive observer in induction-motor drives. *IEEE Transactions on Industrial Electronics*, 58(5):1662–1672, 2010.

[51] F Grouz, L Sbita, and M Boussak. Current sensors gain faults detection and isolation based on an adaptive observer for pmsm drives. In *10th International Multi-Conferences on Systems, Signals & Devices 2013 (SSD13)*, pages 1–6. IEEE, 2013.

[52] Jaroslaw Guzinski, Haitham Abu-Rub, Marc Diguet, Zbigniew Krzeminski, and Arkadiusz Lewicki. Speed and load torque observer application in high-speed train electric drive. *IEEE Transactions on Industrial Electronics*, 57(2):565–574, 2009.

[53] Mohamed El Hachemi Benbouzid, Demba Diallo, and Mounir Zeraoulia. Advanced fault-tolerant control of induction-motor drives for ev/hev traction applications: From conventional to modern and intelligent control techniques. *IEEE transactions on vehicular technology*, 56(2):519–528, 2007.

[54] Jiyu Zhang, Hongyang Yao, and Giorgio Rizzoni. Fault diagnosis for electric drive systems of electrified vehicles based on structural analysis. *IEEE Transactions on Vehicular Technology*, 66(2):1027–1039, 2016.

[55] C Choi and W Lee. Design and evaluation of voltage measurement-based sectoral diagnosis method for inverter open switch faults of permanent magnet synchronous motor drives. *IET electric power applications*, 6(8):526–532, 2012.

[56] Hyunseok Oh, Bongtae Han, Patrick McCluskey, Changwoon Han, and Byeng D Youn. Physics-of-failure, condition monitoring, and prognostics of insulated gate bipolar transistor modules: A review. *IEEE Transactions on power electronics*, 30(5):2413–2426, 2014.

[57] Zhiwei Gao, Carlo Cecati, and Steven X Ding. A survey of fault diagnosis and fault-tolerant techniques—part i: Fault diagnosis with model-based and signal-based approaches. *IEEE transactions on industrial electronics*, 62(6):3757–3767, 2015.

[58] Zhifu Wang, Jingzhe Yang, Huiping Ye, and Wei Zhou. A review of permanent magnet synchronous motor fault diagnosis. In *2014 IEEE Conference and Expo Transportation Electrification Asia-Pacific (ITEC Asia-Pacific)*, pages 1–5. IEEE, 2014.

[59] Antonio Garcia Espinosa, Javier A Rosero, Jordi Cusido, Luis Romeral, and Juan Antonio Ortega. Fault detection by means of hilbert–huang transform of the stator current in a pmsm with demagnetization. *IEEE Transactions on Energy Conversion*, 25(2):312–318, 2010.

[60] Jongman Hong, Doosoo Hyun, Sang Bin Lee, Ji-Yoon Yoo, and Kwang-Woon Lee. Automated monitoring of magnet quality for permanent-magnet synchronous motors at standstill. *IEEE Transactions on Industry Applications*, 46(4):1397–1405, 2010.

[61] Wiehan Le Roux, Ronald G Harley, and Thomas G Habetler. Detecting rotor faults in low power permanent magnet synchronous machines. *IEEE Transactions on Power Electronics*, 22(1):322–328, 2007.

[62] Enzo CC Lau and HW Ngan. Detection of motor bearing outer raceway defect by wavelet packet transformed motor current signature analysis. *IEEE Transactions on Instrumentation and measurement*, 59(10):2683–2690, 2010.

[63] Vincent Choqueuse, Mohamed Benbouzid, et al. Induction machine faults detection using stator current parametric spectral estimation. *Mechanical Systems and Signal Processing*, 52:447–464, 2015.

[64] Wei Zhou, Thomas G Habetler, and Ronald G Harley. Stator current-based bearing fault detection techniques: A general review. In *2007 IEEE International Symposium on Diagnostics for Electric Machines, Power Electronics and Drives*, pages 7–10. IEEE, 2007.

[65] Thierry Boileau, Nicolas Leboeuf, Babak Nahid-Mobarakeh, and Farid Meibody-Tabar. Synchronous demodulation of control voltages for stator interturn fault detection in pmsm. *IEEE Transactions on Power Electronics*, 28(12):5647–5654, 2013.

[66] AJ Marques Cardoso, SMA Cruz, and DSB Fonseca. Inter-turn stator winding fault diagnosis in three-phase induction motors, by park's vector approach. *IEEE Transactions on Energy Conversion*, 14(3):595–598, 1999.

[67] Sergio MA Cruz and AJ Marques Cardoso. Stator winding fault diagnosis in three-phase synchronous and asynchronous motors, by the extended park's vector approach. *IEEE Transactions on industry applications*, 37(5):1227–1233, 2001.

[68] Kyeong-Hwa Kim. Simple online fault detecting scheme for short-circuited turn in a pmsm through current harmonic monitoring. *IEEE Transactions on Industrial Electronics*, 58(6):2565–2568, 2010.

[69] Bochao Du, Shaopeng Wu, Shouliang Han, and Shumei Cui. Interturn fault diagnosis strategy for interior permanent-magnet synchronous motor of electric vehicles based on digital signal processor. *IEEE Transactions on Industrial Electronics*, 63(3):1694–1706, 2015.

[70] M'hamed Drif and Antonio J Marques Cardoso. Stator fault diagnostics in squirrel cage three-phase induction motor drives using the instantaneous active and reactive power signature analyses. *IEEE Transactions on Industrial Informatics*, 10(2):1348–1360, 2014.

[71] Julio-César Urresty, Jordi-Roger Riba, and Luis Romeral. Diagnosis of interturn faults in pmsms operating under nonstationary conditions by applying order tracking filtering. *IEEE Transactions on Power Electronics*, 28(1):507–515, 2012.

[72] Julio-César Urresty, Jordi-Roger Riba, and Luis Romeral. Influence of the stator windings configuration in the currents and zero-sequence voltage harmonics in permanent magnet synchronous motors with demagnetization faults. *IEEE transactions on magnetics*, 49(8):4885–4893, 2013.

[73] Jawad Faiz and Hossein Nejadi-Koti. Demagnetization fault indexes in permanent magnet synchronous motors—an overview. *IEEE Transactions on Magnetics*, 52(4):1–11, 2015.

[74] Joseph Sottile, Frederick C Trutt, and Jeffery L Kohler. Experimental investigation of on-line methods for incipient fault detection [in induction motors]. In *Conference Record of the 2000 IEEE Industry Applications Conference. Thirty-Fifth IAS Annual Meeting and World Conference on Industrial Applications of Electrical Energy (Cat. No. 00CH37129)*, volume 4, pages 2682–2687. IEEE, 2000.

[75] Ying Fan, Chenxue Li, Weixia Zhu, Xiangyang Zhang, Li Zhang, and Ming Cheng. Stator winding interturn short-circuit faults severity detection controlled by ow-svpwm without cmv of a five-phase ftfscw-ipm. *IEEE Transactions on Industry Applications*, 53(1):194–202, 2016.

[76] Behrooz Mirafzal and Nabeel AO Demerdash. On innovative methods of induction motor inter-turn and broken-bar fault diagnostics. In *IEEE International Conference on Electric Machines and Drives, 2005.*, pages 762–769. IEEE, 2005.

[77] Behrooz Mirafzal, Richard J Povinelli, and Nabeel AO Demerdash. Interturn fault diagnosis in induction motors using the pendulous oscillation phenomenon. *IEEE Transactions on Energy Conversion*, 21(4):871–882, 2006.

[78] Jiangbiao He, Andrew Strandt, Alia Manarik, Peng Zhang, and Nabeel AO Demerdash. Diagnosis of stator short-circuit faults in an ipm synchronous machine using a space-vector pendulous oscillation method. In *2013 International Electric Machines & Drives Conference*, pages 727–733. IEEE, 2013.

[79] Hanafy Mahmoud, Ahmed Abou-Elyazied Abdallh, Nicola Bianchi, SM El-Hakim, Adel Shaltout, and Luc Dupré. An inverse approach for interturn fault detection in asynchronous machines using magnetic pendulous oscillation technique. *IEEE Transactions on Industry Applications*, 52(1):226–233, 2015.

[80] Mohamed A Awadallah, Medhat M Morcos, Suresh Gopalakrishnan, and Thomas W Nehl. Detection of stator short circuits in vsi-fed brushless dc motors using wavelet transform. *IEEE Transactions on Energy Conversion*, 21(1):1–8, 2006.

[81] Wiehan Le Roux, Ronald G Harley, and Thomas G Habetler. Detecting faults in rotors of pm drives. *IEEE Industry Applications Magazine*, 14(2):23–31, 2008.

[82] Dimitri Torregrossa, Amir Khoobroo, and Babak Fahimi. Prediction of acoustic noise and torque pulsation in pm synchronous machines with static eccentricity and partial demagnetization using field reconstruction method. *IEEE Transactions on Industrial Electronics*, 59(2):934–944, 2011.

[83] Min Zhu, Wensong Hu, and Narayan C Kar. Acoustic noise-based uniform permanent-magnet demagnetization detection in spmsm for high-performance pmsm drive. *IEEE Transactions on Transportation Electrification*, 4(1):303–313, 2017.

[84] Mohamed Elforjani and Suliman Shanbr. Prognosis of bearing acoustic emission signals using supervised machine learning. *IEEE Transactions on industrial electronics*, 65(7):5864–5871, 2017.

[85] Zhi Yang, Xiaodong Shi, and Mahesh Krishnamurthy. Vibration monitoring of pm synchronous machine with partial demagnetization and inter-turn short circuit faults. In *2014 IEEE Transportation Electrification Conference and Expo (ITEC)*, pages 1–6. IEEE, 2014.

[86] Fabio Immovilli, Alberto Bellini, Riccardo Rubini, and Carla Tassoni. Diagnosis of bearing faults in induction machines by vibration or current signals: A critical comparison. *IEEE Transactions on Industry Applications*, 46(4):1350–1359, 2010.

[87] Sang-Moon Hwang, Kyung-Tae Kim, Weui-Bong Jeong, Yoong-Ho Jung, and Beom-Soo Kang. Comparison of vibration sources between symmetric and asymmetric hdd spindle motors with rotor eccentricity. *IEEE Transactions on Industry Applications*, 37(6):1727–1731, 2001.

[88] Ferhat Çıra. Detection of eccentricity fault based on vibration in the pmsm. *Results in Physics*, 10:760–765, 2018.

[89] Ungtae Kim and Dennis K Lieu. Magnetic field calculation in permanent magnet motors with rotor eccentricity: without slotting effect. *IEEE Transactions on Magnetics*, 34(4):2243–2252, 1998.

[90] Jawad Faiz, Bashir Mahdi Ebrahimi, and Hamid A Toliyat. Effect of magnetic saturation on static and mixed eccentricity fault diagnosis in induction motor. *IEEE Transactions on magnetics*, 45(8):3137–3144, 2009.

[91] Wesley G Zanardelli, Elias G Strangas, and Selin Aviyente. Identification of intermittent electrical and mechanical faults in permanent-magnet ac drives based on time–frequency analysis. *IEEE Transactions on Industry Applications*, 43(4):971–980, 2007.

[92] Zheng Chen, Rong Qi, and Hui Lin. Inter-turn short circuit fault diagnosis for pmsm based on complex gauss wavelet. In *2007 International Conference on Wavelet Analysis and Pattern Recognition*, volume 4, pages 1915–1920. IEEE, 2007.

[93] M Abdesh SK Khan and M Azizur Rahman. Development and implementation of a novel fault diagnostic and protection technique for ipm motor drives. *IEEE Transactions on Industrial Electronics*, 56(1):85–92, 2008.

[94] JA Rosero, L Romeral, J Cusido, A Garcia, and JA Ortega. On the short-circuiting fault detection in a pmsm by means of stator current transformations. In *2007 IEEE Power Electronics Specialists Conference*, pages 1936–1941. IEEE, 2007.

[95] Javier A Rosero, Luis Romeral, Juan A Ortega, and Esteban Rosero. Short-circuit detection by means of empirical mode decomposition and wigner–ville distribution for pmsm running under dynamic condition. *IEEE Transactions on Industrial Electronics*, 56(11):4534–4547, 2009.

[96] Sivakumar Nadarajan, Sanjib Kumar Panda, Bicky Bhangu, and Amit Kumar Gupta. Online model-based condition monitoring for brushless wound-field synchronous generator to detect and diagnose stator windings turn-to-turn shorts using extended kalman filter. *IEEE Transactions on Industrial Electronics*, 63(5):3228–3241, 2016.

[97] Yao Da, Xiaodong Shi, and Mahesh Krishnamurthy. A new approach to fault diagnostics for permanent magnet synchronous machines using electromagnetic signature analysis. *IEEE Transactions on Power Electronics*, 28(8):4104–4112, 2012.

[98] Kyung-Tae Kim, Seung-Tae Lee, and Jin Hur. Diagnosis technique using a detection coil in bldc motors with interturn faults. *IEEE transactions on magnetics*, 50(2):885–888, 2014.

[99] Cristian H De Angelo, Guillermo R Bossio, Santiago J Giaccone, María Inés Valla, Jorge A Solsona, and Guillermo O García. Online model-based stator-fault detection and identification in induction motors. *IEEE Transactions on Industrial Electronics*, 56(11):4671–4680, 2009.

[100] Nicolas Leboeuf, Thierry Boileau, Babak Nahid-Mobarakeh, Guy Clerc, and Farid Meibody-Tabar. Real-time detection of interturn faults in pm drives using back-emf estimation and residual analysis. *IEEE Transactions on Industry Applications*, 47(6):2402–2412, 2011.

[101] Ali Sarikhani and Osama A Mohammed. Inter-turn fault detection in pm synchronous machines by physics-based back electromotive force estimation. *IEEE Transactions on Industrial Electronics*, 60(8):3472–3484, 2012.

[102] Peter J Tavner. Review of condition monitoring of rotating electrical machines. *IET electric power applications*, 2(4):215–247, 2008.

[103] Jawad Faiz, Bashir Mahdi Ebrahimi, Bilal Akin, and Hamid A Toliyat. Comprehensive eccentricity fault diagnosis in induction motors using finite element method. *IEEE Transactions on Magnetics*, 45(3):1764–1767, 2009.

[104] William T Thomson and Alexandra Barbour. On-line current monitoring and application of a finite element method to predict the level of static airgap eccentricity in three-phase induction motors. *IEEE Transactions on Energy Conversion*, 13(4):347–357, 1998.

[105] Bashir Mahdi Ebrahimi, Jawad Faiz, M Javan-Roshtkhari, and A Zargham Nejhad. Static eccentricity fault diagnosis in permanent magnet synchronous motor using time stepping finite element method. *IEEE Transactions on Magnetics*, 44(11):4297–4300, 2008.

[106] Nabil A Al-Nuaim and H Toliyat. A novel method for modeling dynamic air-gap eccentricity in synchronous machines based on modified winding function theory. *IEEE Transactions on energy conversion*, 13(2):156–162, 1998.

[107] Luis Romeral, Julio César Urresty, Jordi-Roger Riba Ruiz, and Antonio Garcia Espinosa. Modeling of surface-mounted permanent magnet synchronous motors with stator winding interturn faults. *IEEE Transactions on Industrial Electronics*, 58(5):1576–1585, 2010.

[108] Ilsu Jeong, Byong Jo Hyon, and Kwanghee Nam. Dynamic modeling and control for spmsms with internal turn short fault. *IEEE Transactions on Power Electronics*, 28(7):3495–3508, 2012.

[109] Bon-Gwan Gu. Study of ipmsm interturn faults part i: Development and analysis of models with series and parallel winding connections. *IEEE Transactions on Power Electronics*, 31(8):5931–5943, 2015.

[110] Najla Haje Obeid, Thierry Boileau, and Babak Nahid-Mobarakeh. Modeling and diagnostic of incipient interturn faults for a three-phase permanent magnet synchronous motor. *IEEE Transactions on Industry Applications*, 52(5):4426–4434, 2016.

[111] Seyed Saeid Moosavi, Abdesslem Djerdir, Y Ait Amirat, and Davod Arab Khaburi. Demagnetization fault diagnosis in permanent magnet synchronous motors: A review of the state-of-the-art. *Journal of magnetism and magnetic materials*, 391:203–212, 2015.

[112] Taner Goktas, Mohsen Zafarani, and Bilal Akin. Discernment of broken magnet and static eccentricity faults in permanent magnet synchronous motors. *IEEE Transactions on Energy Conversion*, 31(2):578–587, 2016.

[113] Jun-Kyu Park and Jin Hur. Detection of inter-turn and dynamic eccentricity faults using stator current frequency pattern in ipm-type bldc motors. *IEEE Transactions on Industrial Electronics*, 63(3):1771–1780, 2015.

[114] Mohsen Zafarani, Taner Goktas, and Bilal Akin. A comprehensive analysis of magnet defect faults in permanent magnet synchronous motors. In *2015 IEEE Applied Power Electronics Conference and Exposition (APEC)*, pages 2779–2783. IEEE, 2015.

[115] Julio-César Urresty, Jordi-Roger Riba, and Luis Romeral. A back-emf based method to detect magnet failures in pmsms. *IEEE Transactions on Magnetics*, 49(1):591–598, 2012.

[116] Bashir Mahdi Ebrahimi and Jawad Faiz. Demagnetization fault diagnosis in surface mounted permanent magnet synchronous motors. *IEEE transactions on Magnetics*, 49(3):1185–1192, 2012.

[117] John F Bangura, Richard J Povinelli, Nabeel AO Demerdash, and Ronald H Brown. Diagnostics of eccentricities and bar/end-ring connector breakages in polyphase induction motors through a combination of time-series data mining and time-stepping coupled fe-state-space techniques. *IEEE Transactions on Industry Applications*, 39(4):1005–1013, 2003.

[118] Nicolas Leboeuf, Thierry Boileau, Babak Nahid-Mobarakeh, Noureddine Takorabet, Farid Meibody-Tabar, and Guy Clerc. Effects of imperfect manufacturing process on electromagnetic performance and online interturn fault detection in pmsms. *IEEE transactions on Industrial electronics*, 62(6):3388–3398, 2015.

[119] Xuewu Dai and Zhiwei Gao. From model, signal to knowledge: A data-driven perspective of fault detection and diagnosis. *IEEE Transactions on Industrial Informatics*, 9(4):2226–2238, 2013.

[120] Seyed Saeid Moosavi, Abdesslem Djerdir, Y Aït-Amirat, and DA Kkuburi. Artificial neural networks based fault detection in 3-phase pmsm traction motor. In *2012 XXth International Conference on Electrical Machines*, pages 1579–1585. IEEE, 2012.

[121] Vilas N Ghate and Sanjay V Dudul. Cascade neural-network-based fault classifier for three-phase induction motor. *IEEE Transactions on Industrial Electronics*, 58(5):1555–1563, 2010.

[122] Takashi Hiyama et al. Improving elman network using genetic algorithm for bearing failure diagnosis of induction motor. In *2009 IEEE International Symposium on Diagnostics for Electric Machines, Power Electronics and Drives*, pages 1–6. IEEE, 2009.

[123] David He, Ruoyu Li, and Junda Zhu. Plastic bearing fault diagnosis based on a two-step data mining approach. *IEEE Transactions on Industrial Electronics*, 60(8):3429–3440, 2012.

[124] Kan Liu and Zi-Qiang Zhu. Position-offset-based parameter estimation using the adaline nn for condition monitoring of permanent-magnet synchronous machines. *IEEE Transactions on Industrial Electronics*, 62(4):2372–2383, 2014.

[125] MA Awadallah and MM Morcos. Diagnosis of stator short circuits in brushless dc motors by monitoring phase voltages. *IEEE Transactions on Energy Conversion*, 20(1):246–247, 2005.

[126] Manjeevan Seera and Chee Peng Lim. Online motor fault detection and diagnosis using a hybrid fmm-cart model. *IEEE transactions on neural networks and learning systems*, 25(4):806–812, 2013.

[127] Mogens Blanke, Michel Kinnaert, Jan Lunze, and Marcel Staroswiecki. Diagnosis and fault tolerant control, 2016.

[128] Mattias Krysander. *Design and analysis of diagnosis systems using structural methods*. PhD thesis, Institutionen för systemteknik, 2006.

[129] Mattias Krysander and Mattias Nyberg. Fault diagnosis utilizing structural analysis. *CCSSE, Norrköping, Sweden*, 2002.

[130] Mattias Krysander and Jan Aslund. Graph theoretical methods for finding analytical redundancy relations in overdetermined differential algebraic systems. *system*, 1:x2, 2005.

[131] Mattias Krysander, Jan Åslund, and Mattias Nyberg. An efficient algorithm for finding minimal overconstrained subsystems for model-based diagnosis. *IEEE Transactions on Systems, Man, and Cybernetics-Part A: Systems and Humans*, 38(1):197–206, 2007.

[132] Mattias Krysander and Erik Frisk. Sensor placement for fault diagnosis. *IEEE Transactions on Systems, Man, and Cybernetics-Part A: Systems and Humans*, 38(6):1398–1410, 2008.

[133] V Flaugergues, Vincent Cocquempot, Mireille Bayart, and Marco Pengov. Structural analysis for fdi: a modified, invertibility-based canonical decomposition. In *Proceedings of the 20th International Workshop on Principles of Diagnosis, DX09*, pages 59–66, 2009.

[134] Mattias Krysander, Jan Åslund, and Erik Frisk. A structural algorithm for finding testable sub-models and multiple fault isolability analysis. In *21st International Workshop on Principles of Diagnosis (DX-10), Portland, Oregon, USA*, pages 17–18. Citeseer, 2010.

[135] Jiyu Zhang and Giorgio Rizzoni. Selection of residual generators in structural analysis for fault diagnosis using a diagnosability index. In *2017 IEEE Conference on Control Technology and Applications (CCTA)*, pages 1438–1445. IEEE, 2017.

[136] Carl Svard and Mattias Nyberg. Residual generators for fault diagnosis using computation sequences with mixed causality applied to automotive systems. *IEEE Transactions on Systems, Man, and Cybernetics-Part A: Systems and Humans*, 40(6):1310–1328, 2010.

[137] Carl Svärd, Mattias Nyberg, and Erik Frisk. Realizability constrained selection of residual generators for fault diagnosis with an automotive engine application. *IEEE Transactions on Systems, Man, and Cybernetics: Systems*, 43(6):1354–1369, 2013.

[138] Carl Svärd, Mattias Nyberg, Erik Frisk, and Mattias Krysander. Automotive engine fdi by application of an automated model-based and data-driven design methodology. *Control Engineering Practice*, 21(4):455–472, 2013.

[139] Christofer Sundström, Erik Frisk, and Lars Nielsen. Selecting and utilizing sequential residual generators in fdi applied to hybrid vehicles. *IEEE Transactions on Systems, Man, and Cybernetics: Systems*, 44(2):172–185, 2013.

[140] Christofer Sundström. *Vehicle level diagnosis for hybrid powertrains*. PhD thesis, Linköping University Electronic Press, 2011.

[141] Zhentong Liu, Qadeer Ahmed, Giorgio Rizzoni, and Hongwen He. Fault detection and isolation for lithium-ion battery system using structural analysis and sequential residual generation. In *ASME 2014 dynamic systems and control conference*. American Society of Mechanical Engineers Digital Collection, 2014.

[142] Jiyu Zhang and Giorgio Rizzoni. Structural analysis for diagnosability and reconfigurability, with pplication to electric vehicle drive system. *IFAC-PapersOnLine*, 48(21):1471–1478, 2015.

[143] Saeed Hasan Ebrahimi, Martin Choux, and Van Khang Huynh. Diagnosis of sensor faults in pmsm and drive system based on structural analysis. In *2021 IEEE International Conference on Mechatronics (ICM)*, pages 1–6. IEEE, 2021.

[144] Saeed Hasan Ebrahimi, Martin Choux, et al. Detection and discrimination of interturn short circuit and demagnetization faults in pmsms based on structural analysis. In *2021 22nd IEEE International Conference on Industrial Technology (ICIT)*, volume 1, pages 184–189. IEEE, 2021.

[145] Andrew L Dulmage and Nathan S Mendelsohn. Coverings of bipartite graphs. *Canadian Journal of Mathematics*, 10:517–534, 1958.

[146] Erik Frisk, Anibal Bregon, Jan Aslund, Mattias Krysander, Belarmino Pulido, and Gautam Biswas. Diagnosability analysis considering causal interpretations for differential constraints. *IEEE Transactions on Systems, Man, and Cybernetics-Part A: Systems and Humans*, 42(5):1216–1229, 2012.

[147] Erik Frisk, Mattias Krysander, and Daniel Jung. A toolbox for analysis and design of model based diagnosis systems for large scale models. *IFAC-PapersOnLine*, 50(1):3287–3293, 2017.

[148] Mattias Krysander and Mattias Nyberg. Structural analysis utilizing mss sets with application to a paper plant. Technical report, LINKOEPING UNIV (SWEDEN), 2002.

[149] Richard W Hamming. Error detecting and error correcting codes. *The Bell system technical journal*, 29(2):147–160, 1950.

[150] Steven M Kay. *Fundamentals of Statistical Signal Processing, Volume II: Detection Theory*. Prentice Hall PTR, 1998.

[151] Steven M Kay. *Fundamentals of Statistical Signal Processing, Volume I: Estimation Theory*. Prentice Hall PTR, 1993.

[152] Vera Szabo, Saeed Hasan Ebrahimi, Martin Choux, and Morten Goodwin. Itsc fault diagnosis in permanent magnet synchronous motor drives using shallow cnns. In *International Conference on Engineering Applications of Neural Networks*, pages 177–189. Springer, 2022.

Appended Papers

Paper A

Modelling Incipient Inter-Turn Short Circuit Fault in Permanent Magnet Synchronous Motors

Saeed Hasan Ebrahimi, Martin Choux, and Van Khang Huynh

This paper has been submitted as:

S. H. Ebrahimi, M. Choux, and V. K. Huynh. Modelling Incipient Inter-Turn Short Circuit Fault in Permanent Magnet Synchronous Motors. In *Proceedings of the 22nd International Conference on the Computation of Electromagnetic Fields (COMPUMAG 2019)*, 2019.

Modelling Incipient Inter-Turn Short Circuit Fault in Permanent Magnet Synchronous Motors

Saeed Hasan Ebrahimi, Martin Choux, and Van Khang Huynh

Department of Engineering Sciences
University of Agder
NO-4879 Grimstad, Norway

Abstract – The inter-turn short circuit (ITSC) fault in the winding of a 1.7 KW interior permanent magnet synchronous motor (IPMSM) is modelled using a time-stepping finite element analysis (FEA). Conventional FEA normally considers the fault symmetrical, but ITSC faults may initiate in one coil and then expand to other coils. This causes unbalance in flux distribution around the faulty coil, and a full model of the motor is therefore analyzed in FEA. Based on the analyzed results of the IPMSM under incipient ITSC faults, different motor signals are further investigated and processed using Fast Fourier transform (FFT) to find out the best indicator to detect ITSC in an early stage.

A.1 Introduction

Permanent magnet synchronous motors (PMSMs) have become more and more common in industry due to their merits of high efficiency, precise controllability, and high reliability [1–3]. However, PMSMs working in a harsh environment are exposed to electrical, thermal, and mechanical stresses, making the stator insulation continuously degrading, leading to inter-turn short circuit (ITSC) fault. Therefore, understanding the machine behavior under the ITSC fault in early stages is of great importance in preventing a complete machine failure.

In this paper, a 2-D time-stepping finite-element analysis (FEA) is used to model the ITSC fault in the winding of a PMSM. The first objective is to model the fault as close as possible to the real faults in PMSMs. Such a phenomenon cannot be investigated by lumped-circuit models and therefore it is recommended to be modeled using FEA [4]. However, finding a health indicator for a PMSM using signals obtained from FEA is missing in the literature. In this paper, motor signals obtained from the time-stepping FEA, namely torque, currents, instantaneous power of phase-a and input power are transformed into frequency domain using Fast Fourier Transform (FFT), since it is fast and efficient to be implemented [5], to find out which one is better as ITSC fault indicator.

A.2 Modelling of Inter-Turn Fault in IPMSM

To model an ITSC fault, a $1.7kW$ IPMSM is re-designed and implemented. Fig. A.1 shows the motor's structure, whereas its parameters are listed in Table A.1. Since it is an

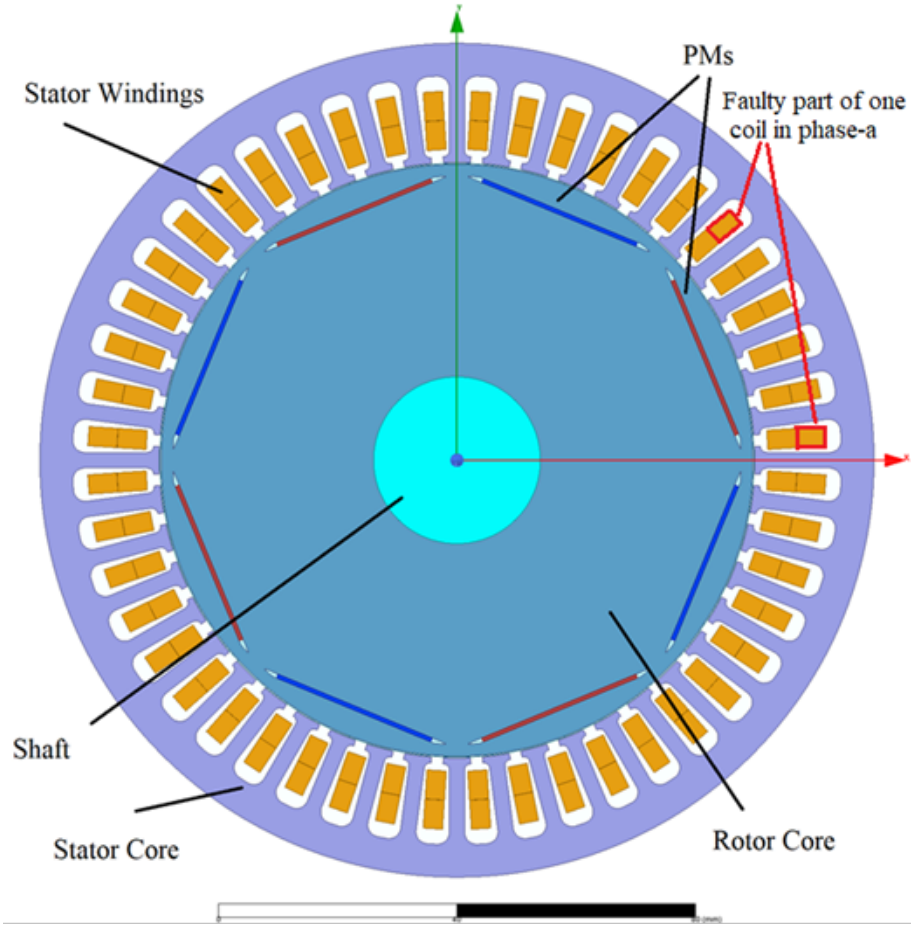

Figure A.1: 2-D model of an 8-pole permanent magnet synchronous motor.

8-pole motor with $q = 2$ (slots per pole per phase), each phase consists of 8 coils connected in series.

An ITSC fault usually starts with a few short turns, and then propagates to the whole coil, leading to phase-to-phase or phase-to-ground faults as well. Here, it is assumed that half of one coil in phase-a, marked in Fig. A.1, is short circuited. Since 8 coils are in series in each phase, 6.25% or 1/16 of phase-a is considered to be short circuited.

A 2-D time-stepping FEA has been performed on the aforementioned PMSM with a time-step of $100\mu s$. Fig. A.2 shows the flux distribution inside the cores of the motor stator and rotor. It is obvious that even a small ITSC fault creates unbalance in flux distribution under the faulty coil. In addition, numerical data of three-phase currents, instantaneous powers, input power, and electromagnetic torque are extracted and analyzed by FFT. In Fig. A.3 and Fig. A.4, FFT analysis reveals that the 3rd and 9th harmonics appear in spectrum of the phase-a current (Ia) and 4th harmonic in phase-a instantaneous power (Pa) under the ITSC fault condition. FFT analysis of input power (Pin) and torque (Te) shows that 2nd, 4th, 8th and 10th harmonics are generated in the presence of ITSC fault as shown in Fig. A.5 and Fig. A.6.

Current signals are a common index and widely investigated in literature due to simplicity of measurement. However, as shown in Fig. A.3, the difference of the 3rd harmonic between faulty and healthy cases is rather small and inconsistent at other harmonics, and

Table A.1: Parameters of the PMSM

Symbol	Parameter	Value	Unit
V_s	Rated voltage	300	V
P_{out}	Output power	1.75	A
T_{out}	Output torque	14.0	$N.m$
n_s	Rated speed	1200	rpm
P	Number of poles	8	
S	Number of slots	48	

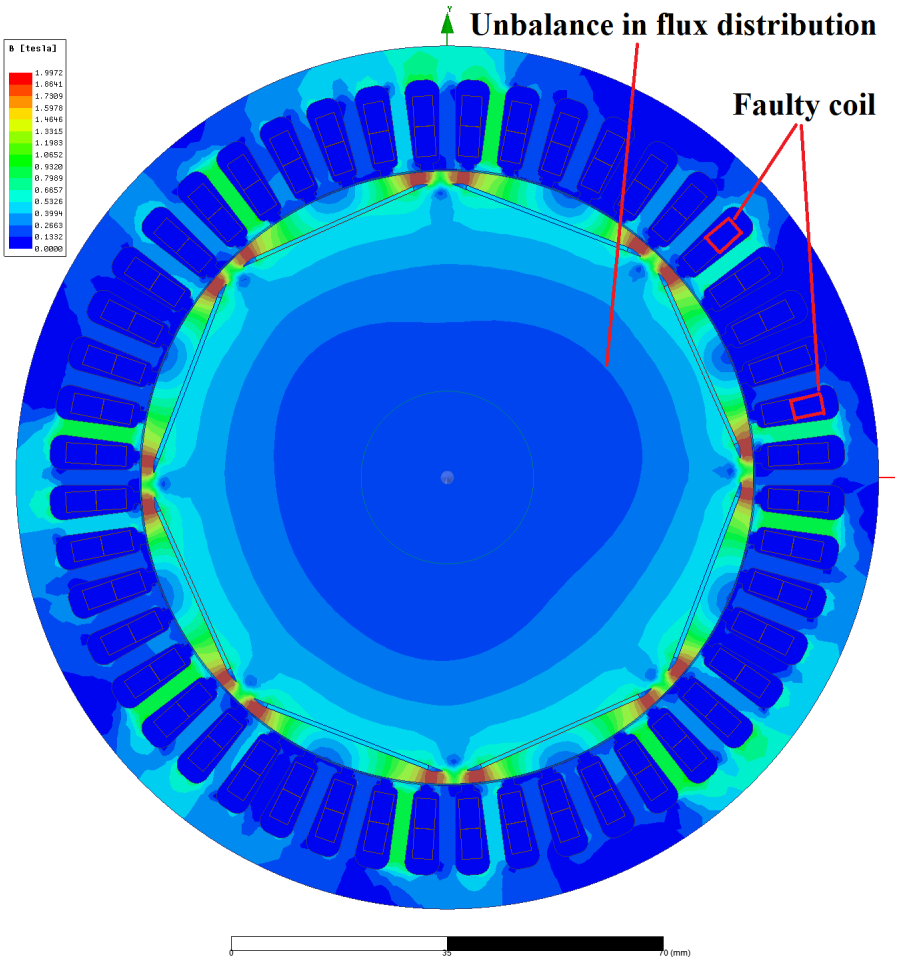

Figure A.2: Flux distribution in the motor.

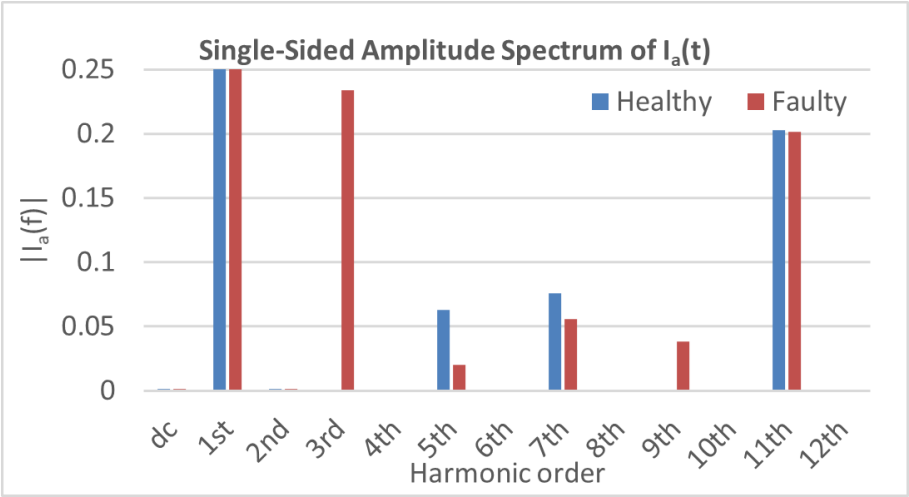

Figure A.3: Comparison of spectrum of I_a in healthy and faulty condition.

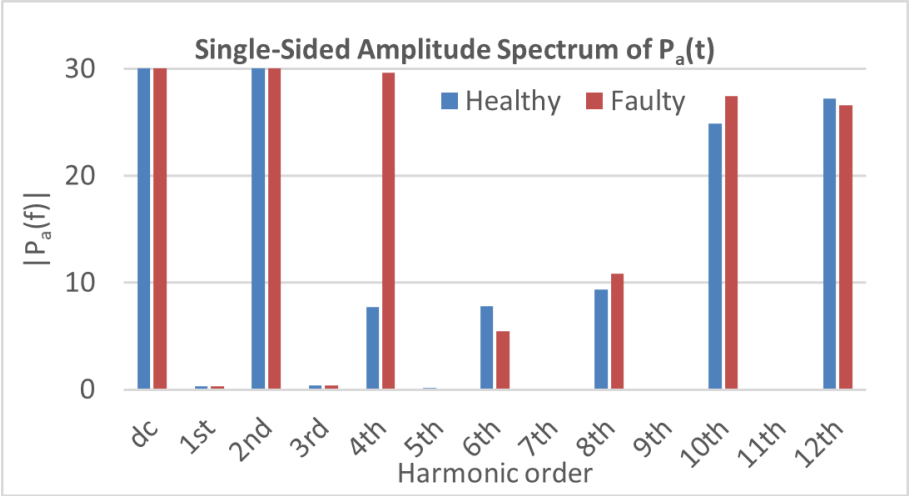

Figure A.4: Comparison of spectrum of P_a in healthy and faulty condition.

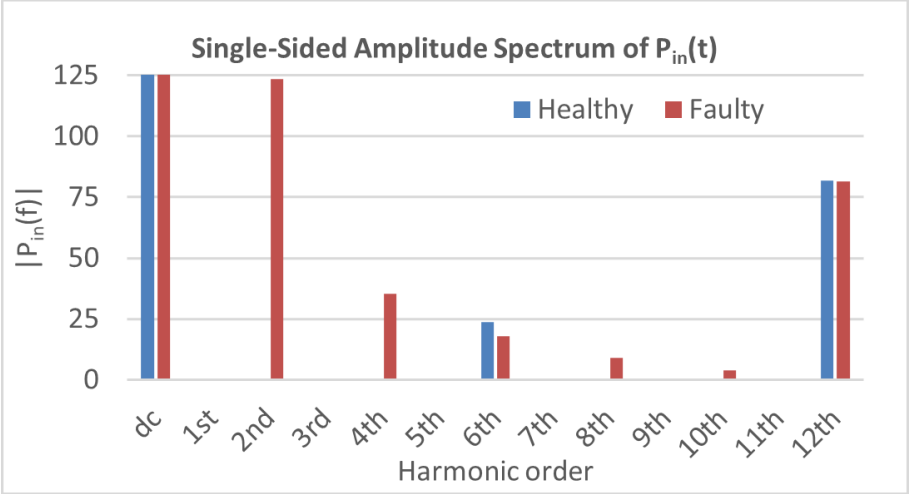

Figure A.5: Comparison of spectrum of P_{in} in healthy and faulty condition.

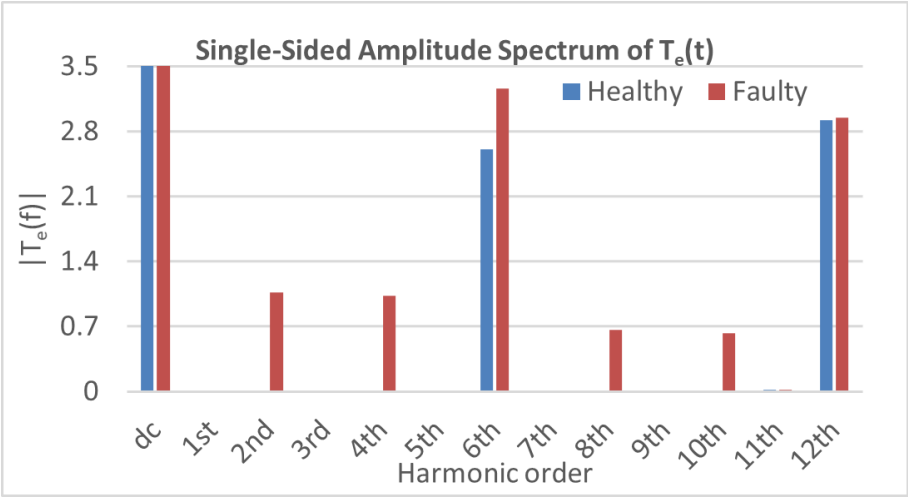

Figure A.6: Comparison of spectrum of T_{out} in healthy and faulty condition.

can hence easily be affected by noise.

Although the torque is a feasible fault indicator, cost of a torque transducer, load dependency and measurement complexity make it less interesting to be considered. Instantaneous power of phase-a seems to be a promising fault indicator compared to both torque and current, since the difference between healthy and faulty components is noticeable. Nevertheless, input power shows better indication of ITSC fault since it contains the information of all the three-phase currents and voltages. Not only are more harmonic components influenced by the fault, but also the difference between healthy and faulty components, especially in 2nd and 4th, are high enough not to be influenced by noise. Furthermore, it can be used for ITSC fault in other phases as well.

A.3 Conclusion

A 2-D time stepping finite element analysis has been performed on an 8-pole IPMSM both in healthy condition and under an ITSC fault in the stator winding. Initial analysis of transform currents, phase-a instantaneous powers, and torque, signals using FFT shows that certain harmonics due to an ITSC fault can be observed in spectra. However, these components in faulty case can be affected either by load change and noise or are inconsistent at higher frequencies and that is why authors recommend using input power as the ITSC fault indicator instead. All in all, using input power as fault indicator brings about a low-cost, fast, efficient, and effective ITSC fault detection method which can be used in various industrial applications.

References

[1] Seokbae Moon, Hyeyun Jeong, Hojin Lee, and Sang Woo Kim. Interturn short fault diagnosis in a pmsm by voltage and current residual analysis with the faulty winding model. *IEEE Transactions on Energy Conversion*, 33(1):190–198, 2017.

[2] Chong Zeng, Song Huang, Yongming Yang, and Dun Wu. Inter-turn fault diagnosis of permanent magnet synchronous machine based on tooth magnetic flux analysis. *IET Electric Power Applications*, 12(6):837–844, 2018.

[3] Richard T Meyer, Raymond A DeCarlo, Scott C Johnson, and Steve Pekarek. Short-circuit fault detection observer design in a pmsm. *IEEE Transactions on Aerospace and Electronic Systems*, 54(6):3004–3017, 2018.

[4] Seungdeog Choi, Moinul Shahidul Haque, Md Tawhid Bin Tarek, Vamsi Mulpuri, Yao Duan, Sanjoy Das, Vijay Garg, Dan M Ionel, M Abul Masrur, Behrooz Mirafzal, et al. Fault diagnosis techniques for permanent magnet ac machine and drives—a review of current state of the art. *IEEE Transactions on Transportation Electrification*, 4(2):444–463, 2018.

[5] Bashir Mahdi Ebrahimi and Jawad Faiz. Feature extraction for short-circuit fault detection in permanent-magnet synchronous motors using stator-current monitoring. *IEEE Transactions on Power Electronics*, 25(10):2673–2682, 2010.

Paper B

Modeling Stator Winding Inter-Turn Short Circuit Faults in PMSMs Including Cross Effects

Saeed Hasan Ebrahimi, Martin Choux, and Van Khang Huynh

This paper has been submitted as:

S. H. Ebrahimi, M. Choux, and V. K. Huynh. Modeling Stator Winding Inter-Turn Short Circuit Faults in PMSMs including Cross Effects. In *Proceedings of 2020 International Conference on Electrical Machines (ICEM)*, 2020. ISBN: 978-1-7281-9946-7.

Modeling Stator Winding Inter-Turn Short Circuit Faults in PMSMs including Cross Effects

Saeed Hasan Ebrahimi, Martin Choux, and Van Khang Huynh

Department of Engineering Sciences
University of Agder
NO-4879 Grimstad, Norway

Abstract – This paper presents a detailed analysis of stator winding inter-turn Short Circuit (ITSC) faults, taking the cross effects in the three phases of a permanent magnet synchronous motor (PMSM) into account by considering insulation degradation resistances. A PMSM with series coils in each phase winding is selected as a case study.The ITSC in one coil of each phase winding is modelled based on deformed fluxes or inductance variations caused by flux linkages, depending on the distribution of the coils in the same phase winding. Different fault ratios are investigated to evaluate different fault severity and scenarios. Therefore, three-phase faulty coils within three-phase winding analysis dynamics will constitute sixth-order assessments. The proposed faulty PMSM model is verified by a 2-D finite element analysis (FEA), showingc a good agreement between the proposed model and FEA.

B.1 Introduction

Permanent magnet synchronous motors (PMSMs) have gained a popularity in industry owing to their merits of high efficiency, high power density, and high reliability [1–3]. PMSMs often work in a harsh industrial environment and therefore, are exposed to electrical, thermal, and mechanical stresses. This creates the ground for different types of faults to appear, including electrical, mechanical, and magnetic faults [4]. Among the electrical faults, the stator winding inter-turn short circuit (ITSC) fault is considered as the most common fault [5], and at the same time, the most critical one due to the excessive heat generated by the high circulating fault current [6]. ITSC occurs with a few shorted turns in one coil due to the stator winding insulation failure. The insulation failure provides a degraded path between the shorted turns with a non-zero fault resistance, R_f, with a circulating fault current of i_f. This path causes unbalance in the magnetic field, generating excessive heat, which may propagate to the whole coil or other phases [7] if not being treated in time. Therefore, understating and detecting the ITSC fault in early stages are of great importance in reducing the costs and down-times caused by the complete machine failure.

Diagnosis of ITSC has gained a significant attention in both industry and academia via previous studies. The ITSC fault can be detected by current signal analysis (CSA) and zero-sequence voltage component (ZSVC) harmonic monitoring using signal processing or filtering techniques, such as Fourier transform [8], wavelet transform [9], and Kalman

filter [10]. These existing signal-based methods are very powerful to detect a fault but have some limitations on determining the fault severity, ITSC faults at different locations of the phase winding, or requiring external resistor network and neutral point of the stator windings [1, 2]. Alternatively, data-driven models, e.g using artificial neural network (ANN), were also proposed to detect or classify the faults. The data driven models are required a lot of historical faulty data for training to be robust and reliable [11]. In addition to signal-based and data-driven techniques, many model-based methods have intensively been employed to detect ITSC fault [12–14], but such models are hard to be applicable to multi-pole PMSMs since they ignore the flux coupling factor between healthy and faulty coils in the same phase winding. This coupling factor was well proposed and investigated in [15]. However, the cross effect of simultaneous fault currents in different phases is not modeled or still missing in literature. Modelling the interaction of one fault on other phases is important to understand the behaviour of magnetic flux and output characteristics of an unbalance PMSM under faults, being useful to develop a fault indicator in both steady and transient states. Although very unlikely for ITSC faults to appear in different phases at the same time, having a comprehensive model that detects and understands this phenomenon is very helpful when it comes to isolate faults in the machine diagnostic systems. Moreover, since the ITSC fault in one phase may propagate to other windings if not treated in time [16], adding this extra layer of fault detection when designing the sequence of faults, helps improve the performance and reliability of the diagnostic system.

The study presents an analytical model of a faulty PMSM considering simultaneous ITSC faults in each of the three-phase windings, in which the insulation degradation and the flux coupling between healthy and faulty coils in each phase are modeled as a resistance (R_f) and a factor (γ), respectively. Further, the cross-effect of fault currents in different phases is analysed by modified mutual inductances and coupling factor, allowing the modeling to be more comprehensive to understand the machine behaviors in a wide range of operations in different fault scenarios. The fault model is developed in a way to obtain deformed fluxes based on inductance variations caused by cross flux linkages, depending on the distribution of the coils in the same phase winding and cross-effects of fault currents in different phases. The remainder of the paper is organized as follows: modelling the ITSC fault in PMSM is detailed in Section II. Section III presents simulation results and a comparison with FEA. Finally, the paper is concluded in Section IV.

B.2 Modeling ITSC fault in the windings of PMSM

An 8-pole surface-mounted PMSM with concentrated winding is chosen as the case study for implementation of simultaneous ITSC faults in different phase windings. The reason that a concentrated winding structure is considered here, is simply because it is easier for this modeling to be implemented on. The same procedure can be applied on a motor with distributed winding with a few modifications in the flux equations. A 2D view of this PMSM is depicted in Fig. B.1 while motor parameters are listed in Table B.1. Some of these parameters are obtained from the manufacturer data-sheet and the rest from a few

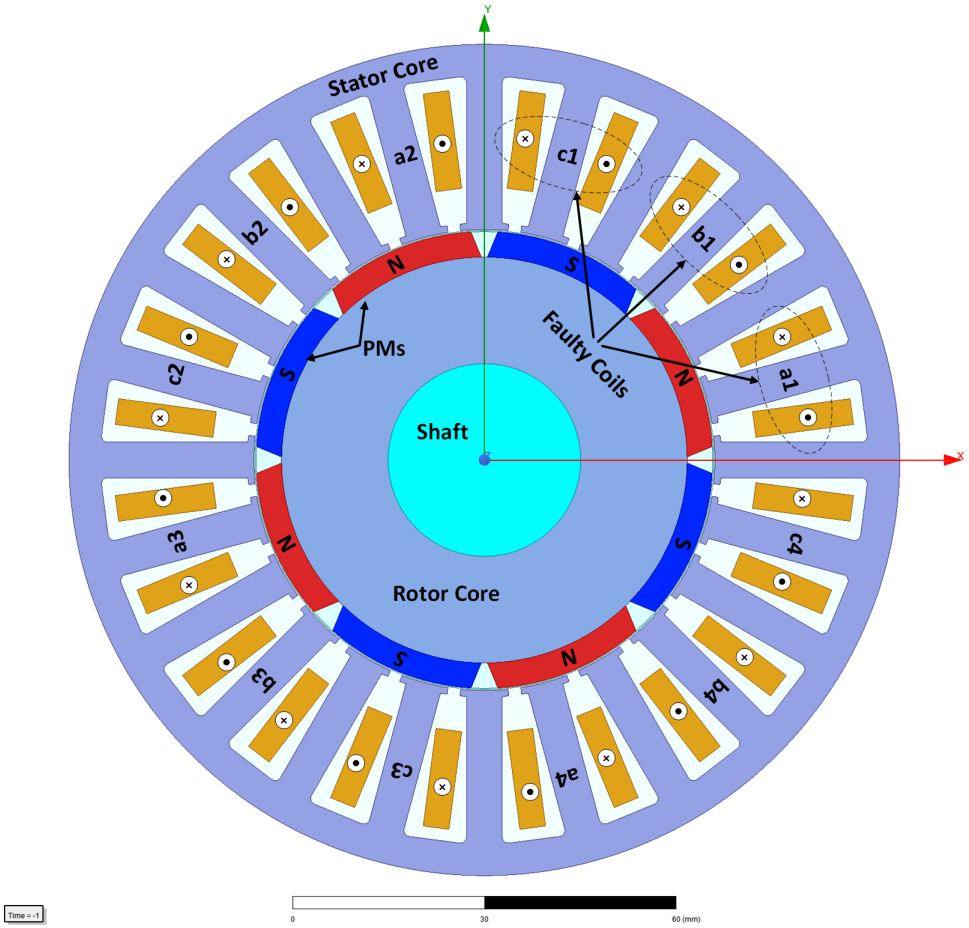

Figure B.1: 2D Structure of PM Synchronous Motor.

FEM Simulations which are explained in [15]. Each phase winding consists of 4 (number of pole-pairs) coils denoted by $a_{1,2,3,4}$, $b_{1,2,3,4}$, and $c_{1,2,3,4}$, which are connected in series. It is assumed that an ITSC fault is present in the first coils of each of the three-phase windings, splitting the coil into one faulty part and one healthy part. The fault severity $\mu_{a,b,c}$ is defined as the ratio of number of the shorted turns to the total number of turns per coil. In addition, the phase fault resistances and circulating fault currents in the degraded path are denoted by $R_{af,bf,cf}$ and $i_{af,bf,cf}$, respectively. Fig. B.2 shows the schematic of winding configuration of series connection under three simultaneous faults in the three phases.

Modeling flux linkages between different coils was first proposed by [15],considering the interaction between the faulty part and healthy part of the same coil with other healthy coils in the same winding. This interaction is considered in the modeling with a coupling factor γ, and is especially important in PMSMs with multiple pole pairs ($p > 1$), where the flux linkages between coils in the same phase winding are affected by many possible flux paths. However, the suggested method is only valid for ITSC in one phase. To extend and generalize the concept for other phases, cross effect of ITSC faults in different phases are modelled in this work.

Table B.1: Parameters of PM Synchronous Motor

Symbol	Parameter	Value	Unit
V_s	Rated line voltage	320	V
I_s	Rated phase current	12.6	A
T_{out}	Output Torque	14	$N.m$
n_s	Rated speed	1200	rpm
R_s	Phase resistance	1.72	Ω
L_s	Phase leakage inductance	16.3652	mH
L_q, L_d	Q and D axes inductances	23.3948	mH
J	Rotor inertia	0.00161	$kg.m^2$
b	Rotor damping factor	0.002973	$N.m.s/rad$
λ_m	Flux linkage of PMs	0.1722	
γ	Winding coupling factor	0.6	
n_s	Number of Slots	24	

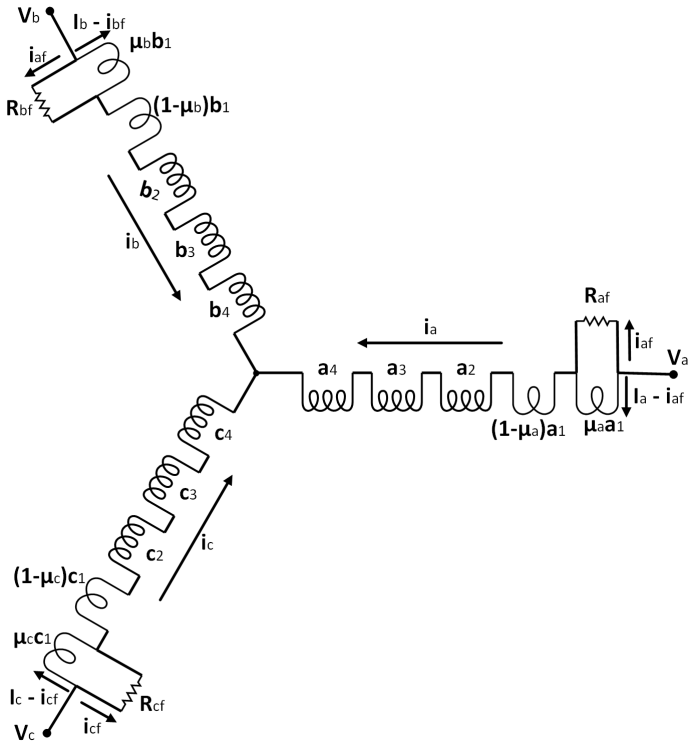

Figure B.2: Winding configuration with series connected coils under a 3-phase ITSC fault.

B.2.1 Deformed Flux-Current Equations of PMSM with ITSC

Taking the effects of simultaneous faults in different phases into account, the flux-current equations for faulty and healthy parts of the stator windings are obtained as follows [15]:

$$\begin{bmatrix}\lambda_{af}\\ \lambda_{ah}\\ \lambda_{bf}\\ \lambda_{bh}\\ \lambda_{cf}\\ \lambda_{ch}\end{bmatrix} = \begin{bmatrix} L_{a_fa_f} & L_{a_fa_h} & L_{a_fb_f} & L_{a_fb_h} & L_{a_fc_f} & L_{a_fc_h}\\ L_{a_ha_f} & L_{a_ha_h} & L_{a_hb_f} & L_{a_hb_h} & L_{a_hc_f} & L_{a_hc_h}\\ L_{b_fa_f} & L_{b_fa_h} & L_{b_fb_f} & L_{b_fb_h} & L_{b_fc_f} & L_{b_fc_h}\\ L_{b_ha_f} & L_{b_ha_h} & L_{b_hb_f} & L_{b_hb_h} & L_{b_hc_f} & L_{b_hc_h}\\ L_{c_fa_f} & L_{c_fa_h} & L_{c_fb_f} & L_{c_fb_h} & L_{c_fc_f} & L_{c_fc_h}\\ L_{c_ha_f} & L_{c_ha_h} & L_{c_hb_f} & L_{c_hb_h} & L_{c_hc_f} & L_{c_hc_h}\end{bmatrix} \begin{bmatrix} i_{af}\\ i_a - i_{af}\\ i_{bf}\\ i_b - i_{bf}\\ i_{cf}\\ i_c - i_{cf}\end{bmatrix} + \begin{bmatrix} \mu_a \sin\theta\\ (1-\mu_a)\sin\theta\\ \mu_b \sin(\theta - \frac{2\pi}{3})\\ (1-\mu_b)\sin(\theta - \frac{2\pi}{3})\\ \mu_c \sin(\theta + \frac{2\pi}{3})\\ (1-\mu_c)\sin(\theta + \frac{2\pi}{3})\end{bmatrix} \tag{B.1}$$

where the self and mutual inductances are modified as below

$$\begin{aligned}
L_{a_fa_f} &= \mu_a^2(L_{sl} + L_{sm})\\
L_{a_fa_h} &= L_{a_ha_f} = -\gamma\mu_a L_{sm} + \mu_a(1-\mu_a)(L_{sl} + L_{sm})\\
L_{a_ha_h} &= [p - 1 + (1-\mu_a)^2](L_{sl} + L_{sm}) - \gamma\mu_a L_{sm}(p - 2\mu_a)\\
L_{b_fb_f} &= \mu_b^2(L_{sl} + L_{sm})\\
L_{b_fb_h} &= L_{b_hb_f} = -\gamma\mu_b L_{sm} + \mu_b(1-\mu_b)(L_{sl} + L_{sm})\\
L_{b_hb_h} &= [p - 1 + (1-\mu_b)^2](L_{sl} + L_{sm}) - \gamma\mu_b L_{sm}(p - 2\mu_b)\\
L_{c_fc_f} &= \mu_c^2(L_{sl} + L_{sm})\\
L_{c_fc_h} &= L_{c_hc_f} = -\gamma\mu_c L_{sm} + \mu_c(1-\mu_c)(L_{sl} + L_{sm})\\
L_{c_hc_h} &= [p - 1 + (1-\mu_c)^2](L_{sl} + L_{sm}) - \gamma\mu_c L_{sm}(p - 2\mu_c)\\
L_{a_fb_f} &= L_{b_fa_f} = -\mu_a\mu_b\frac{L_m}{2p^2}\\
L_{a_fb_h} &= L_{b_ha_f} = -\frac{L_m}{2p^2}\mu_a(p - \mu_b)\\
L_{a_hb_f} &= L_{b_fa_h} = -\frac{L_m}{2p^2}\mu_b(p - \mu_a)\\
L_{a_hb_h} &= L_{b_ha_h} = -\frac{L_m}{2p^2}[p^2 - p(\mu_a + \mu_b) + \mu_a\mu_b]\\
L_{a_fc_f} &= L_{c_fa_f} = -\mu_a\mu_c\frac{L_m}{2p^2}\\
L_{a_fc_h} &= L_{c_ha_f} = -\frac{L_m}{2p^2}\mu_a(p - \mu_c)\\
L_{a_hc_f} &= L_{c_fa_h} = -\frac{L_m}{2p^2}\mu_c(p - \mu_a)\\
L_{a_hc_h} &= L_{c_ha_h} = -\frac{L_m}{2p^2}[p^2 - p(\mu_a + \mu_c) + \mu_a\mu_c]
\end{aligned} \tag{B.2}$$

$$
\begin{aligned}
L_{b_f c_f} &= L_{c_f b_f} = -\mu_b \mu_c \frac{L_m}{2p^2} \\
L_{b_f c_h} &= L_{c_h b_f} = -\frac{L_m}{2p^2} \mu_b (p - \mu_c) \\
L_{b_h c_f} &= L_{c_f b_h} = -\frac{L_m}{2p^2} \mu_c (p - \mu_b) \\
L_{b_h c_h} &= L_{c_h b_h} = -\frac{L_m}{2p^2} [p^2 - p(\mu_b + \mu_c) + \mu_b \mu_c]
\end{aligned}
$$

B.2.2 Modelling PMSM under 3-phase ITSC faults

Stator voltage of a synchronous motor in the stationary frame is obtained as follows:

$$
v_s = r_s i_s + \frac{d\lambda_s}{dt} \tag{B.3}
$$

where

$$
\begin{aligned}
v_s &= \begin{bmatrix} v_{af} & v_{ah} & v_{bf} & v_{bh} & v_{cf} & v_{ch} \end{bmatrix}^T \\
i_s &= \begin{bmatrix} i_{af} & i_a - i_{af} & i_{bf} & i_b - i_{bf} & i_{cf} & i_c - i_{cf} \end{bmatrix}^T \\
r_s &= R_s diag \begin{bmatrix} \mu_a & 1-\mu_a & \mu_b & 1-\mu_b & \mu_c & 1-\mu_c \end{bmatrix}^T
\end{aligned}
$$

By summing up the voltages of faulty and healthy parts in each phase using Eq. B.3, and considering phase winding linkage and leakage inductances to be $L_{sm} = L_m/p(1-\gamma)$ and $L_{sl} = L_l/p$, respectively, the three-phase voltage-current equations of the PMSM under ITSC fault are derived as follows:

$$
\begin{aligned}
&\begin{bmatrix} v_a \\ v_b \\ v_c \end{bmatrix} = R_s \begin{bmatrix} i_a \\ i_b \\ i_c \end{bmatrix} + \begin{bmatrix} L_m + L_l & -\frac{L_m}{2} & -\frac{L_m}{2} \\ -\frac{L_m}{2} & L_m + L_l & -\frac{L_m}{2} \\ -\frac{L_m}{2} & -\frac{L_m}{2} & L_m + L_l \end{bmatrix} \begin{bmatrix} \frac{di_a}{dt} \\ \frac{di_b}{dt} \\ \frac{di_c}{dt} \end{bmatrix} \\
&+ \omega_e \lambda_m \begin{bmatrix} \cos\theta \\ \cos(\theta - \frac{2\pi}{3}) \\ \cos(\theta + \frac{2\pi}{3}) \end{bmatrix} - \frac{R_s}{p} \begin{bmatrix} \mu_a & 0 & 0 \\ 0 & \mu_b & 0 \\ 0 & 0 & \mu_c \end{bmatrix} \begin{bmatrix} i_a \\ i_b \\ i_c \end{bmatrix} \\
&- \frac{1}{p} \begin{bmatrix} L_m + L_l & -\frac{L_m}{2} & -\frac{L_m}{2} \\ -\frac{L_m}{2} & L_m + L_l & -\frac{L_m}{2} \\ -\frac{L_m}{2} & -\frac{L_m}{2} & L_m + L_l \end{bmatrix} \begin{bmatrix} \mu_a & 0 & 0 \\ 0 & \mu_b & 0 \\ 0 & 0 & \mu_c \end{bmatrix} \begin{bmatrix} \frac{di_a}{dt} \\ \frac{di_b}{dt} \\ \frac{di_c}{dt} \end{bmatrix}
\end{aligned} \tag{B.4}
$$

By assuming that $v_{af} = R_{af} i_{af}$,$v_{bf} = R_{bf} i_{bf}$, and $v_{cf} = R_{cf} i_{cf}$ and using Eq. B.3 and Eq. B.4, the fault currents can be derived from:

$$
\begin{aligned}
v_a &= [\frac{pR_{af}}{\mu_a} + R_s(1 - \frac{\mu_a}{p})] i_{af} + \frac{\mu_a}{p} [L_m(\frac{p - 1 + \gamma}{1 - \gamma}) + L_l(p-1)] \frac{di_a}{dt} \\
v_b &= [\frac{pR_{bf}}{\mu_b} + R_s(1 - \frac{\mu_b}{p})] i_{bf} + \frac{\mu_b}{p} [L_m(\frac{p - 1 + \gamma}{1 - \gamma}) + L_l(p-1)] \frac{di_b}{dt} \\
v_c &= [\frac{pR_{cf}}{\mu_c} + R_s(1 - \frac{\mu_c}{p})] i_{ac} + \frac{\mu_c}{p} [L_m(\frac{p - 1 + \gamma}{1 - \gamma}) + L_l(p-1)] \frac{di_c}{dt}
\end{aligned} \tag{B.5}
$$

B.2.3 Performance of PMSM under a ITSC

Using Eq. B.4, the input power of the PMSM is calculated as follows:

$$P_{in} = v_a i_a + v_b i_b + v_c i_c \tag{B.6}$$

After putting aside the terms that contribute to copper losses or stored magnetic energy in Eq. B.7, the output power is extracted as:

$$P_{out} = \omega_e \lambda_m [\cos\theta i_a + \cos(\theta - \frac{2\pi}{3}) i_b + \cos(\theta + \frac{2\pi}{3}) i_c] \tag{B.7}$$

And the output torque can be calculated as:

$$T_{out} = \frac{P_{out}}{\omega_m} = \frac{P_{out}}{\frac{1}{p}\omega_e} = \lambda_m [\cos\theta i_a + \cos(\theta - \frac{2\pi}{3}) i_b + \cos(\theta + \frac{2\pi}{3}) i_c] \tag{B.8}$$

B.3 Simulations and Results

To verify the proposed model, FEA of the PMSM is performed using Ansys-Maxwell. Four different cases including healthy condition, single ITSC fault in phase-a, simultaneous ITSC faults in phase-b and phase-c, and simultaneous ITSC faults in phase-a, phase-b and phase-c are tested to check the accuracy of the proposed model. Output torque, angular speed, three-phase currents, and fault currents characteristics are obtained. Although the proposed model is based on the three-phase currents and three-phase voltages monitoring, other output characteristics including torque and speed are demonstrated just for comparison. For analyzing incipient faults, the fault resistances are considered to be $R_{af,bf,cf} = 0.1\Omega$. Because the ITSC starts with a high degraded path resistance and as the fault grows the degraded path resistance value approaches zero. Further, to eliminate the effects of the drive system and switching noise on the performance of the motor, it is assumed that the motor is fed by a three-phase sinusoidal voltage source.

Fig. B.3 shows the comparison of motor's torque and speed obtained from the proposed model and FEA. It can be seen that even though a bit deviation in the transient part, the produced torque and speed from the proposed model match well those from FEA in. It is worth mentioning that the slot-effect was not investigated in the proposed model and that is the reason of the major difference in the proposed model and FEA results. However, this can be neglected as the produced results are close to the average values of FEA in the steady state. Fig. B.4 shows the comparison of motor's three-phase currents obtained from the proposed model and FEA. Since there is not any faults in the motor, the proposed model three-phase currents match those obtained from FEA.

Fig. B.5 shows the comparison of motor's torque and speed when the motor is experiencing one single ITSC fault in phase-a with 31 shorted turns (out of 71 total turns) and therefore, $\mu_a = 0.4366$, $\mu_b = 0$, and $\mu_c = 0$. It can be seen that ITSC fault creates some distortions in both torque and speed characteristics compared to the healthy condition.

Fig. B.6 shows the comparison of motor's three-phase currents obtained from the proposed model and FEA in this faulty scenario. The ITSC fault in phase-a has caused the phase-a current to be higher than two other phase currents. Fig. B.7 shows the

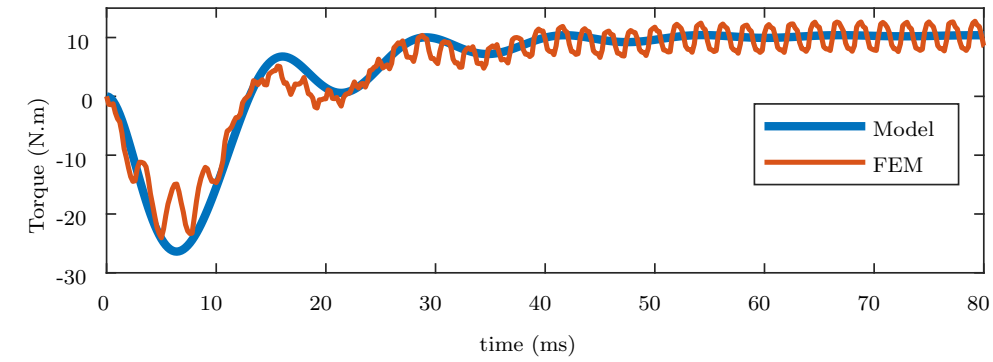

(a)

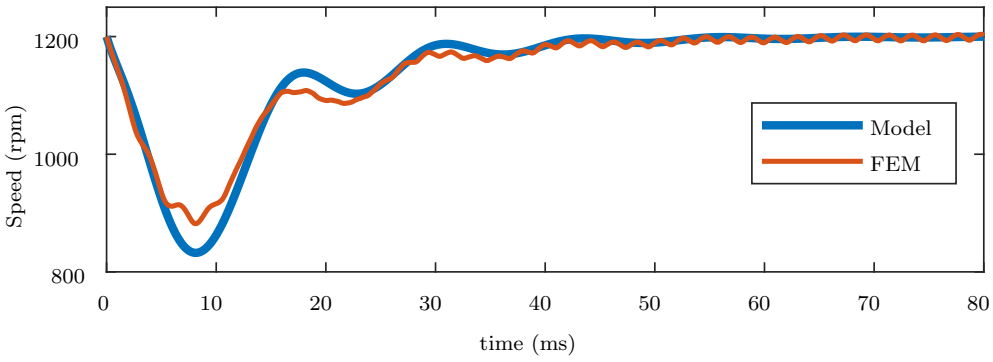

(b)

Figure B.3: (a) Output torque, (b) Motor speed, under healthy condition

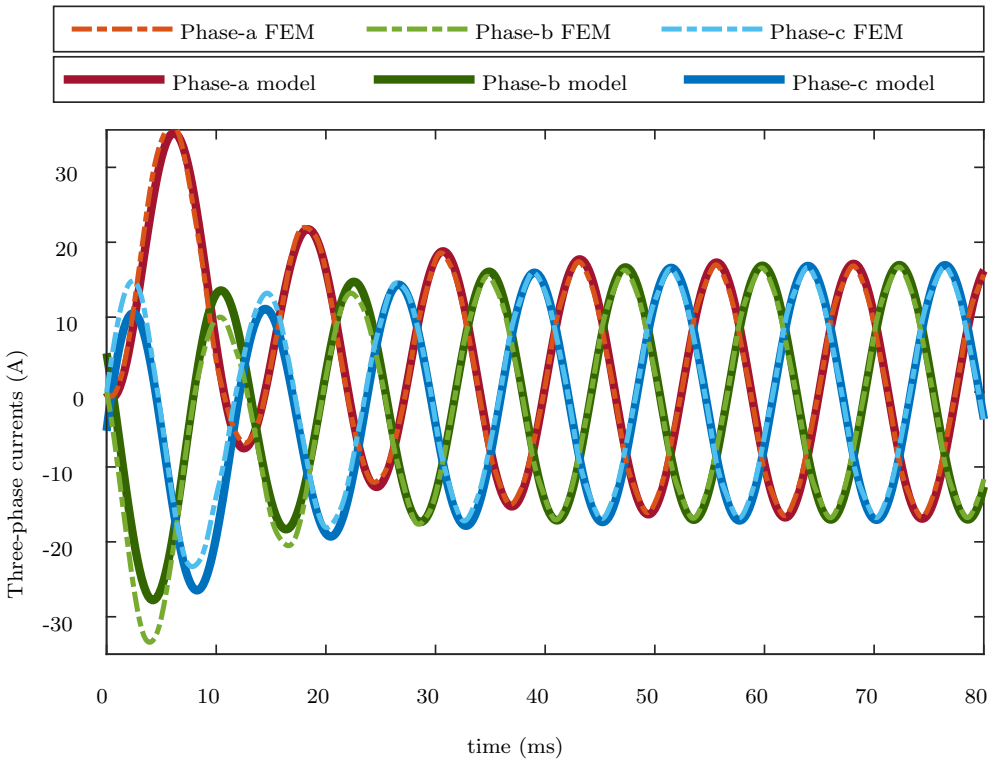

Figure B.4: Three-phase currents under healthy condition

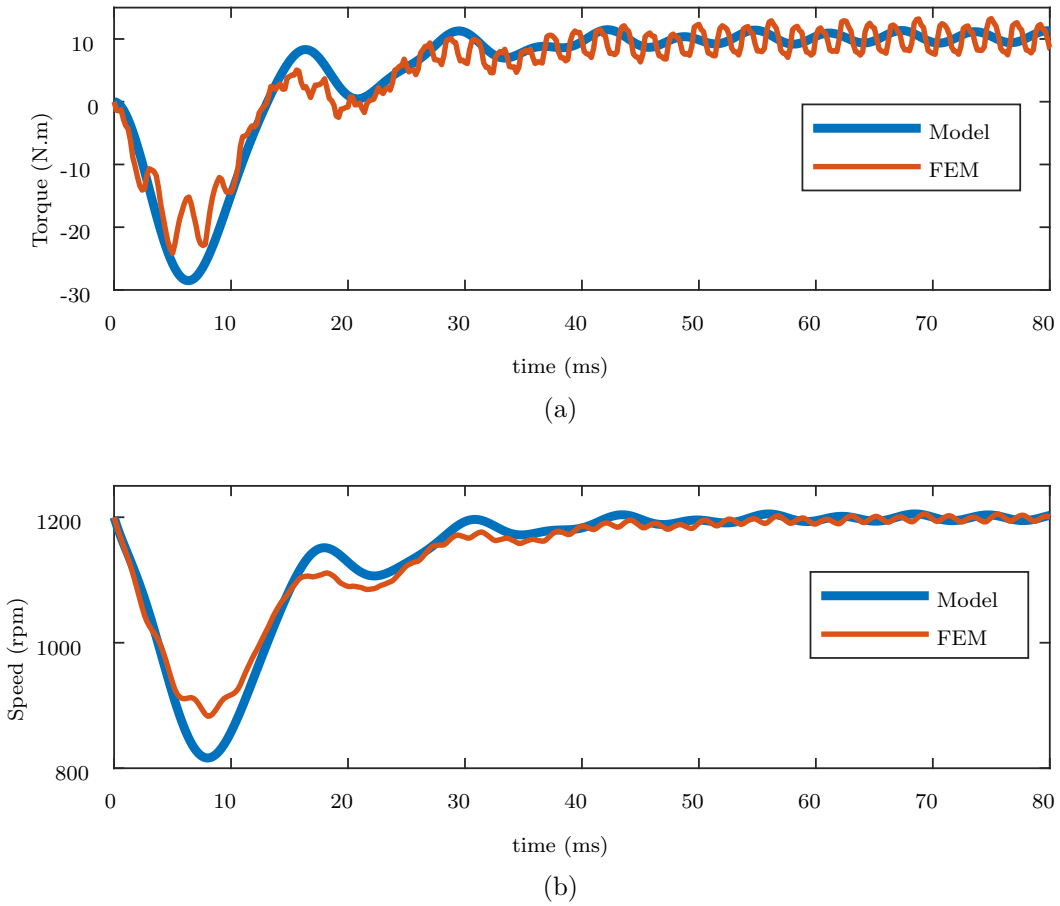

Figure B.5: (a) Output torque, (b) Motor speed, under $\mu_a = 0.4366$

comparison of motor's fault currents obtained from the proposed model and FEA. In this case, phase-b and phase-c fault currents are zero since there is not any faulty parts in these windings, but phase-a contains a fault current circulating in the faulty part of its winding.

Figs. B.8 shows the comparison of motor's torque and speed when the motor is operating under two simultaneous ITSC faults in phase-b with 40 shorted turns and phase-c with 20 shorted turns (out of 71 total turns) and therefore, $\mu_a = 0$, $\mu_b = 0.5634$, and $\mu_c = 0.2617$. The distortions in torque and speed characteristics are also present in this case due to unbalance caused by two faulty coils.

Fig. B.9 shows the comparison of motor's three-phase currents obtained from the proposed model and FEA in this case. The ITSC faults in phase-b and phase-c have caused the currents to be higher than phase-a current. Fig. B.10 shows the comparison of motor's fault currents obtained from the proposed model and FEA. In this case, phase-a fault current is zero since there is not any shorted turns in this windings, but phase-b and phase-c contain fault currents circulating in the faulty part of their windings.

Fig. B.11 shows the comparison of motor's torque and speed when the motor is experiencing three simultaneous ITSC faults in phase-a with 31 shorted turns, phase-b with 40 shorted turns, and phase-c with 20 shorted turns (out of 71 total turns) or $\mu_a = 0.4366$, $\mu_b = 0.5634$, and $\mu_c = 0.2617$. The level of distortions in both torque and speed charac-

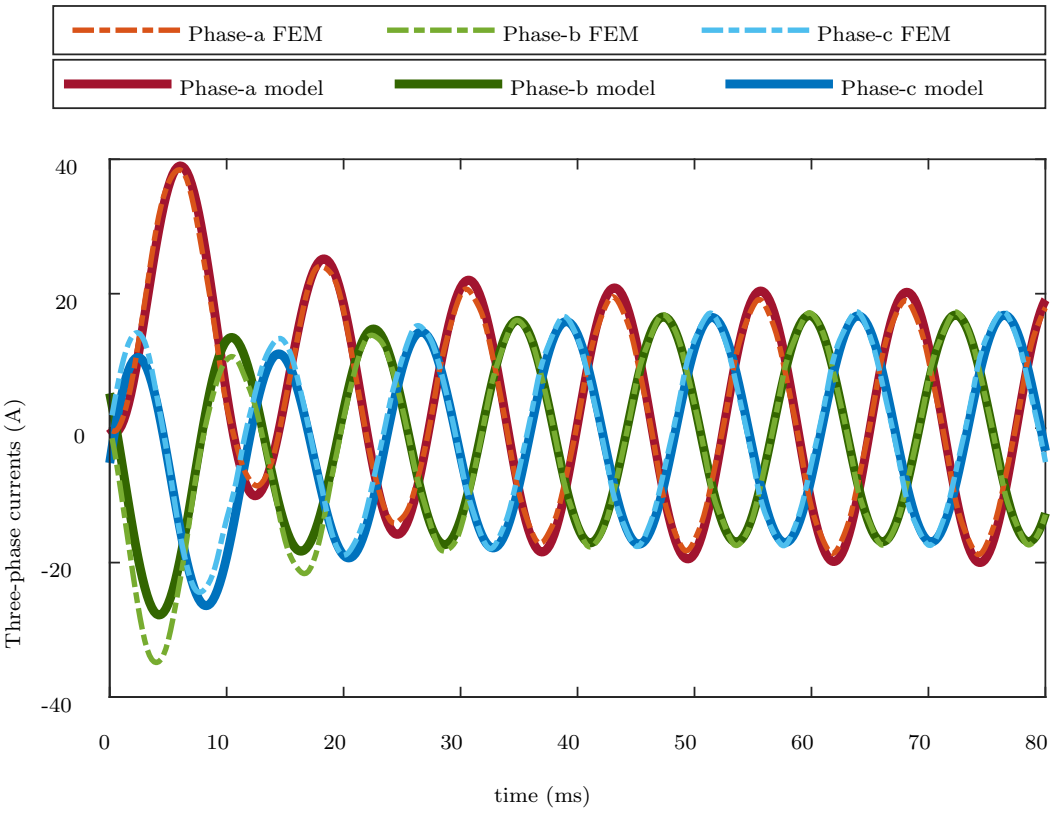

Figure B.6: Three-phase currents under $\mu_a = 0.4366$

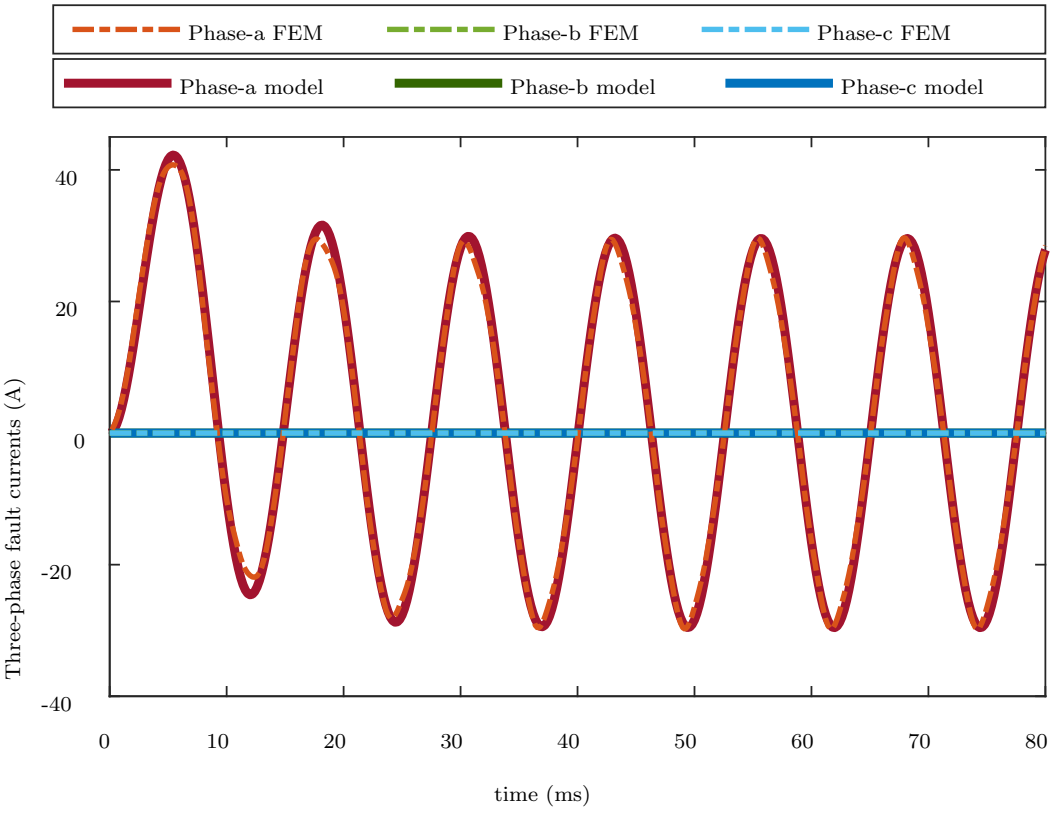

Figure B.7: Three-phase fault currents under $\mu_a = 0.4366$

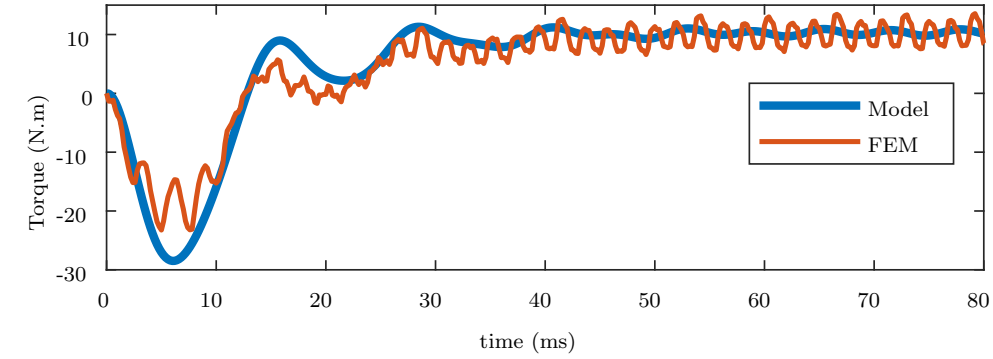

(a)

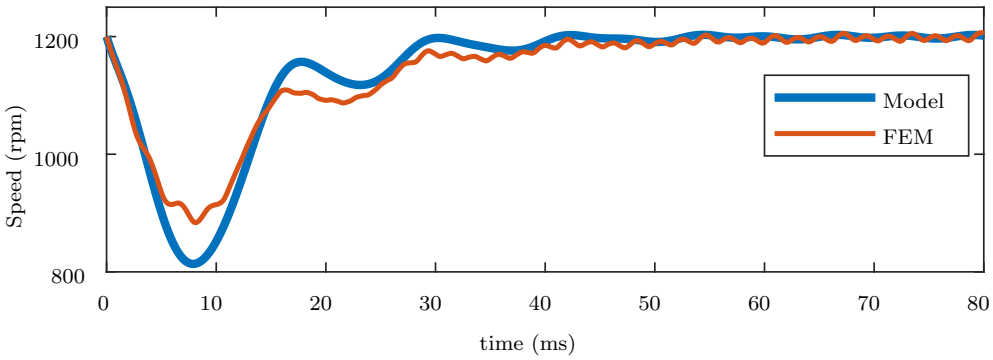

(b)

Figure B.8: (a) Output torque, (b) Motor speed, under $\mu_b = 0.5634$, and $\mu_c = 0.2617$

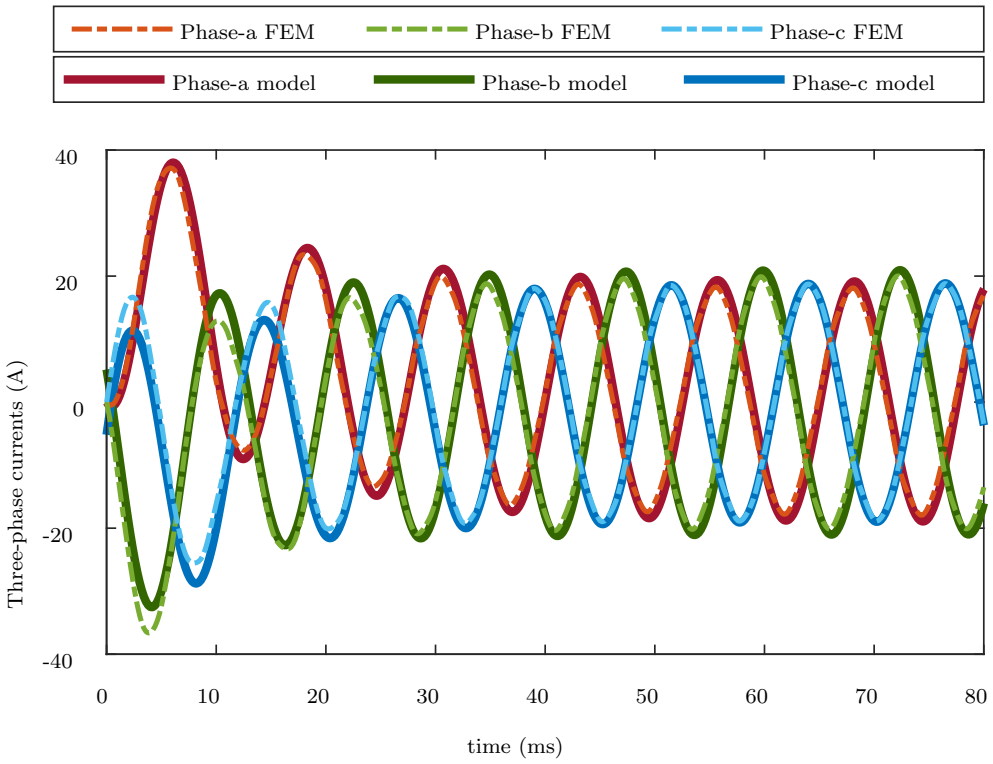

Figure B.9: Three-phase currents under $\mu_b = 0.5634$, and $\mu_c = 0.2617$

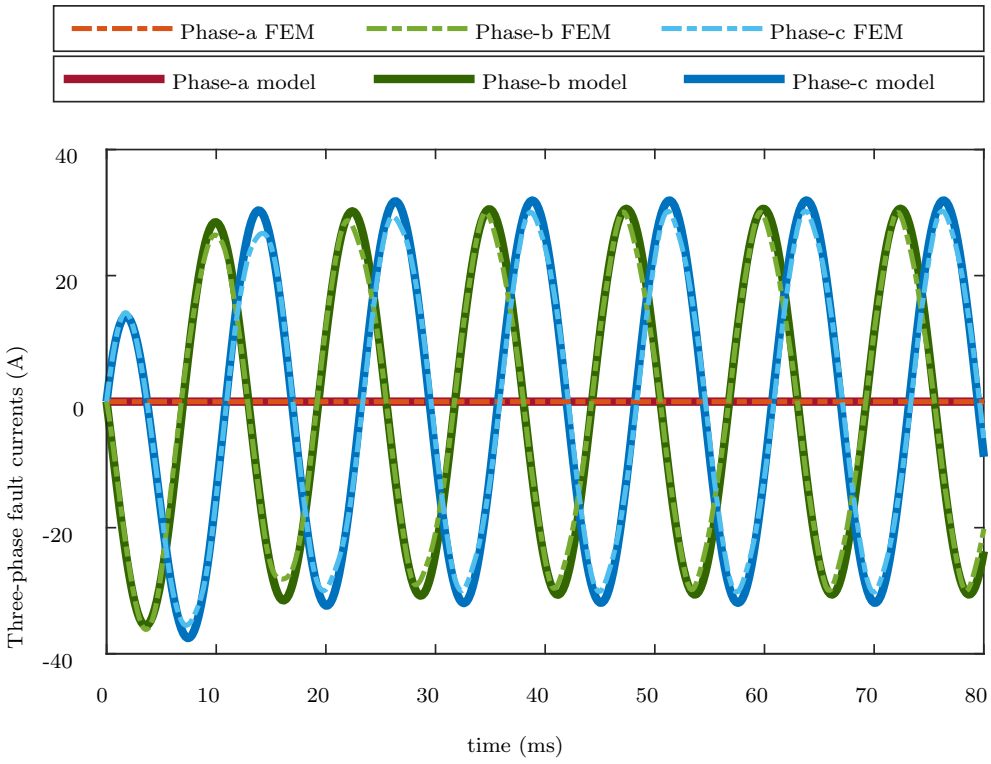

Figure B.10: Three-phase fault currents under $\mu_b = 0.5634$, and $\mu_c = 0.2617$

teristics are a bit decreased in this case compared to previous cases due to balance created by three faulty coils or three-phase fault currents.

Fig. B.12 shows the comparison of motor's three-phase currents obtained from the proposed model and FEA in this case. The ITSC faults in each phase have caused the currents to be higher compared to the healthy condition. Fig. B.13 shows the comparison of motor's fault currents obtained from the proposed model and FEA. In this case, all phases contain fault currents circulating in the faulty part of their windings. Similar to previous cases, there is an acceptable agreement between the proposed model and FEA results in the steady state although there are errors in the transient parts. Moreover, the cross-effects of simultaneous faults are well defined in the proposed model, which allow the model results to match the FEM results.

Fig. B.14 shows the comparison of motor's steady-state torque characteristics in different fault scenarios. It is obvious that motor's behavior is different under each case and this is majorly caused by different amplitudes and phases of current signals in each scenario. In addition, a single ITSC fault (case-1) creates more unbalance compared to two simultaneous ITSC faults (case-2) or three simultaneous ITSC faults (case-3), due to the higher generated negative sequence. This comparison also helps to understand the level of severity and potential damage that each case may have to the motor based on the mechanical stress caused by electromagnetic torque.

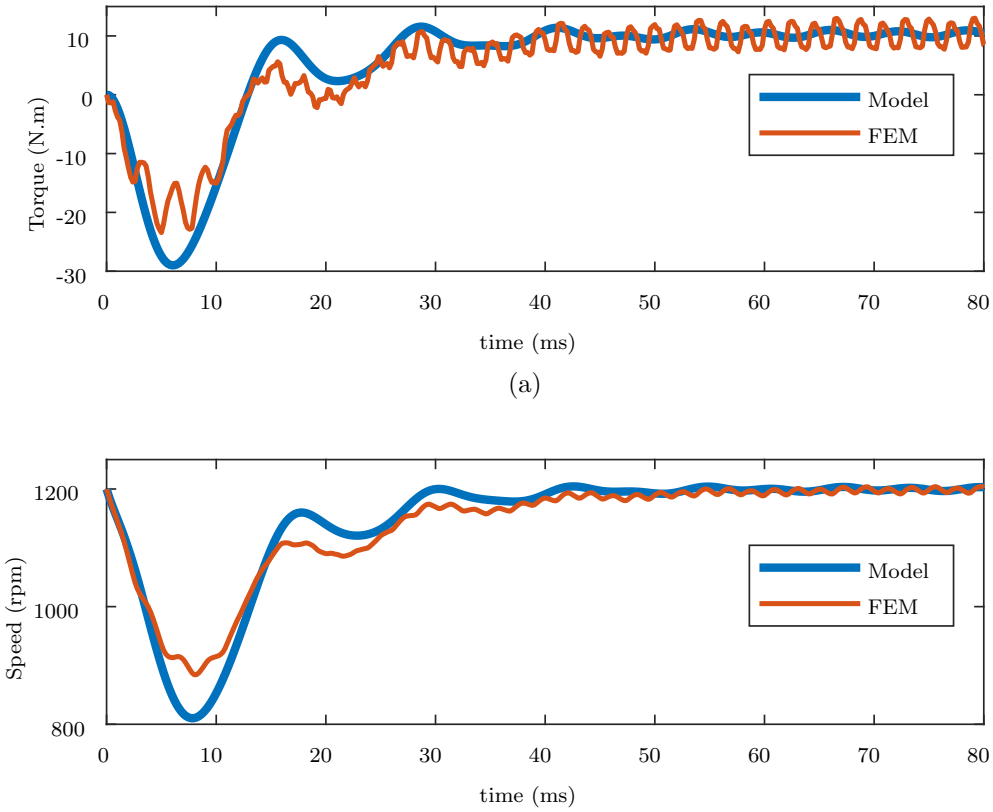

Figure B.11: (a) Output torque, (b) Motor speed, under $\mu_a = 0.4366$, $\mu_b = 0.5634$, and $\mu_c = 0.2617$

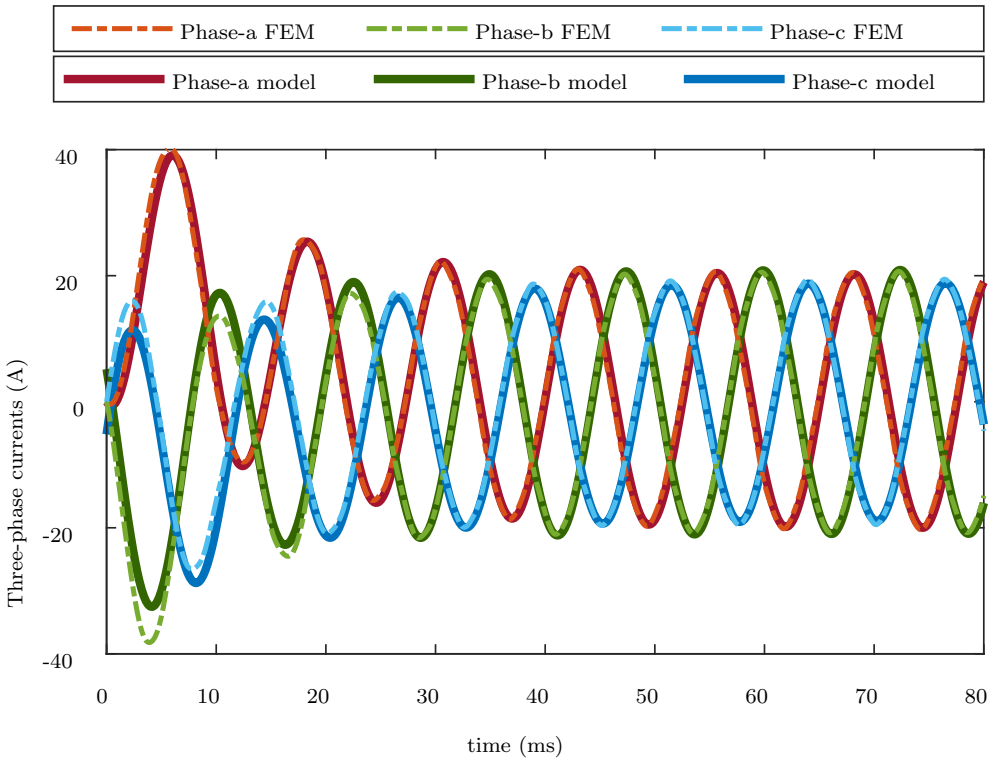

Figure B.12: Three-phase currents under $\mu_a = 0.4366$, $\mu_b = 0.5634$, and $\mu_c = 0.2617$

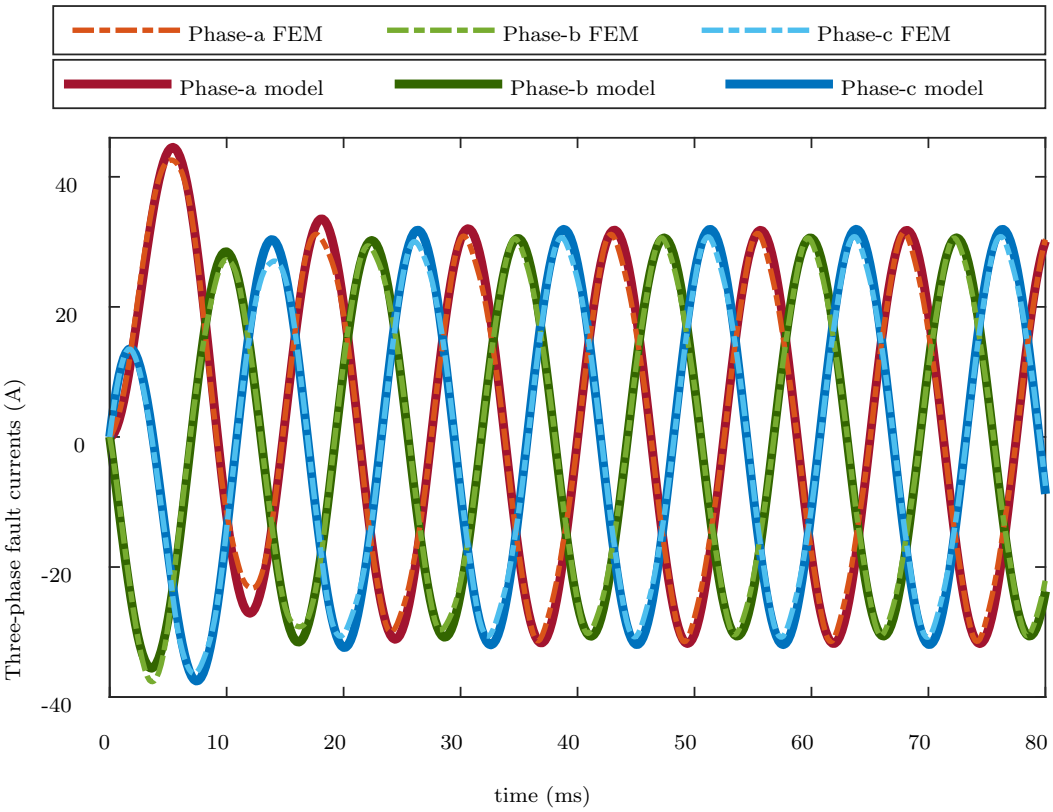

Figure B.13: Three-phase fault currents under $\mu_a = 0.4366$, $\mu_b = 0.5634$, and $\mu_c = 0.2617$

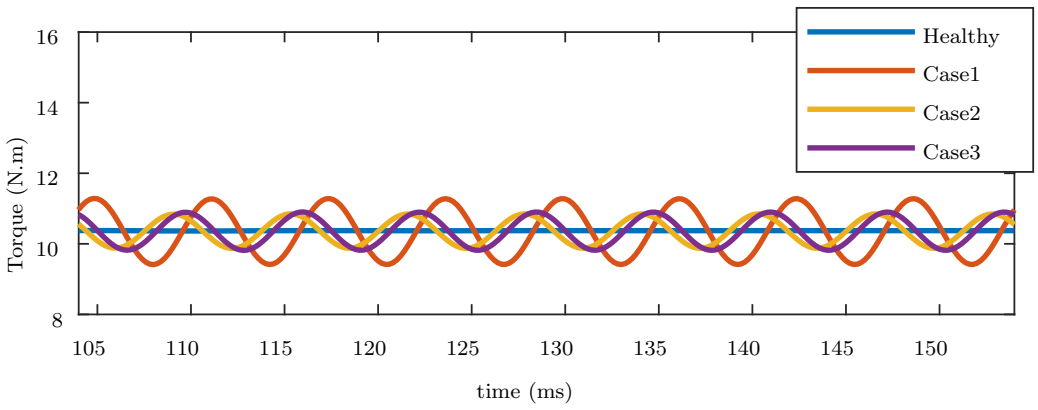

Figure B.14: Comparison of output torque in different cases.

B.4 Conclusion

In this paper, we presented a detailed modeling of ITSC faults in the PMSM. To accomplish this, a fault model was developed to obtain deformed fluxes based on inductance variations, which are caused by cross flux linkages depending on the distribution of the coils in the same phase winding. In addition, the cross-effect of fault currents in different phases was modeled, enabling the model to model not only single faults, but also simultaneous ITSC faults in any of the phases. The fault model requires only three-phase currents, three-phase voltages, and parameters of the motor as input. A time-stepping FEA was implemented to validate the results obtained from the proposed faulty PMSM model. Unlike FEA, the presented dynamic model can well and quickly model the behaviour of PMSM under different fault scenarios, without using detailed dimensions or material information. This allows developing fault indicators or detection methods in future studies.

References

[1] Seungdeog Choi, Moinul Shahidul Haque, Md Tawhid Bin Tarek, Vamsi Mulpuri, Yao Duan, Sanjoy Das, Vijay Garg, Dan M Ionel, M Abul Masrur, Behrooz Mirafzal, et al. Fault diagnosis techniques for permanent magnet ac machine and drives—a review of current state of the art. *IEEE Transactions on Transportation Electrification*, 4(2):444–463, 2018.

[2] Seokbae Moon, Hyeyun Jeong, Hojin Lee, and Sang Woo Kim. Interturn short fault diagnosis in a pmsm by voltage and current residual analysis with the faulty winding model. *IEEE Transactions on Energy Conversion*, 33(1):190–198, 2017.

[3] Richard T Meyer, Raymond A DeCarlo, Scott C Johnson, and Steve Pekarek. Short-circuit fault detection observer design in a pmsm. *IEEE Transactions on Aerospace and Electronic Systems*, 54(6):3004–3017, 2018.

[4] Bashir Mahdi Ebrahimi, Mehrsan Javan Roshtkhari, Jawad Faiz, and Seyed Vahid Khatami. Advanced eccentricity fault recognition in permanent magnet synchronous motors using stator current signature analysis. *IEEE Transactions on Industrial Electronics*, 61(4):2041–2052, 2013.

[5] Mohamed A Awadallah, Medhat M Morcos, Suresh Gopalakrishnan, and Thomas W Nehl. Detection of stator short circuits in vsi-fed brushless dc motors using wavelet transform. *IEEE Transactions on Energy Conversion*, 21(1):1–8, 2006.

[6] Sergio MA Cruz and AJ Marques Cardoso. Multiple reference frames theory: A new method for the diagnosis of stator faults in three-phase induction motors. *IEEE Transactions on Energy Conversion*, 20(3):611–619, 2005.

[7] Babak Vaseghi, Babak Nahid-Mobarakh, Noureddine Takorabet, and Farid Meibody-Tabar. Inductance identification and study of pm motor with winding turn short circuit fault. *IEEE Transactions on Magnetics*, 47(5):978–981, 2011.

[8] Bashir Mahdi Ebrahimi and Jawad Faiz. Feature extraction for short-circuit fault detection in permanent-magnet synchronous motors using stator-current monitoring. *IEEE Transactions on Power Electronics*, 25(10):2673–2682, 2010.

[9] Jeevanand Seshadrinath, Bhim Singh, and Bijaya Ketan Panigrahi. Investigation of vibration signatures for multiple fault diagnosis in variable frequency drives using complex wavelets. *IEEE Transactions on Power Electronics*, 29(2):936–945, 2013.

[10] Brice Aubert, Jeremi Regnier, Stephane Caux, and Dominique Alejo. Kalman-filter-based indicator for online interturn short circuits detection in permanent-magnet synchronous generators. *IEEE Transactions on Industrial Electronics*, 62(3):1921–1930, 2014.

[11] Yaw Nyanteh, Chris Edrington, Sanjeev Srivastava, and David Cartes. Application of artificial intelligence to real-time fault detection in permanent-magnet synchronous machines. *IEEE Transactions on Industry Applications*, 49(3):1205–1214, 2013.

[12] K-H Kim, D-U Choi, B-G Gu, and I-S Jung. Fault model and performance evaluation of an inverter-fed permanent magnet synchronous motor under winding shorted turn and inverter switch open. *IET Electric Power Applications*, 4(4):214–225, 2010.

[13] Arun Gandhi, Timothy Corrigan, and Leila Parsa. Recent advances in modeling and online detection of stator interturn faults in electrical motors. *IEEE Transactions on Industrial Electronics*, 58(5):1564–1575, 2010.

[14] Ilsu Jeong, Byong Jo Hyon, and Kwanghee Nam. Dynamic modeling and control for spmsms with internal turn short fault. *IEEE Transactions on Power Electronics*, 28(7):3495–3508, 2012.

[15] Bon-Gwan Gu, Jun-Hyuk Choi, and In-Soung Jung. Development and analysis of interturn short fault model of pmsms with series and parallel winding connections. *IEEE Transactions on Power Electronics*, 29(4):2016–2026, 2013.

[16] Jewon Lee, Yong-Ju Jeon, Doo-chul Choi, SeungHun Kim, and Sang Woo Kim. Demagnetization fault diagnosis method for pmsm of electric vehicle. In *IECON 2013-39th Annual Conference of the IEEE Industrial Electronics Society*, pages 2709–2713. IEEE, 2013.

Paper C

Detection and Discrimination of Inter-Turn Short Circuit and Demagnetization Faults in PMSMs Based on Structural Analysis

Saeed Hasan Ebrahimi, Martin Choux, and Van Khang Huynh

This paper has been submitted as:

S. H. Ebrahimi, M. Choux, and V. K. Huynh. Detection and Discrimination of Inter-Turn Short Circuit and Demagnetization Faults in PMSMs Based on Structural Analysis. In *Proceedings of 2021 22nd IEEE International Conference on Industrial Technology (ICIT)*, 2021. ISBN: 978-1-7281-5731-3.

Detection and Discrimination of Inter-Turn Short Circuit and Demagnetization Faults in PMSMs Based on Structural Analysis

Saeed Hasan Ebrahimi, Martin Choux, and Van Khang Huynh

Department of Engineering Sciences
University of Agder
NO-4879 Grimstad, Norway

Abstract – This paper presents a fault diagnosis method based on structural analysis of permanent magnet synchronous motors (PMSMs), focusing on detecting and discriminating two of the most common faults in PMSMs, namely demagnetization and inter-turn short circuit faults. The structural analysis technique uses the dynamic mathematical model of the PMSM in matrix form to evaluate the system's structural model. After obtaining the analytical redundancy using the over-determined part of the system, it is divided into redundant testable sub-models. Four structured residuals are designed to detect and isolate the investigated faults, which are applied to the system in different time intervals. Finally, the proposed diagnostic approach is numerically verified through a simulation of an inverter-fed PMSM and white Gaussian noise are added to the measured signals from the motor to verify its diagnosis performances.

C.1 Introduction

Nowadays, Permanent Magnet Synchronous Motors (PMSMs) are widely used in different industrial applications owing to their merits of efficiency, power density, and ease of control [1, 2]. The PMSMs in power-trains normally work in harsh working conditions and exposed to various electrical, mechanical, and thermal stresses [3, 4]. These stresses may eventually degrade the insulator in the stator winding, resulting in an inter-turn short circuit (ITSC) fault, or cause the demagnetisation of permanents magnets (PMs) mounted on the rotor assembly [5]. Since ITSC fault involves very few turns, it generates excessive heat, which may result in first efficiency reduction and later in a catastrophic system breakdown if not being diagnosed in time [6]. In addition, PMs used in PMSMs are considered to be not only the most expensive material, but also very sensitive to the stresses [7]. Monitoring and detection of demagnetization in early stages is therefore important in preventing costly down-times and high maintenance costs [8].

Various approaches have been employed to detect ITSC and demagnetization faults in PMSMs. [9, 10] have implemented a signal-based method to investigate the behavior of ITSC and demagnetization faults by monitoring the vibration and temperature in a PMSM. [11, 12] have used data-driven models to detect and classify ITSC and demagnetization faults in a PMSM by using Neural Network. The signal-based and data-driven techniques can effectively detect the faulty case, but they require either advanced sensors or a lot of data for training, without a clear explanation based on physical models. Alter-

natively, model-based methods are widely employed in the literature [13–15] among which Finite-Element Method (FEM) based models are most recommended due to high analysis accuracy, but they require a deep knowledge of the system, e.g. detailed dimensions and material characteristics [1]. Furthermore, FEM-based models are computational-heavy and are challenging to use in real time. Structural analysis is hence proposed as an alternative solution for detection and isolation of various faults in a complex system, without a prior deep knowledge of the system dynamics [16]. The theory of structural analysis technique has been well developed in the literature [17, 18] and been applied from automotive engine [19], hybrid vehicle [20], to electric drive [16] systems. However, ITSC and demagnetization fault detection and isolation (FDI) for PMSMs is not present in the above-mentioned studies. Investigating sensor faults along with ITSC and demagnetization faults can be challenging especially when it comes to isolation of the sensor faults from ITSC faults since they both add the same fault terms to voltage equations, therefore, sensor measurements are considered not to have any offsets (only noise) and only ITSC and demagnetization faults are studied in this paper.

This paper presents a systematic FDI methodology based on structural analysis for specific investigation of ITSC and demagnetization faults in a PMSM. To accomplish this, a healthy dynamic mathematical model of PMSM in *abc* frame is employed, and specific terms relevant to the presence of ITSC and demagnetization faults are added to the corresponding equations. These added terms include the deviations in the resistance and inductance of the stator winding caused by ITSC fault, and the deviations in the PM linkage flux caused by a demagnetization fault, appearing in the three-phase flux and voltage equations. Further, the analytical redundancy of the model is determined based on the PMSM's structural model. The system is subdivided into smaller over-determined subsystems, in which the faults are detected, and discriminated and four sequential residuals are designed to show the presence of each fault. Eventually, the proposed model is implemented in Matlab/Simulink to verify its effectiveness in different faulty cases with presence of white Gaussian noise in the measured signals.

C.2 Structural Analysis for PMSM under Demagnetization and ITSC Faults

Structural analysis is a model-based technique that can be used in FDI to extract the analytic redundant relations (ARRs) of a system from the mathematical equations describing its dynamic [21, 22]. The structural model is represented by an incidence matrix, in which each row connects an equation to the corresponding unknown variables, known variables, and faults. The analytic redundancy of the system is then obtained through rearranging the rows and columns in a way to form a diagonal structure which is called Dulmage–Mendelsohn (DM) decomposition. From the analytic redundant part of this structure, several smaller over-constrained subsystems can be identified yielding a set of ARRs. Depending on its signature on this set of ARRs, each considered fault might be detected or even discriminated. Subsequently, a few diagnostic tests are designed to inform about the presence of each fault. Here, a structural analysis of a PMSM containing

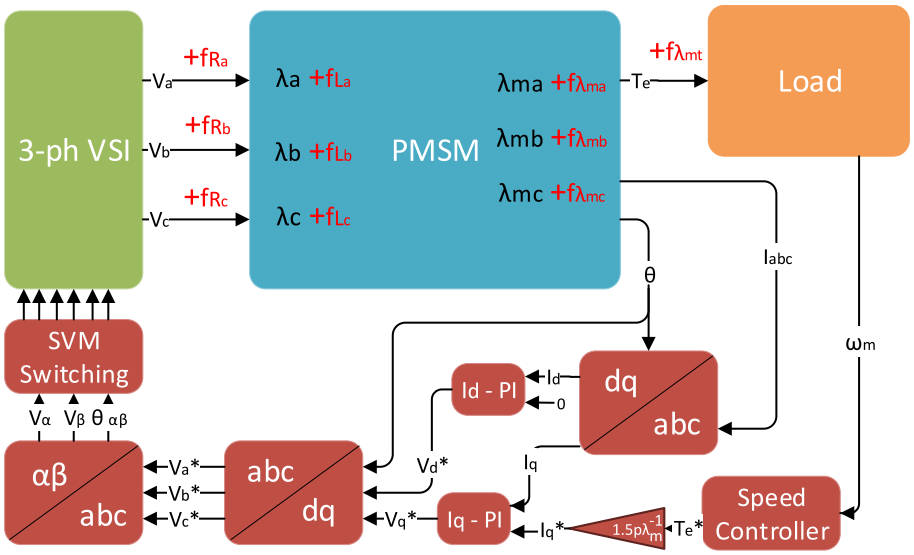

Figure C.1: Modeling diagram of PMSM and drive system.

ITSC and demagnetization faults is presented, and diagnostic tests are proposed for their detection and isolation. Fig. C.1 shows the modeling diagram of faulty PMSM and the drive system components where the parameters are defined below.

C.2.1 PMSM Mathematical Model

The mathematical model of a PMSM with ITSC and demagnetization faults is given by equations $e_1 - e_{12}$ as shown in Eq. (C.1), where v_a, v_b, and v_c are the three phase voltages; i_a, i_b, and i_c are the three phase currents; λ_a, λ_b, and λ_c are the three phase stator flux; λ_{ma}, λ_{mb}, and λ_{mc} are the flux established by PMs in each phase; T_e is the electromagnetic torque, T_L is the Load torque; ω_m is the shaft's angular speed; θ is the electric angular position; R_a, R_b, and R_c are the stator phase resistances and L_a, L_b, and L_c are the stator phase inductances; λ_m is the flux established by PMs; P is the number of poles; J is the rotor inertia, and b is the friction coefficient.

When an ITSC fault appears in one of the phases of motor winding, both resistance and inductance values of that phase is influenced. Here, f_{R_a} and f_{L_a} are added to the corresponding equations of the healthy PMSM to account for ITSC fault in phase-a. Similarly, f_{R_b}, f_{L_b}, f_{R_c}, and f_{L_c} terms are added to account for ITSC faults in phases b and c, respectively.

$$
\begin{aligned}
e1 : v_a &= R_a i_a + \frac{d\lambda_a}{dt} + f_{R_a} \\
e2 : v_b &= R_b i_b + \frac{d\lambda_b}{dt} + f_{R_b} \\
e3 : v_c &= R_c i_c + \frac{d\lambda_c}{dt} + f_{R_c}
\end{aligned}
$$

$$
\begin{aligned}
e4 :&\lambda_a = L_a i_a + \lambda_{ma} + f_{L_a} \\
e5 :&\lambda_b = L_b i_b + \lambda_{mb} + f_{L_b} \\
e6 :&\lambda_c = L_c i_c + \lambda_{mc} + f_{L_c} \\
e7 :&\lambda_{ma} = \lambda_m \sin\theta + f_{\lambda_{ma}} \\
e8 :&\lambda_{mb} = \lambda_m \sin\left(\theta - 2\pi/3\right) + f_{\lambda_{mb}} \\
e9 :&\lambda_{mc} = \lambda_m \sin\left(\theta + 2\pi/3\right) + f_{\lambda_{mc}} \\
e10 :&T_e = \frac{P}{2}\lambda_m [i_a \cos\theta + i_b \cos\left(\theta - 2\pi/3\right) \\
&\quad + i_c \cos\left(\theta + 2\pi/3\right)] + f_{\lambda_{mt}} \\
e11 :&\frac{d\omega_m}{dt} = \frac{1}{J}(T_e - b\omega_m - T_L) \\
e12 :&\frac{d\theta}{dt} = \frac{P}{2}\omega_m
\end{aligned}
\tag{C.1}
$$

Further, $f_{\lambda_{ma}}$, $f_{\lambda_{mb}}$, $f_{\lambda_{mc}}$, and $f_{\lambda_{mt}}$ terms are added to equations in case of the demagnetization fault. The known variables are the three-phase voltages and the measurements of currents and angular speed, i.e., y_{v_a}, y_{v_b}, y_{v_c}, y_{i_a}, y_{i_b}, y_{i_c}, and y_{ω_m}, shown in Eq. (C.2).

$$
\begin{aligned}
&m1 : y_{v_a} = v_a, m2 : y_{v_b} = v_b, m3 : y_{v_c} = v_c \\
&m4 : y_{i_a} = i_a, m5 : y_{i_b} = i_b, m6 : y_{i_c} = i_c \\
&m7 : y_{\omega_m} = \omega_m
\end{aligned}
\tag{C.2}
$$

In addition, the mathematical model includes five differential constraints of unknown variables, which are shown in Eq. (C.3).

$$
\begin{aligned}
d1 :&\frac{d\lambda_a}{dt} = \frac{d}{dt}(\lambda_a) \\
d2 :&\frac{d\lambda_b}{dt} = \frac{d}{dt}(\lambda_b) \\
d3 :&\frac{d\lambda_c}{dt} = \frac{d}{dt}(\lambda_c) \\
d4 :&\frac{d\omega_m}{dt} = \frac{d}{dt}(\omega_m) \\
d5 :&\frac{d\theta}{dt} = \frac{d}{dt}(\theta)
\end{aligned}
\tag{C.3}
$$

C.2.2 Structural Model and Analytical Redundancy of the PMSM

The structural model of PMSM with ITSC and demagnetization faults is obtained based on the defined mathematical model in Eqs. (C.1)-(C.3), as shown in Fig. C.2. The incidence matrix contains 24 rows, representing the 12 defined equations in Eq. (C.1), 7 measured known variables in Eq. (C.2), and the 5 differential constraints of unknown variables as shown in Eq. (C.3). The columns of the matrix is subdivided into three groups of unknown variables, known variables, and faults, and each equation is connected to its relevant constraint in any of the three groups through each row. In order to be able to detect and then isolate a fault, it should lie in the structurally over-determined part of

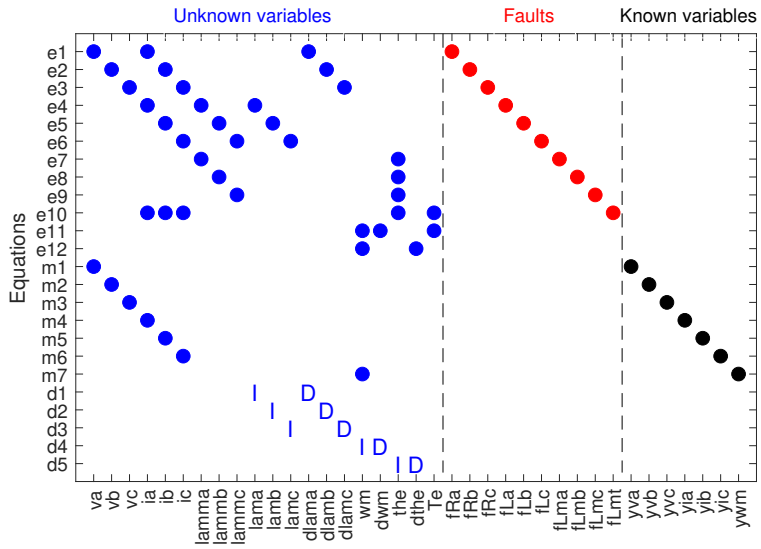

Figure C.2: PMSM structural model.

the model, where there are more equations than unknown variables [18]. To accomplish this, the redundancies of the model are first evaluated by employing DM decomposition tool, which restructures the model into upper triangle shape by rearranging the rows and the columns of the incidence matrix. Fig. C.3 shows the DM decomposition for PMSM structural model, where the analytic redundant part is expressed in the upper left part containing all the faults.

C.3 Diagnostic Test Design

In this section, the procedure of designing diagnostic tests for ITSC and demagnetization faults is discussed. First, the analytic redundant part is divided into smaller redundant subsystems and then sequential residuals are derived to detect each fault.

C.3.1 Finding Testable Sub-Models

Using the algorithm proposed by [23], the system is subdivided into efficient redundant testable sub-models called Minimal Test Equation Supports (MTESs). MTES sets contain specific equations defined in Eq. (C.1), and are found in a way that the considered ITSC (in any of the phases) and demagnetization faults are detected and discriminated. Fig. C.4 shows all the MTES sets found for the considered system here, and Fig. C.5 shows the signature matrix of MTES sets, indicating which faults appear in each MTES. $MTES_1$ includes only $f_{\lambda_{mt}}$ fault term, meaning it can be used for detecting demagnetization fault. $MTES_2$ contains f_{R_c}, f_{L_c}, and $f_{\lambda_{mc}}$ fault terms, therefore, it can be used for detecting ITSC fault in phase c and demagnetization fault. Subsequently, $MTES_3$ can be used for detecting ITSC fault in phase b and demagnetization fault, and $MTES_4$ for detecting ITSC fault in phase a and demagnetization fault.

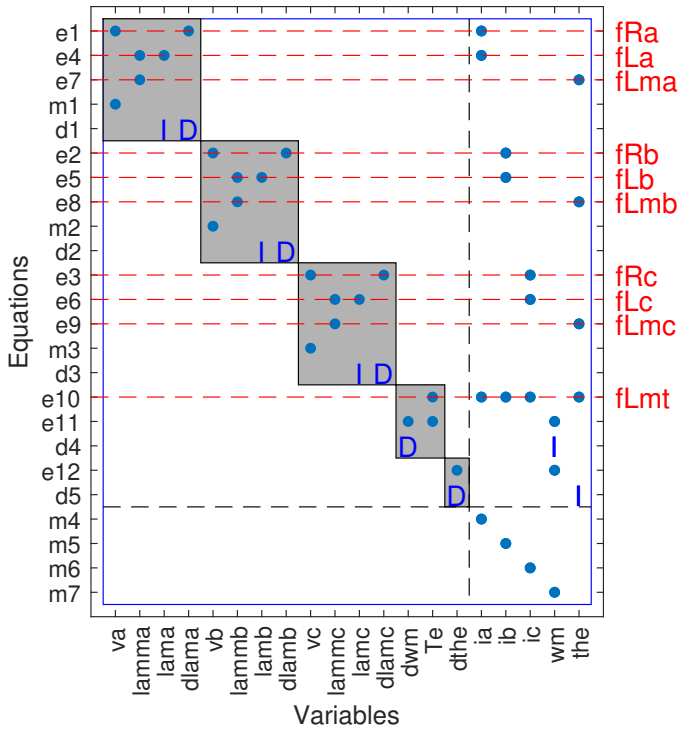

Figure C.3: DM decomposition for PMSM structural model.

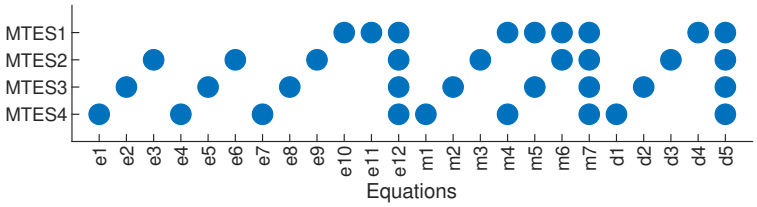

Figure C.4: MTES sets.

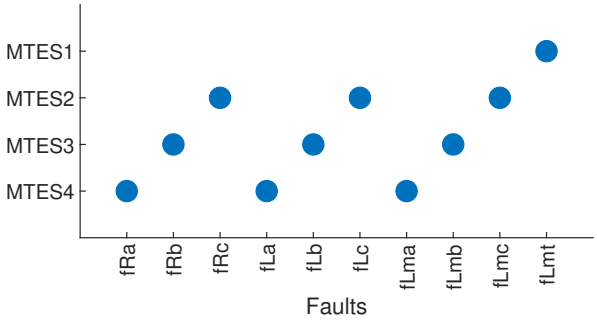

Figure C.5: Fault signature matrix of MTES sets.

C.3.2 Sequential Residuals for Detecting the Faults

In this section, four sequential residuals ($R_1 - R_4$) are derived based on the obtained MTES set. These residuals aim to detect and isolate ITSC fault in phase a, ITSC fault in phase b, ITSC fault in phase c, and demagnetization fault.

1. R_1: $MTES_4$ is used for deriving R_1 based on the difference between measured and calculated voltages of phase a:

$$m1 : R_1 = y_{v_a} - v_a \tag{C.4}$$

And the sequence of deriving v_a is as follows:

$$\begin{aligned} SV &: \theta = \theta_{state} \\ m7 &: y_{\omega_m} = \omega_m \\ e12 &: \frac{d\theta}{dt} = \frac{P}{2}\omega_m \\ e7 &: \lambda_{ma} = \lambda_m \sin\theta \\ m4 &: i_a = y_{i_a} \\ e4 &: \lambda_a = L_a i_a + \lambda_{ma} \\ d1 &: \frac{d\lambda_a}{dt} = \frac{d}{dt}(\lambda_a) \\ e1 &: v_a = R_a i_a + \frac{d\lambda_a}{dt} \end{aligned} \tag{C.5}$$

Where θ_{state} is the State Variables (SV) and will be updated after R_1 is calculated as follows:

$$d5 : \theta_{state} = \int d\theta \tag{C.6}$$

2. R_2 and R_3 follow the same procedure mentioned for R_1 to find the difference between measured and calculated phase b and phase c voltages based on $MTES_3$ and $MTES_2$, respectively.

3. R_4: $MTES_1$ is used for deriving R_4 based on difference between the measured and calculated angular speeds:

$$\begin{aligned} e10 : R_4 = T_e - \frac{P}{2}\lambda_m [i_a \cos\theta + i_b \cos(\theta - 2\pi/3) \\ + i_c \cos(\theta + 2\pi/3)] + f_{\lambda_{mt}} \end{aligned} \tag{C.7}$$

Table C.1: Parameters of PM Synchronous Motor

Symbol	Parameter	Value	Unit
V_{dc}	Rated dc bus voltage	320	V
I_s	Rated rms phase current	12.6	A
T_{out}	Output Torque	14	$N.m$
n_s	Rated speed	1200	rpm
R_s	Phase resistance	1.72	Ω
L_q, L_d	Q and D axes inductances	23.3948	mH
J	Rotor inertia	0.00161	$kg.m^2$
b	Rotor damping factor	0.002973	$N.m.s/rad$
λ_m	Flux linkage of PMs	0.1722	
n_s	Pole-pairs	4	

And the sequence of deriving T_e is as follows:

$$\begin{aligned} SV &: \theta = \theta_{state} \\ m7 &: R_4 = y_{\omega_m} - \omega_m \\ d4 &: \frac{d\omega_m}{dt} = \frac{d}{dt}(\omega_m) \\ e12 &: \frac{d\theta}{dt} = \frac{P}{2}\omega_m \\ e11 &: \frac{d\omega_m}{dt} = \frac{1}{J}(T_e - b\omega_m - T_L) \\ m4 &: i_a = y_{i_a}, m5 : i_b = y_{i_b}, m6 : i_c = y_{i_c} \end{aligned} \tag{C.8}$$

Where θ_{state} is the state variables and are updated after R_4 is calculated:

$$d5 : \theta_{state} = \int d\theta \tag{C.9}$$

C.4 Simulation and Results

To verify the proposed diagnostic method, a Matlab/Simulink model of a PMSM is implemented based on the model proposed in [24]. Using this model, demagnetization and ITSC faults in any of the three phases can be applied on the PMSM and motor signals under faulty condition can be obtained. The parameters of motor are listed in Table C.1. To test the residual responses under variable operating conditions, the reference for the motor drive's speed controller is set to be variable. Fig. C.6a shows the speed reference and the motor's speed and Fig. C.6b shows the output torque of the motor during the time of the simulation. As can be seen in Fig. C.6a, it takes time for the actual speed of the motor to catch the reference speed (which comes from the controller), since the motor is considered to be stationary in the beginning.

During the simulation, the ITSC and demagnetization faults are applied at different time intervals. At $t = 0.06 - 0.08s$, there appears an ITSC fault in phase a with 5%

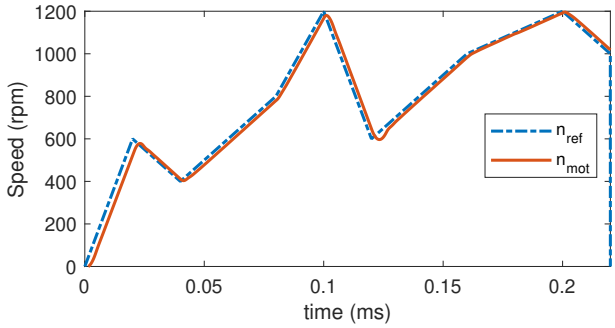

(a)

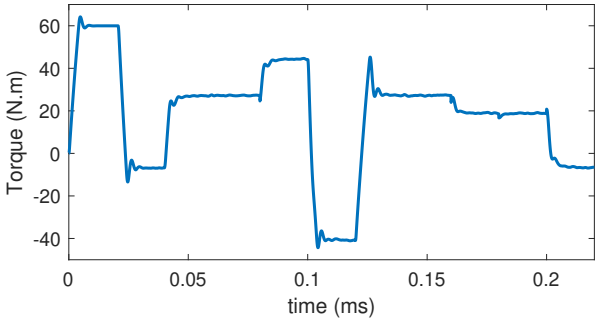

(b)

Figure C.6: Output characteristics of the motor (a) speed, (b) torque.

fault severity (number of shorted turns to total turns in one phase); at $t = 0.1 - 0.12s$, there is an ITSC fault in phase b with 5% fault severity; at $t = 0.14 - 0.16s$, the motor has an ITSC fault in phase c with 5% fault severity; and at $t = 0.18 - 0.2s$, appears a demagnetization fault with 10% fault severity (the flux linkage of PMs is decreased by 20%). To test the effectiveness of the residual responses, a band-limited Gaussian noise is added to the measured values (known variables) here. Without the noise, the residuals can be triggered by any small abnormality in the system and therefore, the diagnostic system can theoretically detect faults with very low severity (e.g. 0.1%) which is not plausible in reality. As mentioned before, the severity of ITSC faults in any of the phases and demagnetization fault are set to 5% and 10%, respectively. This threshold is low enough to be called early detection and yet not that low that the faults are not visible in the figures while having a rather strong noise present in the measurements. However, with a proper signal processing tool even smaller faults are detectable. In addition, Having the same ITSC fault severity in all the phases also enables us to see the difference in the residual responses while subject to the same criteria. This also means that higher fault levels are easily detectable using this method. The noise signal $w(t)$ is generated by a dynamic filter as follows [21]:

$$H(s) = \frac{\sqrt{2\beta}}{s+\beta}\sigma_\omega \tag{C.10}$$

The dynamic filter has the random signal $v(t)$ as input and $w(t)$ as output. The signal $v(t)$ has intensity equal to 1, which indicates the noise has a total power equal to 1. Based on the data from our previous experimental studies and measurements, parameters

Table C.2: Parameters of Noise Signals

Symbol	Parameter	Value
σ_i	Variance and of noise added to currents	0.1583
β_i	Constant of noise added to currents	$100,000$
σ_v	Variance of noise added to voltages	0.2
β_v	Constant of noise added to voltages	10
σ_ω	Variance of noise added to angular speed	0.1
β_ω	Constant of noise added to angular speed	10

of different noise signals are extracted. These parameters which specify the noise added to currents, voltages, and angular speed signals of the motor are listed in Table C.2.

The residual responses for the mentioned faults are obtained and shown in Fig. C.7 (a)–(d). Before the faults are applied, the motor is operating in healthy mode ($t = 0 - 0.06s$) and all the residuals remain zero (neglecting the noise) since there is not any difference between the measured signals and the calculated ones used in each residual. When the ITSC fault in phase a is applied, only R_1 is affected and obtains a non-zero value. Since ITSC fault in phase a (faults in f_{R_a}, f_{L_a}) is only observable in R_1 (derived from $MTES_4$), other residuals remain zero when the motor is experiencing this fault. The same logic can be used for R_2 and R_3 as they obtain non-zero values and only these two residuals are affected when ITSC faults in phase-b and phase-c are applied to the motor. Between $t = 0 - 0.06s$ and when the demagnetization fault is applied on the motor, all the residuals obtain a non-zero value. The behavior and response of the residuals during each fault, can be used as the ground for detecting and discriminating of the mentioned faults in the PMSM.

To isolate the faults based on the response of the residuals, a decision-making system is proposed based on logical blocks and added to the diagnostic system. To detect and isolate ITSC fault in phase a, R_1 should be non-zero while other residuals remain zero. For ITSC fault in phase b, R_2 should be non-zero while other residuals remain zero. For detection and isolation of ITSC in phase c, R_3 should be non-zero while other residuals remain zero. When all the four residuals have a non-zero value, it means that the motor is experiencing a demagnetization fault. Fig. C.8 shows the output signal of the decision-making system.

C.5 Conclusion

In this paper, we presented a novel method to detect ITSC and demagnetization faults in the PMSM. Structural analysis is implemented on the mathematical model of the PMSM to detect and isolate the mentioned faults in the system. After obtaining the redundant part of the structural model by employing DM decomposition tool, the system is divided into redundant sub-models called minimal test equation support. Four sequential residuals

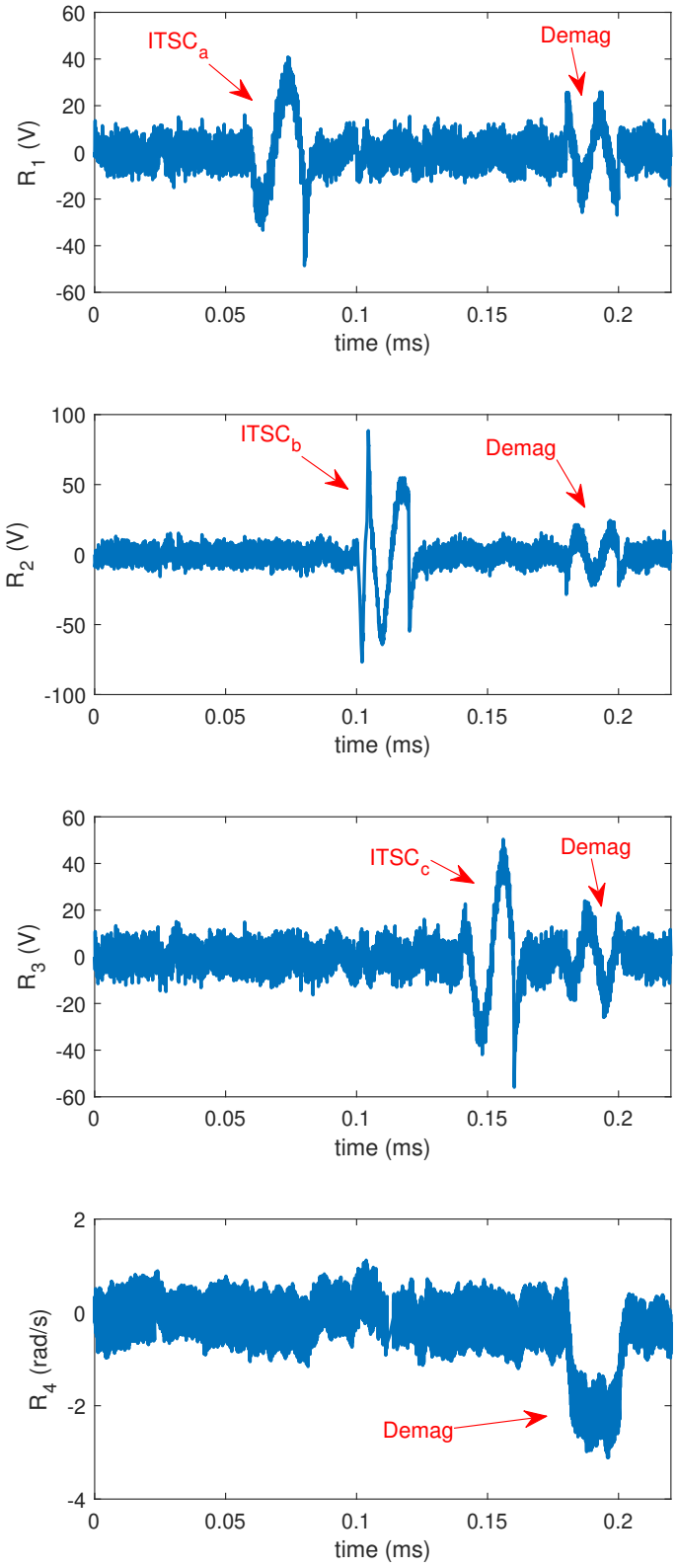

Figure C.7: Response of residuals.

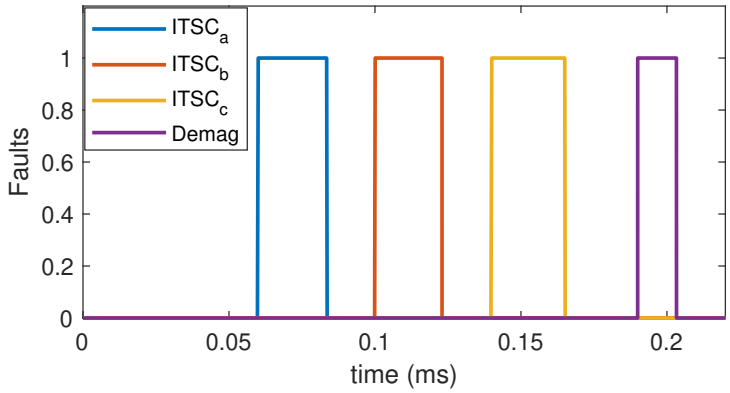

Figure C.8: Discrimination of ITSC and demagnetization faults.

are derived based on the fault terms that appear in each of the MTES sets to detect and isolate four faults in the system including ITSC in phase a, ITSC in phase b, ITSC in phase c, and demagnetization. The proposed model is implemented in Matlab/Simulink and the mentioned faults are applied to the system in different time intervals. The results show that residuals are able to efficiently detect and isolate even small faults in the presence of noise, proving the effectiveness of this diagnostic approach.

References

[1] Seungdeog Choi, Moinul Shahidul Haque, Md Tawhid Bin Tarek, Vamsi Mulpuri, Yao Duan, Sanjoy Das, Vijay Garg, Dan M Ionel, M Abul Masrur, Behrooz Mirafzal, et al. Fault diagnosis techniques for permanent magnet ac machine and drives—a review of current state of the art. *IEEE Transactions on Transportation Electrification*, 4(2):444–463, 2018.

[2] Subhasis Nandi, Hamid A Toliyat, and Xiaodong Li. Condition monitoring and fault diagnosis of electrical motors—a review. *IEEE Transactions on Energy Conversion*, 20(4):719–729, 2005.

[3] Yuan Qi, Emine Bostanci, Vigneshwaran Gurusamy, and Bilal Akin. A comprehensive analysis of short-circuit current behavior in pmsm interturn short-circuit faults. *IEEE Transactions on Power Electronics*, 33(12):10784–10793, 2018.

[4] Bon-Gwan Gu, Jun-Hyuk Choi, and In-Soung Jung. Development and analysis of interturn short fault model of pmsms with series and parallel winding connections. *IEEE Transactions on Power Electronics*, 29(4):2016–2026, 2013.

[5] Martin Riera Guasp, Jose A Antonino Daviu, and Gérard-André Capolino. Advances in electrical machine, power electronic, and drive condition monitoring and fault detection: state of the art. *IEEE Transactions on Industrial Electronics*, 62(3):1746–1759, 2014.

[6] Bo Wang, Jiabin Wang, Antonio Griffo, and Bhaskar Sen. Stator turn fault detection by second harmonic in instantaneous power for a triple-redundant fault-tolerant pm drive. *IEEE Transactions on Industrial Electronics*, 65(9):7279–7289, 2018.

[7] Ehsan Mazaheri-Tehrani, Jawad Faiz, Mohsen Zafarani, and Bilal Akin. A fast phase variable *abc* model of brushless pm motors under demagnetization faults. *IEEE Transactions on Industrial Electronics*, 66(7):5070–5080, 2018.

[8] Hongwen He, Nana Zhou, Jinquan Guo, Zheng Zhang, Bing Lu, and Chao Sun. Tolerance analysis of electrified vehicles on the motor demagnetization fault: From an energy perspective. *Applied Energy*, 227:239–248, 2018.

[9] Zhi Yang, Xiaodong Shi, and Mahesh Krishnamurthy. Vibration monitoring of pm synchronous machine with partial demagnetization and inter-turn short circuit faults. In *2014 IEEE Transportation Electrification Conference and Expo (ITEC)*, pages 1–6. IEEE, 2014.

[10] J Urresty, J Riba, L Romeral, and H Saavedra. Analysis of demagnetization faults in surface-mounted permanent magnet synchronous with inter-turns and phase-to-ground short-circuits. In *2012 XXth International Conference on Electrical Machines*, pages 2384–2389. IEEE, 2012.

[11] Hojin Lee, Hyeyun Jeong, and Sang Woo Kim. Detection of interturn short-circuit fault and demagnetization fault in ipmsm by 1-d convolutional neural network. In *2019 IEEE PES Asia-Pacific Power and Energy Engineering Conference (APPEEC)*, pages 1–5. IEEE, 2019.

[12] Hyeyun Jeong, Hojin Lee, and Sang Woo Kim. Classification and detection of demagnetization and inter-turn short circuit faults in ipmsms by using convolutional neural networks. In *2018 IEEE Energy Conversion Congress and Exposition (ECCE)*, pages 3249–3254. IEEE, 2018.

[13] Seokbae Moon, Hyeyun Jeong, Hojin Lee, and Sang Woo Kim. Detection and classification of demagnetization and interturn short faults of ipmsms. *IEEE Transactions on Industrial Electronics*, 64(12):9433–9441, 2017.

[14] Shen Zhang and Thomas G Habetler. Transient demagnetization characteristics of interior permanent magnet synchronous machines with stator inter-turn short circuit faults for automotive applications. In *2018 IEEE Energy Conversion Congress and Exposition (ECCE)*, pages 1661–1667. IEEE, 2018.

[15] Kyung-Tae Kim, Yoon-Seok Lee, and Jin Hur. Transient analysis of irreversible demagnetization of permanent-magnet brushless dc motor with interturn fault under the operating state. *IEEE Transactions on Industry Applications*, 50(5):3357–3364, 2014.

[16] Jiyu Zhang, Hongyang Yao, and Giorgio Rizzoni. Fault diagnosis for electric drive systems of electrified vehicles based on structural analysis. *IEEE Transactions on Vehicular Technology*, 66(2):1027–1039, 2016.

[17] Mattias Krysander, Jan Åslund, and Mattias Nyberg. An efficient algorithm for finding minimal overconstrained subsystems for model-based diagnosis. *IEEE Transactions on Systems, Man, and Cybernetics-Part A: Systems and Humans*, 38(1):197–206, 2007.

[18] Mattias Krysander and Erik Frisk. Sensor placement for fault diagnosis. *IEEE Transactions on Systems, Man, and Cybernetics-Part A: Systems and Humans*, 38(6):1398–1410, 2008.

[19] Carl Svärd, Mattias Nyberg, Erik Frisk, and Mattias Krysander. Automotive engine fdi by application of an automated model-based and data-driven design methodology. *Control Engineering Practice*, 21(4):455–472, 2013.

[20] Christofer Sundström, Erik Frisk, and Lars Nielsen. Selecting and utilizing sequential residual generators in fdi applied to hybrid vehicles. *IEEE Transactions on Systems, Man, and Cybernetics: Systems*, 44(2):172–185, 2013.

[21] Mogens Blanke, Michel Kinnaert, Jan Lunze, and Marcel Staroswiecki. Diagnosis and fault tolerant control, 2016.

[22] Mattias Krysander. *Design and analysis of diagnosis systems using structural methods*. PhD thesis, PhD thesis, Linköping Univ., Linköping, Sweden, 2006.

[23] Mattias Krysander, Jan Åslund, and Erik Frisk. A structural algorithm for finding testable sub-models and multiple fault isolability analysis. In *21st International Workshop on Principles of Diagnosis (DX-10), Portland, Oregon, USA*, pages 17–18, 2010.

[24] Saeed Hasan Ebrahimi, Martin Choux, et al. Modeling stator winding inter-turn short circuit faults in pmsms including cross effects. In *2020 International Conference on Electrical Machines (ICEM)*, volume 1, pages 1397–1403. IEEE, 2020.

Paper D

Diagnosis of Sensor Faults in PMSM and Drive System Based on Structural Analysis

Saeed Hasan Ebrahimi, Martin Choux, and Van Khang Huynh

This paper has been submitted as:

S. H. Ebrahimi, M. Choux, and V. K. Huynh. Diagnosis of Sensor Faults in PMSM and Drive System Based on Structural Analysis. In *Proceedings of 2021 IEEE International Conference on Mechatronics (ICM)*, 2021. ISBN: 978-1-7281-4443-6.

Diagnosis of Sensor Faults in PMSM and Drive System Based on Structural Analysis

Saeed Hasan Ebrahimi, Martin Choux, and Van Khang Huynh

Department of Engineering Sciences
University of Agder
NO-4879 Grimstad, Norway

Abstract – This paper presents a model-based fault diagnosis method to detect sensor faults in permanent magnet synchronous motor (PMSM) drives based on structural analysis technique. The structural model is built based on the dynamic model of the PMSM in matrix form, including unknown variables, known variables, and faults. The Dulmage–Mendelsohn (DM) decomposition is applied to evaluate the redundancy of the model and obtain redundant testable sub-models. These testable redundant sub-models are used to form residuals to observe the system state, and distinguish between healthy and faulty conditions.This work investigates faults in eleven sensors in a PMSM drive, thus nine structured residuals are designed to detect and isolate the investigated faults, which are applied to the system at different time intervals. Finally, the effectiveness of the proposed diagnostic approach is experimentally validated on an in-house setup of inverter-fed PMSMs.

D.1 Introduction

Permanent Magnet Synchronous Motors (PMSMs) are widely used in many high-performance drive applications including robotic systems, transportation, and offshore industries. Their key features of higher efficiency, power density, and controlability make them more attractive than other motors [1, 2]. Since controlling PMSM drives must rely on different sensors to achieve their goals and ensure full functionality of the overall system, condition monitoring of these sensors is necessary to guarantee the high reliability [3, 4].

Extensive research work has been conducted in diagnosis of sensor faults in an electric drive system [5–7]. Most of these techniques are observer-based to investigate faults in different combinations of sensors involved in the system by comparing the measured signals with corresponding estimated ones. For instance, observer-based speed and load torque sensor faults have been investigated in [6], while an adaptive observer has been employed to detect speed, dc bus voltage, and current faults by estimating sensor signals values [7]. Although these proposed observers have been proven to be effective in early detection of sensor faults, isolating faults may become quite challenging, especially when multiple sensors are involved in the system. Thus, structural analysis was proposed as an alternative model-based approach for detecting and isolating multiple faults in a complex system [8]. The theoretical basis of structural analysis technique has been studied and well developed in the literature [9–11]. So far, structural analysis are implemented on different systems including automotive engine [12], hybrid vehicle [13], and electric drive

system with eight sensors [8], but the existing works only focus on limited fault types and vehicles alone. It is important to extend this approach to deal with faults in PMSM drives in hash environments, like offshore industry, where the fault context might not only have higher number of sensor faults, but also higher fault diversity, i.e, dc capacitors, or dc link.

This paper presents a model-based fault detection and isolation methodology based on structural analysis for investigating eleven sensor faults in PMSMs, being applied to a more generalized electric drive system and motor's structure where many different sensors are required for condition-monitoring of the system. The required measurements include three-phase voltage and current sensors, DC bus voltage and current sensors, motor's angular velocity and position, and load torque. To build a structure model, a combination of healthy dynamic mathematical models of PMSM both in *abc* and *dq* frames including all the aforementioned sensors is employed, and specific terms related to each fault are added to the corresponding equations. These added terms include the deviations in the measured signals of each sensor caused by dc offsets, gain change, amplitude imbalance, and generally any sort of mismeasurement appearing in the corresponding equations. Furthermore, the analytical redundancy of the model is determined based on the motor and drive system's structural model. This redundant model is then subdivided into smaller over-determined testable subsystems, in which the faults are detected, and isolated. The novelty of this study is that not only more sensors are considered and therefore, more measurements, equations, and redundancy are added to the system but also, the effect of dc bus voltage and current as well as load torque sensors is taken into consideration, making the diagnostic system more effective to detect any faults. To observe the presence of faults, nine sequential residuals are designed and implemented from which certain combination of these residuals can be employed to isolate each fault. Finally, the effectiveness of the proposed model is validated on a experimental setup of inverter-fed PM synchronous motors.

D.2 Structural Analysis for PMSM and Drive System

Structural analysis is a mathematical algorithm that extracts the analytic redundant relations (ARRs) of a system based on the mathematical equations describing its dynamic [11, 14]. This structural model is initiated by an incidence matrix in which each row connects an equation to the corresponding unknown variables, known variables, and faults. Next, the rows and columns are rearranged in a way to form a diagonal structure - called Dulmage–Mendelsohn (DM) decomposition - to obtain the analytic redundancy of the system. After finding the exact determined part of the system, in which the number of equations is equal to the number of variables, the other part of the system is an analytic redundant part. This redundant part is used to identify several smaller over-constrained subsystems, being called set of ARRs. Depending on the fault signature of this set of ARRs, each considered fault might be detected or even isolated. Subsequently, several diagnostic tests are designed to inform the presence of each fault. This study

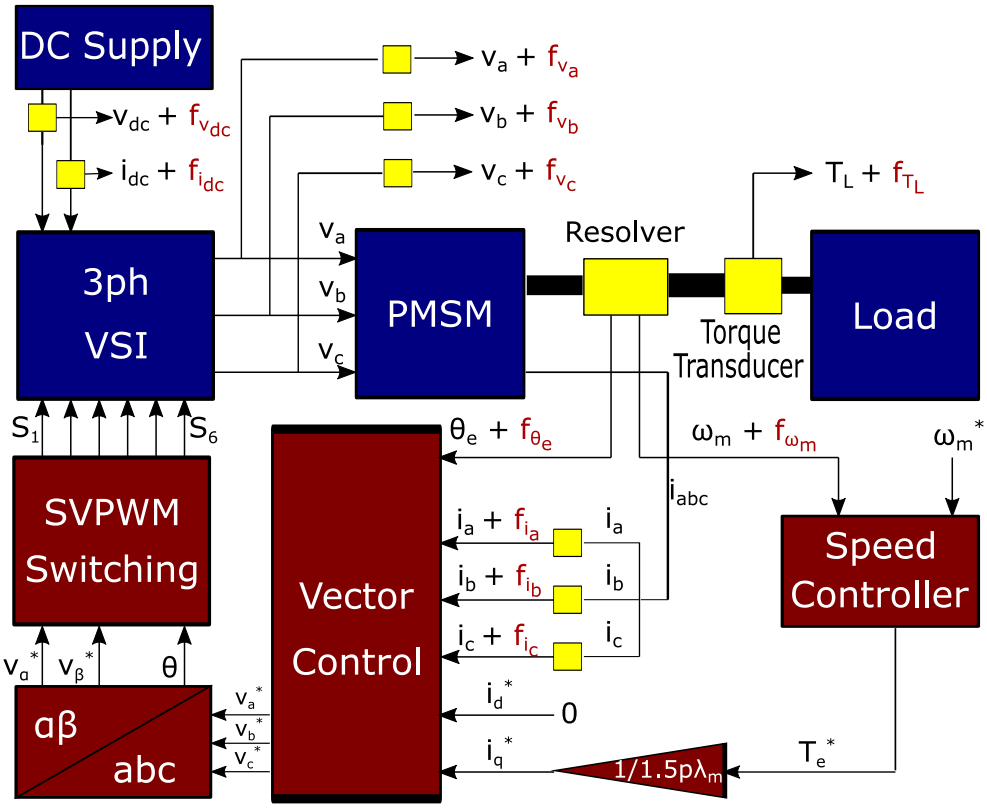

Figure D.1: Modeling diagram of PMSM and drive system.

presents a structural analysis of a PMSM and drive system containing sensor faults, and diagnostic tests are proposed for sensor detection and isolation. Fig. D.1 shows the modeling diagram of the PMSM and drive system components containing sensor faults, whereas the parameters are defined in the following section.

D.2.1 Mathematical Model of PMSM Drive

The mathematical model of a PMSM and drive system with sensor faults is described by equations $e_1 - e_{11}$ as shown in Eq. (D.1), where v_a, v_b, and v_c are the stator three phase voltages. Inside the PMSM block, v_d and v_q are the obtained using $e_1 - e_2$. Through $e_3 - e_4$, i_d and i_q are obtained which are needed for electromagnetic torque T_e calculation in e_9 and consequently, angular speed ω_m calculation in e_{10}. Feedback currents, i_a, i_b, and i_c, are obtained through $e_5 - e_7$. In addition, λ_m is the flux produced by PMs; R_s is the stator phase resistance; L_d and L_q are the dq inductances; v_{dc} and i_{dc} are the dc bus voltage and current; η_{inv} is the inverter's efficiency; T_L is the load torque; θ_e is the electric angular position; p is the number of pole pairs; J is the rotor inertia, and b is the

viscous damping coefficient.

$$
\begin{aligned}
e_1 :& v_d = \frac{2}{3}[v_a \cos\theta_e + v_b \cos(\theta_e - 2\pi/3) \\
& + v_c \cos(\theta_e + 2\pi/3)] \\
e_2 :& v_q = -\frac{2}{3}[v_a \sin\theta_e + v_b \sin(\theta_e - 2\pi/3) \\
& + v_c \sin(\theta_e + 2\pi/3)] \\
e_3 :& \frac{di_d}{dt} = \frac{1}{L_d}[v_d - R_s i_d + p\omega_m L_q i_q] \\
e_4 :& \frac{di_q}{dt} = \frac{1}{L_q}[v_q - R_s i_q - p\omega_m L_d i_d - p\omega_m \lambda_m] \\
e_5 :& i_a = i_d \cos\theta_e - i_q \sin\theta_e \\
e_6 :& i_b = i_d \cos(\theta_e - 2\pi/3) - i_q \sin(\theta_e - 2\pi/3) \\
e_7 :& i_c = i_d \cos(\theta_e + 2\pi/3) - i_q \sin(\theta_e + 2\pi/3) \\
e_8 :& v_{dc} i_{dc} \eta_{inv} = v_a i_a + v_b i_b + v_c i_c \\
e_9 :& T_e = \frac{3}{2} p[(L_d - L_q) i_d + \lambda_m] i_q \\
e_{10} :& \frac{d\omega_m}{dt} = \frac{1}{J}(T_e - b\omega_m - T_L) \\
e_{11} :& \frac{d\theta_e}{dt} = p\omega_m
\end{aligned}
\tag{D.1}
$$

The known variables y in the structural model include three-phase voltages (y_{v_a}, y_{v_b}, y_{v_c}), three-phase currents (y_{i_a}, y_{i_b}, y_{i_c}), dc bus voltage and current ($y_{v_{dc}}$, $y_{i_{dc}}$), electric angular position (y_{θ_e}), angular speed (y_{ω_m}), and load torque (y_{T_L}). Since these known variables come from sensor measurements, corresponding fault terms f are added to the equations, i.e., y_{v_a}, y_{v_b}, y_{v_c}, y_{i_a}, y_{i_b}, y_{i_c}, $y_{v_{dc}}$, $y_{i_{dc}}$, y_{θ_e}, y_{ω_m}, and y_{T_L}, resulting in 11 measurements and faults in total (shown in Eq. (D.2).).

$$
\begin{aligned}
m_1 &: y_{v_a} = v_a + f_{v_a} & m_7 &: y_{v_{dc}} = v_{dc} + f_{v_{dc}} \\
m_2 &: y_{v_b} = v_b + f_{v_b} & m_8 &: y_{i_{dc}} = i_{dc} + f_{i_{dc}} \\
m_3 &: y_{v_c} = v_c + f_{v_c} & m_9 &: y_{\theta_e} = \theta_e + f_{\theta_e} \\
m_4 &: y_{i_a} = i_a + f_{i_a} & m_{10} &: y_{\omega_m} = \omega_m + f_{\omega_m} \\
m_5 &: y_{i_b} = i_b + f_{i_b} & m_{11} &: y_{T_L} = T_L + f_{T_L} \\
m_6 &: y_{i_c} = i_c + f_{i_c}
\end{aligned}
\tag{D.2}
$$

In addition, the mathematical model of PMSM includes 4 differential constraints of unknown variables, which are shown in Eq. (D.3).

$$
\begin{aligned}
d_1 &: \tfrac{di_d}{dt} = \tfrac{d}{dt}(i_d) & d_2 &: \tfrac{di_q}{dt} = \tfrac{d}{dt}(i_q) \\
d_3 &: \tfrac{d\theta_e}{dt} = \tfrac{d}{dt}(\theta_e) & d_4 &: \tfrac{d\omega_m}{dt} = \tfrac{d}{dt}(\omega_m)
\end{aligned}
\tag{D.3}
$$

D.2.2 Structural Model and Analytical Redundancy of the PMSM

The structural model of PMSM drive with sensor faults is obtained based on the defined mathematical model in Eqs. (D.1)-(D.3), as shown in Fig. D.2. The incidence matrix

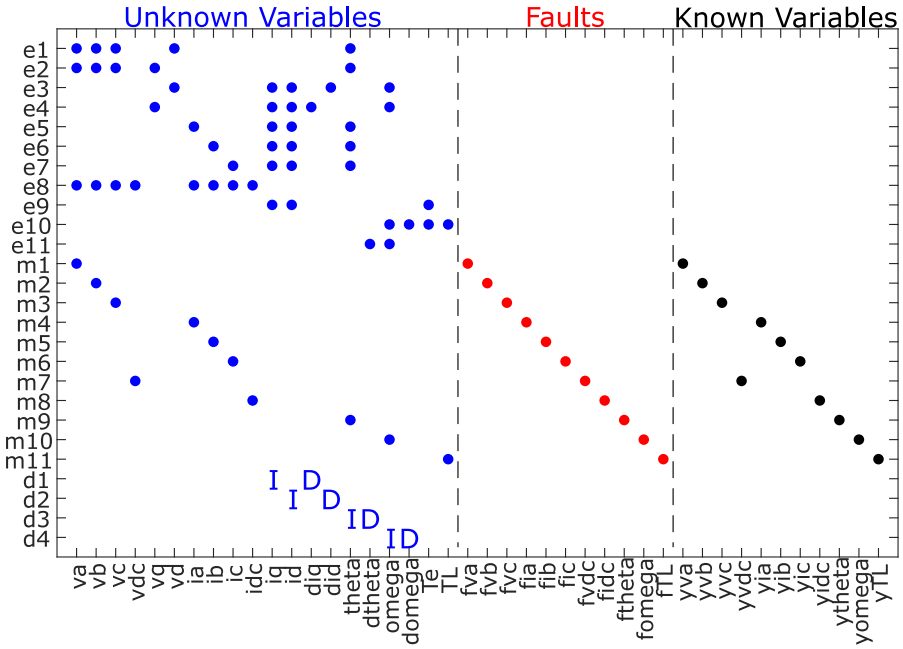

Figure D.2: PMSM drive structural model.

contains 26 rows, representing the 11 defined equations in Eq. (D.1), 11 measured known variables in Eq. (D.2), and the 4 differential constraints of unknown variables as shown in Eq. (D.3). The columns of the incidence matrix are subdivided into three groups of unknown variables, known variables, and faults, and each equation is connected to its relevant constraint in any of the three groups through each row. As shown in Fig. D.2, the differentiated and integrated variable relations are indicated by "D" and "I" signs, respectively.

For a fault to be detectable and then isolable , it should lie in the structurally over-determined part of the structural model, where there are more equations than unknown variables [10]. To accomplish this, DM decomposition tool is employed to evaluate the redundancy of the model. This is done by restructuring the structural model into an upper triangle shape by rearranging the rows and the columns of the incidence matrix. Fig. D.3 shows the DM decomposition for PMSM and drive system structural model, where the analytic redundant part of the system is expressed containing all the faults.

D.3 Diagnostic Test Design

This section presents the procedure of designing diagnostic tests for sensor faults in PMSM and drive system. First, the analytic redundant part is divided into smaller redundant subsystems, and then sequential residuals are derived to detect each fault.

D.3.1 Finding Testable Sub-Models

The analytic redundant part of the system is subdivided into efficient redundant testable sub-models, called Minimal Structurally Over-determined (MSO) sets, as proposed in [9]. The studied PMSM drive renders 20 unknown variables, 11 known variables, 11 fault

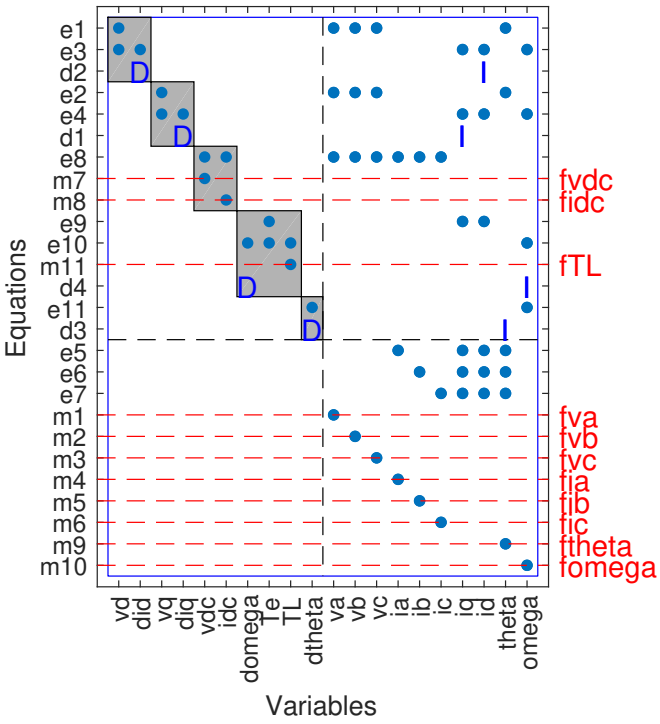

Figure D.3: DM decomposition for PMSM and drive system.

variables, and 26 equations including 4 differential constraints, resulting in the degree of redundancy 6 and 1525 MSO sets. Since the number of MSO sets increases exponentially in the degree of redundancy, Minimal Test Equation Support (MTES) sets is used instead, allowing for significantly reducing computational complexity without reducing the possible diagnosis performance [15]. The reason is that MTES sets are obtained in a way that the effect of faults is considered. In other terms, MTES sets are subsets of MSO sets, in which the effect of faults is visible. Here, the degree of redundancy for MTES sets is 1, and the algorithm yields 168 MTES sets. Next, different combinations of MTES sets are acquired, and the one that yields an acceptable value for diagnosability index (m_D) [16], is chosen to form residuals. Fig. D.4 shows the selected MTES sets found for the considered system, and the equations that are used in each MTES set for which diagnosability index, are obtained as $m_D = 4.45$. Fig. D.5 shows the signature matrix of MTES sets, indicating which faults appear in each MTES set. It is observed that the distance between any two faults ($D(V_{f_i}, V_{f_j})$) in this selection is more than 2, except $D(f_{v_{dc}}, f_{i_{dc}})$ are 0. This means that all the faults except $f_{v_{dc}}$ and $f_{i_{dc}}$ are isolable.

$MTES_1$ includes only f_{θ_e} and f_{ω_m} fault terms. It means that it can be used for either angular position or speed measurement faults. $MTES_3$ contains f_{i_b}, f_{i_c}, f_{θ_e}, and f_{T_L} fault terms, therefore, it can be used to detect load torque measurement fault. $MTES_{153}$ contain f_{v_a}, f_{v_b}, f_{v_c}, $f_{v_{dc}}$, $f_{i_{dc}}$, and f_{θ_e} fault terms, and by calculating the three-phase currents based on these measurements, $f_{v_{dc}}$ and $f_{i_{dc}}$ measurement faults can be detected. Each of the $MTES_{146}$, $MTES_{57}$, and $MTES_{112}$ sets contain two of the phase-voltages, two of the phase currents, and angular position, thus, they can be used in forming the residuals to detect f_{v_a}, f_{v_b}, and f_{v_c} measurement faults. Subsequently, each of the $MTES_{165}$, $MTES_{160}$, and $MTES_{156}$ sets contain the three-phase voltages, one of the phase currents,

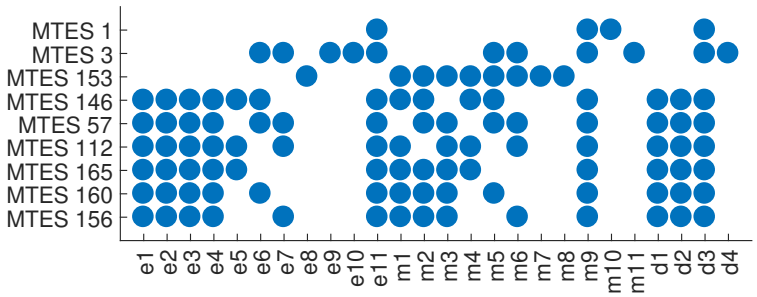

Figure D.4: MTES sets.

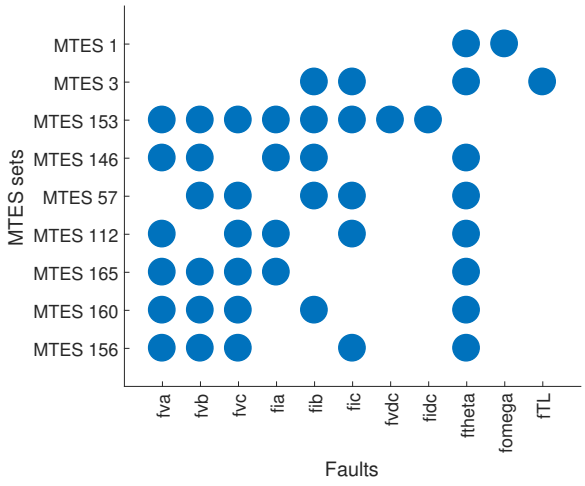

Figure D.5: Fault signature matrix of MTES sets.

and angular position, therefore, they can be used in forming the residuals to detect f_{i_a}, f_{i_b}, and f_{i_c} measurement faults.

D.3.2 Sequential Residuals for Detecting the Faults

In this section, 9 sequential residuals ($R_1 - R_9$) are derived based on the selected MTES sets. These residuals aim to detect all the considered faults and a combination of them can be used to isolate each fault.

1. R_1: $MTES_1$ is used for deriving R_1 based on m_9 in Eq. (D.2):

$$m_9 : R_1 = y_{\theta_e} - \theta_e \tag{D.4}$$

And the sequence of deriving θ_e is as follows:

$$\begin{aligned} SV &: \theta_e = \theta_{state} \\ m_{10} &: y_{\omega_m} = \omega_m \\ e_{11} &: \frac{d\theta_e}{dt} = p\omega_m \end{aligned} \tag{D.5}$$

Where θ_{state} is a state variables (SV) and will be updated after R_1 is calculated using integral form of d_3 in Eq. (D.3).

2. R_2: $MTES_3$ is used for deriving R_2 based on m_{11} in Eq. (D.2):

$$m_{11} : R_2 = y_{T_L} - T_L \tag{D.6}$$

To calculate T_L, e_9 and e_{10} must be used as shown in $MTES_3$ equation sets Fig. D.4. Knowing that θ_e is obtained directly from measurement, ω_m and $\frac{d\omega_m}{dt}$ can be easily calculated using the sequence of d_3, e_{11}, and d_4. Then i_b and i_c measurements are used to calculate i_d and i_q from e_6 and e_7 as follows:

$$\begin{aligned} i_d &= \frac{-2}{\sqrt{3}}[i_b \sin(\theta_e + \frac{2\pi}{3}) - i_c \sin(\theta_e - \frac{2\pi}{3})] \\ i_q &= \frac{-2}{\sqrt{3}}[i_b \cos(\theta_e + \frac{2\pi}{3}) - i_c \cos(\theta_e - \frac{2\pi}{3})] \end{aligned} \tag{D.7}$$

3. R_3: $MTES_{153}$ is used for deriving R_3 based on e_8 in Eq. (D.2):

$$e_8 : R_3 = v_{dc} i_{dc} \eta_{inv} - v_a i_a - v_b i_b - v_c i_c \tag{D.8}$$

where all the variables come from the measurements.

4. R_4: $MTES_{146}$ is used for deriving R_4 based on m_1 in Eq. (D.2):

$$m_1 : R_4 = y_{v_a} - v_a \tag{D.9}$$

To calculate v_a, θ_e is obtained directly from measurement, and ω_m is subsequently calculated using the sequence of d_3 and e_{11}. Similar to Eq. (D.7), two current measurements (i_a and i_b) are used to calculate i_d and i_q but this time from e_5 and e_6. Then $\frac{di_d}{dt}$ and $\frac{di_q}{dt}$ are obtained from d_1 and d_2 and used in e_3 and e_4 to form v_d and v_q. Finally, v_a is calculated from e_1 and e_2 as follows:

$$v_a = v_d \cos\theta_e - v_q \sin\theta_e \tag{D.10}$$

5. R_5 and R_6 follow similar procedure mentioned for R_4 to find the difference between measured and calculated phase b and phase c voltages based on $MTES_{57}$ and $MTES_{112}$, respectively.

6. R_7: $MTES_{165}$ is used for deriving R_7 based on based on m_4 in Eq. (D.2):

$$m_4 : R_7 = y_{i_a} - i_a \tag{D.11}$$

To calculate i_a, θ_e is obtained directly from measurement, and ω_m is subsequently calculated using the sequence of d_3 and e_{11}. Then the measured values of v_a, v_b, and v_c are used in e_1 and e_2 to get to v_d and v_q. Next, $\frac{di_d}{dt}$ and $\frac{di_q}{dt}$ are obtained from d_1 and d_2 and finally i_a is calculated from e_5 as follows:

$$i_a = i_d \cos\theta_e - i_q \sin\theta_e \tag{D.12}$$

7. R_8 and R_9 follow similar procedure mentioned for R_7 to find the difference between measured and calculated phase b and phase c currents based on $MTES_{160}$ and $MTES_{156}$, respectively.

D.4 Experiments and Results

The proposed diagnostic method is validated through experimental results in this section. Fig. D.6 shows the experimental setup, where two identical PMSMs are mechanically coupled to form a motor-generator set. A torque transducer is placed in between the motors to measure the load torque, which can be varied through resistive load of the generator. The motor is controlled by an inverter and the sensors are powered by a low voltage dc supply. Finally, a dSpace MicrolabBox is used to control the motor and collect the sensor data. The parameters of studied PMSMs are listed in Table D.1.

A ramp speed reference was applied on the motor to test the residual responses under nominal operating conditions of 1200 rpm. Fig. D.7 shows the speed reference and the motor's speed during the time of the operation.

After reaching the nominal speed, the measurement faults are applied at different time intervals. To cover all the possible measurement errors, different measurement errors have been applied including dc offset values for current sensors, speed and torque sensors, gain change for voltage sensors, and imbalance in angle measurement. At $t = 1 - 2s$, there appears a $+0.2rad/s$ offset in ω_m measurement; at $t = 3 - 4s$, there is a $+1N.m$ offset in T_L measurement; at $t = 5 - 6s$, the inverter has a $+2\%$ gain increase in v_{dc} measurement; at $t = 7 - 8s$, the inverter has a $+0.04A$ offset in i_{dc} measurement; at $t = 10 - 11s$, there appears a $+4\%$ gain change in v_a measurement;at $t = 12 - 13s$, there is a $+4\%$ gain change in v_b measurement;at $t = 14 - 15s$, appears a $+4\%$ gain change in v_c measurement;at $t = 17 - 18s$, there is a $+2A$ offset in i_a measurement;at $t = 19 - 20s$, there is a $+2A$ offset in i_b measurement;at $t = 21 - 22s$, there is a $+2A$ offset in i_b measurement; and finally at $t = 23 - 24s$, there is a $+0.01$ amplitude imbalance in θ_e measurement. Fig. D.8 shows the sequence of applied sensor faults.

The residual responses for the sensor faults are obtained after the motor reaches steady-state condition i.e. constant 1200 rpm of speed and 14 N.m of load torque ($t = 5 - 25s$

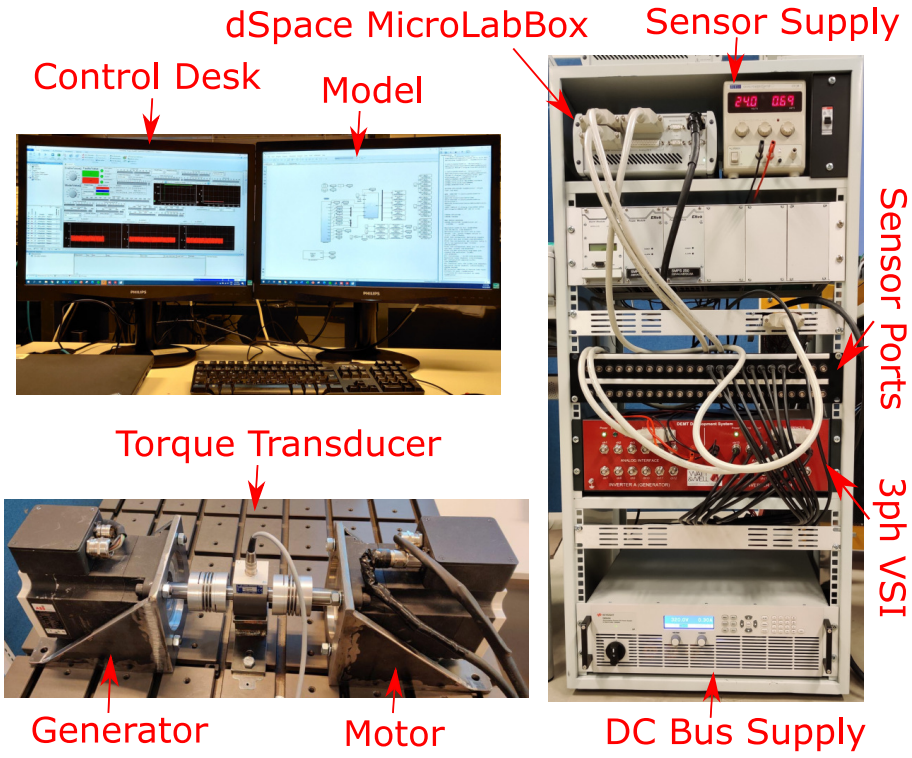

Figure D.6: Experimental setup.

Table D.1: Parameters of PM Synchronous Motor

Symbol	Parameter	Value	Unit
V_{dc}	Rated dc bus voltage	320	V
I_s	Rated rms phase current	5.9	A
T_{out}	Output Torque	14	$N.m$
n_s	Rated speed	1200	rpm
R_s	Phase resistance	1.125	Ω
L_q, L_d	Q and D axes inductances	8.75	mH
J	Rotor inertia	13.558	$kg.cm^2$
b	Rotor damping factor	0.00295	$N.m.s/rad$
λ_m	Flux linkage of PMs	0.1554	Web
p	Pole-pairs	4	

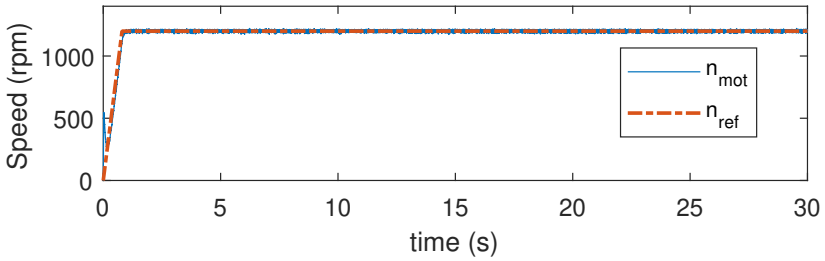

Figure D.7: Motor's speed and reference speed.

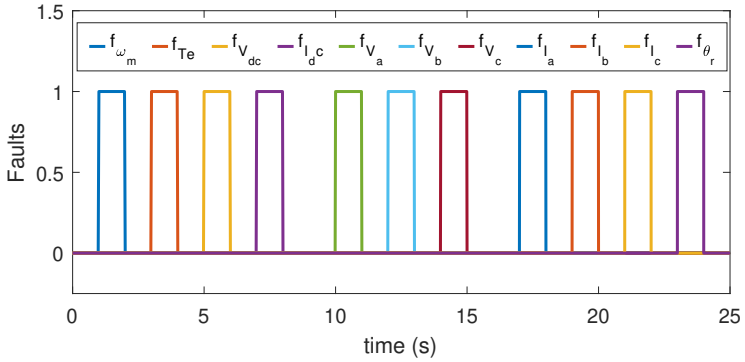

Figure D.8: Sequence of of faults.

in Fig. D.7). All the residual responses are filtered using a low-pass filter for better demonstration and shown in Fig. D.9. For $t = 0 - 1s$, the motor is operating in healthy mode and all the residuals remain averagely zero (neglecting the noise) since the signal values from the measurement and the calculations in each residual are similar. When the first fault i.e. f_{ω_m} occurs, only R_1 is affected and obtains a non-zero value. similarly when f_{T_L} occurs next, only R_2 is affected and obtains a non-zero value. The inverter faults $f_{v_{dc}}$ and $f_{i_{dc}}$ appear next and trigger R_3 at different time intervals. when the phase-a voltage fault f_{v_a} occurs at $t = 10 - 11s$, residuals [R_3, R_4, R_6, R_7, R_8, R_9] are triggered as expected in fault signature matrix (Fig. D.5). Similarly, f_{v_b} and f_{v_c} trigger residuals [R_3, R_4, R_5, R_7, R_8, R_9] and residuals [R_3, R_5, R_6, R_7, R_8, R_9], respectively. Next one is the phase-a current fault f_{i_a} which occurs at $t = 17 - 18s$ and residuals [R_3, R_4, R_6, R_7] are triggered. Similarly, f_{i_b} and f_{i_c} trigger residuals [R_2, R_3, R_4, R_5, R_8] and residuals [R_2, R_3, R_5, R_6, R_9], respectively.

As shown in Fig. D.9, all faults are detectable and each fault can trigger at least one of the designed residuals $R_1 - R_9$. The faults f_{ω_m}, f_{T_L}, $f_{v_{dc}}$, and $f_{i_{dc}}$ only trigger one residual during their presence and therefore, very easy to be isolated. The rest trigger multiple but unique combinations of residuals. Based on this, the behavior and response of specific combinations of residuals can be used as the ground for detection and isolation of these faults in the PMSM and drive system.

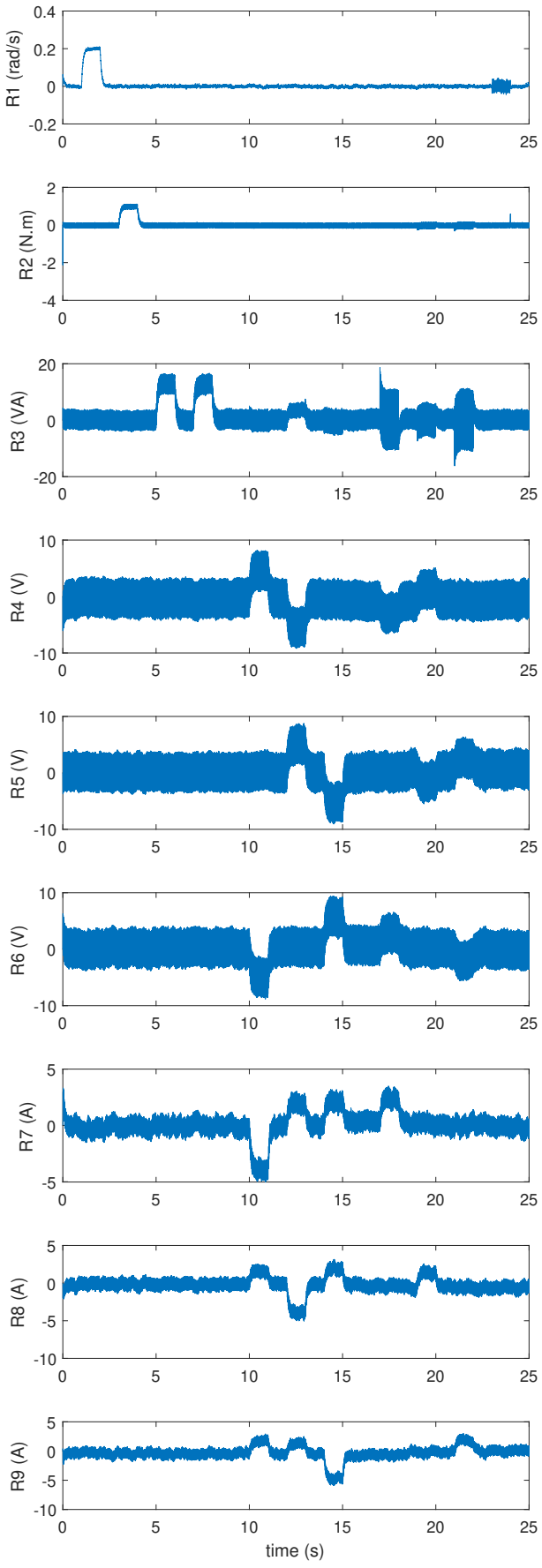

Figure D.9: Response of residuals.

D.5 Conclusion

This paper presents a method to detect and isolate sensor faults in a PMSM drive based on structural analysis. Not only are more sensor faults investigated compared to previous studies, but also the dc bus voltage and current are involved in the system. Structural analysis is employed to obtain the redundant part of the PMSM drive using DM decomposition. 9 sequential residuals are derived based on the fault terms that appear in each of the MTES sets to detect and isolate 11 faults in the sensors including voltage, current, load torque, speed, and angular position sensors. The proposed model is implemented experimentally and the behavior of residuals during mentioned faults are investigated in different time intervals. The experimental results show that residuals are able to efficiently detect and isolate faults in the laboratory test, proving the effectiveness of this diagnostic approach.

References

[1] Jun Hang, Han Wu, Jibo Zhang, Shichuan Ding, Yourui Huang, and Wei Hua. Cost function-based open-phase fault diagnosis for pmsm drive system with model predictive current control. *IEEE Transactions on Power Electronics*, 36(3):2574–2583, 2020.

[2] Xueqing Wang, Zheng Wang, Zhixian Xu, Jiangbiao He, and Wenxiang Zhao. Diagnosis and tolerance of common electrical faults in t-type three-level inverters fed dual three-phase pmsm drives. *IEEE Transactions on Power Electronics*, 35(2):1753–1769, 2019.

[3] Faa-Jeng Lin and Yueh-Shan Lin. A robust pm synchronous motor drive with adaptive uncertainty observer. *IEEE Transactions on Energy Conversion*, 14(4):989–995, 1999.

[4] Se-Kyo Chung, Hyun-Soo Kim, Chang-Gyun Kim, and Myung-Joong Youn. A new instantaneous torque control of pm synchronous motor for high-performance direct-drive applications. *IEEE Transactions on Power Electronics*, 13(3):388–400, 1998.

[5] F Grouz, L Sbita, and M Boussak. Current sensors gain faults detection and isolation based on an adaptive observer for pmsm drives. In *10th International Multi-Conferences on Systems, Signals & Devices 2013 (SSD13)*, pages 1–6. IEEE, 2013.

[6] Jaroslaw Guzinski, Haitham Abu-Rub, Marc Diguet, Zbigniew Krzeminski, and Arkadiusz Lewicki. Speed and load torque observer application in high-speed train electric drive. *IEEE Transactions on Industrial Electronics*, 57(2):565–574, 2009.

[7] Tooraj Abbasian Najafabadi, Farzad R Salmasi, and Parviz Jabehdar-Maralani. Detection and isolation of speed-, dc-link voltage-, and current-sensor faults based on an adaptive observer in induction-motor drives. *IEEE Transactions on Industrial Electronics*, 58(5):1662–1672, 2010.

[8] Jiyu Zhang, Hongyang Yao, and Giorgio Rizzoni. Fault diagnosis for electric drive systems of electrified vehicles based on structural analysis. *IEEE Transactions on Vehicular Technology*, 66(2):1027–1039, 2016.

[9] Mattias Krysander, Jan Åslund, and Mattias Nyberg. An efficient algorithm for finding minimal overconstrained subsystems for model-based diagnosis. *IEEE Transactions on Systems, Man, and Cybernetics-Part A: Systems and Humans*, 38(1):197–206, 2007.

[10] Mattias Krysander and Erik Frisk. Sensor placement for fault diagnosis. *IEEE Transactions on Systems, Man, and Cybernetics-Part A: Systems and Humans*, 38(6):1398–1410, 2008.

[11] Mogens Blanke, Michel Kinnaert, Jan Lunze, and Marcel Staroswiecki. Diagnosis and fault tolerant control, 2016.

[12] Carl Svärd, Mattias Nyberg, Erik Frisk, and Mattias Krysander. Automotive engine fdi by application of an automated model-based and data-driven design methodology. *Control Engineering Practice*, 21(4):455–472, 2013.

[13] Christofer Sundström, Erik Frisk, and Lars Nielsen. Selecting and utilizing sequential residual generators in fdi applied to hybrid vehicles. *IEEE Transactions on Systems, Man, and Cybernetics: Systems*, 44(2):172–185, 2013.

[14] Mattias Krysander. *Design and analysis of diagnosis systems using structural methods*. PhD thesis, PhD thesis, Linköping Univ., Linköping, Sweden, 2006.

[15] Mattias Krysander, Jan Åslund, and Erik Frisk. A structural algorithm for finding testable sub-models and multiple fault isolability analysis. In *21st International Workshop on Principles of Diagnosis (DX-10), Portland, Oregon, USA*, pages 17–18, 2010.

[16] Jiyu Zhang and Giorgio Rizzoni. Selection of residual generators in structural analysis for fault diagnosis using a diagnosability index. In *2017 IEEE Conference on Control Technology and Applications (CCTA)*, pages 1438–1445. IEEE, 2017.

Paper E

Real-Time Detection of Incipient Inter-Turn Short Circuit and Sensor Faults in Permanent Magnet Synchronous Motor Drives Based on Generalized Likelihood Ratio Test and Structural Analysis

Saeed Hasan Ebrahimi, Martin Choux, and Van Khang Huynh

This paper has been submitted as:

S. H. Ebrahimi, M. Choux, and V. K. Huynh. Real-Time Detection of Incipient Inter-Turn Short Circuit and Sensor Faults in Permanent Magnet Synchronous Motor Drives Based on Generalized Likelihood Ratio Test and Structural Analysis. In *MDPI - Sensors*, 2022. EISSN 1424-8220.

Real-Time Detection of Incipient Inter-Turn Short Circuit and Sensor Faults in Permanent Magnet Synchronous Motor Drives Based on Generalized Likelihood Ratio Test and Structural Analysis

Saeed Hasan Ebrahimi, Martin Choux, and Van Khang Huynh

Department of Engineering Sciences
University of Agder
NO-4879 Grimstad, Norway

Abstract – This paper presents a robust model-based technique to detect multiple faults in permanent magnet synchronous motors (PMSMs), namely inter-turn short circuit (ITSC) and encoder faults. The proposed model is based on a structural analysis, which uses the dynamic mathematical model of a PMSM in an *abc* frame to evaluate the system's structural model in matrix form. The just-determined and over-determined parts of the system are separated by a Dulmage–Mendelsohn decomposition tool. Subsequently, the analytical redundant relations obtained using the over-determined part of the system are used to form smaller redundant testable sub-models based on the number of defined fault terms. Furthermore, four structured residuals are designed based on the acquired redundant sub-models to detect measurement faults in the encoder and ITSC faults, which are applied in different levels of each phase winding. The effectiveness of the proposed detection method is validated by an in-house test setup of an inverter-fed PMSM, where ITSC and encoder faults are applied to the system in different time intervals using controllable relays. Finally, a statistical detector, namely a generalized likelihood ratio test algorithm, is implemented in the decision-making diagnostic system resulting in the ability to detect ITSC faults as small as one single short-circuited turn out of 102, i.e., when less than 1% of the PMSM phase winding is short-circuited.

E.1 Introduction

Permanent magnet synchronous motors (PMSMs) have gained popularity in industrial applications such as electric vehicles, robotic systems, and offshore industries due to their merits of efficiency, power density, and controllability [1–3]. PMSMs working in such applications are constantly exposed to electrical, thermal, and mechanical stresses, resulting in different faults such as electrical, mechanical, and magnetic faults [4]. Among these various faults, the stator winding inter-turn short circuit (ITSC) fault is considered as one of the most common faults [5] due to the excessive heat produced by a high circulating current in a few shorted turns of the stator winding [6]. Subsequently, this excessive heat causes further insulation degradation and might lead to a complete machine failure [7] if it is not detected and treated in time. Therefore, developing methods for monitoring and

detecting the ITSC fault in its early stages can substantially lower maintenance costs, downtime of the system, and productivity loss.

ITSC faults can be detected by signal-based, data-driven, and model-based techniques [8]. The first approach aims to detect fault characteristic frequencies in measured motor signals, namely, current, voltage, or vibration signals [9–11], being processed by time–frequency signal analysis tools such as Fourier transform [12], matched filters [13], Hilbert–Haung transform [14], wavelet transforms [15], and Cohen distributions [16]. These signal-based methods face challenges of real-time implementations due to the computational burden, and missing fault characteristic signals does not guarantee that the machine is healthy [8]. The data-driven approach such as an artificial neural network (ANN) [17] and Fuzzy systems [18] requires a lot of historical data to train models and classify localized faults. Historical data is restricted in industry and producing a lot of historical data in healthy and faulty conditions is costly and time-demanding [19]. Alternatively, model-based techniques have been proposed to detect ITSC faults [20–22]. Among them, the finite element method (FEM)-based models have been widely used due to the accuracy and convenience of taking into account physical phenomena, e.g., saturation. FEM models, known as time-demanding and computationally heavy ones, require deep knowledge of the system, e.g., detailed dimensions and material characteristics. Other model-based methods that use mathematical equations to model a motor's behavior have been reported to have challenges regarding validity when experiencing abnormal conditions such as internal faults [8]. To address the mentioned challenges, structural analysis is proposed as an alternative solution for detecting ITSC faults in electrical motors. The structural analysis algorithm has been well studied and developed in the literature [23–25] and applied to different structures. The structural analysis approach has been able to successfully detect faults in automotive engines [26–28], hybrid vehicle [29], and battery systems [30]. In [31, 32]. The algorithm has successfully been applied on PMSM electric drive systems to detect sensor faults such as voltage, current, encoder, and torque sensors. In our previous study [33], it was proposed that the algorithm can be used on an electric drive system to also detect common physical faults in PMSMs such as ITSC and demagnetization, and residual responses were obtained by simulation. However, in previous studies, this algorithm has not been implemented in real-time diagnosis of an industrial PMSM for detection of ITSC faults. Implementing a structural analysis technique on a PMSM and drive, this paper aims to achieve the following contributions:

- Detection of both internal motor faults and external measurement faults, namely ITSC and encoder faults;
- Detection of the lowest level of ITSC fault, with one shorted turn in stator phase winding;
- Early detection of an ITSC fault, i.e., considering a lower fault current in the degradation path as compared to shorted turns;
- Modeling of the noise in drive system measurement signals with unknown amplitude and variance.

This paper presents a systematic fault diagnosis methodology based on structural analysis for detecting multiple faults in PMSM drives, namely ITSC faults and encoder fault. To achieve this, a healthy dynamic mathematical model of PMSM is defined in the *abc* reference frame based on the dynamic constraints, measurements, and derivatives. To model an ITSC fault in any phase, specific fault terms are added to the three-phase flux and voltage equations. These fault terms include the deviations in the voltage, flux, and currents of the stator winding caused by an ITSC fault, since a part of winding is shorted; hence, three-phase voltage and flux signals are subjected to changes. In addition, fault terms are added to the dynamic model to take into account the encoder faults, resulting in errors of the angular speed and angle measurements. Subsequently, the analytical redundant part of the structural model is extracted and divided into minimally over-determined sub-systems from which three sequential residuals are obtained based on the error in the current signal of each phase. Furthermore, a resultant residual is formed in the $\alpha\beta$ frame to achieve a better demonstration of different ITSC fault levels. Finally, a generalized likelihood ratio test is developed to detect the faults in the resultant and encoder residuals under unknown noise parameters assumptions, i.e., unknown amplitude and unknown variance.

E.2 Inter-Turn Short Circuit Fault

The studied PMSM consists of distributed three-phase windings on the stator and PMs on the rotor. Each phase winding contains several coils in parallel, being formed by wrapping bundles of wires together. The wire insulation of the stator windings might be degraded over time under electrical, mechanical, and thermal stresses, which may eventually lead to electrical faults such as an inter-turn short circuit (ITSC), a phase to ground short circuit (PGSC), and a phase to phase short circuit (PPSC).The stator ITSC fault is considered the most common electrical fault [34] and usually occurs in a few shorted turns. The degraded path among the shorted turns is provided by a nonzero resistance of the faulty insulation, leading to a circulating fault current. This circulating fault current results in copper losses and excessive heat in the shorted turns since only a few turns are involved, and the current-limiting impedance is low. The insulation might further degrade and even propagate to nearby turns. This might cause other critical faults such as a PGSC fault, a PPSC fault, and even a complete failure. Therefore, monitoring and detecting the ITSC fault in early stages would reduce costs and downtime caused by the machine failure.

To model ITSC faults in a PMSM, it is necessary to know how the motor signals and parameters are affected by the different levels of the fault. The schematic of a PMSM stator winding under ITSC faults with different levels in each phase is shown in Figure E.1. The level of fault in abc phases is denoted by μ_a, μ_b, and μ_c, respectively, which are defined by the ratio of the number of shorted turns to the total number of turns per *abc* phase winding. In a healthy condition, each phase winding of a PMSM has a resistance of R_s and an inductance of L_s. In the presence of ITSC faults in each phase, the phase winding is split into a faulty part with μR_s and μL_s, and a healthy part with $(1-\mu)R_s$ and $(1-\mu)L_s$ resistance and inductance values. As a result, there is not only mutual

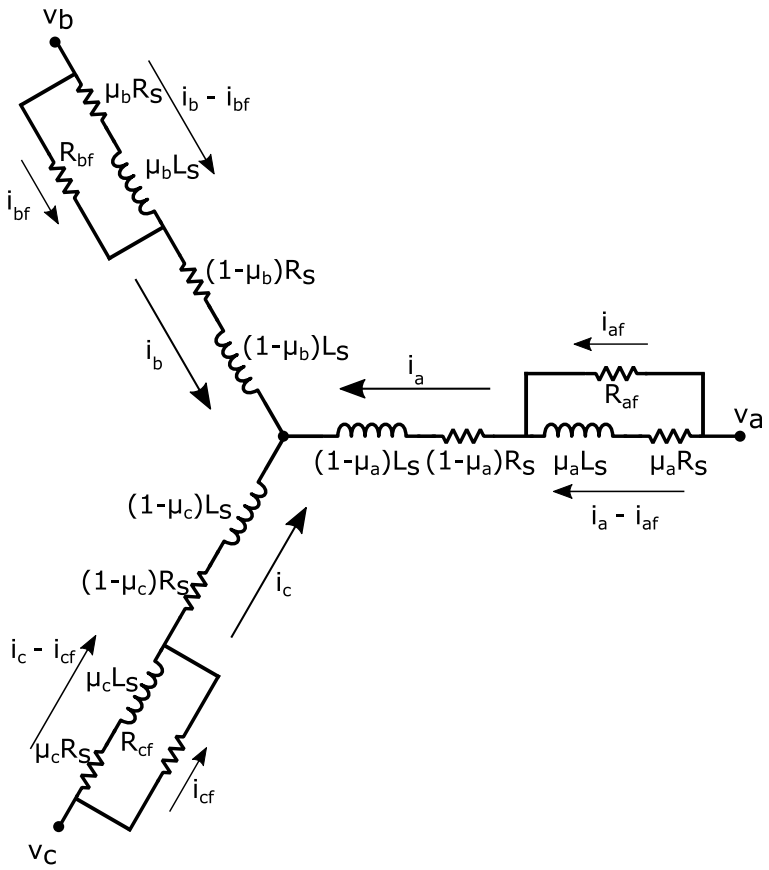

Figure E.1: Schematic of PMSM stator windings under ITSC faults

inductance between healthy and faulty parts in each phase winding, but also between the faulty winding with other phase windings [35]. In addition, the degraded resistance of the insulation in each phase is denoted by R_{af}, R_{bf}, and R_{cf}, while the circulating fault currents are i_{af}, i_{bf}, and i_{cf}, respectively. To detect an incipient ITSC fault, the resistance of the degraded path should be higher than the resistance of the shorted turns [36]. This is due to the fact that an ITSC fault forms gradually over time and starts with a low current circulating through the degraded path.

E.3 Structural Analysis for PMSM with ITSC and Encoder Faults

Structural analysis aims to extract the analytic redundant relations (ARRs) of a system based on the mathematical equations that describe the system's dynamic [23, 37]. A structural analysis algorithm relies on redundancy in a system (a redundant part of the complex system) and yields residuals for fault detection and isolation (FDI) based on ARRs. Assuming that a model M has outputs z and inputs u, a residual is extracted by eliminating all the unknown variables, i.e., substituting an unknown variable with its equivalent obtained value through a redundant path. Therefore, it leads to a relation that contains only the known variables $r(u, z) = 0$ which is known as an ARR if the observation z is consistent with the system model [23]. As a result, this residual's response

will maintain a zero value under a null hypothesis (nonfaulty case) $\mathcal{H}_0$ and a nonzero value under an alternative hypothesis (faulty case) $\mathcal{H}_1$ as follows:

$$\begin{aligned} \mathcal{H}_0 &: r(u, z) = 0 \\ \mathcal{H}_1 &: r(u, z) \neq 0 \end{aligned} \tag{E.1}$$

This methodology is especially effective for fault diagnosis of complex systems where a prior deep knowledge of the whole system is neither needed nor affordable in terms of computational burden and processing time. Instead, a small redundant part of the system is selected and processed to obtain smaller redundant subsystems that can be used in forming residuals for detecting each predefined fault. First, the structural model of a redundant system is formed and represented by an incidence matrix with variables as columns and equations as rows. The variables are categorized as unknown variables, known variables, and faults, while the equations are categorized as dynamic equations, measurements, and differential equations. Each row of the incidence matrix connects an equation to the corresponding variables if they are present in that specific equation. Next, the just-determined and over-determined parts of the system are separated by rearranging the rows and columns in a way to form a diagonal structure that is known as Dulmage–Mendelsohn (DM) decomposition. Using the analytic redundant part of this structure and based on the degree of the redundancy, several smaller sets of ARRs are identified. These smaller sets are called minimally over-constrained sets and have one degree of redundancy, holding exactly one more equation than the number of variables. Subsequently, a fault signature matrix is formed to demonstrate which fault can be detected or even discriminated. Finally, specific diagnostic tests (residuals) are designed to detect faults. Here, a structural analysis of a PMSM experiencing independent ITSC faults in each phase is presented, and diagnostic tests are proposed to detect and discriminate them. Figure E.2 shows the modeling diagram of a faulty PMSM and the drive system where measurements are acquired by sensors and faults are located inside the motor.

E.3.1 PMSM Mathematical Model

The dynamic equations of a faulty PMSM in an *abc* frame with ITSC faults present in three phases are represented by equations $e_1 - e_9$ as shown in (E.2), where v_a, v_b, and v_c are the stator phase voltages; i_a, i_b, and i_c are the stator phase currents; λ_a, λ_b, and λ_c are the stator phase fluxes; T_e is the electromagnetic torque; T_L is the load torque; ω_m is the rotor's angular speed; θ is the electric angular position; R_a, R_b, and R_c are the stator phase resistances and L_a, L_b, and L_c are the stator phase inductances; λ_m is the flux produced by rotor PMs; p is the pole pairs; J is the rotor inertia, and b is the friction coefficient.

As discussed in Section 2, an ITSC fault splits the phase winding into a faulty part with resistance and inductance of μR_s and μL_s and a healthy part with resistance and inductance of $(1 - \mu)R_s$ and $(1 - \mu)L_s$. The changed resistance and inductance of the winding have direct correlation with voltage equations and flux equations. Under a healthy condition, the model of PMSM, especially e_1–e_6, have no fault terms. Therefore, any

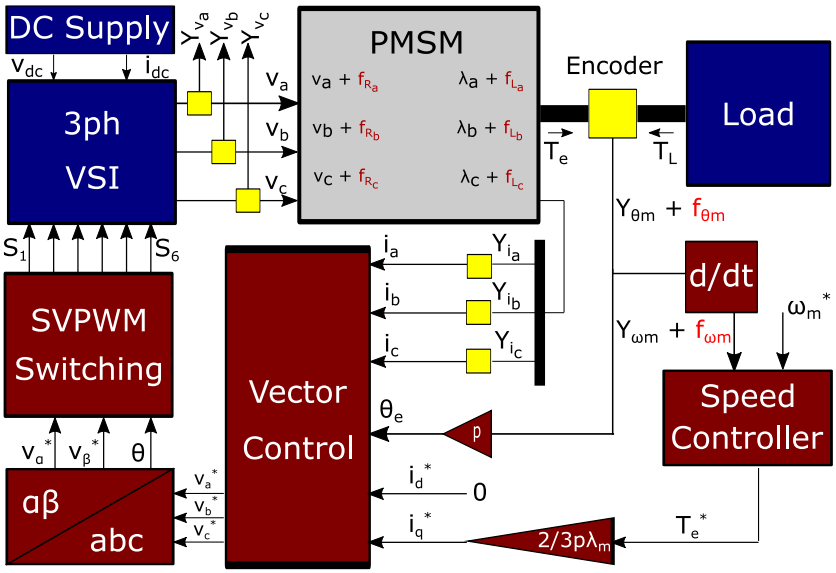

Figure E.2: Modeling diagram of PMSM and drive system.

changes in the inductance will affect both voltage and flux equations (e_1–e_6) directly, and any changes in the resistance will affect only voltage equations (e_1–e_3) directly. Here, f_{v_a} and f_{λ_a} are added to the corresponding equations of the healthy PMSM to account for the ITSC fault in phase a. Similarly, f_{v_b}, f_{v_c}, f_{λ_b}, and f_{λ_c} terms are added to account for ITSC faults in phases b and c, respectively. These fault terms are shown in red in (E.2).

$$
\begin{aligned}
e1 :& v_a = R_a i_a + \frac{d\lambda_a}{dt} + f_{v_a} \\
e2 :& v_b = R_b i_b + \frac{d\lambda_b}{dt} + f_{v_b} \\
e3 :& v_c = R_c i_c + \frac{d\lambda_c}{dt} + f_{v_c} \\
e4 :& \lambda_a = L_a i_a + \lambda_m \cos\theta + f_{\lambda_a} \\
e5 :& \lambda_b = L_b i_b + \lambda_m \cos(\theta - 2\pi/3) + f_{\lambda_b} \\
e6 :& \lambda_c = L_c i_c + \lambda_m \cos(\theta + 2\pi/3) + f_{\lambda_c} \\
e7 :& T_e = -p\lambda_m [i_a \sin\theta + i_b \sin(\theta - 2\pi/3) \\
& \quad + i_c \sin(\theta + 2\pi/3)] \\
e8 :& \frac{d\omega_m}{dt} = \frac{1}{J}(T_e - b\omega_m - T_L) \\
e9 :& \frac{d\theta}{dt} = p\omega_m
\end{aligned}
\tag{E.2}
$$

The known variables consist of the motor signals, which are measured for both control purposes and fault diagnosis. Thus, in addition to the three-phase currents and angular position, i.e., y_{i_a}, y_{i_b}, y_{i_c}, and y_θ that are necessary for the control system. Three-phase voltages, i.e., y_{v_a}, y_{v_b}, and y_{v_c}, are also measured to complete the diagnostic system. Equation (E.3) shows these known variables, where f_θ and f_ω fault terms are also added

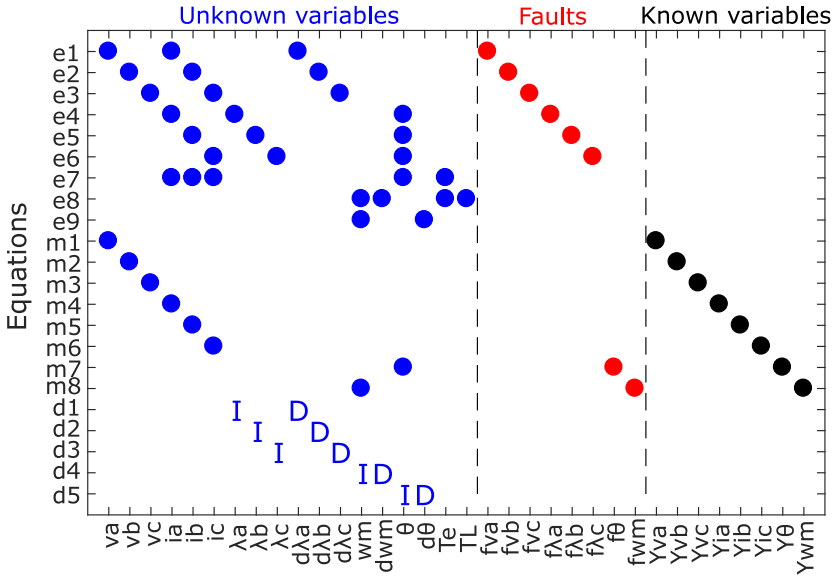

Figure E.3: PMSM structural model.

to account for speed and angle measurement error.

$$\begin{aligned} &m1 : y_{v_a} = v_a \quad m4 : y_{i_a} = i_a \quad m7 : y_\theta = \theta + f_\theta \\ &m2 : y_{v_b} = v_b \quad m5 : y_{i_b} = i_b \quad m8 : y_{\omega_m} = \omega_m + f_{\omega_m} \\ &m3 : y_{v_c} = v_c \quad m6 : y_{i_c} = i_c \end{aligned} \tag{E.3}$$

In addition, since the dynamic model of PMSM includes five differential constraints in the *abc* frame, these are needed to be defined as unknown variables. Equation (E.4) shows the differential constraints for the structural model.

$$\begin{aligned} &d1 : \frac{d\lambda_a}{dt} = \frac{d}{dt}(\lambda_a) \quad d4 : \frac{d\omega_m}{dt} = \frac{d}{dt}(\omega_m) \\ &d2 : \frac{d\lambda_b}{dt} = \frac{d}{dt}(\lambda_b) \quad d5 : \frac{d\theta}{dt} = \frac{d}{dt}(\theta) \\ &d3 : \frac{d\lambda_c}{dt} = \frac{d}{dt}(\lambda_c) \end{aligned} \tag{E.4}$$

E.3.2 Structural Representation of the PMSM Model

The structural model of the PMSM with ITSC and encoder faults is obtained based on the redundant dynamic model in (E.2)–(E.4), as shown in Figure E.3. The incidence matrix contains 22 rows, representing the nine defined equations in (E.2), the eight measured known variables in (E.3), and the five differential constraints of unknown variables as shown in (E.4). The columns of the matrix are subdivided into three groups of unknown variables, known variables, and faults. The known variables are obtained directly from the measurements, while the unknown variables can be calculated based on the known variables. The faults considered in the structural model are variations in phase voltage and flux to represent ITSC faults in each phase.

E.3.3 Analytical Redundancy of the Model

To detect specific faults in a redundant system, faults must first be introduced to the model, and then a proper diagnostic test containing the considered fault is selected. A diagnostic test is a set of equations (or consistency relations) extracted from the system model, in which at least one equation is violated in case of the presence of a considered fault. A system model is called a redundant model if the system model consists of more equations than unknown variables. Assuming that model $M = (C, Z)$ contains constraints (equations) C and variables Z, let unknown variables X be the subset of all variables Z in model M ($X \subseteq Z$). The degree of redundancy of the model M is defined as:

$$\varphi(M) = |C| - |X| \tag{E.5}$$

where $|C|$ denotes the number of equations, and $|X|$ is the number of unknown variables contained in the model M. According to bipartite graph theory, any finite dimensional graph such as $M = (C, Z)$ can be decomposed into three sub-graphs as follows [37]:

- M^-: structurally under-determined part of the model M, where fewer equations than unknown variables lie, and the degree of redundancy is negative $\varphi(M) < 0$.

- M^0: structurally just-determined part of the model M, where equal equations and unknown variables lie, and the degree of redundancy is zero $\varphi(M) = 0$.

- M^+: structurally over-determined part of the model M, where more equations than unknown variables lie, and the degree of redundancy is positive $\varphi(M) > 0$.

For diagnostic purposes, the over-constrained sub-graph is the interesting part because it contains the important redundancy that is necessary for detecting a fault. According to [38], a fault is structurally detectable if the equation that contains the fault variable lies in the over-determined part of the whole model ($e_f \in M^+$). To obtain these sub-graphs, a canonical decomposition of the main structure graph (M) is required. An example of this canonical decomposition is shown in Figure E.4, where three canonical sub-models of the model M are obtained as $\{M^-, M^0, M^+\}$.

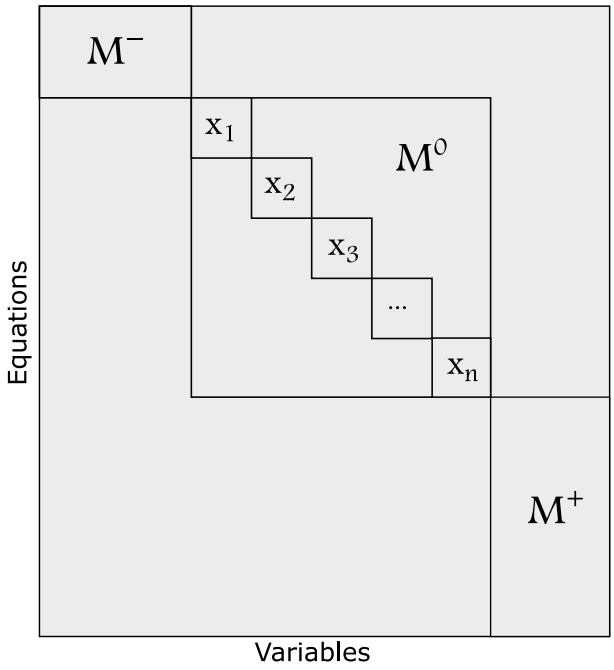

Figure E.4: Canonical decomposition of the structure graph M.

This canonical decomposition is achieved after the rows and the columns of the main structural graph (structural model incidence matrix) are rearranged so that the matched variables and constraints appear on the diagonal. Therefore, having a decomposition tool that analyzes the redundancy of the structural model and forms this diagonal structure is very beneficial. Dulmage–Mendelsohn (DM) is a key decomposition tool that is applied on a structural model directly and obtains a unique diagonal structure by a clever reordering of equations and variables [39]. Figure E.5 shows the DM decomposition for the PMSM structural model, where the analytic redundant part is expressed in the bottom-right part containing all the faults. Since this part includes redundancy and can be monitored, diagnostic tests can be designed with the set of ARRs in M^+. As a result, if a fault is defined in the model and is supposed to be detected by the diagnosis system, a residual that is sensitive to the presence of that fault must exist.

E.4 Diagnostic Test Design

This section presents the procedure of designing diagnostic tests for ITSC and encoder faults. First, the over-determined part of the structural model is separated into smaller redundant subsystems where faults are observable, and then the sequence of obtaining residuals for the detection of each fault is explained.

E.4.1 Minimal Testable Sub-Models

According to the definition given by [38], an equation set M is a TES set if:

1. $F(M) \neq \varnothing$.
2. M is a proper structurally over-determined set.

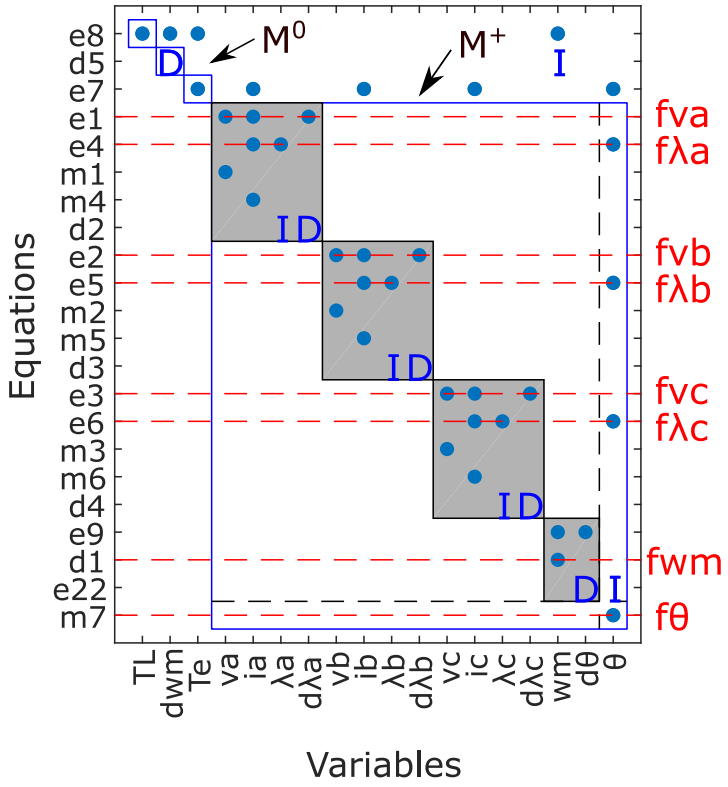

Figure E.5: DM decomposition for PMSM structural model.

3. For any $M^{'} \supsetneq M$ where $M^{'}$ is a proper structurally over-determined set, it holds that $F(M^{'}) \supsetneq F(M)$

where $F(M)$ is the set of faults that influence any of the equations in M. A TES M is a minimal test equation support (MTES) if there exists no subset of M that is a TES holding the degree of redundancy of one. Following the algorithm in [38], the structural model is subdivided into efficient redundant MTES sets. Each MTES set contains a group of ARRs that together hold the degree of redundancy of one, meaning that there is only one equation more than the number of variables involved. In addition, they are obtained in a way that the effect of faults is considered. This reduces computational complexity significantly without reducing the possible diagnosis performance as compared to structurally over-determined (MSO) sets. Figure E.6 shows all the MTES sets found for the considered structural model here, where each row of the matrix connects the corresponding MTES to the equations involved.

Figure E.7 shows the signature matrix of MTES sets, indicating which fault terms are included in each MTES. $MTES_1$ includes f_θ and f_ω fault terms that can be used for detecting a rotor's speed and angle measurement error. $MTES_2$ and $MTES_3$ contain f_{v_c} and f_{λ_c} fault terms for detecting an ITSC fault in phase c. $MTES_4 - MTES_6$ contain f_{v_b} and f_{λ_b} fault terms for detecting an ITSC fault in phase b. Similarly, $MTES_7 - MTES_{10}$ can be used for detecting an ITSC fault in phase a since it has f_{v_a} and f_{λ_a} fault terms. If a MTES set containing the information of changes in voltage and flux of a phase winding is found, it can be used to form a residual that is sensitive to the presence of an ITSC fault in that phase.

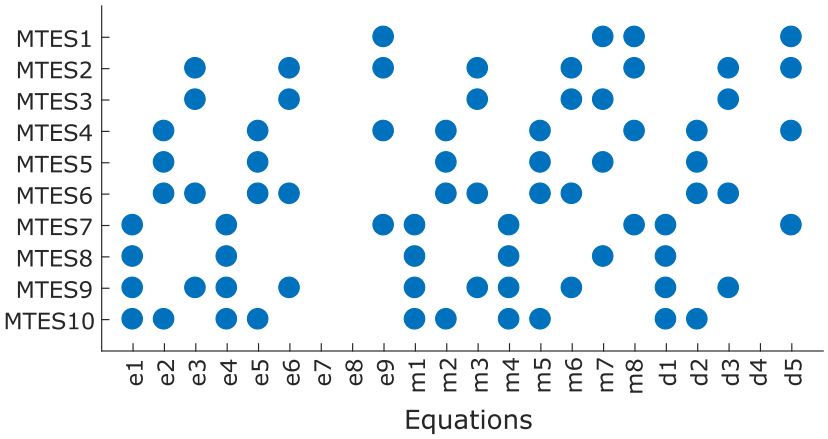

Figure E.6: MTES sets.

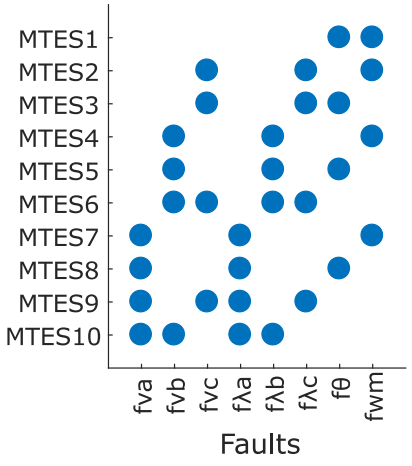

Figure E.7: Fault signature matrix of MTES sets.

E.4.2 Diagnosability Index

An important criterion for selecting MTES sets is to satisfy diagnosability requirements. This includes detectability of any single fault as well as isolability between any two faults. Here, an index for the proper selection of MTES sets that are suitable to be used in sequential residual generators is introduced. Zhang [40] proposed a diagnosability index that is aimed at achieving the maximum degree of diagnosability for each residual by comparing the distance between the fault signature matrices of MTES sets:

$$m_D = \frac{1}{\binom{n+1}{2}} \sum_{i=0}^{n-1} \sum_{j=i+1}^{n} D(V_{f_i}, V_{f_j}) \tag{E.6}$$

where $D(V_{f_0}, V_{f_j})$ stands for the distance between the fault signature of f_j and the healthy case and measures the detectability of fault f_j. $D(V_{f_i}, V_{f_j})$ is the distance between two fault signatures and is defined as the Hamming distance [41] between the two fault signature strings:

$$D(V_{f_i}, V_{f_j}) = \sum_{n=1}^{S} |V_{f_i} - V_{f_j}| \tag{E.7}$$

E.4.3 Sequential Residuals for Detecting ITSC Faults

This section presents the sequence of deriving four residuals ($R_1 - R_4$) based on the obtained MTES sets. These residuals aim to detect ITSC faults in any of the phase windings as well as encoder measurement faults. To form residual R_1 that is sensitive to an ITSC fault in phase a winding, an MTES set should be chosen that contains f_{v_a} and f_{λ_a} fault terms. As can be seen in the fault signature matrix in Figure E.7, $MTES_7 - MTES_{10}$ can be used for forming such a residual because these four MTES sets all contain f_{v_a} and f_{λ_a} fault terms. Among them, an MTES set is preferred that contains a lower number of fault terms because it will be more isolated and less influenced by other faults. $MTES_7$ and $MTES_8$ contain three fault terms, while $MTES_9$ and $MTES_{10}$ contain four fault terms. Therefore, either $MTES_7$ or $MTES_8$ should be chosen, and $MTES_8$ is preferred due to a lower number of involved equations ($MTES_8$ contains six equations, while $MTES_7$ contains eight equations) which leads to less complexity, as seen in Figure E.6. $MTES_4 - MTES_6$ can be used for forming residual R_2 because they contain f_{v_b} and f_{λ_b} fault terms. Among them, $MTES_5$ is preferred because it contains a lower number of fault terms compared to $MTES_6$ and a lower number of equations compared to $MTES_5$. Similarly, $MTES_3$ is chosen to form residual R_3 that is sensitive to an ITSC fault in phase-c winning and contains a lower number of equations compared to $MTES_2$, given the fact that both contain f_{v_c} and f_{λ_c} fault terms. To form residual R_3 that is sensitive to an encoder fault (angular velocity and position measurements), an MTES set is preferred that contains both f_{θ_e} and f_{ω_m}, and the only MTES set that contains such fault terms is $MTES_1$. The combination of these four MTES sets, i.e., $MTES_1$, $MTES_3$, $MTES_5$, and $MTES_8$ yield a high diagnosability index as $m_D = 1.88$, and this maximizes the

chance of discrimination of each fault from others. The sequential residuals are obtained as follows:

1. R_1: $MTES_8$ is used for deriving R_1 based on the error between calculated and measured current of phase a winding, i.e m_4 in (E.3):

$$m_4 : R_1 = i_a - y_{i_a} \tag{E.8}$$

And the sequence of obtaining these variables is as follows:

$$\begin{aligned} SV_1 : \lambda_a &= \lambda_{a_{state}} \\ m_7 : \theta &= y_\theta \\ m_1 : v_a &= y_{v_a} \\ e_4 : i_a &= \frac{1}{L_a}(\lambda_a - \lambda_m \cos\theta) \\ e_1 : d\lambda_a &= v_a - R_a i_a \end{aligned} \tag{E.9}$$

where $\lambda_{a_{state}}$ is a state variable and updated at each time-step as follows:

$$e_{17} : \lambda_{a_{state}} = \int d\lambda_a dt \tag{E.10}$$

2. R_2 and R_3 follow the same procedure mentioned for R_1 based on the error between calculated and measured currents of phase b and phase c using $MTES_5$ and $MTES_3$, respectively.

3. R_4: $MTES_1$ is used for deriving R_4 based on the error between the calculated and measured shaft's angular speed, i.e m_8 in (E.3):

$$m_8 : R_4 = \omega_m - y_{\omega_m} \tag{E.11}$$

and the sequence of obtaining the unknown variable, ω_m, is as follows:

$$\begin{aligned} m_7 : \theta &= y_\theta \\ d_5 : \frac{d\theta}{dt} &= \frac{d}{dt}(\theta) \\ e_9 : \omega_m &= p\frac{d\theta}{dt} \end{aligned} \tag{E.12}$$

$$\tag{E.13}$$

E.5 Experiments and Results

The proposed diagnostic method is implemented and validated through an in-house experimental setup in this section. First, ITSC faults were applied to the phase windings of a four-pole PMSM, as shown in Figure E.8. Each phase winding of the motor has two coils in series, each of which has 51 turns with three parallel branches. For phase a, one of the turns was short circuited, or about a 1% fault level. For the phases b and c, three and five

turns were short circuited, resulting in almost 3% and 5% fault severity, respectively. The connection wires to these extra taps in the phase windings were taken out of the motor and connected to 100 mΩ resistors (similar to R_f Figure E.1) both to limit the short circuit current and to simulate the winding insulation degradation, as shown in Figure E.9. Furthermore, controllable relays were placed between winding taps and fault resistors to activate or deactivate the fault. The faulty motor was mechanically coupled to a generator as a variable load and an incremental encoder to measure the rotor's angle and velocity. The motor was driven by a Watt&Well DEMT 3-ph voltage source inverter, which had embedded voltage and current sensors, being fed by a Keysight N8949A dc supply. In addition, a dSpace MicrolabBox control unit was used as a real-time interface device for implementing both control strategy and data acquisition from Matlab/Simulink with a sampling time of $50\mu s$. The parameters of the studied PMSM are listed in Table E.1.

To test the residual responses and effectiveness of the diagnostic system, the motor was driven from stationary to nominal speed, i.e., 1500 rpm, and kept in a steady-state condition. During the operation of the motor, the encoder and ITSC faults were applied at different time intervals using controllable relays. At t = 1–3 s, the encoder measurement fault was applied with a 1 rad/s error. At t = 4.471–7.238 s, the ITSC fault in phase a was applied which had 1% fault severity (one shorted turn in phase a winding); at t = 9.613–12.76 s, the ITSC fault in phase b appeared with 3% fault severity (three shorted turn in phase b winding); at t = 15.6–18.41 s, the ITSC fault in phase c with 5% fault severity (five shorted turn in phase c winding) was applied on the motor.

The residual responses for the mentioned faults were obtained and are shown in Figure E.10. Before the faults were applied, the motor was operating in a healthy mode (t = 0–1 s), and all the residuals remained averagely zero (neglecting the noise). This is because there was no error between the measured signals and the calculated ones used in each residual. First, when the encoder fault appeared, R_4 obtained a nonzero dc value, and it went back to average zero as soon as the fault disappeared. When the ITSC fault in phase a was applied, R_1 was directly affected and obtains/ed a higher oscillating value. Due to mutual induction of the fault current, this fault was also observable in R_2 and R_3. In addition, the controller response had a role in the increase of other phase currents. Since a part of the winding was gone, more I_q was required to keep the motor speed constant at 1500 rpm. The same logic can be used for ITSC faults in phases b and c as the residuals obtain higher oscillating values. The behavior and response of the residuals during each ITSC fault, can be used as the ground for detection of faults in the PMSM. This is implemented using signal processing–detection theory and explained in the following section.

E.6 Diagnostic Decision

Using the residual responses, a diagnostic decision making system was designed to detect the ITSC faults based on statistical signal processing–detection theory. While R_4 can be directly used to detect encoder faults, a combination of R_1–R_3 is required to effectively detect ITSC faults. The R_1–R_3 residuals obtained in the previous section, are designed

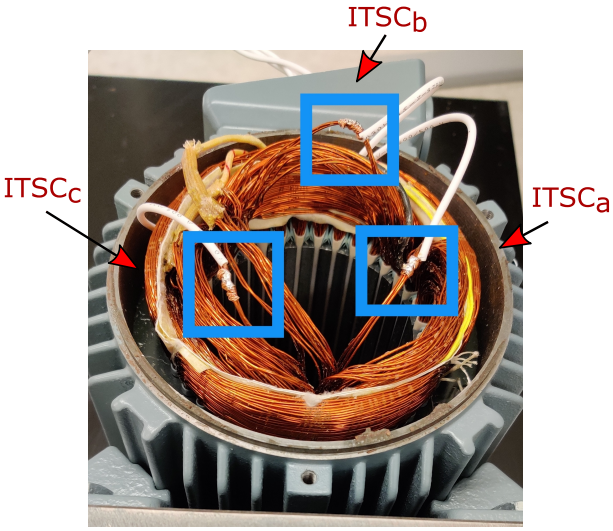

Figure E.8: Applied ITSC faults on PMSM.

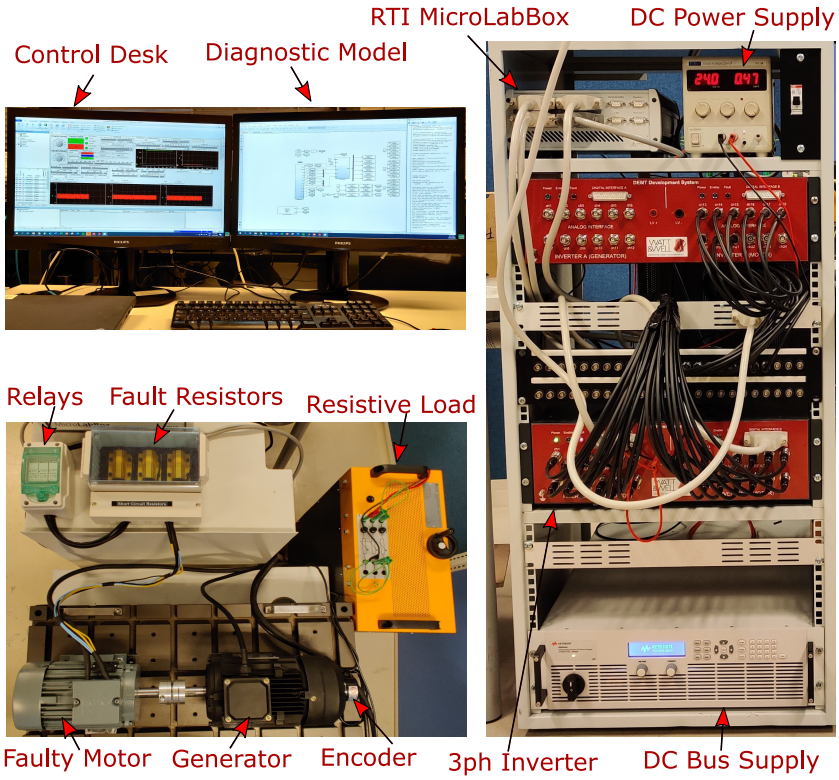

Figure E.9: Experimental Setup for Control and Diagnosis of PMSM

Table E.1: Parameters of PM Synchronous Motor

Symbol	Parameter	Value	Unit
V_{dc}	Rated dc bus voltage	280	V
I_s	Rated rms phase current	5	A
T_{out}	Rated Output Torque	7	$N.m$
n_s	Rated speed	1500	rpm
R_s	Phase resistance	0.8	Ω
L_s	Stator inductance	8.5	mH
J	Rotor inertia	0.0026	$kg.m^2$
b	Rotor damping factor	0.00382	$N.m.s/rad$
λ_m	Flux linkage of PMs	0.3509	Web
p	Pole-pairs	2	

based on *abc* frame voltage equations e_1–e_3 in (E.2), and an ITSC fault in any phase creates unbalance in the residual output. Before designing the statistical detector and to form a better index that obtains a nonzero dc value in case of an ITSC fault, the residuals in the *abc* frame are taken into an $\alpha\beta$ frame using the power invariant Clarke transformation as follows:

$$\begin{bmatrix} R_\alpha \\ R_\beta \end{bmatrix} = \sqrt{\frac{2}{3}} \begin{bmatrix} 1 & -\frac{1}{2} & -\frac{1}{2} \\ 0 & \frac{\sqrt{3}}{2} & -\frac{\sqrt{3}}{2} \end{bmatrix} \begin{bmatrix} R_1 \\ R_2 \\ R_3 \end{bmatrix} \tag{E.14}$$

The absolute value of the resultant is calculated:

$$R_r = |R_\alpha + jR_\beta| \tag{E.15}$$

Figure E.11 shows the absolute value of the resultant residual in an $\alpha\beta$ frame where ITSC faults in all phases are more obvious compared to *abc* residuals R_1–R_3. In implementing a structural analysis, the goal was to form residuals that have a zero value in a healthy scenario and a nonzero value in a faulty scenario. However, derivatives, integrals, and even uncertainties in the dynamic model affect the calculation of unknown variables and cause the variable output signal to be a little bit distorted. In addition, phenomena such as environmental noise and switching noise affect the signals. These lead to a residual output signal that fluctuates around zero instead of having a perfect signal that holds the absolute zero value in a healthy scenario. Even in a faulty scenario, the residual signal fluctuates around a nonzero value as seen in Figure E.11. Therefore, extra signal processing is required to deal with model uncertainties and environmental noise and to be able to distinguish and isolate the indicator signal from noise. Here, a generalized likelihood ratio test (GLRT) is proposed to deal with such model uncertainties and also to provide the ground for calculating and setting thresholds based on the probabilities of detection and false alarms in a formulated and scientific manner.

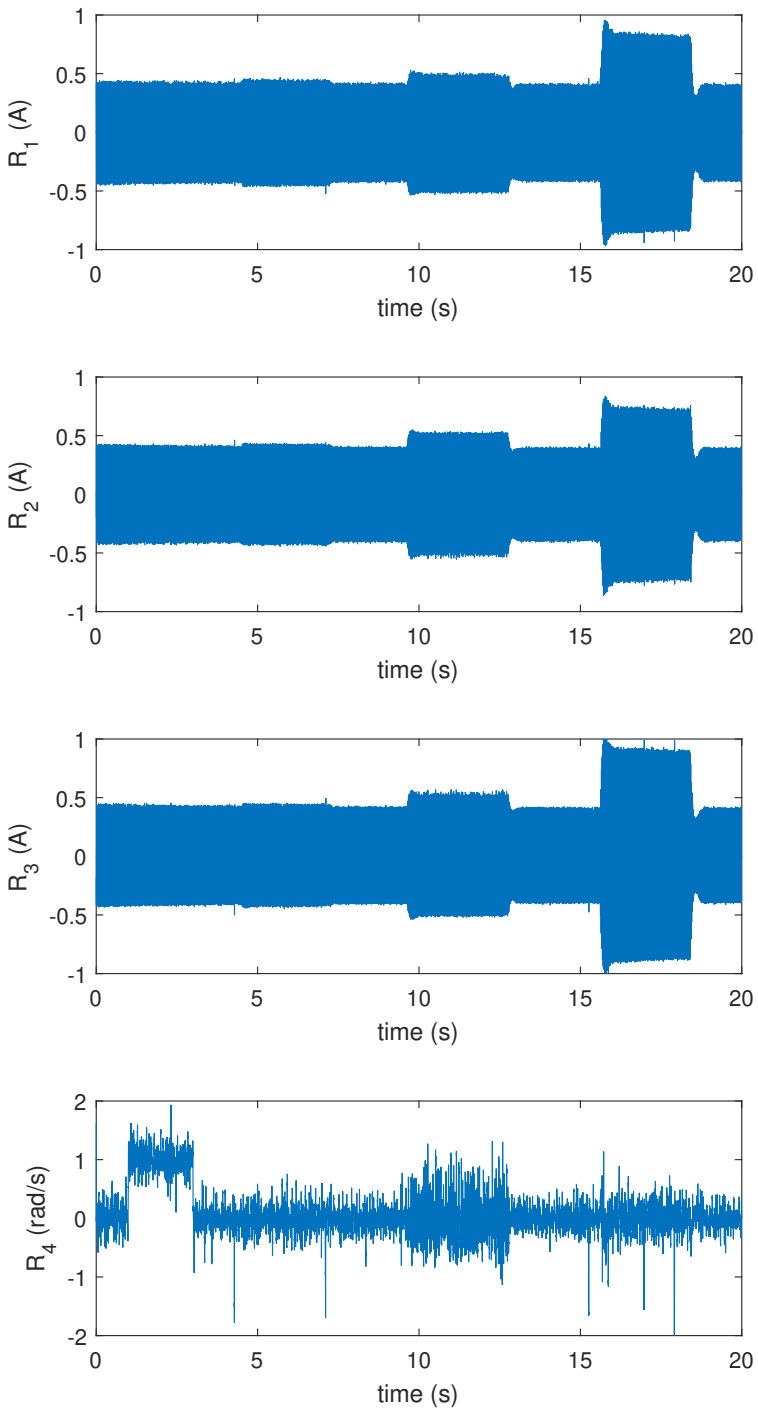

Figure E.10: Residual responses in *abc* phases.

E.6.1 Generalized Likelihood Ratio Test

GLRT is a composite hypothesis testing approach that can be used for detecting a signal in realistic problems [42]. It is noted that GLRT does not require prior knowledge of the unknown parameters such as mean (μ) and variance (σ^2) values in a probability density function (PDF) of a signal. GLRT deals with unknown parameters by replacing them with their maximum likelihood estimates (MLEs). If data x have the PDF $p(x;\hat{\theta}_0,\mathcal{H}_0)$ under a null hypothesis $\mathcal{H}_0$ and $p(x;\hat{\theta}_1,\mathcal{H}_1)$ under alternative hypothesis $\mathcal{H}_1$, the GLRT

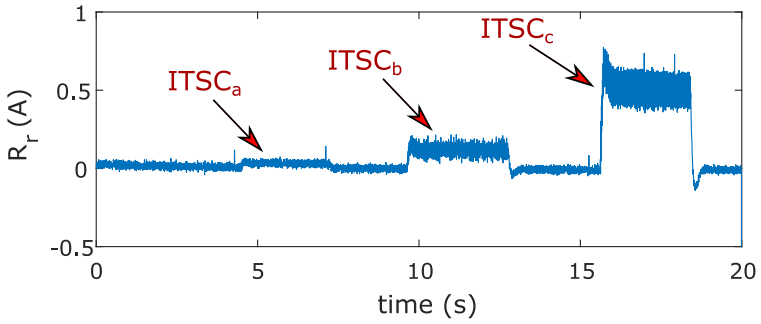

Figure E.11: Resultant residual response in $\alpha\beta$ frame.

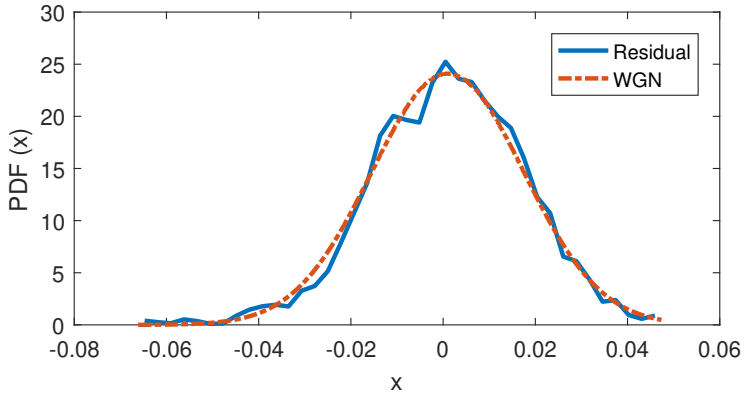

Figure E.12: comparison of PDF of residual and WGN.

decides $\mathcal{H}_1$ if:

$$L_G(x) = \frac{p(x; \hat{\theta}_1, \mathcal{H}_1)}{p(x; \hat{\theta}_0, \mathcal{H}_0)} > \gamma \tag{E.16}$$

where $\hat{\theta}_1$ is the MLE of θ_1 assuming $\mathcal{H}_1$ is true, $\hat{\theta}_0$ is the MLE of θ_0 assuming $\mathcal{H}_0$ is true, and γ is the threshold.

E.6.2 Design of Test Statistic Based on Generalized Likelihood Ratio Test

Before going through the design process, it is beneficial to know the PDF of the measurement noise signal. This gives us enough knowledge to make the assumptions that are close to our realistic problem. Using the first part (t = 0–1 s) of the resultant residual in Figure E.11, the PDF of the noise signal in a noise-only hypothesis is obtained and shown in Figure E.12. The PDF of the noise signal in Figure E.12 is very close to the PDF of a white Gaussian noise (WGN), thus it can be reasonably modeled with a WGN probability distribution function. To design a realistic detector, it is assumed that the arrival time of the fault is completely unknown. Furthermore, the PDF is not completely known, meaning that the parameters mean μ and variance σ^2 are to be estimated using MLE. The noise in the resultant residual during operation in a healthy condition is modeled as WGN. Since the resultant residual (R_r) obtains a nonzero dc value when ITSC

faults appear, the data are considered as only noise under nonfaulty hypothesis $\mathcal{H}_0$, and an added dc level value to the noise under faulty hypothesis $\mathcal{H}_1$. Thus, the detection problem becomes as follows:

$$\begin{aligned} \mathcal{H}_0 &: x[n] = w[n] \qquad n = 0, 1, ..., N-1 \\ \mathcal{H}_1 &: x[n] = A + w[n] \quad n = 0, 1, ..., N-1 \end{aligned} \tag{E.17}$$

where A is unknown amplitude with $-\infty < A < \infty$, and $w[n]$ is WGN with unknown positive variance $0 < \sigma^2 < \infty$. The GLRT decides $\mathcal{H}_1$ if:

$$L_G(x) = \frac{p(x; \hat{A}, \hat{\sigma_1}^2, \mathcal{H}_1)}{p(x; \hat{\sigma_0}^2, \mathcal{H}_0)} > \gamma \tag{E.18}$$

where $\hat{A}$ and $\hat{\sigma_1}^2$ are the MLE of parameters A and σ_1^2 under $\mathcal{H}_1$, and $\hat{\sigma_0}^2$ is the MLE of the parameter σ_0^2 under $\mathcal{H}_0$. By maximizing $p(x; A, \sigma^2, \mathcal{H}_1)$, parameters $\hat{A}$ and $\hat{\sigma_1}^2$ are obtained as follows [43]:

$$\begin{aligned} p(x; A, \sigma^2, \mathcal{H}_1) &= \frac{1}{(2\pi\sigma^2)^{\frac{N}{2}}} \exp[-\frac{1}{2\sigma^2} \sum_{N=0}^{N-1} (x[n] - A)^2] \\ \frac{\partial p(x; A, \sigma^2, \mathcal{H}_1)}{\partial A} &= 0 \Rightarrow \hat{A} = \bar{x} \\ \frac{\partial p(x; A, \sigma^2, \mathcal{H}_1)}{\partial \sigma_1^2} &= 0 \Rightarrow \hat{\sigma_1}^2 = \frac{1}{N} \sum_{N=0}^{N-1} (x[n] - A)^2 \end{aligned} \tag{E.19}$$

which results in:

$$p(x; \hat{A}, \hat{\sigma_1}^2, \mathcal{H}_1) = \frac{1}{(2\pi\hat{\sigma_1}^2)^{\frac{N}{2}}} \exp(-\frac{N}{2}) \tag{E.20}$$

Similarly, by maximizing $p(x; \hat{\sigma_0}^2, \mathcal{H}_0)$, $\hat{\sigma_0}^2$ is obtained as follows:

$$\begin{aligned} p(x; \sigma^2, \mathcal{H}_0) &= \frac{1}{(2\pi\sigma^2)^{\frac{N}{2}}} \exp(-\frac{1}{2\sigma^2} \sum_{N=0}^{N-1} x^2[n]) \\ \frac{\partial p(x; \sigma^2, \mathcal{H}_0)}{\partial \sigma_0^2} &= 0 \Rightarrow \hat{\sigma_0}^2 = \frac{1}{N} \sum_{N=0}^{N-1} x^2[n] \end{aligned} \tag{E.21}$$

which results in:

$$p(x; \hat{\sigma_0}^2, \mathcal{H}_0) = \frac{1}{(2\pi\hat{\sigma_0}^2)^{\frac{N}{2}}} \exp(-\frac{N}{2}) \tag{E.22}$$

Therefore, (E.18) becomes:

$$L_G(x) = (\frac{\hat{\sigma_0}^2}{\hat{\sigma_1}^2})^{\frac{N}{2}} \tag{E.23}$$

which is equivalent to:

$$2lnL_G(x) = Nln\frac{\hat{\sigma_0}^2}{\hat{\sigma_1}^2} \tag{E.24}$$

From (E.19) and (E.21), $\hat{\sigma_1}^2$ can intuitively be obtained as follows:

$$\begin{aligned}\hat{\sigma_1}^2 &= \frac{1}{N}\sum_{N=0}^{N-1}(x[n]-A)^2 = \frac{1}{N}\sum_{N=0}^{N-1}(x[n]-\bar{x})^2 \\ &= \frac{1}{N}\sum_{N=0}^{N-1}(x[n]^2 - 2x[n]\bar{x}+\bar{x}^2) = \frac{1}{N}\sum_{N=0}^{N-1}x[n]^2 - \bar{x}^2 \\ &= \hat{\sigma_0}^2 - \bar{x}^2 \end{aligned} \tag{E.25}$$

which yields:

$$2lnL_G(x) = Nln(1+\frac{\bar{x}^2}{\hat{\sigma_1}^2}) \tag{E.26}$$

Since $ln(1+\frac{\bar{x}^2}{\hat{\sigma_1}^2})$ is monotonically increasing with respect to $\frac{\bar{x}^2}{\hat{\sigma_1}^2}$, an equivalent and normalized test statistic can be obtained as follows:

$$T(x) = \frac{\bar{x}^2}{\hat{\sigma_1}^2} > \gamma' \tag{E.27}$$

The GLRT has normalized the statistic by $\hat{\sigma_1}^2$ which allows the threshold to be determined. Since the PDF of $T(x)$ under null hypothesis $\mathcal{H}_0$ does not depend on σ^2, the threshold is independent of the value σ^2 [42].

E.6.3 GLRT for Large Data Records

As $N \longrightarrow \infty$, the asymptotic PDFs of $\bar{x}$ will converge to normal distributions under both hypotheses as follows:

$$\bar{x} \sim \begin{cases}\mathcal{N}(0,\sigma^2) & \text{under } \mathcal{H}_0 \\ \mathcal{N}(A,\sigma^2) & \text{under } \mathcal{H}_1\end{cases} \tag{E.28}$$

and therefore:

$$\frac{\bar{x}}{\sigma} \sim \begin{cases}\mathcal{N}(0,1) & \text{under } \mathcal{H}_0 \\ \mathcal{N}(\frac{A}{\sigma},1) & \text{under } \mathcal{H}_1\end{cases} \tag{E.29}$$

Squaring the normalized statistic in (E.29) will lead to the modified test statistic $T(x)$ in (E.27) which produces a central chi-squared distribution under $\mathcal{H}_0$ and a noncentral chi-squared distribution under $\mathcal{H}_0$, with one degree of freedom:

$$T(x) = \frac{\bar{x}^2}{\sigma^2} \sim \begin{cases}\mathcal{X}_1^2 & \text{under } \mathcal{H}_0 \\ \mathcal{X}'^2_1(\lambda) & \text{under } \mathcal{H}_1\end{cases} \tag{E.30}$$

where λ is the noncentrality parameter and is calculated as [42]:

$$\lambda = \frac{A^2}{\sigma^2} = \frac{\bar{x}^2}{\sigma^2} \tag{E.31}$$

It was shown in (E.30) that $T(x)$ has a noncentral chi-squared distribution with one degree of freedom, and it is equal to the square of random variable x in (E.29), therefore $x \sim \mathcal{N}(\sqrt{\lambda}, 1)$. Thus, the probability of a false alarm (P_{FA}) can be obtained as:

$$\begin{aligned} P_{FA} &= Pr\{T(x) > \gamma'; \mathcal{H}_0\} \\ &= Pr\{x > \sqrt{\gamma'}; \mathcal{H}_0\} + Pr\{x < -\sqrt{\gamma'}; \mathcal{H}_0\} \\ &= 2Q(\sqrt{\gamma'}) \end{aligned} \tag{E.32}$$

where $Q(x)$ is the right-tail probability of random variable x. Thus, the threshold can be obtained as follows:

$$\gamma' = [Q^{-1}(\frac{P_{FA}}{2})]^2 \tag{E.33}$$

Similarly, the probability of detection P_D can be obtained as follows:

$$\begin{aligned} P_D &= Pr\{T(x) > \gamma'; \mathcal{H}_1\} \\ &= Pr\{x > \sqrt{\gamma'}; \mathcal{H}_1\} + Pr\{x < -\sqrt{\gamma'}; \mathcal{H}_1\} \\ &= Q(\sqrt{\gamma'} - \sqrt{\lambda}) + Q(\sqrt{\gamma'} + \sqrt{\lambda}) \\ &= Q(Q^{-1}(\frac{P_{FA}}{2}) - \sqrt{\lambda}) + Q(Q^{-1}(\frac{P_{FA}}{2}) + \sqrt{\lambda}) \end{aligned} \tag{E.34}$$

E.6.4 GLRT Test on Residual Response

For the case study, the statistical detector should be designed in a way that it is able to detect even the smallest ITSC fault (¡1%). Therefore, the noncentrality parameter λ is calculated based on the implementation of (E.31) on the resultant residual at $t = 4.471$s–7.238 s when the motor is experiencing the lowest ITSC fault level in phase a winding and yields $\lambda = 6.78$. Using this value, the threshold and receiver operating characteristics (ROC) of the detector is obtained based on (E.32)–(E.34) and shown in Figure E.13. The P_{FA} values here are for the lowest ITSC fault level in phase a, which means other ITSC faults in phases b and c have lower P_{FA} values. Using $P_{FA} = 2\%$, the threshold is obtained as $\gamma' = 5.41$, and this results in $P_D = 60.93\%$ for ITSC in phase a. Furthermore, the probability of detection for ITSC faults in phases b and c and the encoder fault are calculated $P_D = 98.13\%$, $P_D = 100\%$, and $P_D = 99.65\%$, respectively.

The test statistics were implemented on the resultant residual as shown in Figure E.14. The values $\bar{x}^2$ and $\hat{\sigma_1}^2$ were calculated using a moving window (FIFO register) with the length of $N = 10,000$, which runs through the resultant residual over time. Figure E.14a shows the output of test statistic on resultant residual along with the threshold of $\gamma' = 5.41$ while Figure E.14b shows the output of the test statistic on R_4. The test statistic's output value is compared with the threshold value over time, and if it exceeds the threshold, the fault alarm is tripped accordingly. Figure E.15 shows the detector's logical output value which attains a low value in a healthy condition and a high value during a faulty case. This proves that the detector has successfully detected all the faults that are fairly close to expected values of P_D, while experiencing no false alarm.

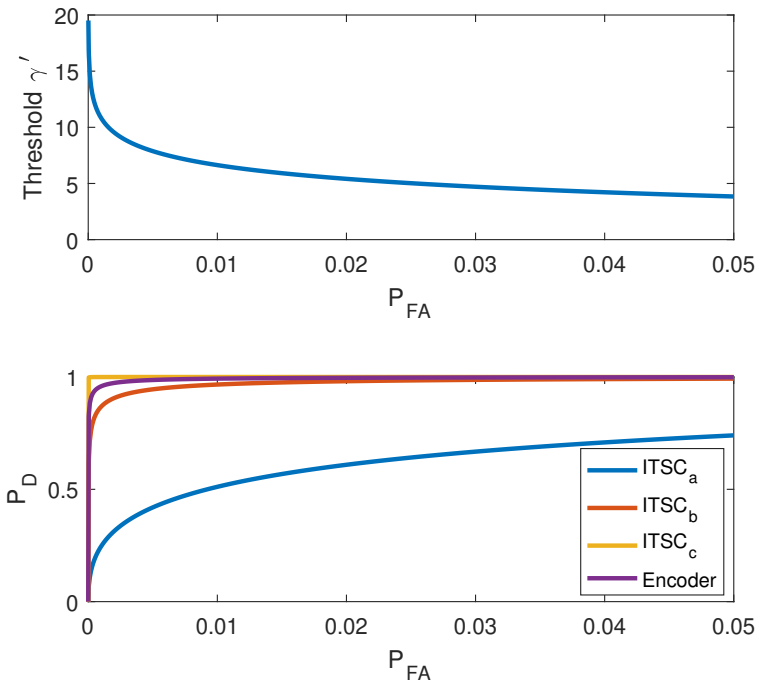

Figure E.13: Threshold and ROC for low values of P_{FA}.

E.7 Discussion

Some remarks can be withdrawn regarding the presented methodology and the obtained results. First, structural analysis for detecting ITSC and encoder faults was successfully implemented on the in-house setup including the PMSM and the drive system, and the residuals were formed based on ARRs. Second, a GLRT-based detector was designed to effectively detect the changes in the residuals even with unknown noise parameters. Third, a scientific threshold was calculated based on the probability of a false alarm (P_{FA}) and the probability of detection (P_D). The suggested combination method is very effective for the fault detection since it can detect the lowest level of ITSC fault, i.e., one single shorted turn (¡1%) in the stator winding. On the other hand, using a Clarke transformation disabled the diagnostic system to isolate the ITSC faults in different phases, and using a moving window with the length of $N = 10,000$ over the test statistics causes a delay in detection of the faults. These small demerits were found when testing the diagnostic method under the smallest ITSC fault.

In previous studies, a GLRT-based detector has been implemented for stator imbalance fault detection in induction motors [44]. The noise parameters were also considered unknown, and therefore, they have been replaced with their MLEs. Moreover, a threshold was calculated based on $P_{FA} = 0.1\%$ and P_D, which makes the diagnostic system experience fewer false alarms. However, the first fault level that the system can detect is 25% of stator-phase resistance, which is a quite high level of fault severity. As a result, the system would go into severe imbalance from the time that the fault appears until the time the diagnostic system detects it. In our case, even if the P_{FA} was chosen as 0.1%, the P_D for ITSC in phase a would be 24.61%, the P_D for ITSC in phase b would be 86.8%, the P_D for ITSC in phase c would be 99.99%, and the P_D for the encoder fault

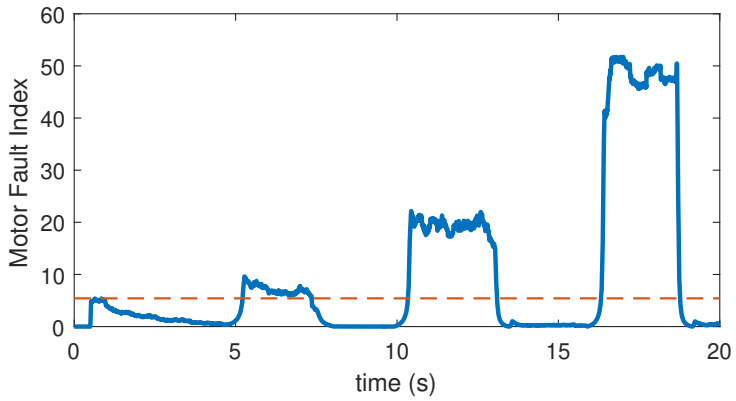

(a)

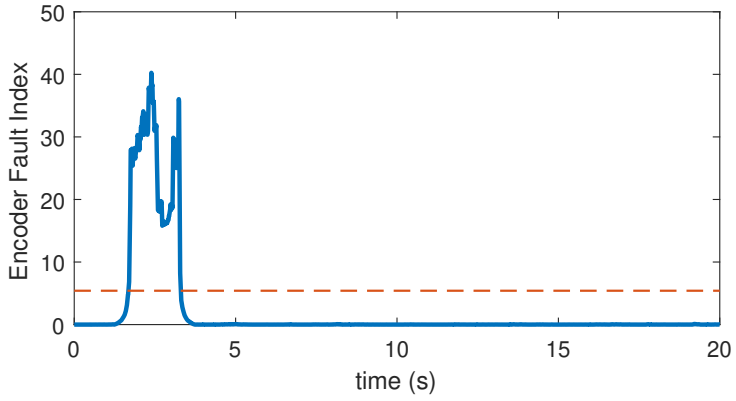

(b)

Figure E.14: Test statistic for ITSC fault and encoder faults.

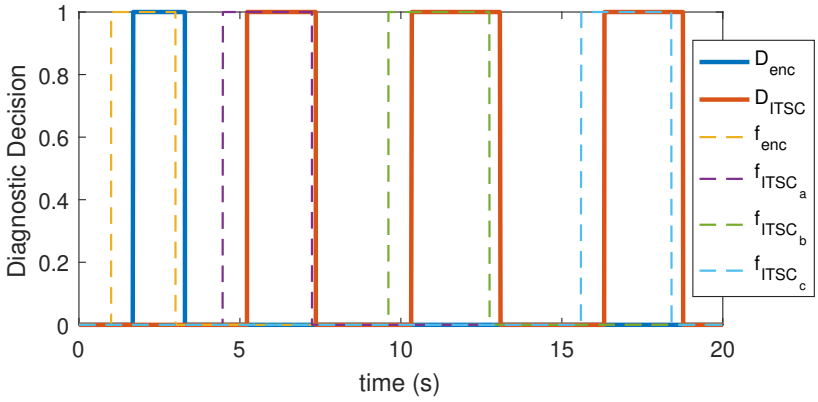

Figure E.15: Timing of actual faults ($f_{enc}, f_{ITSC_a}, f_{ITSC_b}, f_{ITSC_c}$) versus diagnostic system's decision (D_{enc}, D_{ITSC}).

would be 95.86%. Thus, the diagnostic system still detects the smallest fault, even with $P_{FA} = 0.1\%$. However, knowing that a slightly higher probability of a false alarm is not that irritating ($P_{FA} = 2\%$), a better probability of detection is achieved ($P_D = 60.93\%$) in our study based on setting a lower threshold. Other studies with different methods have also chosen a higher level of fault as the starting point. A Kalman filter for detection of

ITSC in PM synchronous generators has been implemented in [45], which can successfully detect fault levels as low as 8%. In addition, a combination of an extended Park's vector approach with spectral frequency analysis was introduced in [46] which could successfully detect three shorted turns in synchronous and induction motors.

E.8 Conclusions

This paper presents a novel method for real-time and effective detection of incipient ITSC and encoder faults in the PMSM. Structural analysis was employed to form the structural model of the PMSM. The Dulmage–Mendelsohn decomposition tool was used to evaluate the analytical redundancy of the structural model. The proposed diagnostic model was implemented on industrial PMSM, ITSC, and encoder faults were applied to the system in different time intervals, and residuals responses were obtained. Subsequently, a GLRT-based detector was designed and implemented based on the behavior of the residuals during healthy (only noise) and faulty (noise + signal) conditions. To make the GLRT-based detector effective to deal with such a realistic problem, the parameters such as mean μ and variance σ^2 in the probability density function of the noise signal were considered to be unknown. By replacing these unknown parameters by their maximum likelihood estimates, a test statistic was achieved for the GLRT-based ITSC and encoder fault detector. Following this step, a threshold was obtained based on choosing the probability of a false alarm P_{FA} and the probability of detection P_D for each detector based on which decision was made to indicate the presence of the fault. The experimental results show that the designed GLRT-based detector is able to efficiently detect even small ITSC and encoder faults in the presence of noise, proving the effectiveness of this diagnostic approach.

References

[1] Jun Hang, Han Wu, Jibo Zhang, Shichuan Ding, Yourui Huang, and Wei Hua. Cost function-based open-phase fault diagnosis for pmsm drive system with model predictive current control. *IEEE Transactions on Power Electronics*, 36(3):2574–2583, 2020.

[2] Xueqing Wang, Zheng Wang, Zhixian Xu, Jiangbiao He, and Wenxiang Zhao. Diagnosis and tolerance of common electrical faults in t-type three-level inverters fed dual three-phase pmsm drives. *IEEE Transactions on Power Electronics*, 35(2):1753–1769, 2019.

[3] Chong Zeng, Song Huang, Yongming Yang, and Dun Wu. Inter-turn fault diagnosis of permanent magnet synchronous machine based on tooth magnetic flux analysis. *IET Electric Power Applications*, 12(6):837–844, 2018.

[4] Bashir Mahdi Ebrahimi, Mehrsan Javan Roshtkhari, Jawad Faiz, and Seyed Vahid Khatami. Advanced eccentricity fault recognition in permanent magnet synchronous motors using stator current signature analysis. *IEEE Transactions on Industrial Electronics*, 61(4):2041–2052, 2013.

[5] Mohamed A Awadallah, Medhat M Morcos, Suresh Gopalakrishnan, and Thomas W Nehl. Detection of stator short circuits in vsi-fed brushless dc motors using wavelet transform. *IEEE Transactions on Energy Conversion*, 21(1):1–8, 2006.

[6] Sergio MA Cruz and AJ Marques Cardoso. Multiple reference frames theory: A new method for the diagnosis of stator faults in three-phase induction motors. *IEEE Transactions on Energy Conversion*, 20(3):611–619, 2005.

[7] Babak Vaseghi, Babak Nahid-Mobarakh, Noureddine Takorabet, and Farid Meibody-Tabar. Inductance identification and study of pm motor with winding turn short circuit fault. *IEEE Transactions on Magnetics*, 47(5):978–981, 2011.

[8] Seungdeog Choi, Moinul Shahidul Haque, Md Tawhid Bin Tarek, Vamsi Mulpuri, Yao Duan, Sanjoy Das, Vijay Garg, Dan M Ionel, M Abul Masrur, Behrooz Mirafzal, et al. Fault diagnosis techniques for permanent magnet ac machine and drives—a review of current state of the art. *IEEE Transactions on Transportation Electrification*, 4(2):444–463, 2018.

[9] Hong Liang, Yong Chen, Siyuan Liang, and Chengdong Wang. Fault detection of stator inter-turn short-circuit in pmsm on stator current and vibration signal. *Applied Sciences*, 8(9):1677, 2018.

[10] Jeevanand Seshadrinath, Bhim Singh, and Bijaya K Panigrahi. Vibration analysis based interturn fault diagnosis in induction machines. *IEEE Transactions on Industrial Informatics*, 10(1):340–350, 2013.

[11] Jun Hang, Jianzhong Zhang, Ming Cheng, and Jin Huang. Online interturn fault diagnosis of permanent magnet synchronous machine using zero-sequence components. *IEEE Transactions on Power Electronics*, 30(12):6731–6741, 2015.

[12] Wesley G Zanardelli, Elias G Strangas, and Selin Aviyente. Identification of intermittent electrical and mechanical faults in permanent-magnet ac drives based on time–frequency analysis. *IEEE Transactions on Industry Applications*, 43(4):971–980, 2007.

[13] Bilal Akin, Seungdeog Choi, Umut Orguner, and Hamid A Toliyat. A simple real-time fault signature monitoring tool for motor-drive-embedded fault diagnosis systems. *IEEE Transactions on Industrial Electronics*, 58(5):1990–2001, 2010.

[14] Antonio Garcia Espinosa, Javier A Rosero, Jordi Cusido, Luis Romeral, and Juan Antonio Ortega. Fault detection by means of hilbert–huang transform of the stator current in a pmsm with demagnetization. *IEEE Transactions on Energy Conversion*, 25(2):312–318, 2010.

[15] Najla Haje Obeid, Alexandre Battiston, Thierry Boileau, and Babak Nahid-Mobarakeh. Early intermittent interturn fault detection and localization for a permanent magnet synchronous motor of electrical vehicles using wavelet transform. *IEEE Transactions on Transportation Electrification*, 3(3):694–702, 2017.

[16] Javier A Rosero, Luis Romeral, Juan A Ortega, and Esteban Rosero. Short-circuit detection by means of empirical mode decomposition and wigner–ville distribution for pmsm running under dynamic condition. *IEEE Transactions on Industrial Electronics*, 56(11):4534–4547, 2009.

[17] Xiang-Qun Liu, Hong-Yue Zhang, Jun Liu, and Jing Yang. Fault detection and diagnosis of permanent-magnet dc motor based on parameter estimation and neural network. *IEEE transactions on industrial electronics*, 47(5):1021–1030, 2000.

[18] MA Awadallah and MM Morcos. Diagnosis of stator short circuits in brushless dc motors by monitoring phase voltages. *IEEE Transactions on Energy Conversion*, 20(1):246–247, 2005.

[19] Yaw Nyanteh, Chris Edrington, Sanjeev Srivastava, and David Cartes. Application of artificial intelligence to real-time fault detection in permanent-magnet synchronous machines. *IEEE Transactions on Industry Applications*, 49(3):1205–1214, 2013.

[20] Manuel A Mazzoletti, Guillermo R Bossio, Cristian H De Angelo, and Diego R Espinoza-Trejo. A model-based strategy for interturn short-circuit fault diagnosis in pmsm. *IEEE Transactions on Industrial Electronics*, 64(9):7218–7228, 2017.

[21] Gabriel Forstner, Andreas Kugi, and Wolfgang Kemmetmüller. A magnetic equivalent circuit based modeling framework for electric motors applied to a pmsm with winding short circuit. *IEEE Transactions on Power Electronics*, 35(11):12285–12295, 2020.

[22] Manel Fitouri, Yemna Bensalem, and Mohamed Naceur Abdelkrim. Modeling and detection of the short-circuit fault in pmsm using finite element analysis. *IFAC-PapersOnLine*, 49(12):1418–1423, 2016.

[23] Mattias Krysander. *Design and analysis of diagnosis systems using structural methods*. PhD thesis, Department of Electrical Engineering Linköping University, 2006.

[24] Mattias Krysander, Jan Åslund, and Mattias Nyberg. An efficient algorithm for finding minimal overconstrained subsystems for model-based diagnosis. *IEEE Transactions on Systems, Man, and Cybernetics-Part A: Systems and Humans*, 38(1):197–206, 2007.

[25] Mattias Krysander and Erik Frisk. Sensor placement for fault diagnosis. *IEEE Transactions on Systems, Man, and Cybernetics-Part A: Systems and Humans*, 38(6):1398–1410, 2008.

[26] Carl Svard and Mattias Nyberg. Residual generators for fault diagnosis using computation sequences with mixed causality applied to automotive systems. *IEEE Transactions on Systems, Man, and Cybernetics-Part A: Systems and Humans*, 40(6):1310–1328, 2010.

[27] Carl Svärd, Mattias Nyberg, and Erik Frisk. Realizability constrained selection of residual generators for fault diagnosis with an automotive engine application. *IEEE Transactions on Systems, Man, and Cybernetics: Systems*, 43(6):1354–1369, 2013.

[28] Carl Svärd, Mattias Nyberg, Erik Frisk, and Mattias Krysander. Automotive engine fdi by application of an automated model-based and data-driven design methodology. *Control Engineering Practice*, 21(4):455–472, 2013.

[29] Christofer Sundström, Erik Frisk, and Lars Nielsen. Selecting and utilizing sequential residual generators in fdi applied to hybrid vehicles. *IEEE Transactions on Systems, Man, and Cybernetics: Systems*, 44(2):172–185, 2013.

[30] Zhentong Liu, Qadeer Ahmed, Giorgio Rizzoni, and Hongwen He. Fault detection and isolation for lithium-ion battery system using structural analysis and sequential residual generation. In *ASME 2014 dynamic systems and control conference*. American Society of Mechanical Engineers Digital Collection, 2014.

[31] Jiyu Zhang, Hongyang Yao, and Giorgio Rizzoni. Fault diagnosis for electric drive systems of electrified vehicles based on structural analysis. *IEEE Transactions on Vehicular Technology*, 66(2):1027–1039, 2016.

[32] Saeed Hasan Ebrahimi, Martin Choux, and Van Khang Huynh. Diagnosis of sensor faults in pmsm and drive system based on structural analysis. In *2021 IEEE International Conference on Mechatronics (ICM)*, pages 1–6. IEEE, 2021.

[33] Saeed Hasan Ebrahimi, Martin Choux, et al. Detection and discrimination of inter-turn short circuit and demagnetization faults in pmsms based on structural analysis. In *2021 22nd IEEE International Conference on Industrial Technology (ICIT)*, volume 1, pages 184–189. IEEE, 2021.

[34] Bo Wang, Jiabin Wang, Antonio Griffo, and Bhaskar Sen. Stator turn fault detection by second harmonic in instantaneous power for a triple-redundant fault-tolerant pm drive. *IEEE Transactions on Industrial Electronics*, 65(9):7279–7289, 2018.

[35] Saeed Hasan Ebrahimi, Martin Choux, and Van Khang Huynh. Modeling stator winding inter-turn short circuit faults in pmsms including cross effects. In *2020 International Conference on Electrical Machines (ICEM)*, volume 1, pages 1397–1403. IEEE, 2020.

[36] Monia Ben Khader Bouzid and Gérard Champenois. New expressions of symmetrical components of the induction motor under stator faults. *IEEE Transactions on Industrial Electronics*, 60(9):4093–4102, 2012.

[37] Mogens Blanke, Michel Kinnaert, Jan Lunze, and Marcel Staroswiecki. Diagnosis and fault tolerant control, 2016.

[38] Mattias Krysander, Jan Åslund, and Erik Frisk. A structural algorithm for finding testable sub-models and multiple fault isolability analysis. In *21st International Workshop on Principles of Diagnosis (DX-10), Portland, Oregon, USA*, pages 17–18, 2010.

[39] Andrew L Dulmage and Nathan S Mendelsohn. Coverings of bipartite graphs. *Canadian Journal of Mathematics*, 10:517–534, 1958.

[40] Jiyu Zhang and Giorgio Rizzoni. Selection of residual generators in structural analysis for fault diagnosis using a diagnosability index. In *2017 IEEE Conference on Control Technology and Applications (CCTA)*, pages 1438–1445. IEEE, 2017.

[41] Richard W Hamming. Error detecting and error correcting codes. *The Bell system technical journal*, 29(2):147–160, 1950.

[42] Steven M Kay. *Fundamentals of Statistical Signal Processing, Volume II: Detection Theory*. Prentice Hall PTR, 1998.

[43] Steven M Kay. *Fundamentals of Statistical Signal Processing, Volume I: Estimation Theory*. Prentice Hall PTR, 1993.

[44] Elhoussin Elbouchikhi, Yassine Amirat, Gilles Feld, and Mohamed Benbouzid. Generalized likelihood ratio test based approach for stator-fault detection in a pwm inverter-fed induction motor drive. *IEEE Transactions on Industrial Electronics*, 66(8):6343–6353, 2018.

[45] Brice Aubert, Jeremi Regnier, Stephane Caux, and Dominique Alejo. Kalman-filter-based indicator for online interturn short circuits detection in permanent-magnet synchronous generators. *IEEE Transactions on Industrial Electronics*, 62(3):1921–1930, 2014.

[46] Sergio MA Cruz and AJ Marques Cardoso. Stator winding fault diagnosis in three-phase synchronous and asynchronous motors, by the extended park's vector approach. *IEEE Transactions on industry applications*, 37(5):1227–1233, 2001.

Paper F

Statistical Detection of Demagnetization and Inter-Turn Short Circuit Faults in PMSM Using Recursive GLRT with Adaptive Threshold

Saeed Hasan Ebrahimi, Martin Choux, and Van Khang Huynh

This paper has been submitted as:

S. H. Ebrahimi, M. Choux, and V. K. Huynh. Statistical Detection of Demagnetization and Inter-Turn Short Circuit Faults in PMSM Using Recursive GLRT with Adaptive Threshold. Under review in *IEEE Transactions on Industrial Electronics*, 2022. ISSN 0278-0046.

Statistical Detection of Demagnetization and Inter-Turn Short Circuit Faults in PMSM Using Recursive GLRT with Adaptive Threshold

Saeed Hasan Ebrahimi, Martin Choux, and Van Khang Huynh

Department of Engineering Sciences
University of Agder
NO-4879 Grimstad, Norway

Abstract – This paper presents a real-time model-based technique for detecting two common faults in permanent magnet synchronous motors, namely demagnetization and inter-turn short circuit faults. A structural analysis is implemented on the dynamic mathematical model of the PMSM in *abc* and *dq* reference frames to evaluate the system's structural model in matrix form. In addition, specific additive fault terms are added to the model to account for the distortion caused by demagnetization and inter-turn short circuit faults. To extract the analytical redundant part of the system, a Dulmage–Mendelsohn decomposition is applied to the structural model, separating the model into just-determined and over-determined parts. The analytical redundant relations in the over-determined part of the system are used to form smaller minimally redundant testable sub-models based on the number of defined fault terms. Using the acquired redundant sub-models, several structured residuals are designed to detect inter-turn and demagnetization faults. Further, the proposed model is validated on an inverter-fed permanent magnet synchronous motor, and experimental results are obtained to verify the effectiveness of the model. The faults are applied at different levels and time intervals using external controllable relays and the real-time controller. Finally, a statistical decision-making diagnostic system is designed based on generalized likelihood ratio test considering unknown noise parameters, fault level, and arrival time. A recursive cumulative algorithm is set on the GLRT to obtain an adaptive threshold, which results in the detection of all the studied faults with low detection and recovery time delay, and without facing any false alarm.

F.1 Introduction

Permanent magnet synchronous motors (PMSMs) have gained a lot of interest in electric vehicles, robotic systems, and offshore applications because of their high efficiency, high power density, and high controllability [3–5]. To prevent costly downtimes, high maintenance costs, and catastrophic system breakdowns, condition monitoring and fault detection of PMSMs have been among interesting topics in both industry and academia [6]. Faults in PMSMs can be categorized as electrical, mechanical, and magnetic faults that occur due to electrical, thermal, and mechanical stresses in industrial environments [7]. According to surveys in [8–10], 80% of motor stator faults begin as inter-turn short circuit (ITSC) fault while ITSC alone, accounts for $21-37\%$ of all faults in PMSMs. In addition,

demagnetization fault has been continuously reported in PMSMs due to the growing use of these motors in industrial applications [11]. Permanent magnets (PMs) are among the most critical and expensive materials used in PMSMs, and the motor's performance, efficiency, and reliability heavily depend on them [12].

Previous studies have investigated the detection of demagnetization and ITSC faults using various approaches. Most researchers have used time-frequency analysis tools such as Fourier transform [13], matched filters [14], Hilbert-Haung transform [15], wavelet transforms [16], and Cohen distributions [17]. These mathematical tools are employed to process and monitor harmonic components of motor signals such as current [18], voltage [19], magnetic-flux [20], and torque signals [21] or external sensor signals such as acoustic behavior [22] and vibration signals [23] and find anomalies that appear during the presence of faults. Although proven to be very powerful detection techniques, these signal-processing-based diagnosis tools have faced implementation challenges in real-time processors due to computational complexity. Some other researchers have proposed data-driven approaches such as artificial neural network (ANN) [24–26] and Fuzzy systems [27, 28] which perform healthy-faulty classification by extracting features of data. These data-driven techniques require a lot of data for training from both healthy and faulty conditions to operate in a robust and reliable way, and this is considered as a drawback of such methods [25]. As an alternative solution to signal-based and data-driven approaches, various types of model-based methods have been proposed to overcome the mentioned technicalities. One of the reasons that model-based methods have gained popularity over other diagnosis techniques is their ease of implementation. These models require neither powerful DSPs for real-time implementation, nor a lot of data for training, although, one common dispute is that these models are dependent on motor parameters and their performance is affected by model uncertainties. Nevertheless, model-based methods have been used extensively to detect ITSC and demagnetization faults in electric motors [29–32]. Among model-based approaches, finite-element method (FEM) based models are recommended by many researchers since they have shown promising analysis accuracy, especially regarding the location of the fault and the unbalance caused by it. However, since these FEM-based models operate based on valid equations and physical considerations, they require a rather deep knowledge of the system, e.g. detailed dimensions and material characteristics which also makes them computational-heavy and time-demanding [11]. Therefore, structural analysis based on lumped-parameter models in *abc* or *dq* frames is proposed as a decent solution that is fast enough to be used in real-time diagnostics and yet does not require a deep prior knowledge of the system dynamics [33]. The theoretical basis of structural analysis has been well presented and developed in the literature [34, 35] and has been applied to different electrical and mechanical systems. The structural analysis approach has been able to successfully detect faults in automotive engine [36], hybrid vehicle [37], and electric drive [33] systems. In our previous study [38], this algorithm was implemented on PMSM and drive system to detect ITSC and sensor faults. In this paper we aim to achieve:

- Detection of internal physical motor faults based on structural analysis, namely ITSC and reversible demagnetization faults

- Detection of the lowest level of ITSC fault, with 1 shorted turn in stator phase winding
- Early detection of ITSC and demagnetization fault
- Modeling of the noise in drive system measurement signals, with unknown amplitude and variance
- Improving the detection by implementing a recursive cumulative GLRT with adaptive threshold algorithm

In this paper, a systematic fault diagnosis methodology based on structural analysis for detection of ITSC and demagnetization faults in PMSMs are presented. The following sections of the paper are arranged as follows: In section. F.2, a summary of ITSC and demagnetization faults and their effects on behavior of the motor is given. Section. F.3 presents structural analysis of PMSM and drive system, using a dynamic mathematical model of PMSM defined in *dq* frame. Specific fault terms are added to relevant equations to account for the deviations caused by with ITSC and demagnetization faults. Using a Dulmage-Mendelsohn decomposition tool, the analytical redundant part of the structural model is extracted and divided into minimally over-determined sub-systems. Using these, residuals are designed which are sensitive to the presence of the targeted faults. In section. F.4, the proposed model is implemented on a real-time PMSM drive system and experimental results are obtained. Section. F.5, a generalized likelihood ratio test detector is designed to be used as a statistical decision-making system.

F.2 Effect of Demagnetization and ITSC Faults on Motor Signals

In order to form a model of the PMSM under demagnetization and ITSC faults, it is necessary to understand how the motor signals are influenced by these two common faults. In the following subsections, the effect of demagnetization and ITSC faults on PMSM signals are explained.

F.2.1 Demagnetization Fault

Permanent magnets are used in the structure of PMSMs to achieve high power density, efficiency, and controllability. PMs can experience reversible or irreversible demagnetization due to thermal stress, external magnetomotive force (MMF), electrical stress, and environmental factors. Since PMs are among the most critical and expensive materials used in PMSMs, it is important to monitor and detect demagnetization faults to prevent efficiency loss, increased vibration, and rotor faults. A PM material is described by its magnetic hysteresis loop. For investigating demagnetization behavior, the second quadrant of the B-H curve must be focused on. This quadrant is also known as the demagnetization curve and depicts how the magnetic flux density is influenced by the intensity of the reverse field. The demagnetization curve is linear over a range and has

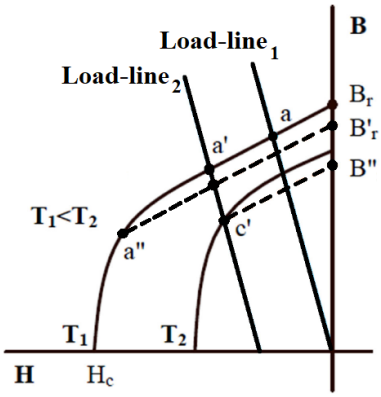

Figure F.1: Demagnetization of a permanent magnet

a sharp drop near the knee point. Fig. F.1 shows the demagnetization curve of NdFeB PM used in PMSMs, affected by the impact of reverse MMF as well as heat. Assuming that the normal operating point of the PMSM is at point a and it moves to point a' due to load change or an external MMF such as terminal short-circuit. After the magnetic field is removed, the PM follows the dashed line $a' - B_r$ whereas the original residual flux density of B_r is restored after experiencing a temporary reversible demagnetization. In a different scenario, the normal operating point of the PMSM at point a might move to point a'' due to loading or a milder external MMF. After the magnetic field is removed, the PM follows the dashed line $a'' - B'_r$ which causes the residual flux density to move from B_r under the normal case to a lower value of B'_r after experiencing temporary stress. In this case, an irreversible demagnetization has occurred since the residual flux density of B_r is not restored.

In addition to external MMF, heat can also facilitate the demagnetization occurrence by shrinking the B-H curve. Assuming that the temperature rises from T_1 to T_2 for a PMSM whose normal operating point is at point a', Fig. F.1 shows how the operating point is displaced from a' to c' even under normal condition. Given the fact that c' is under the knee of the demagnetization curve, the PM follows the recoil line $c' - B''_r$ after the magnetic field is removed. In this case, even if the temperature decreases back to T_1, the operating point does not follow the previous demagnetization curve and its recoil line will be similar to $a'' - B'_r$. As a result, an irreversible demagnetization has occurred due to the loss of magnetic properties of the PM.

Depending on the root cause, demagnetization may occur with either a symmetric or asymmetric pattern in PMSMs. In both cases, the flux established by the PMs in the whole machine is reduced which can be used as a reliable indicator for the detection of such faults. Different studies have used indicators such as the flux linkage, variation of modeled inductance [39, 40], and the shift of d and q axis flux linkage (λ_d and λ_q) compared with the healthy condition for detecting demagnetization in PM machines [40]. For BLDC motors with trapezoidal flux, the torque constant K_t is used as an indicator of demagnetization fault [41, 42].

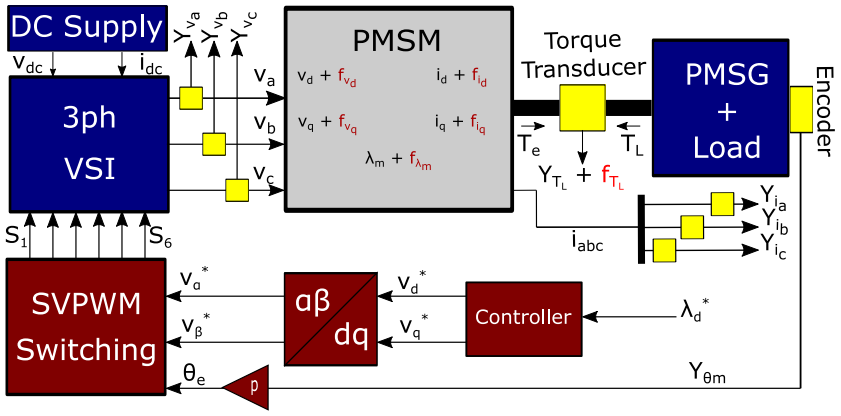

Figure F.2: Modeling diagram of PMSM and drive system.

F.2.2 Inter-Turn Short Circuit Fault

The fault model proposed in [43] is chosen as the reference model for investigating ITSC fault in PMSM. In this model, the level of ITSC faults in *abc* phases are denoted by μ_a, μ_b, and μ_c (defined as the ratio of the number of shorted turns to the total number of turns per *abc* phase-windings). In a healthy condition, each phase-winding of PMSM has a resistance of R_s and an inductance of L_s. In the presence of ITSC faults in each phase, the phase-winding is split into a faulty part with μR_s and μL_s, and also a healthy part with $(1-\mu)R_s$ and $(1-\mu)L_s$ resistance and inductance values. In addition, the degraded resistance of the insulation in each phase is denoted by R_{af}, R_{bf}, and R_{cf} while the circulating fault currents are i_{af}, i_{bf}, and i_{cf}, respectively.

F.3 Structural Analysis for PMSM under Demagnetization and ITSC Fault

A structural analysis algorithm is implemented on the PMSM and drive system to extract the analytic redundant relations (ARRs) of the system [44,45]. First, the structural model of this redundant PMSM and drive system is formed using the mathematical equations that describe the system's dynamic. The structural model is shown in the form of an incidence matrix where each row represents an equation and connects it to variables in the corresponding columns if they are present in that specific equation. To obtain the ARRs, the structural model needs to be reorganized in a way that the over-determined, just-determined, and under-determined parts of the system are separated. This is achieved by using a Dulmage–Mendelsohn (DM) decomposition tool which rearranges the rows and columns of the structural model to form a diagonal structure. The over-determined part of the structure is then used to form several minimally over-constrained relations which are used in constructing residuals that detect specific faults. Fig. F.2 shows the modeling diagram of the studied PMSM and the drive system including demagnetization and ITSC fault terms, sensor measurements, and control units.

F.3.1 PMSM Mathematical Model

The first step in implementing structural analysis is defining the mathematical model of the studied system. The dynamic equations of a PMSM and drive system are represented by equations $e_1 - e_{10}$ as shown in Eq. (F.1), where v_d and v_q are stator dq voltages; v_a, v_b, and v_c are stator phase voltages; i_d and i_q are stator dq currents; i_a, i_b, and i_c are stator phase currents; T_e is the electromagnetic torque, T_L is the Load torque; ω_m is the rotor's angular speed; θ is the electric angular position; R_s is the stator phase resistances; L_d are L_q are the stator dq inductances; λ_m is the flux established by PMs; p is pole pairs; J is the rotor inertia, and b is the friction coefficient.

ITSC and demagnetization faults may have different signatures, but both influence the flux and currents of the PMSM. Therefore, to account for the deviations caused by these two faults, specific fault terms are added to relevant equations. Here, f_{v_d} and f_{v_q} terms are added to the equations e_1 and e_2 to include the effect of flux deviation caused by either of the faults. Similarly, f_{i_d} and f_{i_q} terms are added to the equations e_5 and e_6 to account for the changes in stator dq currents caused by faults. These fault terms are shown by red color in Eq. (F.1).

$$
\begin{aligned}
e_1 :& v_d = \frac{2}{3}[v_a \cos\theta_e + v_b \cos(\theta_e - 2\pi/3) \\
& + v_c \cos(\theta_e + 2\pi/3)] + f_{v_d} \\
e_2 :& v_q = -\frac{2}{3}[v_a \sin\theta_e + v_b \sin(\theta_e - 2\pi/3) \\
& + v_c \sin(\theta_e + 2\pi/3)] + f_{v_q} \\
e_3 :& \frac{di_d}{dt} = \frac{1}{L_d}[v_d - R_s i_d + p\omega_m L_q i_q] \\
e_4 :& \frac{di_q}{dt} = \frac{1}{L_q}[v_q - R_s i_q - p\omega_m L_d i_d - p\omega_m \lambda_m] \\
e_5 :& i_d = \frac{2}{3}[i_a \cos\theta_e + i_b \cos(\theta_e - 2\pi/3) \\
& + i_c \cos(\theta_e + 2\pi/3)] + f_{i_d} \\
e_6 :& i_q = -\frac{2}{3}[i_a \sin\theta_e + i_b \sin(\theta_e - 2\pi/3) \\
& + i_c \sin(\theta_e + 2\pi/3)] + f_{i_q} \\
e_7 :& T_e = \frac{3}{2}p[(L_d - L_q)i_d + \lambda_m]i_q + f_{\lambda_m} \\
e_8 :& \frac{d\omega_m}{dt} = \frac{1}{J}(T_e - b\omega_m - T_L) \\
e_9 :& \frac{d\theta_e}{dt} = p\omega_m
\end{aligned}
\tag{F.1}
$$

The equations defined in Eq. (F.1) contain three different types of variables, i.e. unknown variables, known variables, and faults. As faults were identified, known variables must also be defined which leaves just unknown variables to be determined in the structural analysis. The known variables here consist of the motor signals which are measured via sensors and include y_{i_a}, y_{i_b}, and y_{i_c} as three-phase currents; y_{v_a}, y_{v_b}, and y_{v_c} as three-phase

voltages; y_θ as angular speed; and y_{T_L} as load torque. The known variables are organized in their own set of equations, as shown in Eq. (F.2).

$$\begin{aligned} &m1 : y_{v_a} = v_a \quad m4 : y_{i_a} = i_a \quad m7 : y_{\theta_e} = \theta_e \\ &m2 : y_{v_b} = v_b \quad m5 : y_{i_b} = i_b \quad m8 : y_{T_L} = T_L \\ &m3 : y_{v_c} = v_c \quad m6 : y_{i_c} = i_c \end{aligned} \tag{F.2}$$

In addition to dynamic equations and measurements, several differential constraints must be also included in the mathematical model. These differential constraints have appeared in Eq. (F.1) and contain differentials of unknown variables i_d, i_q, ω_m, and θ_e. Eq. (F.3) shows the differential constraints for the structural model.

$$\begin{aligned} &d1 : \frac{di_d}{dt} = \frac{d}{dt}(i_d) \quad d3 : \frac{d\theta_e}{dt} = \frac{d}{dt}(\theta_e) \\ &d2 : \frac{di_q}{dt} = \frac{d}{dt}(i_q) \quad d4 : \frac{d\omega_m}{dt} = \frac{d}{dt}(\omega_m) \end{aligned} \tag{F.3}$$

F.3.2 Structural Representation of the PMSM Model

Using the algorithm proposed by [46], the structural model of PMSM with ITSC and demagnetization faults is extracted based on the redundant dynamic model in Eqs. (F.1)-(F.3) and shown in Fig. F.3. The structural model is portrayed in form of an incidence matrix that contains 21 rows, representing the nine dynamic equations in Eq. (F.1), eight measured known variables in Eq. (F.2), and the four differential constraints of unknown variables as defined in Eq. (F.3). The columns of the incidence matrix represent model variables and are categorized as unknown variables (blue dots), known variables (red dots), and fault variables (black dots). Each row of the incidence matrix represents an equation in the model and is connected to the corresponding variables if they are present in that specific equation.

F.3.3 Analytical Redundancy of the Model

The next step is to analyze the analytic redundancy of structural model by using a Dulmage-Mendelsohn (DM) decomposition tool. When DM decomposition is applied on the structural model, an upper triangle structure is obtained by rearranging of the rows and the columns of the incidence matrix. Subsequently, the structural model is subdivided into three main parts, the over-determined part M^+ with more equations than variables, the just-determined part M^0, and the under-determined part M^-. The structurally over-determined part of the model M^+ is where faults are observable and detectable if included. Fig. F.4 shows the DM decomposition for PMSM structural model, where the analytic redundant part is expressed in the middle box and contains all the faults. Therefore, this part is chosen for the extracting set of ARRs which can be used in forming residuals sensitive to the presence of a fault.

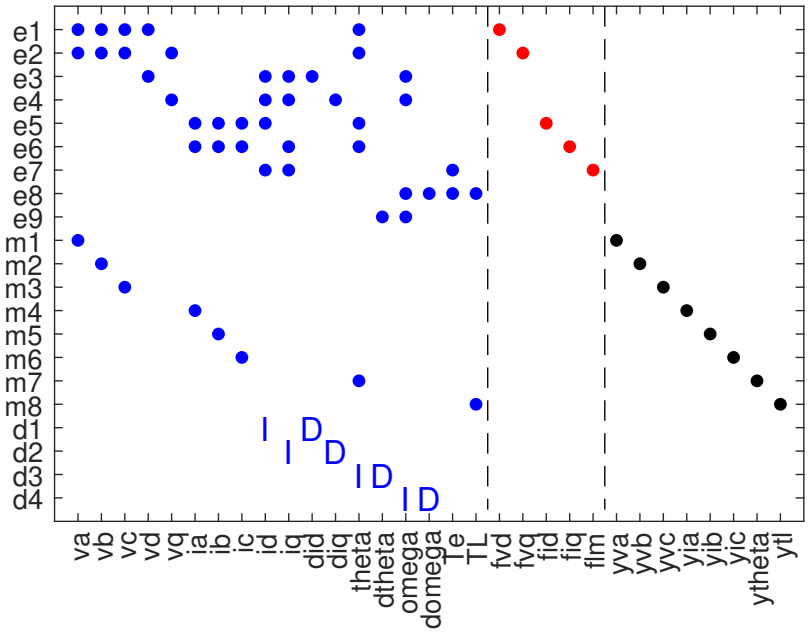

Figure F.3: PMSM structural model.

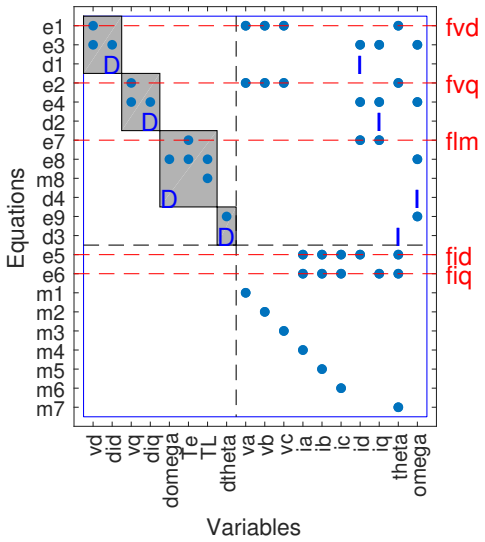

Figure F.4: DM decomposition for PMSM structural model.

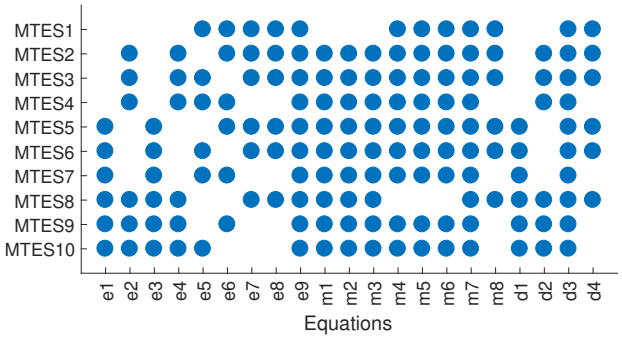

Figure F.5: MTES sets.

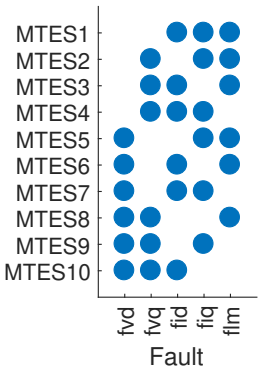

Figure F.6: Fault signature matrix of MTES sets.

F.3.4 Minimal Testable Sub-Models and Fault Signature

To obtain set of ARRs, efficient redundant testable sub-models called Minimal Test Equation Support (MTES) sets must be extracted. An MTES set is a group of ARRs which has a minimal degree of redundancy as 1, meaning that there is only one equation more than the number of variables involved. In the process of obtaining MTES sets, the effect of faults is considered which reduces computational complexity significantly without decreasing the possible diagnosis performance. The MTES sets of the considered structural model here are found and shown in Fig. F.5. The signature matrix of MTES sets is shown in Fig. F.6, indicating the fault terms are included in each MTES set.

F.3.5 Sequential Residuals for Detecting Faults

In this section, five sequential residuals ($R_1 - R_5$) are derived based on the obtained MTES sets that yield the highest distance [38, 46]. These residuals aim to provide strong sensitivity to added fault terms in the PMSM equations and are obtained as follows:

1. R_1: $MTES_2$ is used for deriving R_1 based on the error between calculated and measured electromagnetic torque T_e, i.e e_7 in Eq. (F.1):

$$e_7 : R_1 = T_e - \frac{3}{2} p[(L_d - L_q) i_d + \lambda_m] i_q \tag{F.4}$$

2. R_2: $MTES_4$ is used for deriving R_2 based on the error between calculated and

measured q-axis voltage v_q, i.e e_2 in Eq. (F.1):

$$e_2 : R_2 = v_q + \frac{2}{3}[v_a \sin\theta_e + v_b \sin(\theta_e - 2\pi/3) + v_c \sin(\theta_e + 2\pi/3)] \tag{F.5}$$

3. R_3: $MTES_5$ is used for deriving R_3 based on the error between calculated and measured q-axis current i_q, i.e e_6 in Eq. (F.1):

$$e_6 : R_3 = i_q + \frac{2}{3}[i_a \sin\theta_e + i_b \sin(\theta_e - 2\pi/3) + i_c \sin(\theta_e + 2\pi/3)] \tag{F.6}$$

4. R_4: $MTES_6$ is used for deriving R_4 based on the error between calculated and measured d-axis current i_d, i.e e_5 in Eq. (F.1):

$$e_5 : R_4 = i_d - \frac{2}{3}[i_a \cos\theta_e + i_b \cos(\theta_e - 2\pi/3) + i_c \cos(\theta_e + 2\pi/3)] \tag{F.7}$$

5. R_5: $MTES_{10}$ is used for deriving R_5 based on the error between calculated and measured d-axis voltage v_d, i.e e_1 in Eq. (F.1):

$$e_5 : R_5 = v_d - \frac{2}{3}[v_a \cos\theta_e + v_b \cos(\theta_e - 2\pi/3) + v_c \cos(\theta_e + 2\pi/3)] \tag{F.8}$$

F.4 Experiments and Results

In this section, the proposed diagnostic model is validated through experimental analysis. An IE5-PS2R-100L4H-TPM140 manufactured by VEM is selected as the case study PMSM and the parameters are listed in Table F.1. Three levels of 1%, 3%, and 5% ITSC faults are applied to each phase of the PMSM three-phase windings. Three external resistors are connected to each phase's shorted part to represent the winding insulator degradation path as well as limiting the short-circuit circulating current. The full setup is shown in Fig. F.7 which consists of a motor-generator set coupled with torque transducer and rotary encoder, a 3-ph voltage source inverter with embedded voltage and current sensors, and controllable relays in between winding taps and fault resistors to activate or deactivate the fault. In addition, a dSpace MicroLabBox is used as the real-time interface device for implementing both drive strategy and data acquisition.

Using the drive strategy in Fig. F.2, the PMSM is started by setting a flux reference. After reaching the steady-state mode , the ITSC and reversible demagnetization faults are applied at different time intervals. ITSC faults applied using controllable relays while kept a constant reference on the flux controller. On the other hand, the reversible demagnetization faults are applied by creating a reverse field in the stator winding as opposed to the field of PMs on the rotor. This moves the operating point of the PM to another

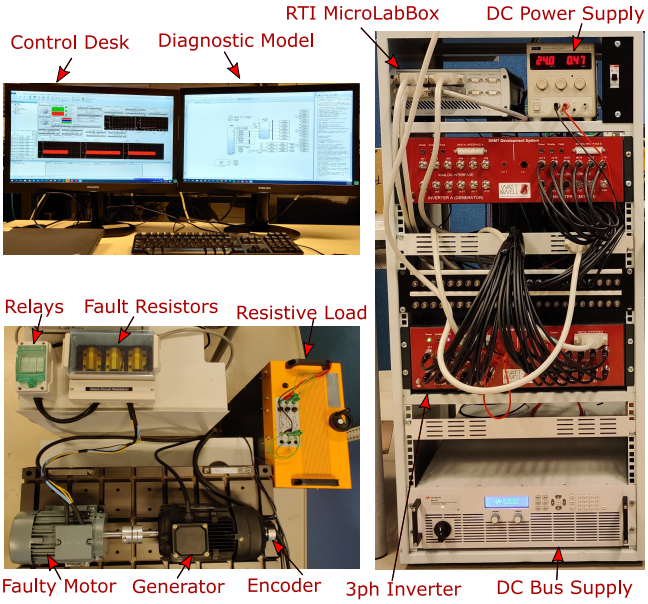

Figure F.7: Experimental Setup for Control and Diagnosis of PMSM

Table F.1: Parameters of PM Synchronous Motor

Symbol	Parameter	Value	Unit
V_{dc}	Rated dc bus voltage	280	V
I_s	Rated rms phase current	5	A
T_{out}	Rated Output Torque	7	$N.m$
n_s	Rated speed	1500	rpm
R_s	Phase resistance	0.8	Ω
L_s	Stator inductance	8.5	mH
J	Rotor inertia	0.0026	$kg.m^2$
b	Rotor damping factor	0.00382	$N.m.s/rad$
λ_m	Flux linkage of PMs	0.3509	Web
p	Pole-pairs	2	

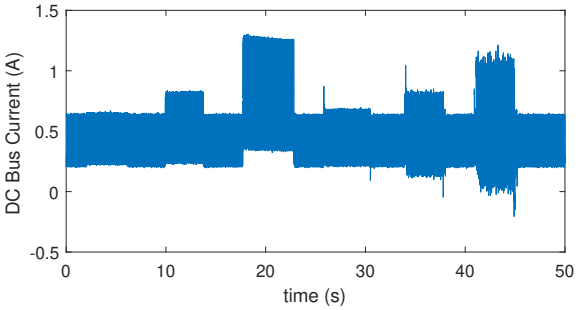

Figure F.8: DC bus current of PMSM drive.

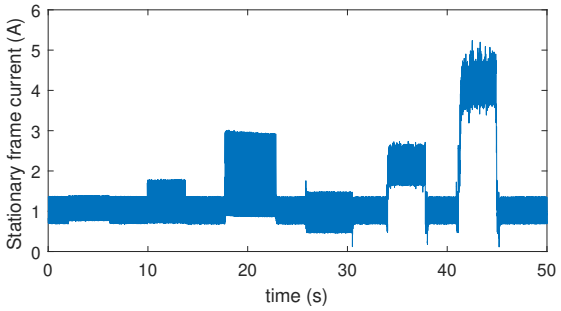

Figure F.9: Linkage flux in the PMSM.

point just above the knee in Fig. F.1 and hence, when the reverse field is removed, the original residual flux density of B_r is restored. This is done by controlling v_d and v_q reference voltages and using a field-weakening technique while keeping the terminal voltage constant. The severity of demagnetization faults are defined as:

$$f_{DM} = 1 - \frac{\lambda_{linkage_F}}{\lambda_{linkage_H}} \tag{F.9}$$

where $\lambda_{linkage_H}$ is the linkage flux under healthy condition and $\lambda_{linkage_F}$ is the weakened linkage flux after the demagnetization fault has appeared. At $t = 2.022 - 6.174s$, the ITSC fault in phase a is applied which has 1% fault severity (1 shorted turn in phase a winding); at $t = 9.918 - 13.73s$, the ITSC fault in phase b appears with 3% fault severity(3 shorted turn in phase a winding); at $t = 17.7 - 22.82s$, the ITSC fault in phase c with 5% fault severity (1 shorted turn in phase a winding) is applied. ; at $t = 25.83 - 30.48s$, the first reversible demagnetization with 2% severity is applied; at $t = 33.92 - 38.01s$, the second reversible demagnetization with 5% severity is applied; and at $t = 40.91 - 45.2s$, the second reversible demagnetization with 9% severity is applied on the PMSM. Fig. F.8 shows the real-time dc bus current signal where the ITSC faults have created an a step-up while demagnetization faults have caused oscillation. Fig. F.9 shows the real-time linkage flux signal where the ITSC faults have created oscillation while demagnetization faults have created an obvious step-down.

During the operation of the PMSM in $50s$, the real-time residual responses for the two group of faults, i.e. three levels of ITSC fault and three levels of demagnetization fault, are obtained and shown in Fig. F.10. Before each faults is applied, the motor is operating under healthy condition and all the residuals remain averagely zero, only containing noise.

Although the focus is on detection and not isolation, it is worth mentioning that the two group of faults cannot be separated from an structural analysis point of view due to the fact that all five residuals are sensitive to the presence of the introduced fault terms. Nevertheless, all the studied faults including the smallest ITSC, are detectable and this accomplishment is worth further processing. The residuals are affected differently by the faults. For instance, residuals R_1 and R_3 have a rather noisy behavior and respond to the presence of ITSC faults by obtaining a negative dc level, while trying to obtain a positive dc level for demagnetization faults. The response of residual R_4 to both group of faults is not satisfactory, since dc levels are very noisy and not very distinctive. Among all, residuals R_2 and R_5 show the best reactions to the presence of both group of faults by creating distinctive dc level changes and keeping an average zero value under healthy condition. Between these two, R_2 has a better dc level balance compared to R_5, showing lower distance between the lowest ITSC and the highest demagnetization fault levels. Hence, R_2 is selected as the most promising candidate for detection ITSC and demagnetization faults. Nevertheless, further signal processing is required to form an indicator and set a threshold independent of the probability of false-alarm and probability of detection while considering unknown noise parameters as nuisance factor. This is accomplished using generalized likelihood ratio test and explained in the following section.

F.5 Diagnostic Decision

Using the residual response R_2, a diagnostic decision making system is designed to detect the ITSC and demagnetization faults based on Generalized Likelihood Ratio Test (GLRT). GLRT is a composite hypothesis testing approach that can be used for detecting a signal in realistic problems. A huge advantage of GLRT is that it does not require prior knowledge of the unknown parameters such as mean (μ) and variance (σ^2) values in Probability Density Function (PDF) of a signal. The way GLRT deals with unknown parameters is to replace them by their Maximum Likelihood Estimates (MLEs). If data x has the PDF $p(x;\hat{\theta_0},\mathcal{H}_0)$ under null hypothesis $\mathcal{H}_0$ and $p(x;\hat{\theta_1},\mathcal{H}_1)$ under alternative hypothesis $\mathcal{H}_1$, the GLRT decides $\mathcal{H}_1$ if [47]:

$$L_G(x) = \frac{p(x;\hat{\theta_1},\mathcal{H}_1)}{p(x;\hat{\theta_0},\mathcal{H}_0)} > \gamma \tag{F.10}$$

where $\hat{\theta_1}$ is the MLE of θ_1 assuming $\mathcal{H}_1$ is true, $\hat{\theta_0}$ is the MLE of θ_0 assuming $\mathcal{H}_0$ is true, and γ is the threshold.

F.5.1 GLRT for unknown noise parameters and DC levels

First, it is assumed that arrival time of the fault is known (M) while the PDF of signal is not completely known, meaning the parameters mean μ and variance σ^2 are to be estimated using MLE. Furthermore, the noise in the residual signal under healthy condition is modeled as WGN. In a generalized form, the residual (R_1) has different dc levels (A_1 and A_2) before and after the jump time M. Therefore, it is assumed that $A_1 = A_2$ under

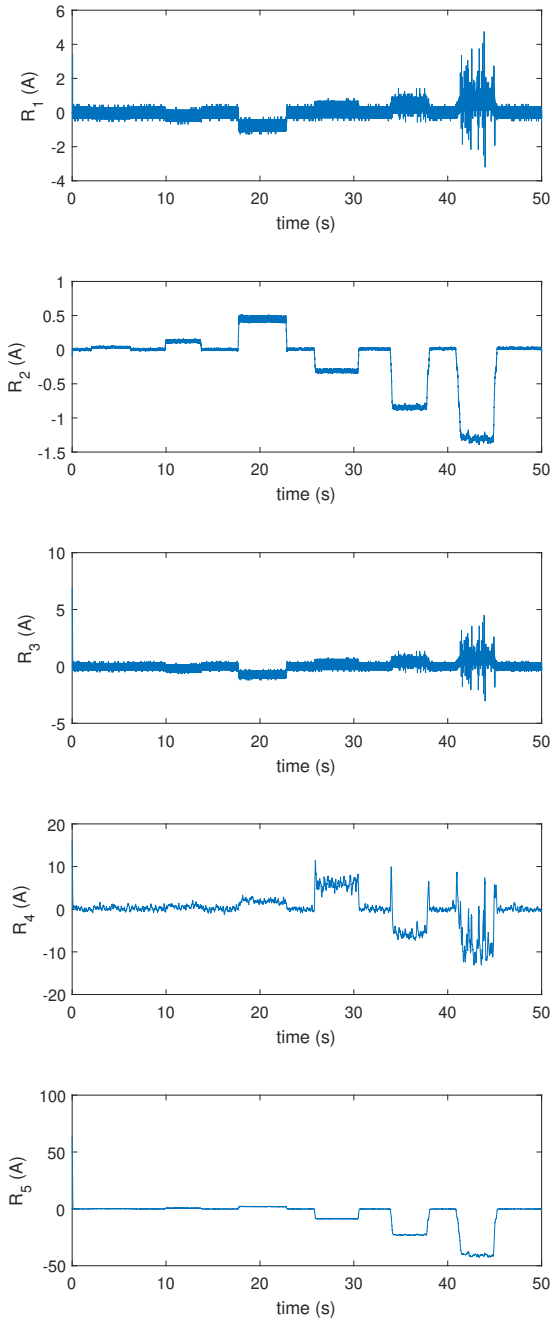

Figure F.10: Real-time residual signals.

non-faulty hypothesis $\mathcal{H}_0$, and $A_1 \neq A_2$ under faulty hypothesis $\mathcal{H}_1$. Thus, the detection problem becomes as follows:

$$\begin{aligned} \mathcal{H}_0 &: x[n] = A + w[n] \qquad n = 0, 1, ..., N-1 \\ \mathcal{H}_1 &: \begin{cases} x[n] = A_1 + w[n] & n = 0, 1, ..., M-1 \\ x[n] = A_2 + w[n] & n = M, ..., N-1 \end{cases} \end{aligned} \tag{F.11}$$

where the jump time occurs after M observations $0 < M < N-1$. The GLRT decides $\mathcal{H}_1$ if:

$$L_G(x) = \frac{p(x; \hat{A}_1, \hat{A}_2, \hat{\sigma_1}^2, \hat{\sigma_2}^2, \mathcal{H}_1)}{p(x; \hat{A}, \hat{\sigma_0}^2, \mathcal{H}_0)} > \gamma \tag{F.12}$$

where $\hat{A}$ and $\hat{\sigma_0}^2$ are the MLE of parameters A and σ_0^2 under $\mathcal{H}_0$ and $\hat{A}_1$, $\hat{A}_2$, $\hat{\sigma_1}^2$, and $\hat{\sigma_2}^2$ are the MLEs of the parameters A_1, A_2, σ_1^2, and σ_2^2 under $\mathcal{H}_1$. The MLEs are determined by maximizing $p(x; \hat{A}_1, \hat{A}_2, \hat{\sigma_1}^2, \hat{\sigma_2}^2, \mathcal{H}_1)$ and $p(x; \hat{A}, \hat{\sigma_0}^2, \mathcal{H}_0)$ over containing unknown parameters and are obtained as follows [1]:

$$\begin{aligned}
\hat{A} &= \frac{1}{N}\sum_{N=0}^{N-1} x[n], \qquad \hat{A}_1 = \frac{1}{M}\sum_{N=0}^{M-1} x[n] \\
\hat{A}_2 &= \frac{1}{N-M}\sum_{N=M}^{N-1} x[n], \quad \hat{\sigma_0}^2 = \frac{1}{N}\sum_{N=0}^{N-1}(x[n]-A)^2 \\
\hat{\sigma_1}^2 &= \frac{1}{M}\sum_{N=0}^{M-1}(x[n]-\hat{A}_1)^2, \quad \hat{\sigma_2}^2 = \frac{1}{N-M}\sum_{N=M}^{N-1}(x[n]-\hat{A}_2)^2
\end{aligned} \tag{F.13}$$

By using MLEs in the PDFs under $\mathcal{H}_0$ and $\mathcal{H}_1$, the Eq.F.12 becomes:

$$2lnL_G(x) = Nln(\frac{\hat{\sigma_0}^2}{(\hat{\sigma_1}^2)^{\frac{M}{N}}(\hat{\sigma_2}^2)^{\frac{N-M}{N}}}) > \gamma' \tag{F.14}$$

where $\gamma' = 2ln\gamma$.

F.5.2 GLRT for unknown noise parameters, DC levels, and arrival time

To account for the unknown jump time, it is assumed that it occurs far from the boundaries of the observation interval, i.e. $M_{min} < M < M_{max}$ where $M_{min} >> 0$ and $M_{max} << N-1$. Therefore, the GLRT decides $\mathcal{H}_1$ if:

$$L_G(x) = \frac{p(x; \hat{M}, \hat{A}_1, \hat{A}_2, \hat{\sigma_1}^2, \hat{\sigma_2}^2, \mathcal{H}_1)}{p(x; \hat{A}, \hat{\sigma_0}^2, \mathcal{H}_0)} > \gamma \tag{F.15}$$

where $\hat{M}$ is the MLE of arrival time M under $\mathcal{H}_1$. Equivalently:

$$L_G(x) = \frac{\max_M p(x; \hat{M}, \mathcal{H}_1)}{p(x; \mathcal{H}_0)} \tag{F.16}$$

Since the PDF under $\mathcal{H}_0$ does not depend on M and is non-negative, the test becomes:

$$L_G(x) = \max_M(2ln\frac{p(x; \hat{M}, \mathcal{H}_1)}{p(x; \mathcal{H}_0)}) > 2ln\gamma \tag{F.17}$$

And the GLRT decides $\mathcal{H}_1$ if:

$$L_G(x) = \max_M(Nln(\frac{\hat{\sigma_0}^2}{(\hat{\sigma_1}^2)^{\frac{M}{N}}(\hat{\sigma_2}^2)^{\frac{N-M}{N}}})) > \gamma' \tag{F.18}$$

where $\gamma' = 2ln\gamma$.

F.5.3 Recursive cumulative GLRT with adaptive threshold

In our previous study, it was noticed that using moving average and variance in forming the test statistic and a fixed threshold can cause detection and recovery delays and potentially false-alarms [38]. Here, a recursive cumulative GLRT with adaptive threshold and upper bounded is implemented to create a fault indicator based on the test statistic obtained in F.18 which can be used as the reference for decision-making system. This method helps reduce the time to detect motor faults, reduce the false alarm rate, revert to non-faulty case when a fault disappears, and increase the detection probability. The algorithm is described as follows [2]:

- Initialization:

$$\begin{aligned} h &= 90 \qquad \text{Upper bound} \\ \gamma_0 &= 40 \qquad \text{Initial threshold} \end{aligned}$$

- Loop

$$\begin{aligned} g_k &= L_G(x_k) - \gamma_{k-1} \\ \gamma_k &= L_G(x_k) - sign(L_G(x_k)) \min(|g_k|, |g_k - h|) \\ g_k &= max(0, g_{k-1} + g_k) \\ g_k &= min(h, g_k) \end{aligned} \tag{F.19}$$

- Result:

$$g_k \text{ for increasing time } t_k$$

F.5.4 GLRT Test and Decision Based on Residual Response

The GLRT test statistics of the faults $f_1 - f_6$ are obtained using Eq. F.18 and shown in Fig. F.11. Using the recursive cumulative GLRT with adaptive threshold algorithm in Eq. F.19, the fault indicators are determined (Fig. F.11). Since the recursive algorithm described in Eq. F.19 saturates the output signal between min and max values (0 and 90), false-alarm condition is not an issue anymore. In other terms, the probability of detection and false-alarm in not influenced by the threshold anymore. Therefore, an arbitrary threshold of 10 is chosen for the decision-making system.The fault indicator's output value is compared with the threshold value over time, and if it exceeds the threshold the fault alarm is tripped accordingly. Although the test statitics and fault indicators create only positive level in reaction to the presence of both group of faults, this does not imply that ITSC faults are not isolable from demagnetization fault. As shown in Fig. F.10, residual R_2 responds to the presence of ITSC and demagnetization faults by obtaining positive and negative dc levels, respectively. Thus, the residuals' response could be used alongside the fault indicators' to help segregate the faults. The decision for presence of faults $f_1 - f_6$ as well as the actual faults are shown in Fig. F.11. The detector's logical output value attains a low value in healthy condition and a high value during a faulty case. As can been seen, the detector has successfully detected all the faults, while experiencing no false alarm.

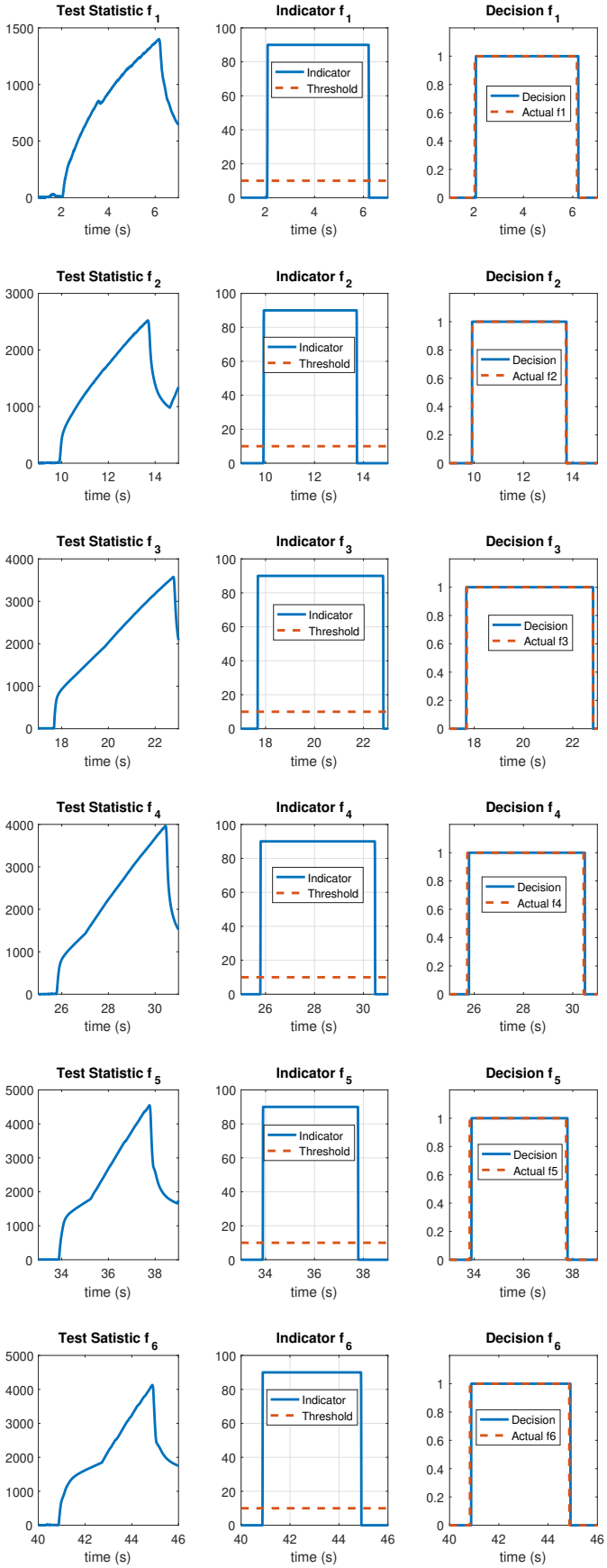

Figure F.11: Teat statistic, fault indicator, and decision of faults.

F.6 Conclusion

In this paper, a novel real-time method is presented for effective detection of ITSC and demagnetization faults in PMSM. Structural analysis is employed to form the structural model of the PMSM, based on its dynamic equations, measurements, and defined faults. DM decomposition tool is used to extract the analytical redundant part of the structural model where fault terms are observable, and the redundant part is used to form residuals which react to presence of specific faults by obtaining a nonzero value. The proposed diagnostic model is implemented on a 4-pole PMSM which experiences three levels of ITSC faults, namely 1%, 3%, and 5% as well as three levels of reversible demagnetization faults, namely 2%, 5%, and 9% in different time intervals. A GLRT-based detector is designed and implemented to deal with uncertainties created by noise in the residuals. In addition to unknown noise parameters, unknown arrival time is taken into consideration when designing the test statistic. Further, a recursive cumulative GLRT with adaptive threshold algorithm is implemented to obtain a more processed fault indicator that decreases the detection and recovery delay time. The fault indicator achieved by this recursive algorithm is compared to an arbitrary threshold and a decision is made in real-time performance. The experimental results show that the statistical detector is able to efficiently detect all the unexpected faults in the presence of unknown noise and without experiencing any false-alarm, proving the effectiveness of this diagnostic approach.

References

[1] Steven M Kay. *Fundamentals of Statistical Signal Processing, Volume I: Estimation Theory*. Prentice Hall PTR, 1993.

[2] Martin Choux, Mogens Blanke, and Geir Hovland. *Nonlinear, adaptive and fault-tolerant control for electro hydraulic servo systems*. DTU Electrical Engineering, 2011.

[3] Jun Hang, Han Wu, Jibo Zhang, Shichuan Ding, Yourui Huang, and Wei Hua. Cost function-based open-phase fault diagnosis for pmsm drive system with model predictive current control. *IEEE Transactions on Power Electronics*, 36(3):2574–2583, 2020.

[4] Xueqing Wang, Zheng Wang, Zhixian Xu, Jiangbiao He, and Wenxiang Zhao. Diagnosis and tolerance of common electrical faults in t-type three-level inverters fed dual three-phase pmsm drives. *IEEE Transactions on Power Electronics*, 35(2):1753–1769, 2019.

[5] Subhasis Nandi, Hamid A Toliyat, and Xiaodong Li. Condition monitoring and fault diagnosis of electrical motors—a review. *IEEE Transactions on Energy Conversion*, 20(4):719–729, 2005.

[6] Hongwen He, Nana Zhou, Jinquan Guo, Zheng Zhang, Bing Lu, and Chao Sun. Tolerance analysis of electrified vehicles on the motor demagnetization fault: From an energy perspective. *Applied Energy*, 227:239–248, 2018.

[7] Yuan Qi, Emine Bostanci, Vigneshwaran Gurusamy, and Bilal Akin. A comprehensive analysis of short-circuit current behavior in pmsm interturn short-circuit faults. *IEEE Transactions on Power Electronics*, 33(12):10784–10793, 2018.

[8] Mohamed A Awadallah, Medhat M Morcos, Suresh Gopalakrishnan, and Thomas W Nehl. Detection of stator short circuits in vsi-fed brushless dc motors using wavelet transform. *IEEE Transactions on Energy Conversion*, 21(1):1–8, 2006.

[9] Richard T Meyer, Raymond A DeCarlo, Scott C Johnson, and Steve Pekarek. Short-circuit fault detection observer design in a pmsm. *IEEE Transactions on Aerospace and Electronic Systems*, 54(6):3004–3017, 2018.

[10] Chunyan Lai, Aiswarya Balamurali, Vicki Bousaba, K Lakshmi Varaha Iyer, and Narayan C Kar. Analysis of stator winding inter-turn short-circuit fault in interior

and surface mounted permanent magnet traction machines. In *2014 IEEE Transportation Electrification Conference and Expo (ITEC)*, pages 1–6. IEEE, 2014.

[11] Seungdeog Choi, Moinul Shahidul Haque, Md Tawhid Bin Tarek, Vamsi Mulpuri, Yao Duan, Sanjoy Das, Vijay Garg, Dan M Ionel, M Abul Masrur, Behrooz Mirafzal, et al. Fault diagnosis techniques for permanent magnet ac machine and drives—a review of current state of the art. *IEEE Transactions on Transportation Electrification*, 4(2):444–463, 2018.

[12] Tomy Sebastian. Temperature effects on torque production and efficiency of pm motors using ndfeb magnets. *IEEE Transactions on Industry Applications*, 31(2):353–357, 1995.

[13] Wesley G Zanardelli, Elias G Strangas, and Selin Aviyente. Identification of intermittent electrical and mechanical faults in permanent-magnet ac drives based on time–frequency analysis. *IEEE Transactions on Industry Applications*, 43(4):971–980, 2007.

[14] Bilal Akin, Seungdeog Choi, Umut Orguner, and Hamid A Toliyat. A simple real-time fault signature monitoring tool for motor-drive-embedded fault diagnosis systems. *IEEE Transactions on Industrial Electronics*, 58(5):1990–2001, 2010.

[15] Antonio Garcia Espinosa, Javier A Rosero, Jordi Cusido, Luis Romeral, and Juan Antonio Ortega. Fault detection by means of hilbert–huang transform of the stator current in a pmsm with demagnetization. *IEEE Transactions on Energy Conversion*, 25(2):312–318, 2010.

[16] Najla Haje Obeid, Alexandre Battiston, Thierry Boileau, and Babak Nahid-Mobarakeh. Early intermittent interturn fault detection and localization for a permanent magnet synchronous motor of electrical vehicles using wavelet transform. *IEEE Transactions on Transportation Electrification*, 3(3):694–702, 2017.

[17] Javier A Rosero, Luis Romeral, Juan A Ortega, and Esteban Rosero. Short-circuit detection by means of empirical mode decomposition and wigner–ville distribution for pmsm running under dynamic condition. *IEEE Transactions on Industrial Electronics*, 56(11):4534–4547, 2009.

[18] Jongman Hong, Doosoo Hyun, Sang Bin Lee, Ji-Yoon Yoo, and Kwang-Woon Lee. Automated monitoring of magnet quality for permanent-magnet synchronous motors at standstill. *IEEE Transactions on Industry Applications*, 46(4):1397–1405, 2010.

[19] Jawad Faiz and Ehsan Mazaheri-Tehrani. Demagnetization modeling and fault diagnosing techniques in permanent magnet machines under stationary and nonstationary conditions: An overview. *IEEE Transactions on Industry Applications*, 53(3):2772–2785, 2016.

[20] Jewon Lee, Yong-Ju Jeon, Doo-chul Choi, SeungHun Kim, and Sang Woo Kim. Demagnetization fault diagnosis method for pmsm of electric vehicle. In *IECON*

2013-39th Annual Conference of the IEEE Industrial Electronics Society, pages 2709–2713. IEEE, 2013.

[21] Wiehan Le Roux, Ronald G Harley, and Thomas G Habetler. Detecting faults in rotors of pm drives. *IEEE Industry Applications Magazine*, 14(2):23–31, 2008.

[22] Dimitri Torregrossa, Amir Khoobroo, and Babak Fahimi. Prediction of acoustic noise and torque pulsation in pm synchronous machines with static eccentricity and partial demagnetization using field reconstruction method. *IEEE Transactions on Industrial Electronics*, 59(2):934–944, 2011.

[23] Zhi Yang, Xiaodong Shi, and Mahesh Krishnamurthy. Vibration monitoring of pm synchronous machine with partial demagnetization and inter-turn short circuit faults. In *2014 IEEE Transportation Electrification Conference and Expo (ITEC)*, pages 1–6. IEEE, 2014.

[24] Seyed Saeid Moosavi, Abdesslem Djerdir, Y Aït-Amirat, and DA Kkuburi. Artificial neural networks based fault detection in 3-phase pmsm traction motor. In *2012 XXth International Conference on Electrical Machines*, pages 1579–1585. IEEE, 2012.

[25] Yaw Nyanteh, Chris Edrington, Sanjeev Srivastava, and David Cartes. Application of artificial intelligence to real-time fault detection in permanent-magnet synchronous machines. *IEEE transactions on industry applications*, 49(3):1205–1214, 2013.

[26] Xiang-Qun Liu, Hong-Yue Zhang, Jun Liu, and Jing Yang. Fault detection and diagnosis of permanent-magnet dc motor based on parameter estimation and neural network. *IEEE transactions on industrial electronics*, 47(5):1021–1030, 2000.

[27] Mohamed A Awadallah, Medhat M Morcos, Suresh Gopalakrishnan, and Thomas W Nehl. A neuro-fuzzy approach to automatic diagnosis and location of stator inter-turn faults in csi-fed pm brushless dc motors. *IEEE Transactions on Energy Conversion*, 20(2):253–259, 2005.

[28] MA Awadallah and MM Morcos. Diagnosis of stator short circuits in brushless dc motors by monitoring phase voltages. *IEEE Transactions on Energy Conversion*, 20(1):246–247, 2005.

[29] Seokbae Moon, Hyeyun Jeong, Hojin Lee, and Sang Woo Kim. Detection and classification of demagnetization and interturn short faults of ipmsms. *IEEE Transactions on Industrial Electronics*, 64(12):9433–9441, 2017.

[30] Kyung-Tae Kim, Yoon-Seok Lee, and Jin Hur. Transient analysis of irreversible demagnetization of permanent-magnet brushless dc motor with interturn fault under the operating state. *IEEE Transactions on Industry Applications*, 50(5):3357–3364, 2014.

[31] Gabriel Forstner, Andreas Kugi, and Wolfgang Kemmetmüller. A magnetic equivalent circuit based modeling framework for electric motors applied to a pmsm with

winding short circuit. *IEEE Transactions on Power Electronics*, 35(11):12285–12295, 2020.

[32] Manel Fitouri, Yemna Bensalem, and Mohamed Naceur Abdelkrim. Modeling and detection of the short-circuit fault in pmsm using finite element analysis. *IFAC-PapersOnLine*, 49(12):1418–1423, 2016.

[33] Jiyu Zhang, Hongyang Yao, and Giorgio Rizzoni. Fault diagnosis for electric drive systems of electrified vehicles based on structural analysis. *IEEE Transactions on Vehicular Technology*, 66(2):1027–1039, 2016.

[34] Mattias Krysander, Jan Åslund, and Mattias Nyberg. An efficient algorithm for finding minimal overconstrained subsystems for model-based diagnosis. *IEEE Transactions on Systems, Man, and Cybernetics-Part A: Systems and Humans*, 38(1):197–206, 2007.

[35] Mattias Krysander and Erik Frisk. Sensor placement for fault diagnosis. *IEEE Transactions on Systems, Man, and Cybernetics-Part A: Systems and Humans*, 38(6):1398–1410, 2008.

[36] Carl Svärd, Mattias Nyberg, Erik Frisk, and Mattias Krysander. Automotive engine fdi by application of an automated model-based and data-driven design methodology. *Control Engineering Practice*, 21(4):455–472, 2013.

[37] Christofer Sundström, Erik Frisk, and Lars Nielsen. Selecting and utilizing sequential residual generators in fdi applied to hybrid vehicles. *IEEE Transactions on Systems, Man, and Cybernetics: Systems*, 44(2):172–185, 2013.

[38] Saeed Hasan Ebrahimi, Martin Choux, and Van Khang Huynh. Real-time detection of incipient inter-turn short circuit and sensor faults in permanent magnet synchronous motor drives based on generalized likelihood ratio test and structural analysis. *Sensors*, 22(9):3407, 2022.

[39] Jongman Hong, Sanguk Park, Doosoo Hyun, Tae-june Kang, Sang Bin Lee, Christian Kral, and Anton Haumer. Detection and classification of rotor demagnetization and eccentricity faults for pm synchronous motors. *IEEE Transactions on Industry Applications*, 48(3):923–932, 2012.

[40] Seokbae Moon, Jewon Lee, and Sang Woo Kim. Demagnetization fault diagnosis of pmsm based on analytic inductance calculation. In *2015 European Control Conference (ECC)*, pages 3186–3190. IEEE, 2015.

[41] Yao Duan and Hamid Toliyat. A review of condition monitoring and fault diagnosis for permanent magnet machines. In *2012 IEEE Power and Energy Society General Meeting*, pages 1–4. IEEE, 2012.

[42] Heung-Kyo Shin, Tae Heoung Kim, and Cherl-Jin Kim. A study on irreversible permanent magnet demagnetization in flux-reversal machines. In *2011 International Conference on Electrical Machines and Systems*, pages 1–4. IEEE, 2011.

[43] Saeed Hasan Ebrahimi, Martin Choux, et al. Modeling stator winding inter-turn short circuit faults in pmsms including cross effects. In *2020 International Conference on Electrical Machines (ICEM)*, volume 1, pages 1397–1403. IEEE, 2020.

[44] Mogens Blanke, Michel Kinnaert, Jan Lunze, and Marcel Staroswiecki. Diagnosis and fault tolerant control, 2016.

[45] Mattias Krysander. *Design and analysis of diagnosis systems using structural methods*. PhD thesis, PhD thesis, Linköping Univ., Linköping, Sweden, 2006.

[46] Mattias Krysander, Jan Åslund, and Erik Frisk. A structural algorithm for finding testable sub-models and multiple fault isolability analysis. In *21st International Workshop on Principles of Diagnosis (DX-10), Portland, Oregon, USA*, pages 17–18, 2010.

[47] Steven M Kay. *Fundamentals of Statistical Signal Processing, Volume II: Detection Theory*. Prentice Hall PTR, 1998.

Paper G

ITSC Fault Diagnosis in Permanent Magnet Synchronous Motor Drives Using Shallow CNNs

Vera Szabo, Saeed Hasan Ebrahimi, Martin Choux, and Morten Goodwin

This paper has been submitted as:

V. Szabo, S. H. Ebrahimi, M. Choux, M. Goodwin. ITSC Fault Diagnosis in Permanent Magnet Synchronous Motor Drives Using Shallow CNNs. In *Proceedings of 23rd International Conference on Engineering Applications of Neural Networks*, 2022. ISSN: 1865-0937.

ITSC Fault Diagnosis in Permanent Magnet Synchronous Motor Drives Using Shallow CNNs

Vera Szabo, Saeed Hasan Ebrahimi, Martin Choux, and Morten Goodwin

Department of Engineering Sciences
University of Agder
NO-4879 Grimstad, Norway

Abstract – Due to its features, permanent magnet synchronous motor (PMSM) has gained popularity and is used in various industrial applications, including those with high downtime costs like offshore equipment. Inter-turn short-circuit (ITSC) fault is one of the most typical PMSM faults and therefore is its early diagnostics in real-time highly valuable. Solving the problem using conventional signal, model-based, or data-driven approaches faces challenges such as computational complexity, time demand, or need for detailed domain expertise. This paper presents a computationally simple, robust, and accurate method based on the 2D convolutional neural network (CNN). The proposed data-driven model has first been validated with the help of experimental data obtained from an inverter fed PMSM subject to ITSC faults in different time intervals, and secondly its performances have been compared to a model-based structural analysis approach using Dulmage-Mendelsohn decomposition tool. The comparison is based on the same data. Results show that the accuracy of the CNN model for diagnosing early faults is more than 98% without doing additional comprehensive fine-tuning. In addition, the paper presents a robust method that can be successfully used as a metric for fast fault detection benchmark.

G.1 Introduction

Permanent magnet synchronous motors (PMSMs) are deployed in various industrial systems, such as offshore equipment, wind generators, robotics or electric vehicles. While having conventional three phase windings in the stator, PMSMs produce their rotor magnetic flux by the mean of permanent magnets, either embedded tangentially around the rim of the rotor as seen in Fig. G.1, or buried radially for higher performances. Their efficiency (92% - 97%) is significantly higher compared to traditional asynchronous motors (75% - 92%) [1], while low reactive power consumption, improved dynamic performance, light weight, and small dimensions are further reasons for their increased popularity. More than 40% of all faults in synchronous motors start as stator related [2]. Among those, the inter-turn short-circuit (ITSC) faults are the most common, however difficult to detect automatically [3], which is partially caused by ITSC faults having little effect to the motor performance in early stages. However, if not discovered and mended in time, the ITSC fault can quickly grow into severe motor damage and consequently lead to total failure

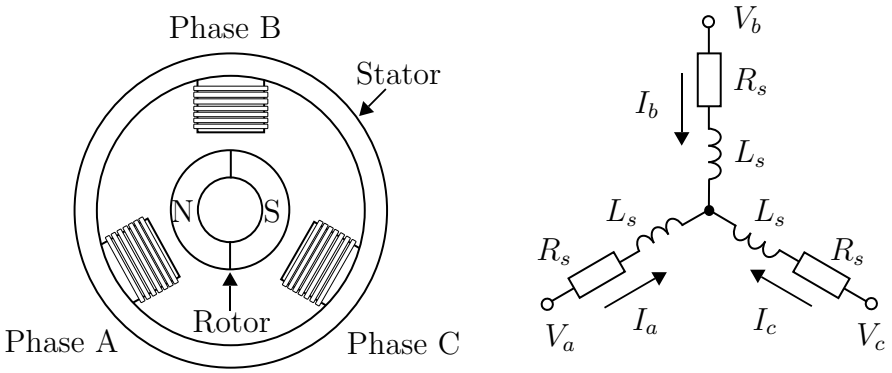

Figure G.1: Basic structure of a PMSM

of the system [4]. The drive to cut operating and maintenance costs and increase operational safety is pushing the agenda in the industry towards the adoption of predictive maintenance strategies. In this process, fault diagnosis, i.e. fault detection and isolation, represents an important part. A proven method for diagnosis of ITSC faults in their early phase, that is easy to implement in practice, is therefore in great demand.

This paper focuses on a simple detection and diagnosis method for ITSC faults. While deep CNNs have several layers, often of various types, shallow CNNs have only one besides the input and the output layer. One objective of this study is to explore whether the simplest CNNs can be successfully used as ITSC fault classifiers, i.e with high enough accuracy, as they do not overfit on small datasets and require less computational time and energy consumption than deep CNNs. Indeed, awareness about CO_2 emission in machine learning research started to arise lately [5]. According to the EU Annual Report on SMEs (2019), in the EU just 6% of the SMEs use AI, although they represent 99.8% of all enterprises in the EU-27, with lack of skill to be one of the main obstacles. Therefore, any model that is easy to use, does not require high computational power and shows robustness is of huge demand by the industry. Following a short literature overview in section 2, the proposed method is described in section 3 while section 4 details the results and compares the performances with a model-based method using the same experimental setup and dataset. Finally, conclusions are drawn in Section 5.

G.2 Literature Review

Fault diagnosis can be divided from data processing into model-based, signal-based and data-driven methods. The literature on PMSMs show that faults, as for example inter-turn short circuit or demagnetisation faults, can be early detected using either of the methods. Comprehensive reviews of methods for detection and diagnosis of ITSC faults in PMSMs are presented in [3] and [6].

The model-based methods establish a mathematical model based on principles of physics that describes the actual machine. The most accurate results have been achieved with finite element analysis (FEA) models which compared to other models also have the highest computational cost as well [6]. Other types of models, such as equivalent circuit,

field reconstruction and linear PMSM models, are beneficial in understanding how the fault behaves assuming that they are detailed enough [3]. The signal-based and data driven methods use statistical tools and mathematical transformations to identify and extract fault patterns from signals such as current, voltage, vibrations and so on. Motor current signal analysis (MCSA) is the most common model and is extensively studied [6].

Artificial intelligence (AI) and machine learning (ML) -based approaches show increased performance compared to conventional signal-based models providing a solution for the complexity introduced by increased data quantity. However, it is often not easy to apply traditional ML techniques in practice, due to lack of efficient methods to obtain training data, and specific knowledge needed to train the models [7, 8]. The traditional ML with tailor made and handcrafted features — typically used by applying feature extraction and learning algorithms such as support vector machine (SVM), random forest (RF), principle component analysis (PCA) or linear decrement analysis (LDA) [9] — has been used for many years while deep learning (DL) methods emerged in 2006.

DL represents a breakthrough in the field of AI and shows state-of-the-art performance when compared to traditional machine learning in many fields. Constructing a ML system needs careful engineering and high domain expertise to design a feature extractor that transforms the raw data into a suitable representation from which the learning model can detect or classify patterns [10].

In contrast, when it comes to DL, the features are learned automatically from raw data. DL models used in motor fault detection and diagnosis include for instance deep belief networks [11], generative adversarial networks (GAN) [12, 13], long short term memory models (LSTM) [14]. Among DL methods for fault diagnosis, extensively used are CNNs [15]. 1D CNNs are, among others, used with direct input of time-domain signals collected in motors [16,17], while 2D CNNs are, among others, used by converting the time-domain raw signals into 2D grey images without further feature extraction [18].

G.3 The proposed Method

This section presents the proposed data-driven method based on a shallow 2D CNN. The input to the model is obtained from an experimental setup where a PMSM is run through a healthy and three faulty sequences. Switching the faults on and off is done by controllable relays placed between the winding taps. The three faulty sequences represent the three ITSC faults. Each fault is applied on a designated phase by short-circuiting different numbers of turns, resulting in different fault percentage, enabling establishing a fault of less than 1% in terms of number of short-circuited turns per total number of turn in one phase. Altogether, ten different features (four voltages, four currents, position of the rotor and speed) in their raw form, without any prepossessing, have been used as input to the model.

CNNs, primarily used for pattern recognition tasks, especially within images, usually consist of three types of layers: convolutional, pooling, and fully-connected layers. As the name indicates, the convolutional layers play the most important role, where the learnable parameters origin from kernels. The structure of the proposed classification

Table G.1: Motor parameters

Parameter	Value
Rated DC bus voltage	280 V
Rated rms phase current	5 A
Rated output torque	7 Nm
Rated speed	1500 rpm
Stator resistance	0.8 Ω
Stator inductance	0.5 mH
Rotor inertia	30.065 kgm^2
Pole pairs	2

model is outlined in Fig. G.2. It has only one convolutional layer. The output of the model is one of the 4 classes: no-fault and ITSC faults at phases A, B and C. We use SHAP

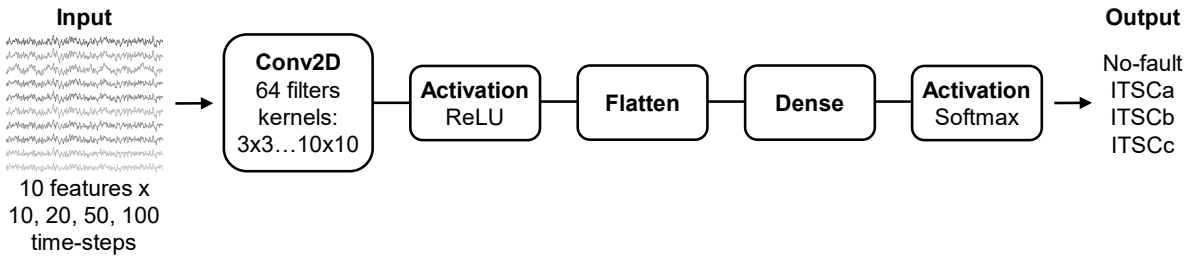

Figure G.2: The proposed shallow 2D CNN architecture

(Shapley Additive exPlanations), a method introduced in 2017 [19] to explain individual predictions of models on global and local level. On the global level it can show which features contribute to the model output and how significant their contribution is. On the local level it can examine each data point and investigate why the model made a certain decision.

G.4 Experiment and Results

The proposed method has been validated on the experimental setup used in [20], i.e. with a 4-pole PMSM whose parameters are given in Table. G.1. Each of the motor phase windings consists in two coils of 51 turns in series, with hence 102 turns per phase. As shown in Fig. G.3, ITSC faults have been applied on each phase by short-circuiting different number of turns resulting in a different fault percentage at each phase as shown in Table. G.2. The experiment lasted for 20s with sampling time for data acquisition of 50μs. ITSC faults in phase A, B and, C were applied in the time intervals $t = 4.471 - 7.238$s, $t = 9.613 - 12.760$s and, $t = 15.600 - 18.410$s respectively, see Fig. G.4. The 10 inputs of the model are shown in Fig. G.5 around the transition between the no fault region (green) and the ITSC fault in phase A (red) at t=4.471s. Samples of different

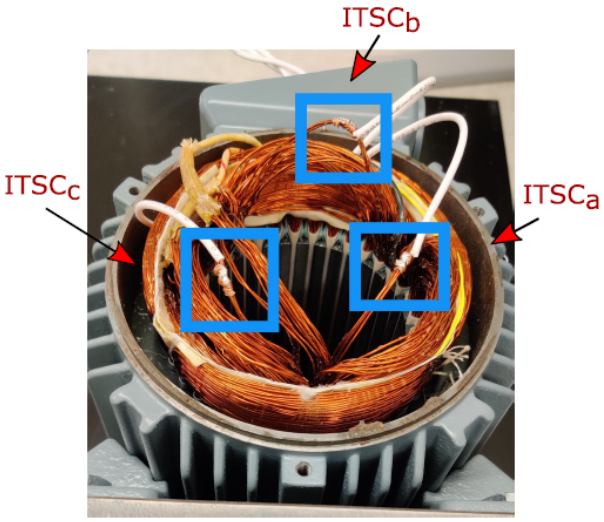

Figure G.3: Applied ITSC faults

Table G.2: Applied ITSC faults per phase

Fault type	Phase	Nr. of short-circuited turns	Applied ITSC fault in %	Nr. of records
ITSCa	A	1	0.89	55300
ITSCb	B	3	2.94	62800
ITSCc	C	5	4.90	56000
No-fault	—	0	0.00	185600

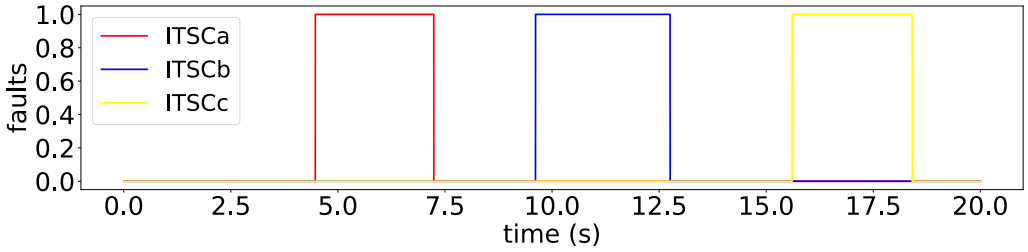

Figure G.4: Timeline of applied ITSC faults

Table G.3: Model attributes - approach 1

Sample length [time-steps]	No. of training samples	Batch size	Learning rate	Average training time [min]
10	25 177	32	0.001	6.14
20	12 588	32	0.001	3.48
50	5 035	32	0.001	2.08
100	2 517	32	0.001	1.37

lengths have been stacked one under the other making a 2D input of size 10 times sample length. The proposed method is evaluated using two approaches:

- Approach 1 - input data as separate non-overlapping samples.
- Approach 2 - input data as overlapping samples using sliding windows.

Sample sizes range over 10, 20, 50 and 100 time-steps corresponding to 0.5, 1, 2.5 and 5 ms. Each model is trained on 500 epochs using kernel sizes from 3x3 to 10x10 in order to achieve optimal results in terms of accuracy, simplicity, computational and energy efficiency. The number of filters has been set to 64. Adam optimizer with learning rate of 0.001 is used for all model configurations. Data has been divided into train and validation/test set in 70:30 ratio after random shuffling, resulting in train and validation/test sets being different for each training session. The final accuracies for the different model configurations have been determined as the average value of accuracies obtained after 30 trainings.

Trainings are performed on 4 NVIDIA Tesla V100 GPUs using Uber's horovod framework for distributed learning on TensorFlow. All available data has been used for training and testing, which results in slightly imbalanced classification due to data size in ratios of 52% (no fault), 15% (ITCSa), 17% (ITSCb), 16% (ITSCc).

G.4.1 Approach 1 - Non-overlapping Samples

This subsection investigates what is the optimal length of the input samples. We start with the simplest approach, slicing the sequences into non-overlapping segments of 10, 20, 50 and 100 time-steps. By using 2D inputs into the convolutional network we expect from the model to find pattern between the different features sampled at the same time. In case of clear patterns, we expect that shorter lengths can deliver as good results as longer ones, potentially even better. The attributes of the model variations, together with the average time needed for training are given in Table G.3 while Table G.4 shows the corresponding validation accuracies. The max accuracies achieved for the best performing models are given in Fig. G.6 and Fig. G.7.

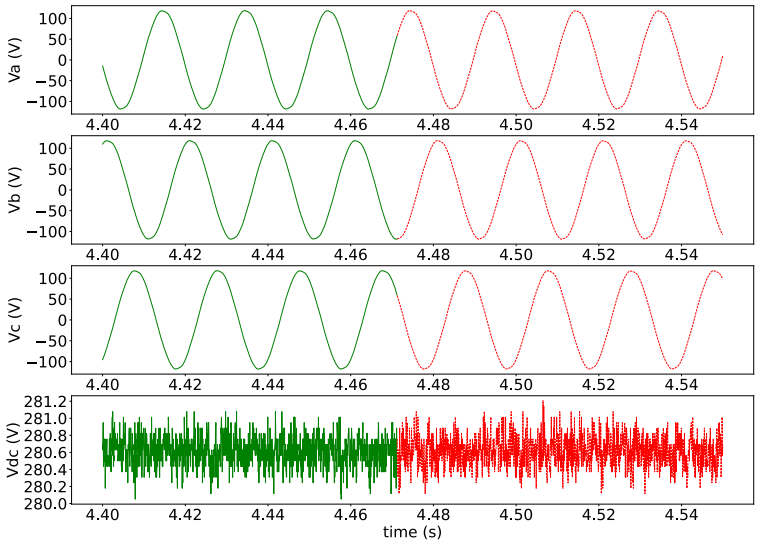

(a) Voltages

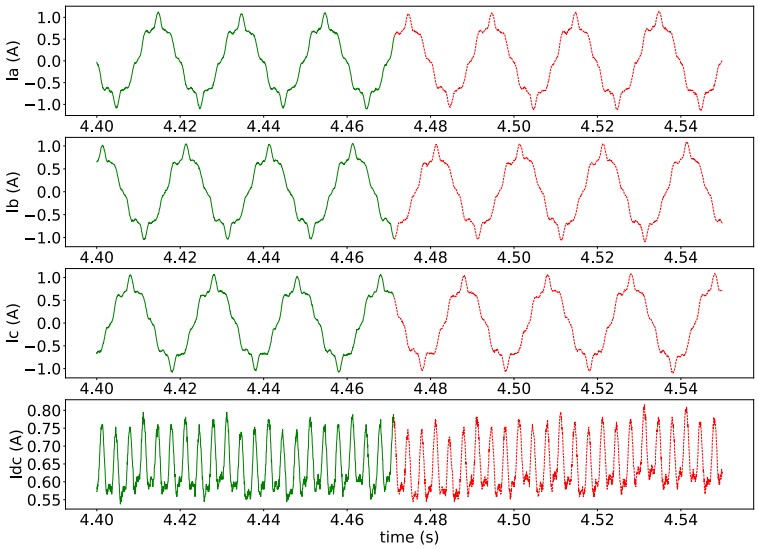

(b) Currents

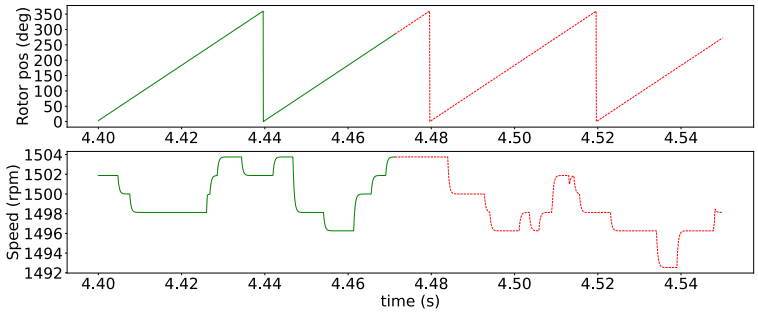

(c) Rotor position and speed

Figure G.5: 10 features - input to 2D CNN.

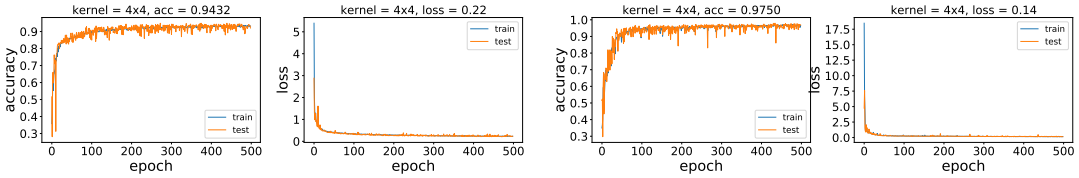

(a) Time-steps = 10

(b) Time-steps = 20

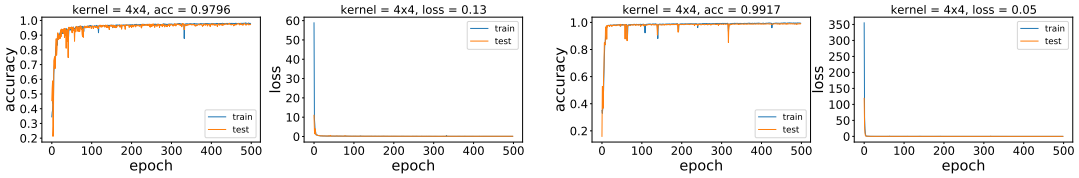

(c) Time-steps = 50

(d) Time-steps = 100

Figure G.6: Best performing models - max accuracies - appr. 1

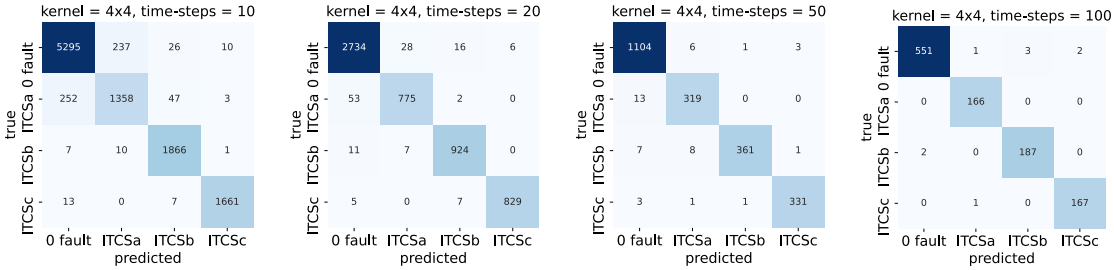

Figure G.7: Best performing models - confusion matrices - appr. 1

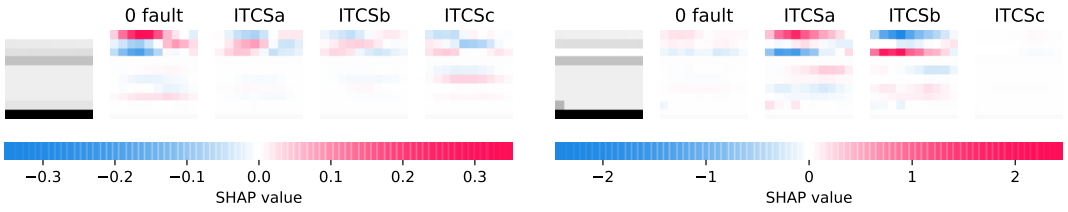

(a) No fault

(b) ITSCa fault

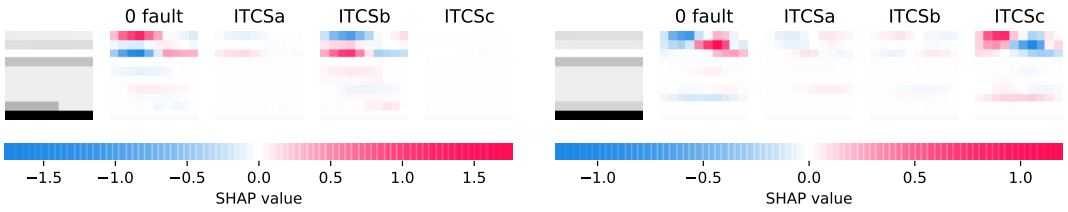

(c) ITSCb fault

(d) ITSCc fault

Figure G.8: SHAP values: kernel = 4x4, time-steps = 10, appr.1

Table G.4: Validation acc. [%] - approach 1

Kernel size	Sample length [time-steps]							
	10		20		50		100	
	μ	σ	μ	σ	μ	σ	μ	σ
3x3	91.00	1.81	94.92	1.76	94.95	2.46	97.91	0.90
4x4	92.46	1.23	96.33	0.95	96.74	0.61	98.42	0.72
5x5	88.16	2.68	94.49	2.53	93.73	4.64	97.32	1.54
6x6	88.26	2.45	94.18	2.82	94.49	2.45	97.04	1.85
7x7	87.81	2.27	94.25	3.74	95.41	0.93	96.36	3.57
8x8	88.00	1.56	94.60	1.12	94.82	2.57	96.60	2.80
9x9	86.68	1.44	92.79	2.15	93.84	2.23	86.11	11.59
10x10	67.20	12.42	61.13	14.73	66.29	15.11	58.96	10.41

G.4.1.1 Discussion

The proposed method results in high accuracies. The accuracy of the models shows general increase with the length of timesteps for all kernels, except for kernels 9x9 and 10x10 that show slight deviation. The best performing model is the one based on 100 time-steps and kernel size 4x4. It achieves an average accuracy of 98.42%. Fig. G.8 shows SHAP values corresponding to four different outcomes: no-fault, and three ITSC faults. As seen, the voltages in phases A, B and C play an important role together with the currents. However, the last two features (rotor position and speed) have a minimum or no impact on the results. Fig. G.8 shows the best performing model for time-steps length of 10, however the conclusions are valid for all models.

G.4.2 Approach 2 - Sliding Windows

In this subsection we investigate whether we can get better results by using overlapping segments of 10, 20, 50 and 100 time-steps. We approximately double the number of train input samples and test whether introducing additional sequences of data gives more information. The model attributes and the validation accuracies are given in Table G.5 and Table G.6. The max accuracies achieved for the best performing models (kernel size 4x4) are given in Fig. G.9 and Fig. G.10.

G.4.2.1 Discussion

This approach shows similar results as approach 1, however it generally achieves slightly lower accuraccies for the same number of epochs (97.47% compared to 98.42%). The best performing model is again the one based on 100 time-steps and kernel size 4x4. Fig. G.11 shows SHAP values for four different outcomes with the same conclusions as earlier. The voltages and currents in phases A, B and C play an important role while the last two features contribute less.

Table G.5: Model attributes - approach 2

Sample length [time-steps]	No. of training samples	Batch size	Learning rate	Average training time [min]
10	50350	32	0.001	12.93
20	25171	32	0.001	7.03
50	10065	32	0.001	3.45
100	5028	32	0.001	2.31

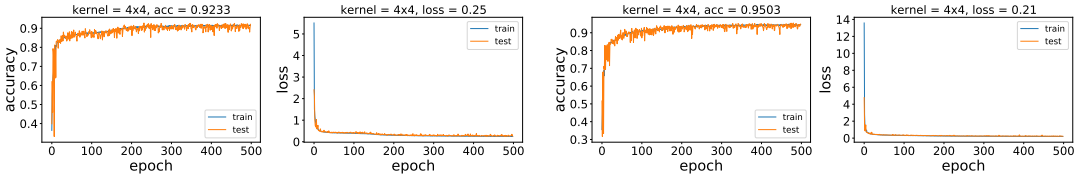

(a) Time-steps = 10

(b) Time-steps = 20

(c) Time-steps = 50

(d) Time-steps = 100

Figure G.9: Best performing models - max accuracies - appr. 2

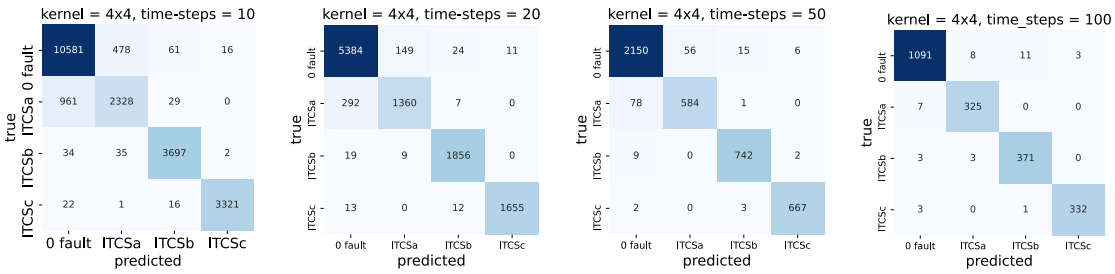

Figure G.10: Best performing models - confusion matrices - appr. 2

Table G.6: Validation acc. [%] - approach 2

Kernel size	Sample length [time-steps]							
	10		20		50		100	
	μ	σ	μ	σ	μ	σ	μ	σ
3x3	89.89	1.42	92.43	1.02	89.52	2.12	95.75	0.89
4x4	90.92	0.90	93.80	0.86	93.83	1.54	97.47	0.51
5x5	86.78	1.72	88.93	2.77	86.96	2.48	92.64	5.87
6x6	87.40	1.67	88.67	2.68	87.76	2.23	95.07	1.74
7x7	87.52	2.13	90.42	0.87	89.64	1.65	94.44	3.10
8x8	87.34	1.79	90.20	1.67	90.32	1.58	95.28	1.24
9x9	87.17	1.74	87.98	1.06	87.77	2.63	88.99	7.20
10x10	67.15	12.33	56.60	10.14	51.61	0.00	58.90	11.16

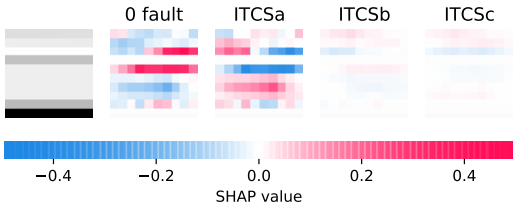

(a) No fault

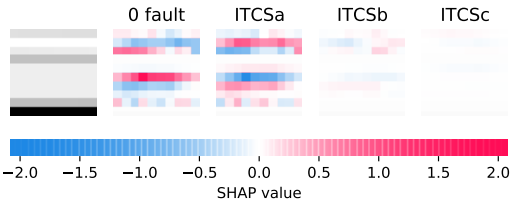

(b) ITSCa fault

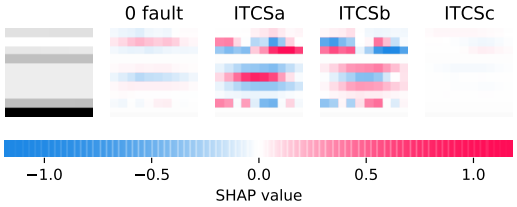

(c) ITSCb fault

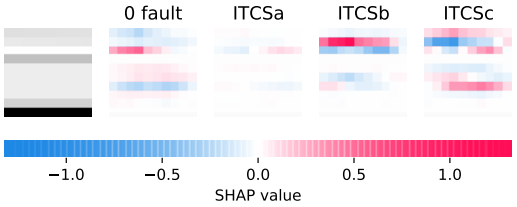

(d) ITSCc fault

Figure G.11: SHAP values: kernel = 4x4, time-steps = 10, appr.2

G.4.3 Comparison with Model-based Approach

The main difference between data-driven (NNs) approach and signal- or model-based approach is the need of a priori understanding of the system. While both signal- and model-based approaches require a deep domain knowledge of the underlying system, data-driven approach discovers dependencies automatically. However, large amount of historical data for training the models, both healthy and faulty, is needed which is usually not available in such scale. Moreover, producing such data comes with high cost.

A model-based approach developed on the same underlying data [20] is used in this secton to allow for direct comparison. This method relies on structural analysis, where a dynamic mathematical model of the system is presented in matrix form, and where Dulmage-Mendelsohn decomposition tool has been used to extract small redundant parts and to design the error residuals further used for detection of the three ITSC faults

Table G.7: Best performing model - appr. 1 - performance metrics

	Binary classification	Multiclass classification			
Metrics	No-fault/fault	ITSCa	ITCSb	ITSCc	W. avg
Precision	0.9843	0.9722	0.9759	0.9900	0.9793
Sensitivity	0.9883	0.9960	0.9713	0.9839	0.9832
Specificity	0.9852	0.9948	0.9949	0.9982	0.9959
F1 score	0.9863	0.9839	0.9736	0.9870	0.9812
P_D	0.9883	0.9960	0.9713	0.9839	0.9832
P_{FA}	0.0148	0.0052	0.0051	0.0018	0.0041
Support	557/523	166	189	168	-

through a statistical test based on the generalized likelihood ratio test (GLRT). This approach has achieved detection rates (P_D) of 60.93% for ITSCa, 98.13% for ITSCb and 100% for ITSCc fault, given that the probability of false alarm (P_{FA}) has been set to 2%. It should be noted that this approach only detects the presence of the fault but does not distinguish among types of faults.

The achieved overall detection rate of the 2D CNN model presented in this paper is 98.83% when calculating on the best performing model. The overall and the detection rates for ITSCa, ITSCb and ITSCc faults, together with other performance metrics are shown in Table. G.7. The main limitation of the model is the need for sufficient amount of training data, especially faulty data that can be challenging to obtain outside of experimental setup.

G.5 Conclusions

This paper presented a straightforward method for detection and diagnosis of ITSC faults in PMSMs based on shallow 2D CNNs that compared to a model-based method showed a few advantages. The main advantage shown is the ability to deliver high accuracies without high calculation cost and without need for any feature pre-processing. In the future work, we intend to implement this type of approach to real-time monitoring of the motors located on an offshore rig. The input data is available, however not used and offered to customers as a service, mainly due to lack of a robust and easy to implement modeling. In addition, companies face a challenge during the official accreditation of the service due to the inability to explain the results of the model used. This challenge can be successfully faced with methods such as SHAP briefly outlined in this paper.

References

[1] Karolis Dambrauskas, Jonas Vanagas, Tomas Zimnickas, Artūras Kalvaitis, and Mindaugas Ažubalis. A method for efficiency determination of permanent magnet synchronous motor. *Energies*, 13(4):1004, 2020.

[2] RN Bell, CR Heising, P O'donnell, C Singh, and SJ Wells. Report of large motor reliability survey of industrial and commercial installations. ii. *IEEE Transactions on Industry applications*, 21(4):865–872, 1985.

[3] Yuan Qi, Emine Bostanci, Mohsen Zafarani, and Bilal Akin. Severity estimation of interturn short circuit fault for pmsm. *IEEE Transactions on Industrial Electronics*, 66(9):7260–7269, 2018.

[4] Austin H Bonnett and George C Soukup. Cause and analysis of stator and rotor failures in three-phase squirrel-cage induction motors. *IEEE Transactions on Industry applications*, 28(4):921–937, 1992.

[5] Eva García-Martín, Crefeda Faviola Rodrigues, Graham Riley, and Håkan Grahn. Estimation of energy consumption in machine learning. *Journal of Parallel and Distributed Computing*, 134:75–88, 2019.

[6] Yong Chen, Siyuan Liang, Wanfu Li, Hong Liang, and Chengdong Wang. Faults and diagnosis methods of permanent magnet synchronous motors: A review. *Applied Sciences*, 9(10):2116, 2019.

[7] Andrew KS Jardine, Daming Lin, and Dragan Banjevic. A review on machinery diagnostics and prognostics implementing condition-based maintenance. *Mechanical systems and signal processing*, 20(7):1483–1510, 2006.

[8] Sven Myrdahl Opalic, Morten Goodwin, Lei Jiao, Henrik Kofoed Nielsen, Ángel Álvarez Pardiñas, Armin Hafner, and Mohan Lal Kolhe. Ann modelling of co2 refrigerant cooling system cop in a smart warehouse. *Journal of Cleaner Production*, 260:120887, 2020.

[9] Rui Zhao, Ruqiang Yan, Zhenghua Chen, Kezhi Mao, Peng Wang, and Robert X Gao. Deep learning and its applications to machine health monitoring. *Mechanical Systems and Signal Processing*, 115:213–237, 2019.

[10] Yann LeCun, Yoshua Bengio, and Geoffrey Hinton. Deep learning. *nature*, 521(7553):436–444, 2015.

[11] Xiaoli Zhao, Minping Jia, and Zheng Liu. Semisupervised graph convolution deep belief network for fault diagnosis of electormechanical system with limited labeled data. *IEEE Transactions on Industrial Informatics*, 17(8):5450–5460, 2020.

[12] Sen Wang, Jieqiu Bao, Siyang Li, Hongkui Yan, Tianyao Tang, and Di Tang. Research on interturn short circuit fault identification method of pmsm based on deep learning. In *2019 22nd International Conference on Electrical Machines and Systems (ICEMS)*, pages 1–4. IEEE, 2019.

[13] Yuanjiang Li, Yanbo Wang, Yi Zhang, and Jinglin Zhang. Diagnosis of inter-turn short circuit of permanent magnet synchronous motor based on deep learning and small fault samples. *Neurocomputing*, 442:348–358, 2021.

[14] Fatima Husari and Jeevanand Seshadrinath. Sensitive inter-tum fault identifcation in induction motors using deep learning based methods. In *2020 IEEE International Conference on Power Electronics, Smart Grid and Renewable Energy (PESGRE2020)*, pages 1–6. IEEE, 2020.

[15] Jinyang Jiao, Ming Zhao, Jing Lin, and Kaixuan Liang. A comprehensive review on convolutional neural network in machine fault diagnosis. *Neurocomputing*, 417:36–63, 2020.

[16] Turker Ince, Serkan Kiranyaz, Levent Eren, Murat Askar, and Moncef Gabbouj. Real-time motor fault detection by 1-d convolutional neural networks. *IEEE Transactions on Industrial Electronics*, 63(11):7067–7075, 2016.

[17] I-Hsi Kao, Wei-Jen Wang, Yi-Horng Lai, and Jau-Woei Perng. Analysis of permanent magnet synchronous motor fault diagnosis based on learning. *IEEE Transactions on Instrumentation and Measurement*, 68(2):310–324, 2018.

[18] Long Wen, Xinyu Li, Liang Gao, and Yuyan Zhang. A new convolutional neural network-based data-driven fault diagnosis method. *IEEE Transactions on Industrial Electronics*, 65(7):5990–5998, 2017.

[19] Scott M Lundberg and Su-In Lee. A unified approach to interpreting model predictions. *Advances in neural information processing systems*, 30, 2017.

[20] Saeed Hasan Ebrahimi, Martin Choux, and Van Khang Huynh. Real-time detection of incipient inter-turn short circuit and sensor faults in permanent magnet synchronous motor drives based on generalized likelihood ratio test and structural analysis. *Sensors*, 22(9):3407, 2022.